POLYTECHNIC SCHOOL AT THE UNIVERSITY OF SÃO PAULO
GRADUATE PROGRAM IN CIVIL ENGINEERING

TIAGO HADDAD MARUM

ANALYTICAL AND NUMERICAL STUDY ON CONCRETE LOCAL BEHAVIOR IN THRUST PHASE OF TBM-CONSTRUCTED TUNNELS

SÃO PAULO

2022

POLYTECHNIC SCHOOL AT THE UNIVERSITY OF SÃO PAULO
GRADUATE PROGRAM IN CIVIL ENGINEERING

TIAGO HADDAD MARUM

ANALYTICAL AND NUMERICAL STUDY ON CONCRETE LOCAL BEHAVIOR IN THRUST PHASE OF TBM-CONSTRUCTED TUNNELS

Revised Version

Dissertation presented to the Polytechnic School
at the University of São Paulo as a requirement for obtaining
the Master's Degree in Science

Area of Concentration: Civil and Urban Construction Engineering

Advisor: Prof. Dr. Antonio Domingues de Figueiredo
Co-Advisor: Prof. Dr. Luís A. G. Bitencourt Jr.

SÃO PAULO

2022

Este exemplar foi revisado e corrigido em relagao à versão original, sob responsabilidade unica do autor e com a anuencia de seu orientador.

Sao Paulo, 26 de agosto de 2022

Assinatura do autor: TIAGO HADDAD MARUM: 43480627811

TIAGO HADDAD MARUM:43480627811 C=BR, O=ICP-Brasil, OU=AC SOLUTI Multipla v5, OU=18799897000120, OU=Videoconferencia, OU=Certificado PF A1, CN=TIAGO HADDAD MARUM: 43480627811 I am the author of this document your signing location here

Assinatura do orientador:

Catalogagao-na-publicagao

Marum, Tiago Haddad
Analytical and numerical study on concrete local behavior in thrust phase of TBM-constructed tunnels / T. H. Marum -- versão corr. – Sao Paulo, 2022.
170 p.

Dissertagao (Mestrado) - Escola Politecnica da Universidade de Sao Paulo. Departamento de Engenharia de Construgao Civil.

1.TBM-constructed tunnels 2.Precast concrete tunnel segments 3.Thrust phase 4.Splitting behavior 5.Analytical and numerical models I.Universidade de Sao Paulo. Escola Politecnica. Departamento de Engenharia de Construgao Civil II.t.

*Aos meus pais, **Alfredo e Claudia,** que me ensinaram os valores e princípios que levo comigo. Ao meu irmão, **Mateus**, que sempre esteve ao meu lado em todos os momentos. A vocês, que são os maiores incentivadores das minhas conquistas, muito obrigado.*

*À **Luiza**, a melhor companheira que eu poderia ter ao meu lado, que me ajuda a enfrentar as dificuldades, superá-las e me tornar uma pessoa melhor. Muito obrigado por todo amor, carinho, paciência, compreensão e companheirismo.*

AGRADECIMENTOS

À minha família, pelo apoio incondicional ao longo desta jornada, especialmente nos momentos difíceis e turbulentos.

Aos irmãos de consideração Guilherme Paolini e Vinicius Castanho, que me acompanham desde o começo da trajetória acadêmica e contribuíram e contribuem para meu crescimento pessoal e profissional.

Ao professor Antonio Domingues de Figueiredo pelas inúmeras conversas, conselhos, orientação, oportunidades e dedicação ao longo de todos esses anos. Muito mais que um orientador, ele é um amigo e uma referência que tive a sorte de ter encontrado no meio da graduação dentro da Escola Politécnica.

Ao professor e amigo Luís A. G. Bitencourt Júnior pela paciência, dedicação e aceitação do desafio que era introduzir-me ao universo da simulação estrutural e produzir um trabalho multidisciplinar integrado de pesquisa com nível de excelência. A interação com ele contribuiu não somente para o desenvolvimento deste trabalho, como também para o aperfeiçoamento da minha análise crítica como engenheiro.

Ao engenheiro Marco Aurélio Peixoto pelo incentivo, oportunidade e dedicação dados desde a concepção do projeto de pesquisa até as últimas discussões da dissertação.

Aos amigos que participaram do presente trabalho em diferentes etapas, sem os quais não seria possível sua conclusão: Victor Schwenck, Paulo Vitor Calmon, Ricardo Nunhez e Ronney Agra.

Aos professores que me acompanharam em diversas etapas dessa jornada, cujo tempo partilhado, ensinamentos, oportunidades, conversas e conselhos foram de extrema importância pessoal e profissional: Denise D'Abronzo, Jurema, Márcia Martins, João Covenha, Flávio Maranhão, Valério Almeida, Fernando Kurokawa, Luís Fernando de Abreu, Celma de Oliveira Ribeiro, Renata Monte, Pablo Pujadas, Albert de La Fuente, Guilherme Franzini, Alfredo Gay Neto, Pedro Wellington Teixeira e Alexandre Maximiano.

Aos colegas e amigos: Denise Fernanda, Nicole Xavier, Ramoel Serafini, Thiago Moherdaui, Henrique Curci, Alan Estrada, Felipe Santos, Julie, Ludmilly Pereira, Maria Luísa Ribeiro, Yasmin Trindade, Catarina Guido, Larissa Zipoli, Ivan Lúcio Mesquita, Rodrigo Resende, Pedro Augusto Ortiz, Guilherme Eiji, Renan Andrade e Márcio Paixão.

A todos aqueles que mesmo não estando aqui citados fazem parte da minha trajetória.

Muito obrigado!

ABSTRACT

Longitudinal cracks are one of the most frequent and severe damages observed in Tunnel Boring Machine (TBM) constructed tunnels. They often appear in the thrust phase as a result of uneven support and load conditions. In order to excavate the soil and advance, the TBM-hydraulic jacks apply high concentrated loads in the last installed ring, which acts as a reaction frame. It generates splitting stresses in the precast segments which might cause those cracks. In addition, steel reinforcements are used to withstand these stresses. Usually, the design of these structural members under jack thrust of TBM are performed based on the finite element method and strut-and-tie theory. The present work aims to discuss the applicability of these models to predict splitting in precast concrete tunnel segments and its comparison with experimental results available in the literature. Considering this purpose, a literature review about experimental tests is made to summarize and comprehend different characteristics tested and to standardize notation evolving material parameters and specimens' dimensions. The comparison of the analytical models to predict splitting is carried out by a statistical analysis concerning the difference between models' predictions and the experimental results. Also, a numerical modeling approach is used to simulate the effect of reinforcement by discrete fibers on the mechanical local behavior, with a focus on cracking initiation. From the statistical analysis the study suggested two different analytical models with corrections to estimate the load to initiate splitting in concretes. These models with the suggested corrections can be used to design precast segments considering concrete parameters. As for the post-cracking behavior, the study concluded that numerical modeling approach adopted was proven useful to evaluate and represent the reinforcement response with sensitivity to variations in fiber content and damage patterns. The results obtained can help to reduce costs related to repair interventions on TBM tunnels construction, once they're related to ensure a better cracking control in the most critical construction phase of these tunnels, the thrust phase.

Keywords: TBM-constructed tunnels, thrust phase; splitting behavior; precast segments; concentrated load; analytical model; finite element model.

LIST OF FIGURES

LIST OF TABLES

SUMMARY

1 INTRODUCTION

Urban mobility problems have been growing in big cities while collective underground transportation has gained a bigger role in the metropolis scenario. The expansion of the subway system is a good alternative to soften the road mesh problems.

The Tunnel Boring Machines (TBMs) construction technique has proven to be effective and socially acceptable in many situations and, especially, in challenging environments like soft grounds (Lance, 2006), and its use can be adapted depending on geological and hydrological conditions (Bäppler, 2016) which may vary in long tunnels projects. The machine excavates and assembles precast concrete segments to form the lining. In order to advance, the last installed ring works as a reaction frame receiving the load applied by the TBM to perform the excavation.

The precast segments must be designed to withstand transitional loads in construction stages such as demolding, stocking, transportation, handling and thrust phase. Figure 1 shows these main construction stages.

Figure 1-Transitional loads in construction stages of a TBM tunnel: (a) demolding, (b) handling, (c) stocking, and (d) transportation. (de la Fuente, 2017)

As studied in Sugimoto (2006), the thrust phase can be associated with the most frequent and severe damages observed in practice. The major segment damages are cracks in the

longitudinal direction of the tunnel and chipping of the segment corner. The latter is a result of contact deficiency on longitudinal joints and/or mishandling during installation (Cavalaro *et al*. (2011)). The longitudinal cracks are related to the high compression loads applied by the thrust jacks (CEB-FIP, 2017), the support conditions of the segments (Cavalaro *et al.*, 2012) and loading conditions, such as jacks' configurations and eccentricity (Waal, de, 2000).

De Waal (2000) presents different possibilities of configurations for the TBM jacks and the stress pattern for each one during push off on the tunnel segment (Figure 2). Groeneweg (2007) indicates these conditions using the denomination commonly used in Europe: the German and the French thrust jack configurations (Figure 3). In addition, the same author also indicates the effectiveness of French configuration to spread the introduced jack forces when compared to the German one, contributing to its major use in tunnel segments.

Figure 2 – Different possibilities of jacks' configuration during thrust phase of a TBM tunnel (Waal, de, 2000)

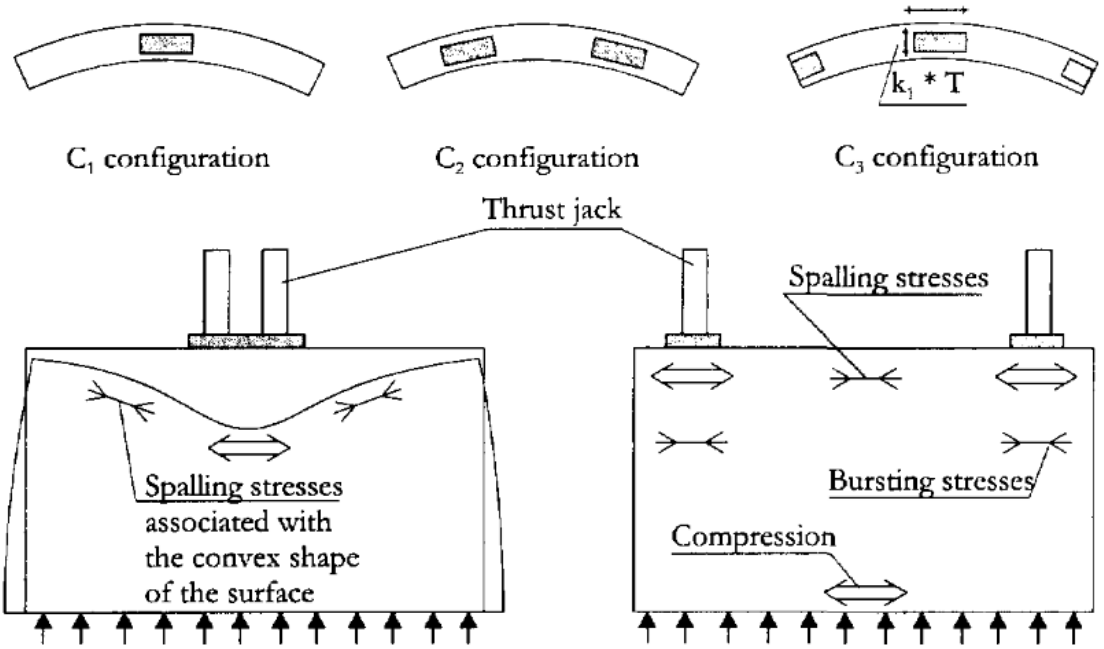

Figure 3 – German and French TBM thrust jack configurations (Groeneweg, 2007)

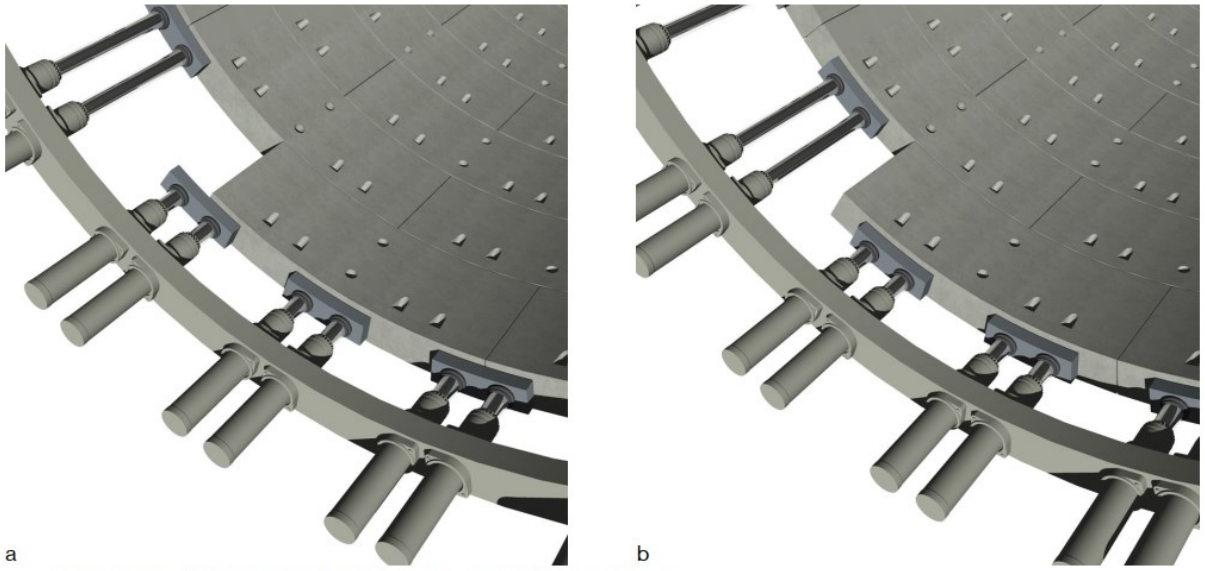

Thrust jack configurations: a) German method; b) French method

The eccentricity conditions (internal and external face of a segment) and the inclination between segment and thrust jack are discussed in Burgers (2006). Different support conditions (both for normal or uneven support) for segments tested in laboratory can be found in Sorelli and Toutlemonde (2005), Burgers (2006), Poh *et al*. (2009), Cavalaro *et al*. (2011) and Beno and Hilar (2013). Figure 4 shows some of these conditions. The variety of segments

configurations leads to different stress distributions and, consequently, different cracking patterns, as illustrated in Figure 5.

Figure 4 - Different support conditions for segments tested in laboratory available on in the literature: a) Sorelli and Toutlemonde (2005); b) Burgers (2006); c) Poh *et al*. (2009); d) Cavalaro *et al*. (2011); and e) Beno and Hilar (2013)

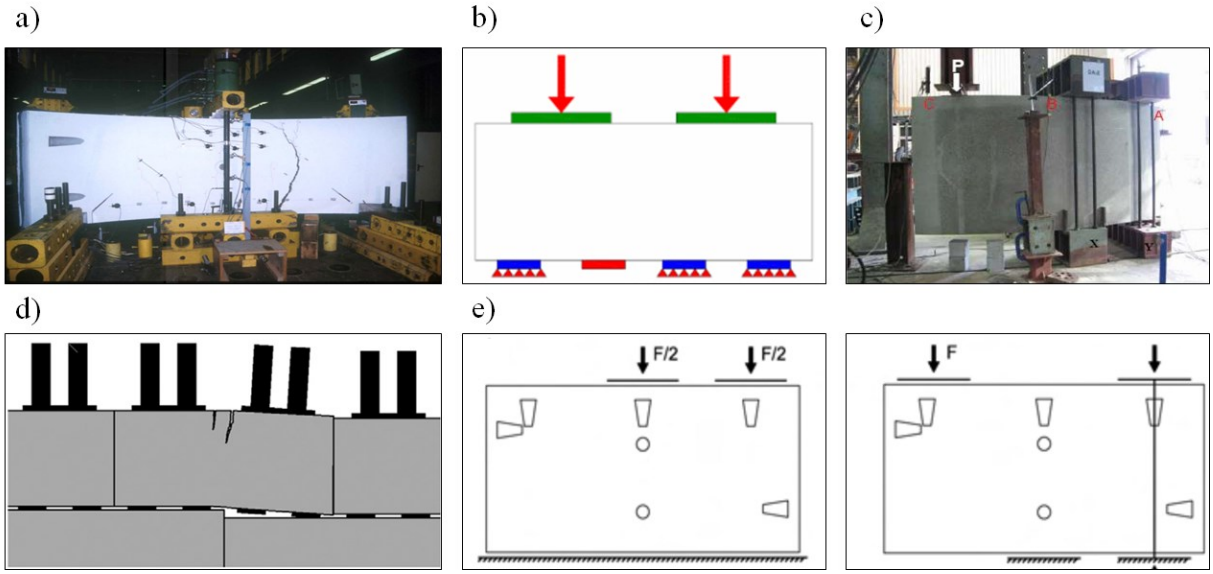

Figure 5 - Different stress distributions and cracking patterns: a) Groeneweg (2007); b) Liao et al. (2015); c) Hillar *et al*. (2012), d) Beno and Hilar (2013); and e) Poh *et al.* (2009)

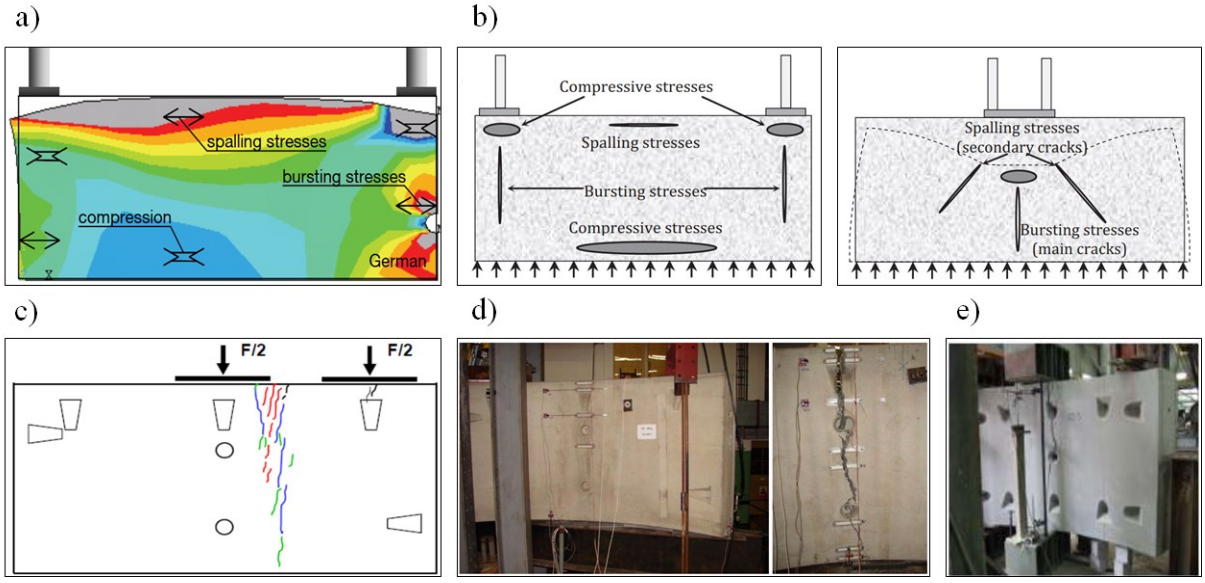

The combined effect of TBM high-concentrated loads for each segment can lead to tensile stresses in tangential and radial directions. Concerning the French loading configuration with perfect support conditions, the failure mechanism is described in Groeneweg (2007, p. 56):

> “In case of the French thrust jack configuration this system will occur just like described. By the applied positioning of thrust jacks on the segment, each jack plate is located at the exact centre line of its own half of a segment (two thrust jack plates per segment). Now the thrust jack force of each jack plate is able to spread over the width of its own segmental half and the tensile bursting stresses will appear as described. The high force introduced and the lateral contraction property of concrete result in deformations of the segmental shape close to the thrust jacks. As a result, tensile stresses will appear in the deformed sections and cracks might occur. However, if cracking does occur the deformation is no longer restricted and the tensile stresses will fade away.”

Figure 6 shows the mechanism of stress generation proposed by Groeneweg (2007). The spreading of compression (represented as elastic compressive trajectory lines) in both directions (tangential and radial) is shown in Figure 7.

Figure 6 – Stress pattern for French TBM load configuration – adapted from Groeneweg (2007)

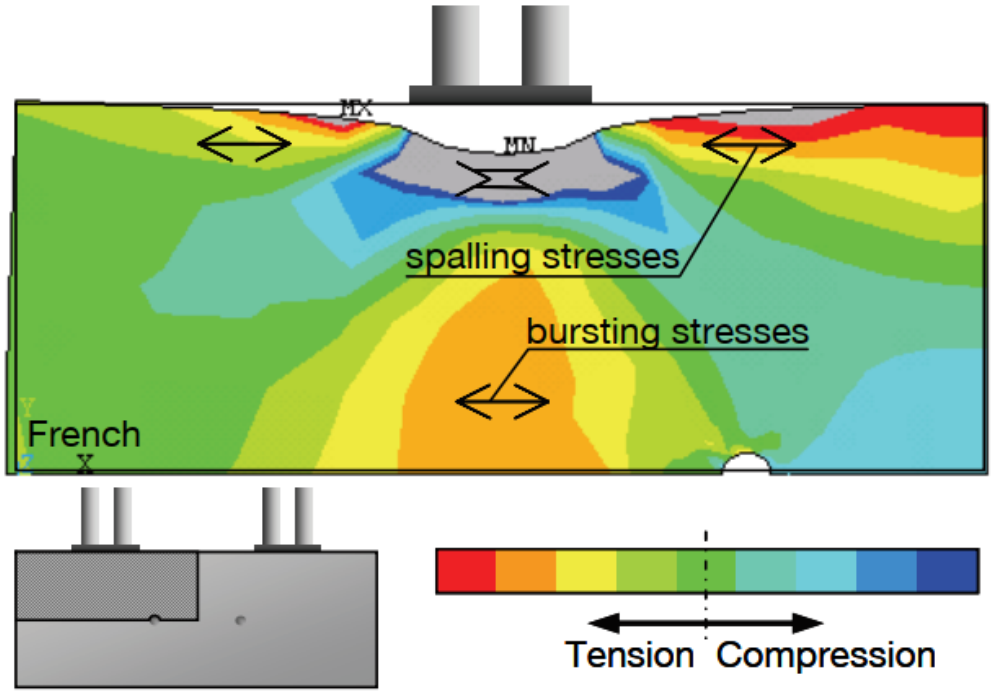

Figure 7 – Compression stress trajectories in tangential and radial directions – Groeneweg (2007)

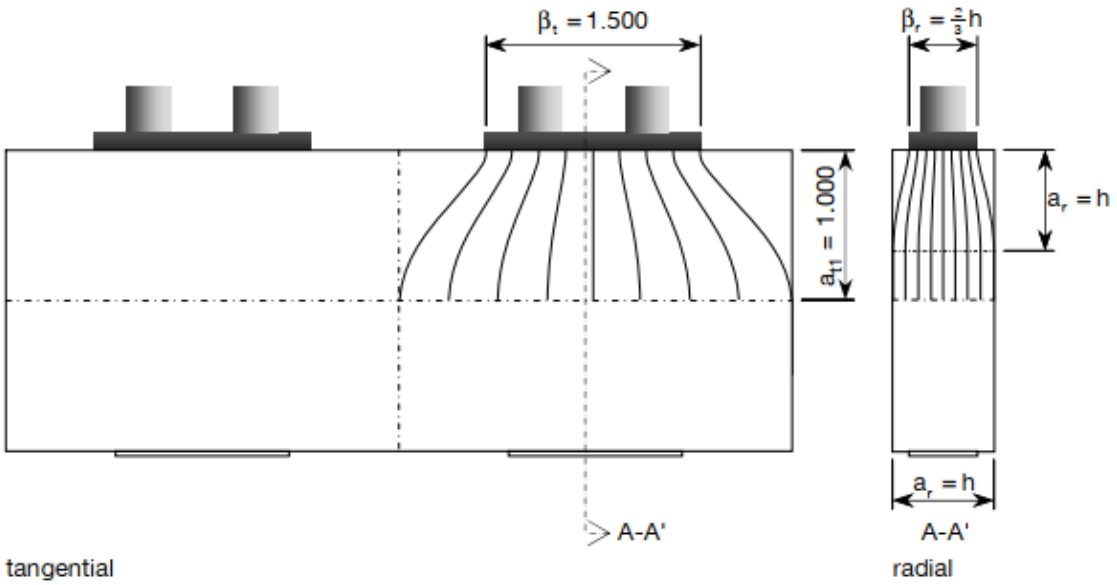

Concerning this pattern distribution, the fib Bulletin 83 – Precast tunnel segments in fibre-reinforced concrete: state-of-the-art report (2017) proposes two different levels of investigation for TBM thrust phase: local and global segment behavior. The first one corresponds to stress concentrations under or between the actuators. The global one is normally related to the

distribution of the highly-concentrated loads throughout the middle-plane of the segments and strictly depends on the boundary conditions placed on them.

For local segment behavior, two types of cracking can occur: splitting (or bursting) and spalling cracks. The splitting is located under the bearing pads and the spalling is characterized by its location between the jacks. Figure 8 shows the transverse stress distribution in centerlines (center load lines and block centerline) in a schematic representation and an experimental result from testing a concrete block.

Figure 8 – Splitting and spalling phenomena – Conforti *et al*. (2016a)

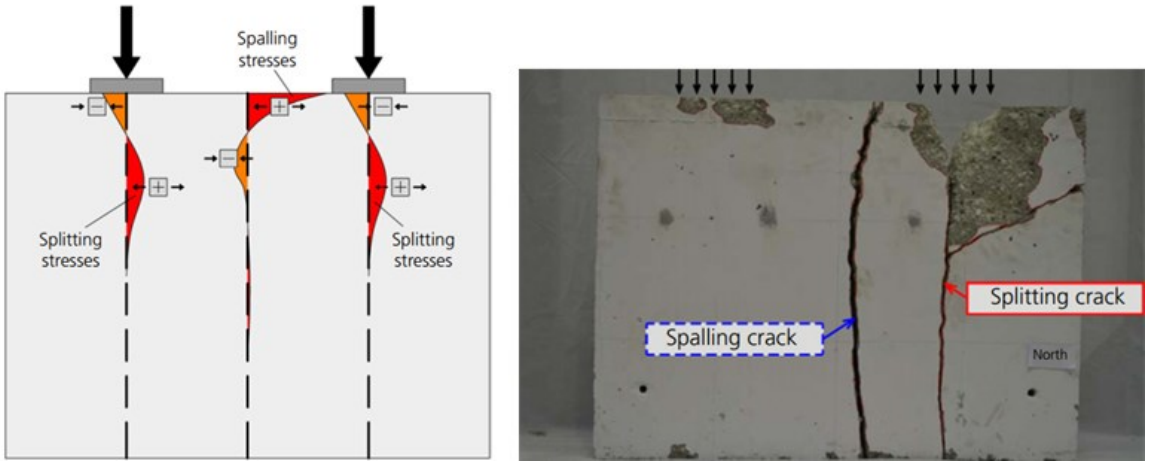

When analyzing the splitting phenomena, as described by Groeneweg (2007), the stress pattern presents some discontinuities. In concrete structures, such discontinuities can occur due to concentrated loads, support conditions and geometrical discontinuities (such as holes and connections). The regions with these stress discontinuities are called ‘’D regions’’. Saint-Venant’s Principle states that the stress fields that are distant to the region in which loading is being applied, do not depend on the applied load distribution itself. It is not a true principle but a property of the static solutions concerning the linear elasticity theory. According to this principle, these ‘’D regions’’ are limited by a ‘’disturbance length’’ which has approximately the magnitude of the cross-section dimensions.

The regions that are distant to the applied loads or to the geometrical discontinuities are called ‘’B regions’’ and in such, Bernoulli’s hypothesis validates a linear strain distribution along the cross section. In this sense, the stress pattern at the base of the segments depends on the relation between segment width and length: when there is enough length to spread the compressive stresses to a uniform distribution, and when there is not enough length to spread the stresses. Figure 9 shows the spreading of compressive stresses to a uniform compressive

stress distribution after the disturbance length and Figure 10 shows an assumption made in García (2012) and employed by Liao *et al*. (2015) to compressive distribution at the concrete element base of an element with no distance to achieve the “B region”.

Figure 9 – State-of-stress in the D region beneath the loading bearing plate, adapted from He and Liu (2010)

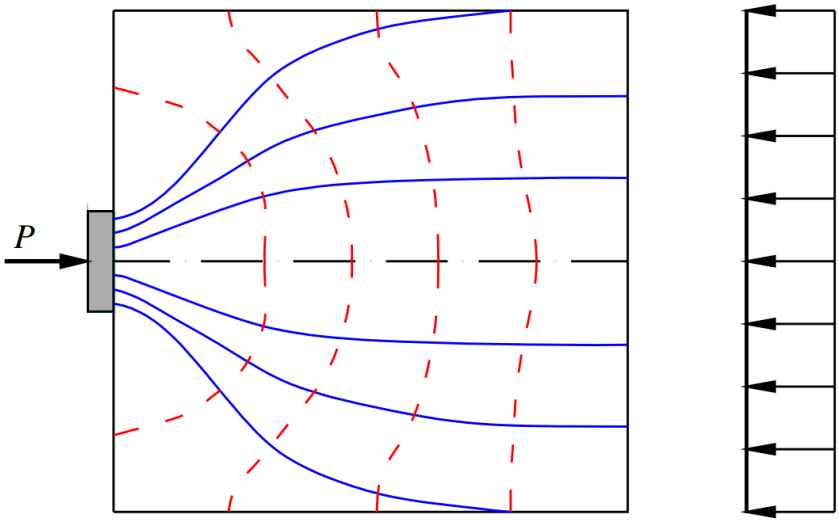

Figure 10 – Linear stress distribution at a base of a concrete element with width smaller than its length – García (2012)

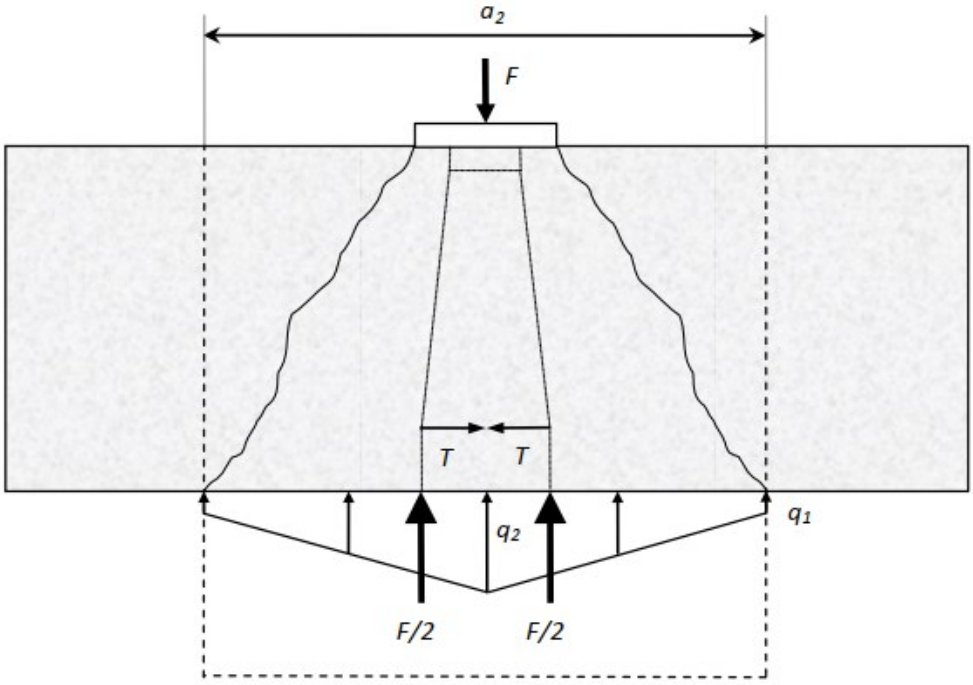

Due to the brittle behavior of concrete, especially in tension, the precast segments are reinforced to withstand the tensile stresses. The reinforcement can be done with steel bars (rebars/conventional reinforcement), fiber reinforcement or hybrid reinforcement (rebars and

discrete fibers). Many studies have presented the benefits of adding fibers in concrete as an application to TBM-constructed tunnels (see Bulletin 83 – Precast tunnel segments in fibre-reinforced concrete: state-of-the-art report (2017)). The studies have proven that fiber reinforcement enables a stable development of cracks; a reduction in crack widths (in comparison to conventional reinforcement) and a local re-distribution of the stresses generated during the advance, increasing bearing capacity and toughness of the elements.

Many researches have performed studies focusing local and global segment behavior with varying reinforcement strategies. More specifically to study the splitting phenomena, several experimental campaigns on small and full-scale specimens are available in the literature. Numerical modeling based on the finite element formulation has also been used to improve splitting study and to provide more accurate predictions. The approaches used are commonly related to discrete and smeared crack models to simulate concrete mechanical behavior. As an example of using numerical modeling to predict the splitting structural response, more recently, Neu *et al*. (2022) proposed a reliability-based optimization for the steel fibers in tunnel lining segments subjected to thrust loads.

Besides the experimental campaigns and numerical models, several analytical models, such as the strut-and-ties models or models based on two-dimensional elasticity theory or concrete plasticity theory have been proposed to predict splitting in concrete segments subjected to concentrated forces. Some of these models are adapted for design purposes.

Considering the lack of an integrated analysis between the different approaches to predict splitting in precast concrete tunnel segments, the present work contributes for the investigation of the applicability of the numerical and analytical models. To achieve this objective, the use of experimental results obtained in literature was an important factor that needs to be taken into account.

2 OBJECTIVES

The main objective of this work is to discuss the applicability of analytical models to predict splitting in segmental tunnel linings, and to assess the capability of a numerical modeling approach to consider the effect of discrete fibers on the local mechanical behavior with focus on cracking initiation.

The following specific objectives are listed below:

- Review the available experimental campaigns related to precast segments under concentrated loads to summarize and comprehend different characteristics tested and to standardize notation evolving material parameters and specimens' dimensions
- Review and compare the available analytical models to predict splitting in concrete in order to assess the capabilities and limitations of these models regarding their formulations
- Verify the applicability of these analytical models based on experimental data available in the literature and to indicate which models are more adequate to predict splitting in concrete, regarding possible improvement suggestions
- Numerically simulate the local behavior of concrete tunnel segments for plain and fiber reinforced concrete for better understanding the splitting phenomena with a focus on cracking initiation.

3 LITERATURE REVIEW

3.1 EXPERIMENTAL CAMPAIGNS

This section presents a literature review on experimental campaigns considering several experimental programs related to precast segments under concentrated loads. The experimental studies available in the literature are an important support for the analysis of the analytical and numerical models that are evaluated in this dissertation. Table 1 lists these campaigns.

Table 1 - Literature review on experimental campaigns of precast segments under concentrated loads

Author	Year	Author	Year	Author	Year
Hemmy	2001	Hillar *et al*. and Beno *et al*.	2012, 2013	Caratelli *et al*.	2016
Schnutgen and Erdem	2001	Breitenbücher *et al*.	2014	Conforti *et al*.	2017
Gettu *et al*.	2004	Abbas *et al*. and Nehdi *et al*.	2014, 2015	Conforti *et al*.	2019
Sorelli and Toutlemonde	2005	Tiberti *et al*.	2015	Meda *et al*.	2019
De Rivaz and De Rivaz *et al*.	2008, 2009	Liao *et al*.	2015	Spagnuolo	2020
Poh *et al*.	2009	Meda *et al*.	2016	Trabucchi *et al*.	2021
Caratelli *et al*.	2011	Conforti *et al*. (a)	2016		
Caratelli *et al*.	2012	Conforti *et al*. (b)	2016		

Comprehensive parametric studies have been done in these campaigns. The studies can be divided into two main groups according to the specimens such as concrete blocks and full/partial-scale specimens (testing concrete segments with curvature). A layout of geometrical dimensions for both cases is proposed, as illustrated in Figure 11, where “t”, “b”, “h” are the specimens’ thickness, base length and height, respectively. The parameter “c” is a dimension created for indirectly measure segments curvature and “b_{int}” is an internal base length of the segments.

Figure 11 – Layout of geometrical dimensions for concrete blocks and full/partial-scale segments

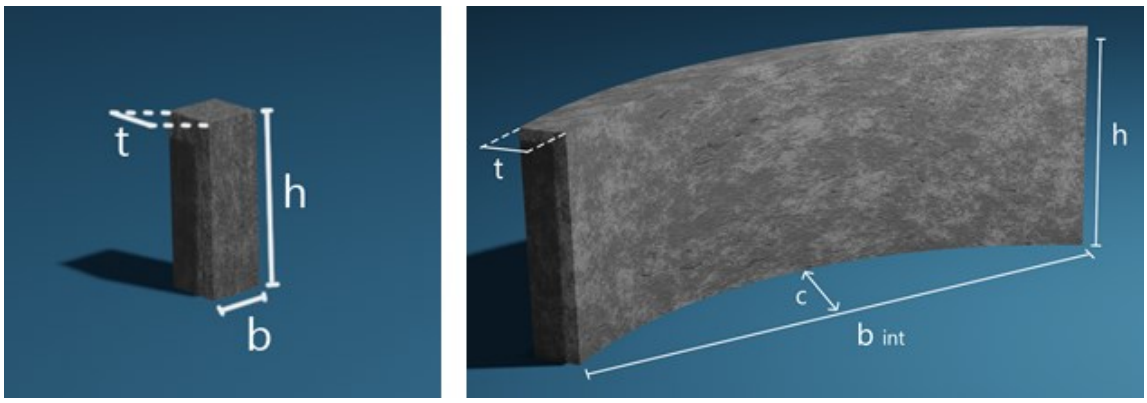

Table 2 shows the geometrical dimensions of concrete blocks and Table 3 lists the parameters for concrete segments. In the latter, the parameter "b" indicates the specimen's length at the mid-surface, "b_1" corresponds to the loading pad length and "f_c" the concrete compressive strength.

Table 2 – Geometrical dimensions and compressive strength of concrete blocks in experimental campaigns

Author	b(mm)	b_1(mm)	h(mm)	t(mm)	f_c (MPa)
Hemmy (2001)	3000	-	1000	300	60
Schnutgen and Erdem (2001)	350	150	700	350	60
Gettu *et al*. (2004)	520	520	900	175	50
Breitenbucher *et al*. (2014)	150	50,75,100	300	150	75-95
Tiberti *et al*. (2015)	250	100	750	250	50-60
Liao *et al*. (2015) - b200	200	50,150	300	150	40-50
Liao *et al*. (2015) - b250	250	50,150	300	150	40-50
Liao *et al*. (2015) - b400	400	150	300	150	40-50
Liao *et al*. (2015) - b750	750	150	300	150	40-50
Conforti *et al*. (a) (2016)	250	100,150	750	250	40
Conforti *et al*. (b) (2016)	1000	100,150	750	150	50-60
Trabucchi *et al.* (2021)	250	100	750	250	35-40

Table 3 – Geometrical dimensions and compressive strength of concrete segments in experimental campaigns

Author	b(mm)	b_1(mm)	h(mm)	t(mm)	c(mm)	b_{int}(mm)	f_c (MPa)
Sorelli and Toutlemonde (2005)	4147	-	1420	300	627	3670	75-100
De Rivaz (2008) and De Rivaz *et al*. (2009)	1840	-	1200	250	-	-	35
Poh *et al*. (2009)	2723	-	1400	700	251	2359	60
Caratelli *et al*. (2011)	3784	946	1500	200	575	3400	50
Caratelli *et al*. (2012)	1840	480	1200	500	217	1468	35
Hillar *et al*. (2012) and Beno *et al*. (2013)	2570	-	1500	500	277	2237	60
Abbas *et al*. (2014) and Nehdi *et al*. (2015)	1042	200	500	100	100	1000	150-170
Meda *et al*. (2016)	3000	-	1400	300	-	-	80
Caratelli *et al*. (2016)	4150	-	1483	250	-	-	50
Conforti *et al*. (2017)	1810	480	1200	500	210	1447	50
Conforti *et al*. (2019)	3020	734	1420	300	-	-	40
Meda *et al*. (2019) and Spagnuolo (2020)	3000	-	1400	600	-	-	50

For the studies presented in Table 2: The specimens' aspect ratio (h/b) varied from 0.33 to 3.00, considering both configurations with more and with less than the disturbance length. Gettu *et al*. (2004) and Breitenbucher *et al*. (2014) presented test setups with load eccentricity. The test setup considered by Conforti *et al*. (2016a) consisted of an axial loading applied by two jacks (equally spaced from center). Only Breitenbucher *et al*. (2014) presented a point line condition for loading application, i.e., an experimental setup in which the loading was not applied entirely along the specimens' thickness. The other campaigns consisted of a test setup with one centered jack in a line load condition with different reinforcement conditions. The concrete compressive strength varied from 40 to 60 MPa for all campaigns, except for Breitenbucher *et al*. (2014), which presented a range from 75-95 MPa. The reinforcement materials used in these campaigns varied from the use of steel to polymeric fibers, conventional reinforcing bars (steel bars), hybrid solutions (reinforcing bars and fibers) or a plain concrete condition (i.e., no reinforcement at all). The steel fibers amount ranged from 35 to 80 kg/m³ and the synthetic ones presented contents around 10 kg/m³. All the concrete blocks were tested under perfect support conditions.

For the studies presented in Table 3: The specimens' aspect ratio (h/b) varied from 0.34 to 0.66. Sorelli and Toutlemonde (2005) tested a setup with extremely off-centered loading. The supports were as widely apart as possible from the axis in order to maximize the bending moment. Poh *et al*. (2009), Hillar *et al*. (2012), Beno *et al*. (2013), Meda *et al*. (2016) and Spagnuolo (2020) tested cantilever configurations for support and/or loading conditions. The other campaigns consisted in test setups with one or two centered jacks in a line load condition with different reinforcement conditions and perfect support. The concrete compressive strength

varied from 35 to 60 MPa for most of the campaigns, except for Sorelli and Toutlemonde (2005), Abbas *et al*. (2014), Nehdi *et al*. (2015), Meda *et al*. (2016). The reinforcement materials used in these campaigns were the same as mentioned in the campaigns showed in Table 2. The content of steel fibers ranged from 10 to 60 kg/m³ and the synthetic ones presented contents around 10 kg/m³. Figure 12 shows two different loading configurations employed in the experimental campaigns mentioned. The experimental results in terms of cracking patterns for the experimental campaigns evaluated are consistent with the main types as spalling or splitting as presented in Figure 5.

Figure 12 – Test setup for experimental campaigns in Hillar *et al*. (2012) and Beno *et al*. (2013) (left) and Caratelli *et al*. (2011)

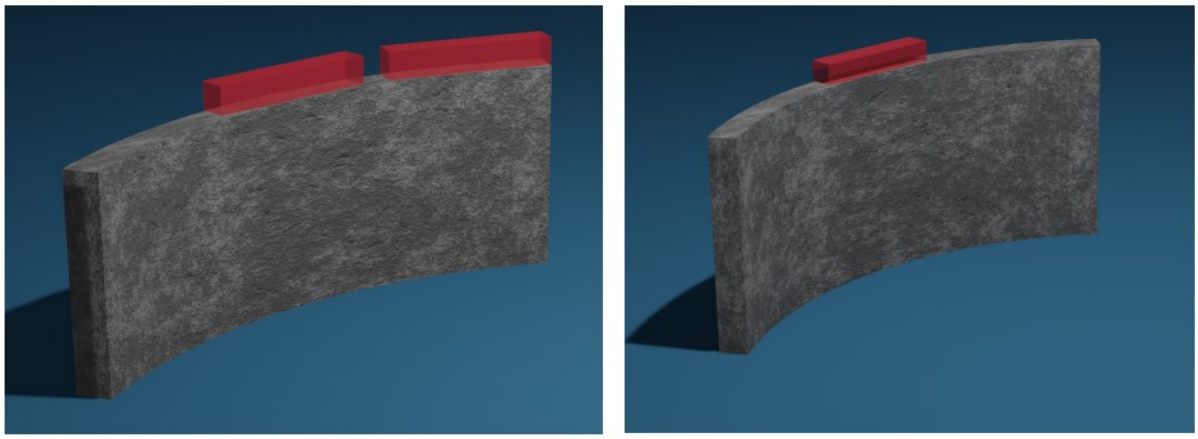

In order to evaluate the applicability of analytical models, the concrete blocks and segments with perfect support conditions and centered jacks were analyzed in terms of splitting loads. Each analytical model gives a formula to estimate the cracking load (denoted by F_{cr}). This analysis is from now on denominated "F_{cr} analysis". The observed splitting cracking loads in the campaigns, either in blocks or segments, are defined as the necessary forces to initiate the splitting cracks process in the specimens. These observed experimental forces are denoted by "F_{obs}". Gettu *et al*. (2004) indicate a force in which cracking had already begun with significant crack opening and, thus, this result was not considered for F_{cr} analysis. In Caratelli *et al*. (2011), Abbas *et al*. (2014), Nehdi *et al*. (2015) and Spagnuolo (2020), the maximum applied force did not produce any splitting cracks. In Conforti *et al*. (2017) the results were presented only by means of loading intervals and, us, given the high uncertainty of loading measurements (see Figure 13), this study was not considered in F_{cr} analysis.

Concerning experiments that fit this work criterion to study splitting loads: in situations with substantially different compressive strengths (usually related to different reinforcement solutions) more than one F_{obs} were defined (one for each configuration); in campaigns with more than one specimen per sample (usually seen in concrete blocks) or more than one jack pad per specimen, the F_{obs} was taken as the average of splitting values for each specimen (for samples) or under each jack pad (for concrete blocks or segments with more than one thrust ram).

Figure 13 – Experimental results available in Conforti *et al*. (2017) by means of splitting loads intervals

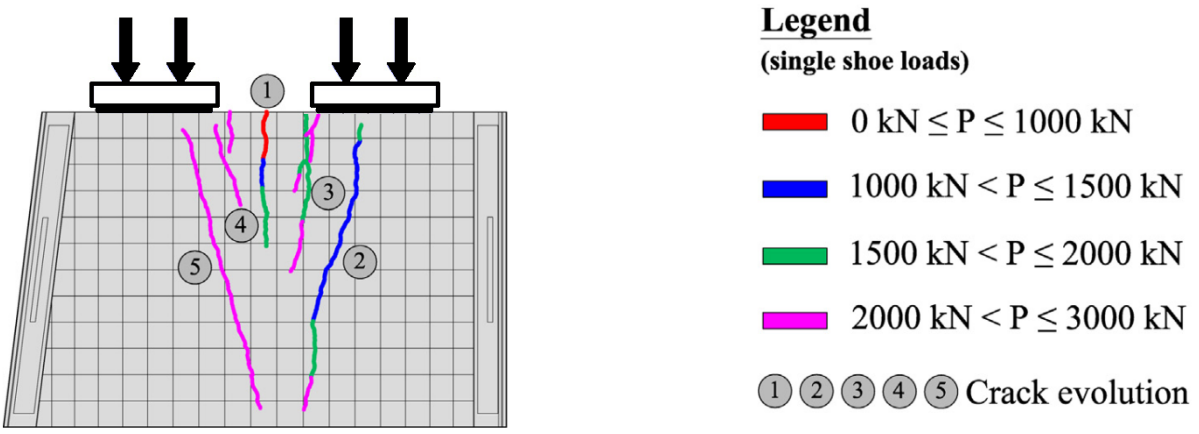

Table 4 gathers some experimental splitting forces (F_{obs}) available in the literature. It can be noticed that seven studies provided 26 different F_{obs} values. Most of these results refer to concrete blocks, with only two results for full-scale concrete segments. Also, only three studies provided responses with more than one jack bearing pad configuration (Conforti *et al*. (2016a), Caratelli *et al*. (2012) and Conforti *et al*. (2019)).

Table 4 – F_{obs} values available in the literature

Author	Specimen	Configuration	F_{obs} (kN)
Schnutgen and Erdem (2001)	Block	SFRC-A (f_{cm}=58.2MPa)	2000
Schnutgen and Erdem (2001)	Block	SFRC-B (f_{cm}=50.2MPa)	1875
Liao *et al*. (2015)	Block	b = 200 - PC (f_c = 40MPa)	407
Liao *et al*. (2015)	Block	b = 200 - PC (f_c = 50MPa)	417
Liao *et al*. (2015)	Block	b = 200 - SFRC (f_c = 40MPa)	406
Liao *et al*. (2015)	Block	b = 200 - SFRC (f_c = 50MPa)	429
Liao *et al*. (2015)	Block	b = 250 - PC (f_c = 40MPa)	410
Liao *et al*. (2015)	Block	b = 250 - PC (f_c = 50MPa)	434
Liao *et al*. (2015)	Block	b = 250 - SFRC (f_c = 40MPa)	374
Liao *et al*. (2015)	Block	b = 250 - SFRC (f_c = 50MPa)	527
Liao *et al*. (2015)	Block	b = 400 - PC (f_c = 40MPa)	633
Liao *et al*. (2015)	Block	b = 400 - SFRC (f_c = 40MPa)	631
Liao *et al*. (2015)	Block	b = 400 - SFRC (f_c = 50MPa)	641

Liao *et al*. (2015)	Block	b = 750 - PC (f_c = 40MPa)	744
Liao *et al*. (2015)	Block	b = 750 - SFRC (f_c = 40MPa)	660
Liao *et al*. (2015)	Block	b = 750 - SFRC (f_c = 50MPa)	715
Tiberti *et al*. (2015)	Block	PC	1044
Tiberti *et al*. (2015)	Block	PFRC	917
Conforti *et al*. (a) (2016)	Block	-	790
Conforti *et al*. (b) (2016)	Block	b_1 = 100 - PC	1465
Conforti *et al*. (b) (2016)	Block	b_1 = 100 - PFRC	1470
Conforti *et al*. (b) (2016)	Block	b_1 = 150 - PC	1700
Conforti *et al*. (b) (2016)	Block	b_1 = 150 - PFRC	1598
Caratelli *et al*. (2012)	Segment	-	2688
Conforti *et al*. (2019)	Segment	-	2389
Trabucchi *et al* (2021)	Block	-	747

It is also relevant to mention that Liao *et al*. (2015) characterized concretes tensile strength indirectly by means of the Brazilian and Barcelona tests (UNE-EN 12390-6 (2010)). Some studies presented only the compressive strength for concrete characterization. In these cases, the Equation (1), with possible use of Equation (2), presented in *fib* Model Code 2010 (2013) can be used to estimate concretes characteristic tensile strength as function of the characteristic compressive strength (f_{ck}) or, indirectly, using the average compressive strength (f_{cm}).

$$f_{ctm} = 0.3\, f_{ck}^{2/3} \quad (1)$$

$$f_{cm} = f_{ck} + \Delta f \quad (2)$$

where, Δf = 8MPa.

3.2 ANALYTICAL MODELS

A literature review on analytical models proposed for splitting phenomena was performed. In this review, the analytical force to initiate the splitting cracking for each model was denoted by "F_{cr}". The splitting is also relevant in concrete prestressed beams context, in which the anchorage zones in the end block are subjected to compressive concentrated loads resulting in the stress pattern shown in Figure 9. Some analytical models to predict splitting can be found in literature either for the TBM constructed tunnels or for the design of conventional reinforcement in prestressed concrete beams. In the latter, the called "bursting force" is mentioned as the transverse force necessary to initiate the splitting crack. The strut-and-tie model is one of the approaches commonly used for designing conventional reinforcement for splitting.

E. Morsch (1924) proposed a model in which the compressive stress trajectories are simplified in a symmetric bilinear stress path. From the applied load node, an oblique strut is designed to take into account an approximation of the angle performed by the compressive stress trajectory (Figure 14). The tie, on the other hand, is in the center of the disturbance length, where a resultant bursting force is located. Through the imposition of equilibrium, an analytical equation for the force (Z) is obtained as a function of the applied load (P) and the ratio between the load application area and the cross-section area (b_1/b).

Figure 14 - Strut-and-tie model proposed by E. Morsch (1924)

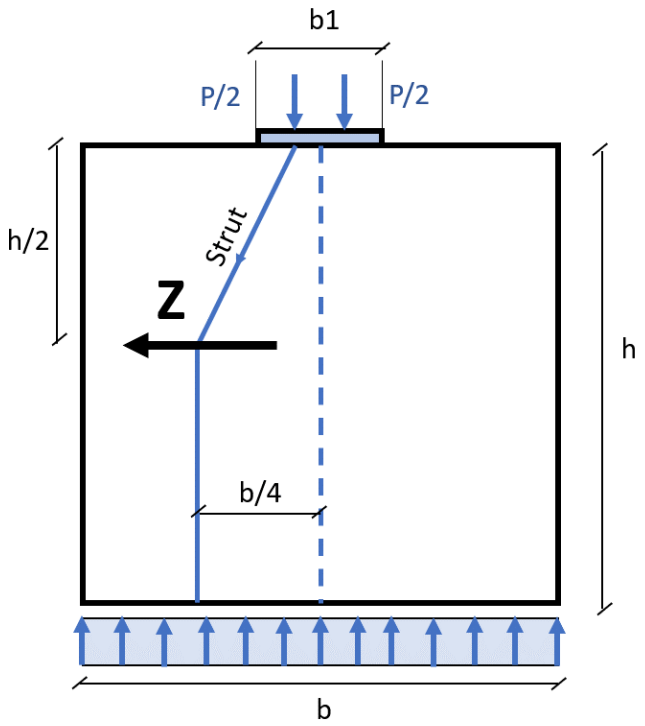

F. Leonhardt and E. Moning (1973) proposed a different way to calculate the bursting force. According to these authors, under the loading area, the transverse tensile stresses diagram along a centered vertical axis is drawn and an equation for the bursting force is proposed.

The resultant equations for bursting forces (Z) proposed by E. Morsch's and Leonhardt's studies are, respectively:

$$Z = 0.25P\left(1 - \frac{b1}{b}\right) (3)$$

$$Z = 0.30P\left(1 - \frac{b1}{b}\right) (4)$$

where, P is the applied load and b_1 and b follows the layout presented in Figure 11.

It can be noticed that, even though through different methods, Leonhardt's solution can be represented by a modified strut-and-tie model.

More recently, Liao *et al*. (2015) proposed a similar strut-and-tie structure whose dimensions were calibrated through experimental observations. In this study, these authors aimed to predict the splitting load in TBM constructed tunnels context and, thus, its formulation differentiate short and long blocks, i.e., blocks with more than and less than the disturbance length, respectively. This differentiation is important by taking into account the boundary conditions and the non-uniform distribution of compressive stress patterns at the base of the long blocks (Figure 10). The analytical equations for both models are exposed in Equation (5) and Equation (6). It is also relevant to mention one of Liao's models main hypotheses, in which the splitting load (F_{cr}) is independent of the fiber content present in the block. This assumption can be stated for some fiber types and contents applied in engineering, once it is expected that fiber mechanical contribution is more accentuated when the cementitious bulk is cracked (Bentur e Mindess, 2007). When it occurs, fiber bridging crack behavior starts, providing residual strength and increasing the element's bearing capacity. Therefore, this assumption applied to all studied analytical models can be appropriate to identify splitting forces for both plain and reinforced concretes. Thus, for the F_{cr} analysis, it is assumed that the splitting load is not influenced by the type of reinforcement employed.

$$Fcr_{short\ blocks} = \frac{8t(h' - 2k_1b_1)(h' - k_1b_1)f_{ct}}{3(b - b_1)} (5)$$

$$Fcr_{long\ blocks} = \frac{8t(h' - 2k_1b_1)(h' - k_1b_1)f_{ct}}{3(4a_2 - b_1)} (6)$$

where, the parameter k_1 = 0.33, h' and a_2 are functions of geometric characteristics (such as specimens' width, height and others) and functions of the angle β=23º, while b_1 follows the layout presented in Figure 11.

Another approach to determine splitting loads in concrete is based on the elasticity theory. Guyon (1953) proposed an approximated solution, with corrections to satisfy elasticity compatibility equations for a concentrated load applied in a semi-infinite strip. Thus, an equation for the peak tensile transverse stress was developed by the author. By taking in consideration this peak tensile stress as the uniaxial concrete tensile strength (f_{ct}), the loading P can be assumed as the splitting load (F_{cr}). The splitting load for this case is given by the Equation (7).

$$Fcr = \frac{b_1 t}{1.1(0.47)(1-(b1/b))} f_{ct} \quad (7)$$

where, t is specimens' thickness and b_1 and b follows the layout presented in Figure 11.

Iyengar (1962) proposed an exact analytical solution using the two-dimensional elastic theory in order to predict the splitting stress distribution in concrete blocks critical areas. One of the graphical solutions for stress flow obtained in this work can be seen in Figure 15. Conforti *et al*. (2016b) adapted this solution to analyze splitting and crushing loads in concrete blocks with square transverse sections. In this study, the proposed models were evaluated by means of an experimental campaign with splitting tests. An experimental failure scheme is represented when a concrete block with enough height to overcome the disturbance length is tested with fiber steel reinforcement, as it can be seen in Figure 16.

Figure 15 - Solution proposed by Iyengar (1962) for loading relative areas (Conforti *et al.* (2016b))

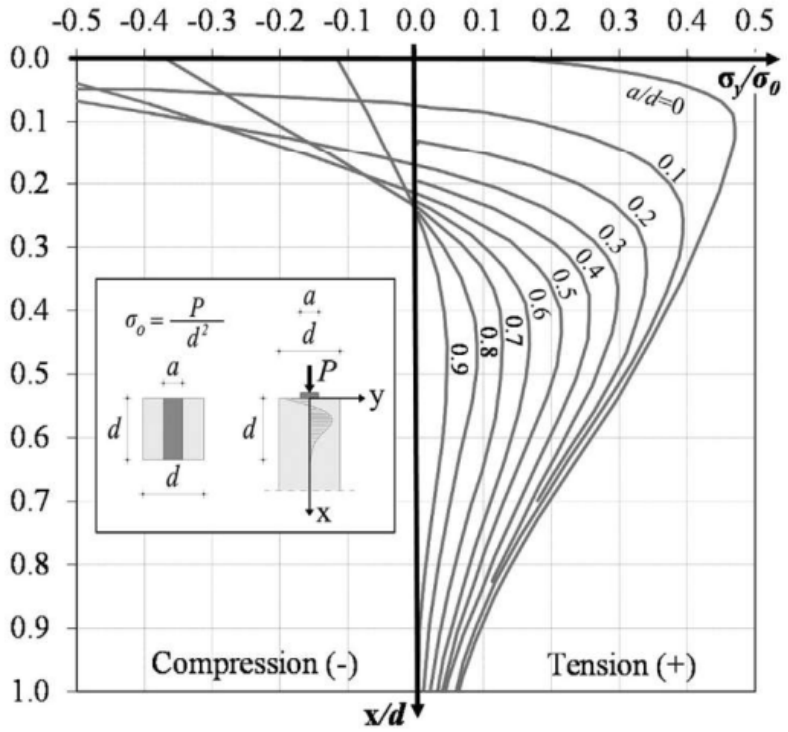

Figure 16 – Cracking process in a sample characterized by a splitting failure (Conforti *et al.* (2016b))

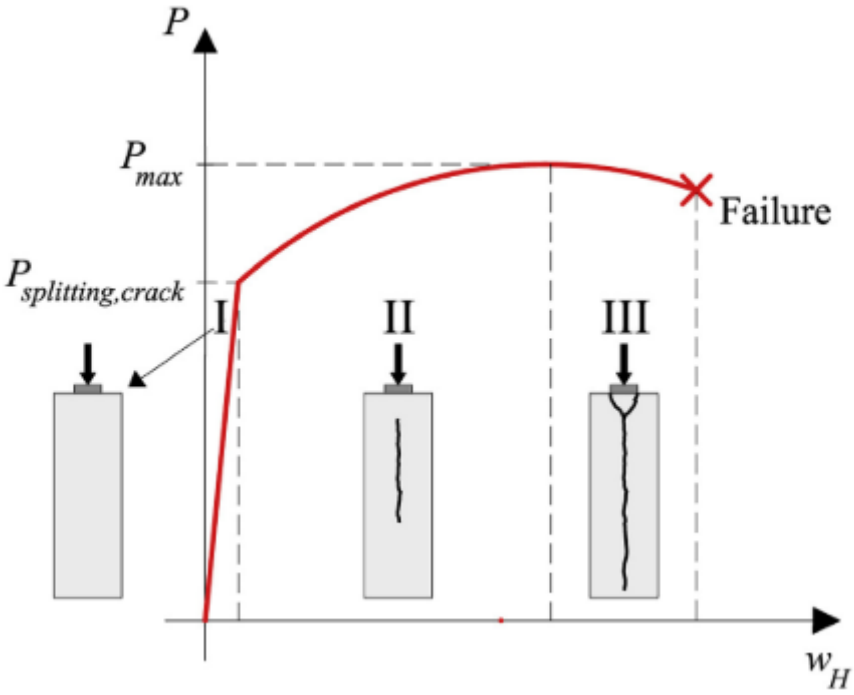

The experimental curve is displayed in graphs with the LVDT horizontal displacement versus the applied load and consist with three stages: the first one is characterized by a linear elastic branch that initiates with loading application and finishes when loading level reaches the

splitting crack load (F_{cr}) or some loading levels nearby. When these levels are reached, a change in the curves slope is observed, representing the modification in the stiffness behavior due to cracking initiation. In this moment, with cracking development, the reinforcement starts to play a more important role in structural response that marks the transition of first to second stage. This transition can be abrupt or gradual, as can be seen in the experimental results obtained in Schnutgen and Erdem (2001) (Figure 40). In plain concrete, the end of the first stage is also the collapse of the structure.

The second stage starts the splitting crack propagation, with increasing cracking widths and depth. This stage is major ruled by tension stresses, even though the system is solicited in a biaxial state-of-stress. It is also verified a propagation of diagonal cracks caused by concrete crushing in the vicinity of the loading area in direction to the vertical splitting crack. The maximum test load is reached with the encounter of the diagonal and the splitting cracks. This marks the end of the second stage.

The third stage initiates from the maximum applied load and is major ruled by compression and shear stresses. In this stage are verified the larger crack widths and depths and the forming of a conical wedge due to the encounter of the diagonal and vertical cracks. At this point, with increasing loads, occurs the failure of the structure and, thus, the end of the test. Is also important to notice that this failure scheme represents a reinforcement system with hardening post-cracking behavior.

In the present work analysis (Chapter 5.1), the analytical equation proposed by Conforti *et al*. (2016b) is adapted to blocks with rectangular transverse sections, enabling its use for other experimental results. The adapted equation for this model is presented in Equation (8).

$$Fcr = \frac{bt}{0.44(1-(b1/b))} f_{ct} \quad (8)$$

where, t is specimens' thickness and b_1 and b follows the layout presented in Figure 11.

Another alternative approach used to predict splitting phenomena in concrete specimens is presented in He and Liu (2010). In this case the prediction is based on compression-dispersion models, in which the load paths are mathematically visualized by infinite isostatic lines with their own geometric and physical boundary conditions. According to this study, the splitting load in a centered load configuration is given by the Equation (9):

$$Fcr = \frac{2bt}{(1-(b1/b))} f_{ct} \quad (9)$$

where, t is specimens' thickness and b_1 and b follows the layout presented in Figure 11.

The most recent analytical model found in literature to predict splitting is presented by Boye *et al*. (2019). In this study, a linear regression model is proposed based on numerical results with the aim to improve predictions with low width ratios (b_1/b) and eccentricity effects (denoted by the letter "e"). The equation is designed for the peak transverse tensile stress and the applied load stress ratio (denoted as σ_{peak}/σ_o). The equation in its generic form can be written as shown in Equation (10):

$$\frac{\sigma_{peak}}{\sigma_o} = \alpha + \beta \frac{b_1}{b} \quad (10)$$

where, α and β are functions of "b" and "e". The use of this analytical model was made by adopting the same strategy used in Guyon's model for the peak and applied stresses, enabling the direct calculus of F_{cr}.

From all analytical models presented it can be noticed that each one presents different characteristics to consider the splitting behavior: the elastic solutions provided by Guyon (1953) and Iyengar (1962) are based on the expected stress flow along specimens height to distribute the stresses; the strut and tie model improved by Liao *et al*. (2015) considers this mechanism and also the boundary conditions of the segments; the He and Liu (2010) showed mathematical formulations in order to give a parametric approach for the compression-dispersion; and Boye *et al*. (2019) improved solutions regarding eccentricity effects and low width ratios.

The presented analytical models are used in the F_{cr} analyses. However, the strut and tie model proposed by Morsch (1924) and the F. Leonhardt and E. Moning (1973) solution were not considered, once their formulations did not provide ways to calculate F_{cr} as function of tensile stresses, only by means of bursting forces. A summary is presented in Table 5 gathering the models used in F_{cr} analysis with their formulas and main characteristics.

Table 5 – Analytical models' summary table

Model	F_{cr}	Context	Assumptions	Formulation
Guyon (1952)	$\frac{b_1 t}{1.1(0.47)(1-(b1/b))} f_{ct}$	Prestressed concrete	Semi-infinite strip	Elastic solution with corrections
Conforti *et al.* (2016b)	$\frac{bt}{0.44(1-(b1/b))} f_{ct}$	TBM tunnels	Semi-infinite strip	Exact elastic solution
He and Liu (2010)	$\frac{2bt}{(1-(b1/b))} f_{ct}$	Prestressed concrete	Semi-infinite strip	Compression-dispersion model
Liao *et al.* (2015)	$\frac{8t(h-2k_1b_1)(h-k_1b_1)f_{ct}}{3(b-b_1)}$ $\frac{8t(h'-2k_1b_1)(h'-k_1b_1)}{3(4a_2-b_1)}$	TBM tunnels	Short blocks Long blocks	Strut-and-tie model
Boye *et al.* (2019)	$\frac{\sigma_{peak}}{\sigma_o} = \alpha + \beta \frac{b_1}{b}$	TBM tunnels	Semi-infinite strip	Linear regression based on numerical model improvements

4 NUMERICAL MODELING

In this section the numerical model approach used for numerically simulate the local behavior of concrete tunnel segments for plain and fiber reinforced concrete with a focus on cracking initiation is presented. Unlike the analytical models presented in Chapter 3.2, the numerical simulation will consider the post-cracking behavior due to the reinforcement strategy adopted. As described previously, the analytical models were designed to predict the load in which a crack is initiated by splitting stresses, regardless of the reinforcement.

The numerical model based on the finite element method uses a discrete and explicit approach to represent the reinforcements, and continuum damage constitutive models to describe both reinforcement-concrete interaction and the mechanical behavior of the concrete. In the context of this work, the reinforcement can be conventional steel rebars or steel fibers.

4.1 MODELING OF CONCRETE

Several numerical models are available in the literature to predict the mechanical behavior of the concrete. The finite element method (FEM) is the most widely used to simulate the failure behavior of concrete. The existing strategies to simulate the failure process of concrete can be classified in two groups: discrete and continuous. An overview about these models can be found in Tejchman & Bobinski (2013). The discrete models are characterized by displacement or strain discontinuities into standard finite elements to represent cracks. As for the continuous models, the elastoplastic, smeared crack and damage models are widely used. This work uses a material model based on Continuum Damage Mechanics Theory (CMDT) to represent the concrete and steel-concrete interaction.

For this type of model, the failure process is distributed along the element's damaged or yielded regions. Some basic concepts are used to formulate this type of model. First, two types of stresses are defined: apparent (nominal) and effective. The apparent stress in a cross section is obtained through the ratio between the perpendicular force to the surfaces' cross section and the undamaged area. The effective stress uses the same force, but instead of using an intact area, uses the "effective area" calculated by the difference between the original (undamaged) and the damaged areas. Figure 17 shows a cross section and the different areas. More details about the hypothesis of mechanical equivalence between the damage and undamaged material can be found in Altenbach (2012).

In this work, for the constitutive models based on CDMT, the effective stress tensor, $\bar{\sigma}$, will assume the form presented in Equation (11):

$$\bar{\sigma} = \boldsymbol{C}: \varepsilon \ (11)$$

where, **C** is the fourth order linear-elastic constitutive tensor, ε is the second order strain tensor and (:) is the tensorial product contracted in two indices.

Figure 17 – Damage schematic evolution: a) nominal cross section, and b) damaged cross section. (Rodrigues (2015))

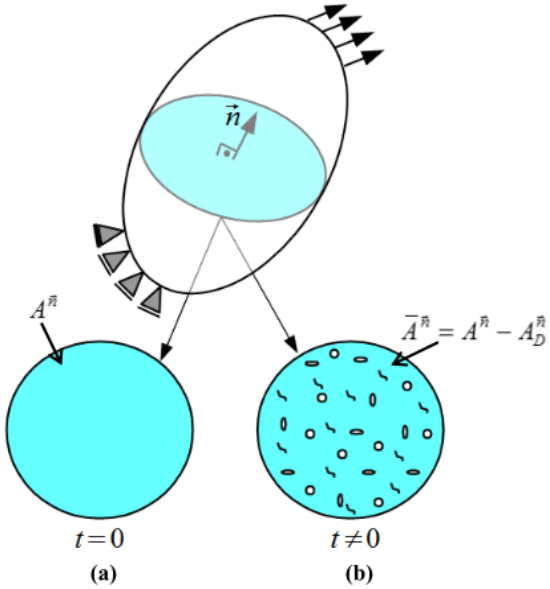

To describe the nonlinear behavior of concrete using a continuous approach, Cervera *et al*. (1996) proposed the rate independent version of a constitutive model based on CDMT. This model can describe the distinct tensile and compressive responses of concrete by means of two-scalar damage variables, d^+ and d^-, respectively. The damage variable (d) is defined as the ratio between the damaged and undamaged elements cross sections areas. Its absolute value is found in the interval $0 \leq d \leq 1$, where d=0 represents the original (undamaged) state, and d=1 the complete failure.

The effective stress tensor (equation (11)) is split into tensile ($\bar{\sigma}^+$) and compressive ($\bar{\sigma}^-$) components, such as presented in Equation (12):

$$\bar{\sigma} = \bar{\sigma}^+ + \bar{\sigma}^- (12)$$

The apparent (nominal) stress tensor (σ) for this model is obtained by reducing each part of the effective stress tensor, according to its respective damage variable in tension and compression, as presented in Equation (13):

$$\sigma = (1 - d^+)\bar{\sigma}^+ + (1 - d^-)\bar{\sigma}^- (13)$$

The equivalent effective tensile and compression norms are defined by Equation (14) and Equation (15), respectively. These positive scalar variables are used to define concepts as loading, unloading and reloading for general stress states.

$$\bar{\tau} = \sqrt{\bar{\sigma}^{+} : C^{-1} : \bar{\sigma}^{+}} (14)$$

$$\bar{\tau} = \sqrt{\sqrt{3}\, K \bar{\sigma}_{oct}^{-} + \bar{\tau}_{oct}^{-}} (15)$$

where, $K = \sqrt{2}(\beta - 1)(2\beta - 1)$ is a material property that depends on the relation between the uniaxial and biaxial compressive strength of the concrete, β. According to Cervera *et al*.(1996), typical values for concrete are: β =1.16 and *K*=0.171. In the Equation (15), $\bar{\sigma}_{oct}^{-}$ and $\bar{\tau}_{oct}^{-}$ are the octahedral normal and shear stresses, respectively, obtained from $\bar{\sigma}^{-}$. Two independent damage criteria, one for tension and other for compression, are expressed as indicated in Equation (16):

$$\bar{\phi}^{+}\, \bar{\tau}^{+}, r^{+} = \bar{\tau}^{+} - r^{+} \leq 0, and\ \bar{\phi}^{-}\, \bar{\tau}^{-}, r^{-} = \bar{\tau}^{-} - r^{-} \leq 0\ (16)$$

where, r^{+} and r^{-} are the current damage thresholds, which are updated continuously to control the size of the expanding damage surface. The boundary damage surfaces for the effective stresses are expressed by $\bar{\phi}^{+}(\bar{\tau}^{+}, r^{+}) = 0$ and $\bar{\phi}^{-}(\bar{\tau}^{-}, r^{-}) = 0$. At the onset of the analysis, the initial value attributed to damage thresholds are $r_0^{+}=f_t$ and $r_0^{-}=f_{c0}$, where f_t is the tensile strength and f_{c0} the compression stress threshold for damage. The evolution of the damage thresholds can be expressed in a closed form, always using the highest values reached by r^{+}=máx(r_0^{+},$\bar{\tau}^{+}$) and r^{-}=máx(r_0^{-},$\bar{\tau}^{-}$).

To describe the evolution of the damage variables d^{+} and d^{-}, two exponential functions to represent the material degradation process in tension and compression are defined. These damage variables are able to determine the softening behavior in tension and the hardening/softening in compression, after reaching the initial elastic limit in tension and compression, respectively, as shown in Equation (17a) and Equation (17b):

$$d^{+} = 1 - \frac{r_0^{+}}{r^{+}} \exp\left(A^{+}\left(1 - \frac{r^{+}}{r_0^{+}}\right)\right) (17a)$$

$$d^{-} = 1 - \frac{r_0^{-}}{r^{-}} 1 - A^{-} - A^{-} \exp\left(B^{-}\left(1 - \frac{r^{-}}{r_0^{-}}\right)\right) (17b)$$

where the parameter A^- is derived from the ratio between the material fracture energy and the geometric factor, l_{ch}, termed characteristic length, which corresponds to the width zone where the degradation concentrates, such that presented in Equation (18):

$$\frac{1}{A^+} = \frac{1}{2\bar{H}^+}\left(\frac{1}{l_{ch}} - \bar{H}^+\right) \geq 0 \quad (18)$$

where $\bar{H}^+ = (f_t)^2/2EG_f^+$ is written in terms of the tensile strength, f_t, the elastic modulus, E, and the (tensile) fracture energy of the material, G_f^+. The characteristic length, depends on the spatial discretization, and in this work, is assumed to be the square root of the finite element area.

The parameters A^- and B^- are defined so that the stress-strain curve of the concrete satisfies two previously selected points of a uniaxial experimental test. More details about the formulation can be found in Cervera *et al*. (1996).

An important aspect of the algorithm used for modeling material failure is its robustness. When a crack propagates within the strain softening regime, the algorithmic tangent operator may become singular, and as a consequence, the solution of the resulting systems of nonlinear equations using a fully implicit discretization methodology cannot be obtained. In order to treat this problem, the modified implicit-explicit integration scheme (IMPL-EX) proposed by Oliver *et al*. (2008) and adapted by Bitencourt Jr (2015) can be used as an interesting alternative. In this work, the Cervera *et al*. (1996) damage model is used with the IMPL-EX integration scheme.

4.2 MODELLING OF REINFORCEMENT

The reinforcements are represented by two-node finite elements (truss finite element) and their behavior is described by one-dimensional elastoplastic model.

4.2.1 ONE-DIMENSIONAL ELASTOPLASTIC MODEL

The one-dimensional elastoplastic model can be expressed by two phases: a linear elastic in the beginning and a phase with plastic deformation (after the yield stress is reached). The material behavior in the latter can be defined as hardening (H>0), perfect elastoplastic (H=0) or softening (H<0). These behaviors can be seen in Figure 18.

Figure 18 – One-dimensional elastoplastic material model (Trindade, 2018)

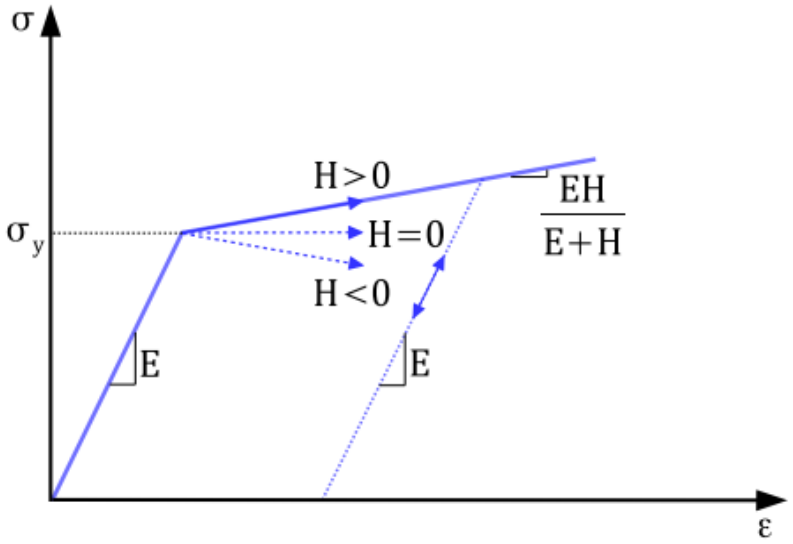

In the present work a perfect elastoplastic material behavior is adopted to model the reinforcement.

4.2.2 STEEL FIBER DISTRIBUTION

When the reinforcement strategy contains steel fibers, a cloud of fibers is generated for numerical simulations. The fibers are generated with a random isotropic distribution of fibers, considering geometry boundaries and its effects with the algorithm utilized in Trindade (2018). Figure 19 illustrates the generation of fibers in 3D and its projection in a plane.

Figure 19 – Generation of fibers: a) 3D distribution and (b) projection of the fibers onto a plane (Trindade, 2018)

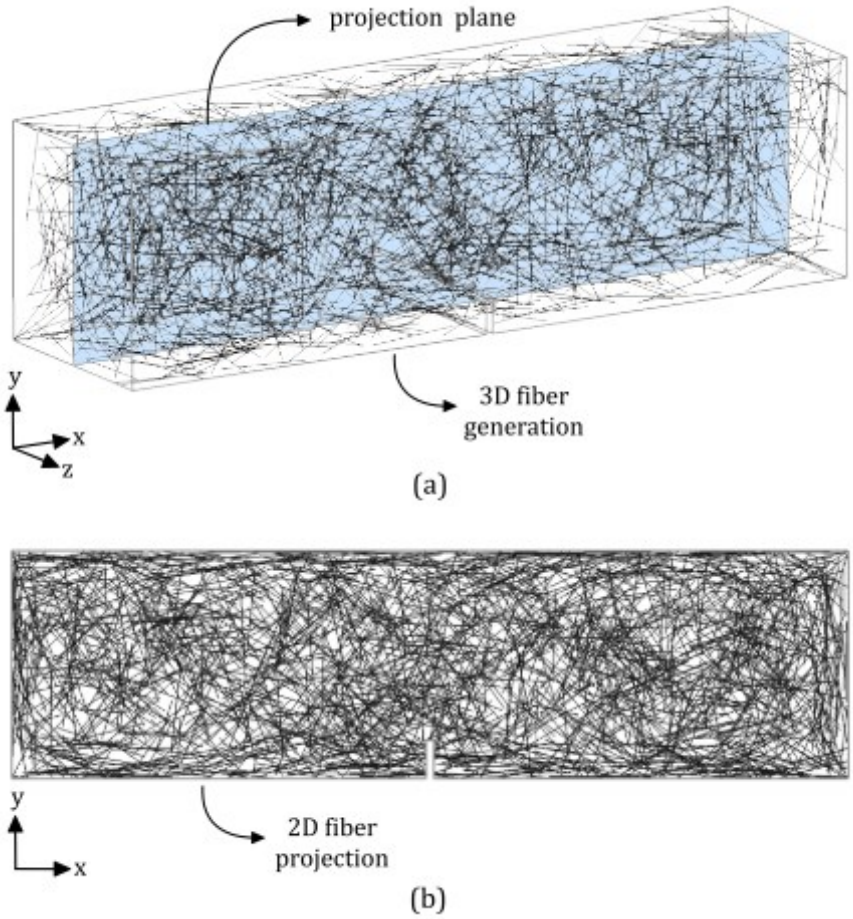

4.3 CONCRETE-REINFORCEMENT INTERACTION

The rebars and steel fibers are modeled using the same approach presented in Bitencourt Jr. *et al*. (2015) by using Coupling Finite Elements (CFE). The discrete and explicit representation of reinforcement is based on the use of CFEs, that describe the force interaction between each fiber (or a rebar) node and its corresponding underlying concrete finite element. Consequently, for each node of reinforcement elements, a CFE is created and, after the insertion of all CFEs (coupling procedure), the global internal force vector and the stiffness matrix can be formulated as indicated in equations (19) and (20), respectively. Figure 20 shows the procedure to construct the numerical model.

$$\boldsymbol{F^{int}} = A_{e=1}^{nel(C)} \boldsymbol{F_e^{int}}(C) + A_{e=1}^{nel(RF)} \boldsymbol{F_e^{int}}(RF) + A_{e=1}^{nel(CFE)} \boldsymbol{F_e^{int}}(CFE) \quad (19)$$

$$\boldsymbol{K} = A_{e=1}^{nel(C)} \boldsymbol{K}_e\,(C) + A_{e=1}^{nel(RF)} \boldsymbol{K}_e\,(RF) + A_{e=1}^{nel(CFE)} \boldsymbol{K}_e\,(CFE) \quad (20)$$

where, A is the finite element assembly operator and the first, second and third terms correspond to concrete, reinforcement and coupling elements, respectively. More details can be found in Bitencourt Jr. *et al*. (2015).

Figure 20 - Coupling procedure for finite element model: (a) discretization of the concrete in finite elements; (b) generation and discretization of a cloud of steel fibers; (c) creation and discretization of rebar; (d) creation and insertion of the CFEs and (e) detail of the coupling in overlapping meshes – adapted from Teixeira (2018).

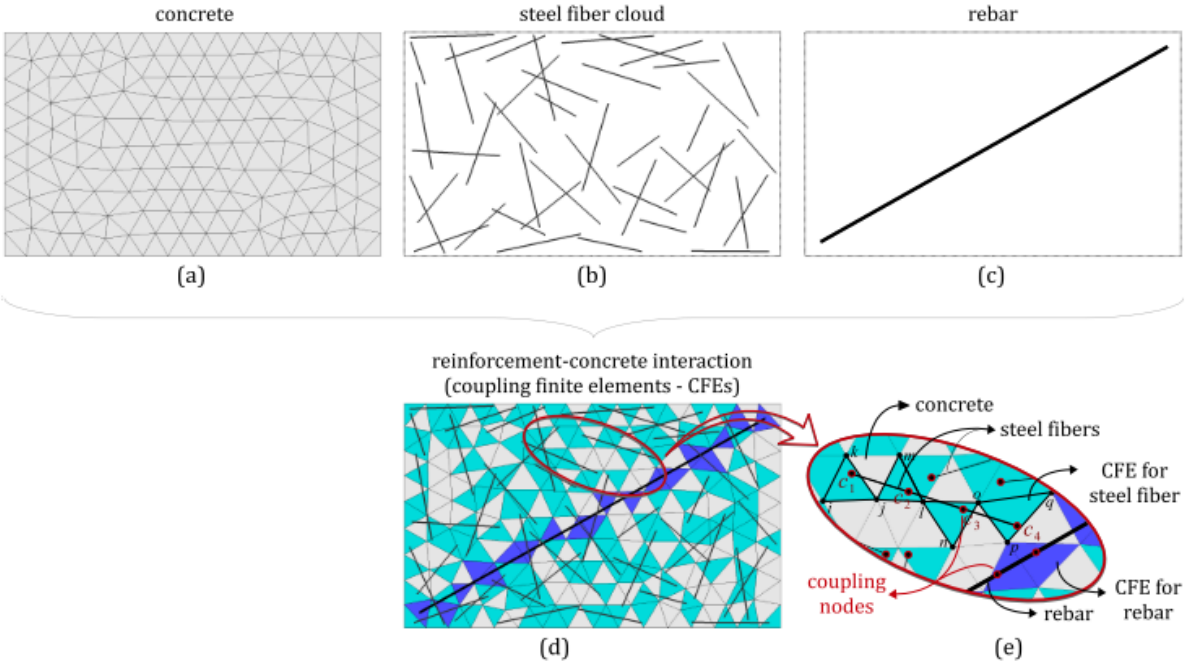

A continuum damage model is utilized to describe the bond-slip behavior. The equation (21) and Figure 21 illustrates the constitutive relation adopted.

$$\tau(s) = \begin{cases} \tau_{max}\left(\frac{s}{s_1}\right)^{\alpha} & \text{if} \quad s \leqslant s_1 \\ \tau_{max} - \frac{(\tau_{max} - \tau_f)(s - s_1)}{s_2 - s_1} & \text{if} \quad s_1 \leqslant s \leqslant s_2 \\ \tau_f & \text{if} \quad s > s_2 \end{cases} \tag{21}$$

Figure 21 – Continuum damage model used to describe the bond-slip behaviour.

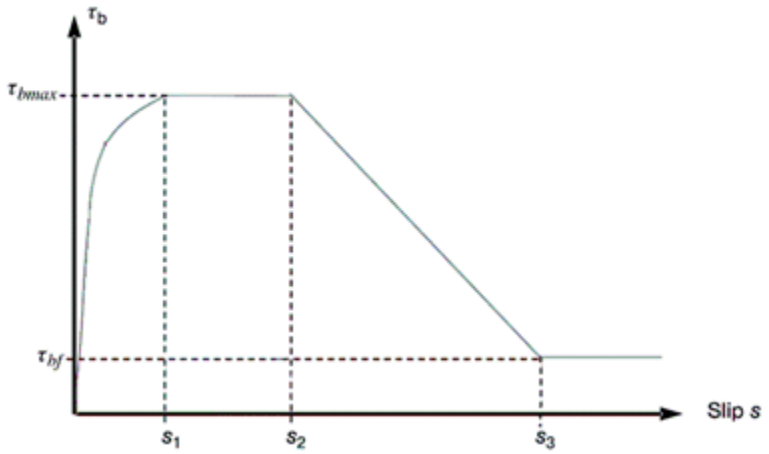

5 RESULTS

5.1 ANALYTICAL MODELS' PERFORMANCE COMPARISON – F_{CR} ANALYSIS

The applicability of the analytical models when compared to the experimental data is analyzed from a statistical standpoint, focusing on the difference between the predicted splitting load (F_{cr}) and the observed experimental load (F_{obs}). The statistical analysis considered the concept of relative error (RE), as:

$$RE = 100\frac{(F_{obs} - F_{cr})}{F_{obs}}$$

where, RE is the relative error (in %); F_{obs} is the observed experimental load (in kN); and F_{cr} is the splitting load predicted by the analytical model (in kN).

The results are presented in boxplot diagrams, violin plots, qqplots, probability density function graphs, and descriptive statistics. In the representation of figures, a differentiation in the symbology is employed to represent the specimens' type (block or segment) and number of jacks to enable a discussion about size effect. The discussion employed the concept of interquartile range (IQR), which is represented by the boxes' range in the boxplot diagrams. At this stage, the central tendency, dispersion, and distribution of relative errors were evaluated. Then, the influence of the width ratio (b_1/b) and aspect ratio (h/b) on the results of the analytical models was evaluated by means of linear regression models between the RE and each of the factors of influence. This evaluation was conducted considering all the analytical models separately.

As described previously, the analytical models return a prediction for the splitting load, that is the loading necessary to initiate a crack due to splitting. These models were developed regardless of reinforcement configurations, such as reinforcement strategy (fiber reinforcement, conventional rebar reinforcement or hybrid reinforcement) and reinforcement contents. Thus, the present analysis will be focused on the applicability of the analytical models regarding specimens' dimensions and concrete material parameters, such as concretes tensile and compressive strengths.

The analytical models' performance comparison is conducted in two steps: at first, the influence of tensile strength (f_{ct}) parameter in the models' response is evaluated. This analysis is from now on denominated "parametric analysis", and it is made with the results exposed in

the experimental campaign made by Liao *et al*. (2015). Then, the global performance comparison (F_{cr} analysis) is made with all available results (shown in Table 4). The equations (1) and (2) are used in this case to obtain the parameter f_{ct}.

5.1.1 PARAMETRIC ANALYSIS – TENSILE STRENGTH (f_{ct})

As mentioned, a parametric analysis is conducted for the experimental results presented in Liao *et al*. (2015), since this study has provided two different experimental tests to estimate concretes uniaxial tensile strength (f_{ct}): f_{t1}, the tensile strength obtained from Barcelona test and f_{t2}, the tensile strength obtained by the Brazilian test. Also, the equations (1) and (2) are used, to give a third option in terms of possibilities for estimating f_{ct}.

In this work, the results are presented by means of "model and f_{ct} input" with the notation "model_fct_input". For example, the response of model of Guyon (1953) with the ft_2 input is denoted by "Guyon_ft2". The results for f_{ct} calculated from equations (1) and (2) are taken as standard and, thus, only the name of the model is written. In this case, taking a result for He and Liu (2010) model with this f_{ct} input as an example, its denomination is only "HeLiu" in the next tables and figures.

Table 6 indicates the mean compressive strength, ft_1 and ft_2 obtained in the experimental campaign of Liao *et al*. (2015).

Table 6 – Test results of characterization specimens - Liao *et al*. (2015)

Series	f_{cm} (MPa)	f_{t1} (MPa)	f_{t2} (MPa)
PC-40	43,7	4,33	4,30
SFRC-40	39,4	3,99	4,70
PC-50	53,3	4,09	4,40
SFRC-50	51,8	4,32	4,50

Table 12 (Appendix A.1) presents the parametric analysis results for each tested configuration. The Appendixes A.2 and A.3 show barplots for each tested configuration either to compare loadings or relative errors, respectively.

In order to summarize and visualize the overall response of analytical models per f_{ct} input, boxplots and violin plots are used in terms of relative errors and presented in Figure 22.

Figure 22 - Boxplots and violin plots for parametric analysis (f_{ct}) results in terms of relative errors (in %)

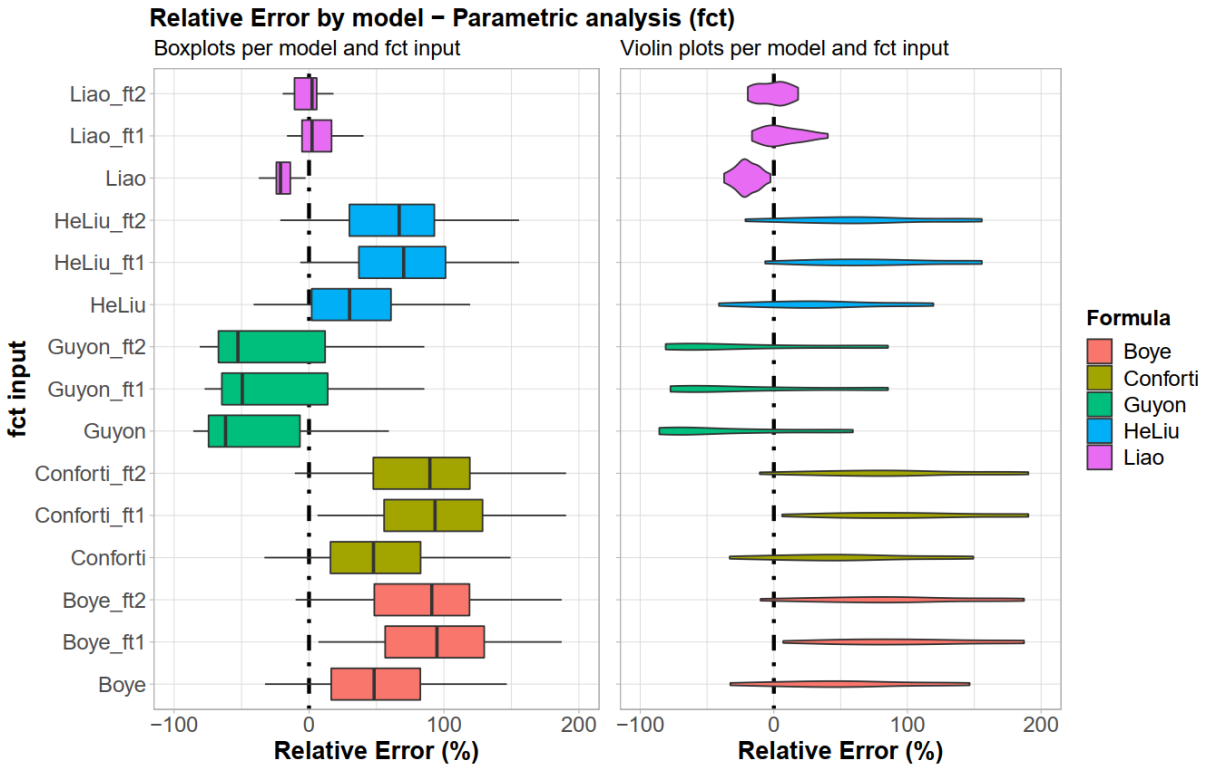

It can be seen that, for all tested formulas, the f_{ct} input obtained from equations (1) and (2) presented a tendency of leading the relative errors "more negative" (towards the left) in comparison to f_{t1} and f_{t2}. For the Boye *et al*. (2019), Conforti *et al.* (2016b) and He and Liu (2010) formulas, this tendency led the relative errors closer to zero, since they exhibited overestimation of F_{cr}. For Guyon (1953) and Liao *et al.* (2015) models, this behavior led to a detachment from origin, with more significant differences between this standard value in comparison to f_{t1} and f_{t2} for Liao *et al.* (2015) model. Also, the violin plots indicate very wide distributions for all models' responses but Liao *et al.* (2015). The latter presented a range of relative errors lower than 50% regardless of f_{ct} input.

Liao *et al.* (2015) model also showed relative errors approximately centered at zero for both experimental tensile inputs. This behavior can indicate a higher precision for the estimation of F_{cr} based on experimental inputs, in comparison to the estimation from the compressive strength (equations (1) and (2)).

In order to detail the response obtained from Liao *et al.* (2015) model as function of f_{ct} input, Figure 23 shows a smoothed density estimate (by means of Kernel density estimate) and normal qqplots for each configuration.

Figure 23 - Probability density estimates and normal qqplots for the relative errors (%) per f_{ct} input

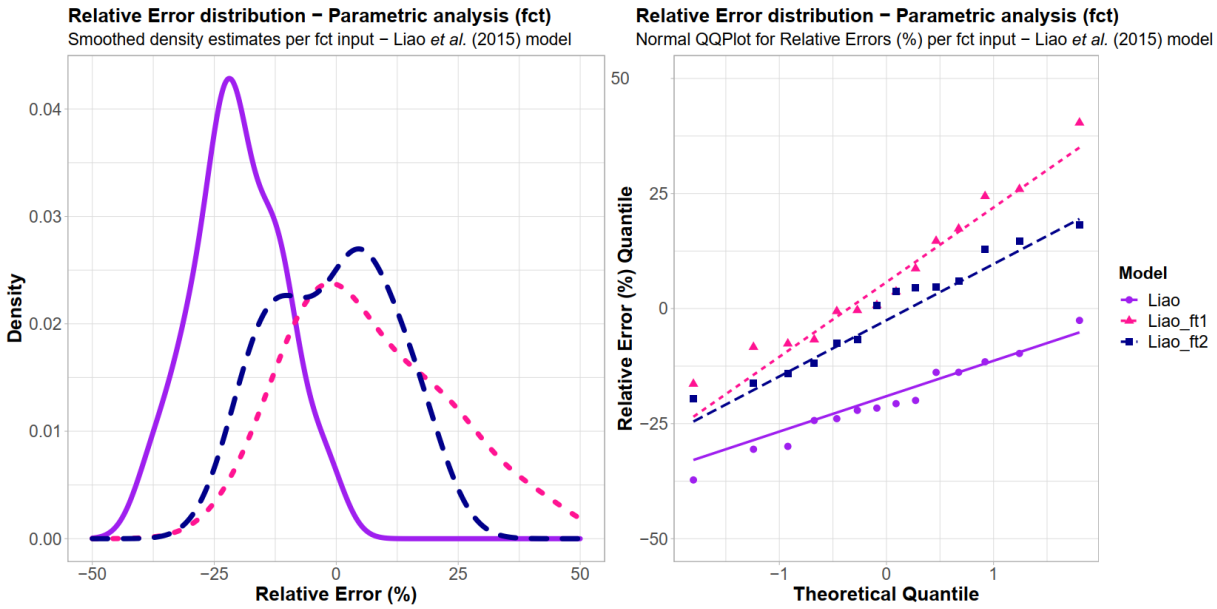

The density estimates shown that the standard f_{ct} input presented a more concentrated distribution compared to the other ones (coherent with Figure 22), even though this distribution is centered approximately in -25% (i.e., the model in average underestimates the splitting load by 25%). Also, the response for f_{t2} presented a two-peak distribution, while the f_{t1} presented the most centered distribution relative to the origin. As for the shape of the distributions, the normal qqplots showed good adherence for all f_{ct} inputs.

From the parametric analysis on f_{ct} it can be concluded that: The relative errors for all models showed a decrease in its nominal values from the estimation of f_{ct} on equations (1) and (2) in comparison with experimental tensile inputs. Liao *et al.* (2015) model provided better F_{cr} estimates, regardless of f_{ct} input; For Liao *et al.* (2015) model, the f_{t1} input showed a centered relative error distribution with good agreement to a normal distribution, and the f_{ct} input provided from FIB equations (the "standard" one) showed the lower dispersion, with an underestimation of F_{cr} prediction.

5.1.2 F_{CR} ANALYSIS

For the F_{cr} analysis only the standard f_{ct} input was considered, since the other available experimental results (besides the ones presented in Liao *et al.* (2015)) did not provide experimental tensile strength tests. Thus, all analytical models and experimental results were used with the same conditions for the input parameters (i.e., in homogeneous conditions).

Table 13 (Appendix A.1) presents the F_{cr} analysis results for each tested configuration. The Appendixes A.4 and A.5 show barplots for each tested configuration either to compare loadings or relative errors, respectively.

In order to summarize and visualize the analytical models' overall response, boxplots are used in terms of relative errors and presented in Figure 24 A differentiation in the symbology is made in order to show different results as function of specimens' type (block or segment) and number of jacks.

Figure 24 - Boxplots - F_{cr} analysis results in terms of relative errors (in %)

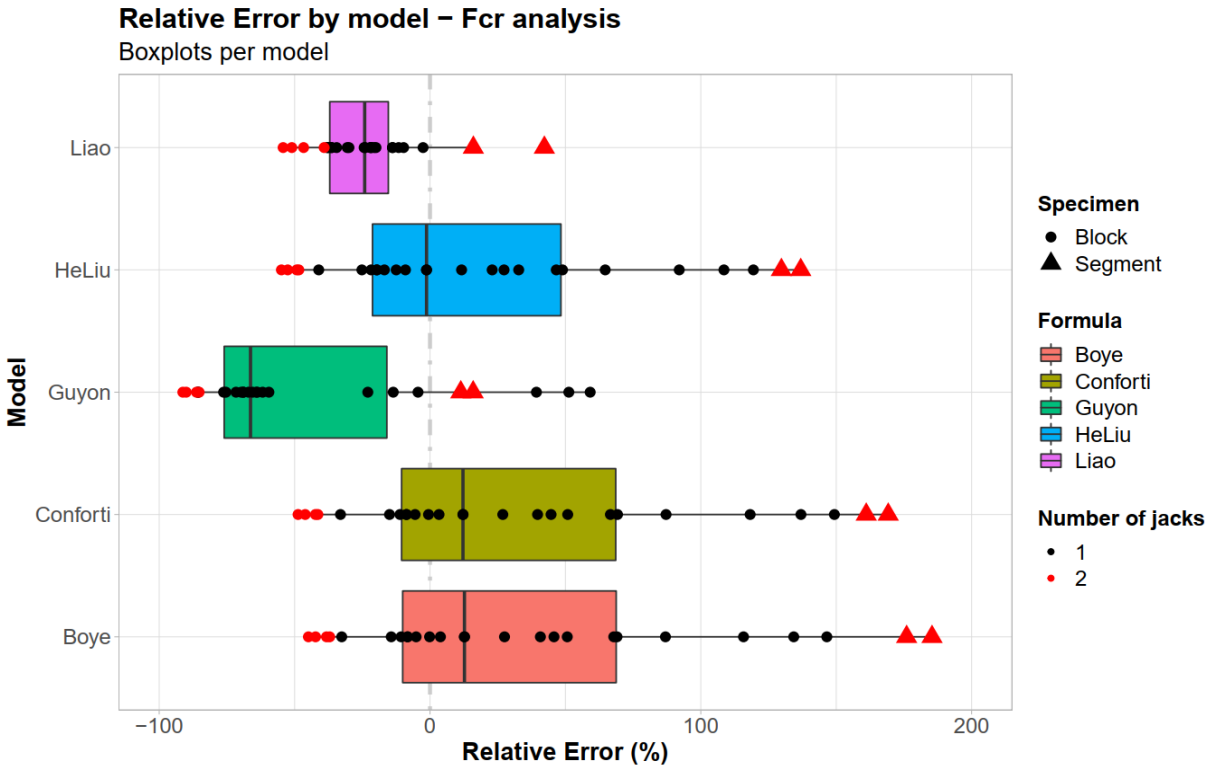

It can be seen that all models showed underestimation of splitting load for the blocks tested with two jacks (red points). On the other hand, except for Guyon (1953) model, the highest positive relative errors observed occur when real scale segments with two jacks were tested. These results show the sensitivity of the analytical models' prediction, as function of the geometry, most related to size/scale effect in this case (for the configuration with two jacks). Unfortunately, the limited number of results available in these conditions (either blocks or segments with two jacks), makes statistical comparisons between configurations impossible. The inferential comparisons could help to decide whether the results must be separated (verifying if it can be assumed, they originated from different populations) or to be analyzed in a unified way (i.e., assuming they originated from the same population). In this work, the results

are assumed to be originated from the same population, given the limited number of available results, for the experimental setups with real scale segments and/or with more than one applying jack load.

In terms of central tendency, the models exhibited different behaviors. Guyon (1953) and Liao *et al.* (2015) models presented medians and interquartile ranges (represented by the boxes in the boxplots) with underestimation for the splitting load, i.e., with negative relative errors, centered in, approximately, -70% and -25% of relative error, respectively. He and Liu (2010) model showed a tendency centered in zero, with more dispersion for positive relative errors. Conforti *et al.* (2016b) and Boye *et al.* (2019) models presented positive central tendencies with very similar relative error distributions. This behavior is expected for centered thrust jacks (i.e., with no eccentricity) in specimens with moderate to high width ratios (b_1/b), since in these cases Boye *et al.* (2019) prediction tends to an elastic solution, which is the basis of Conforti *et al.* (2016b) model. As eccentricity effects and low width ratios are introduced, the two models are expected to provide significant different results.

In terms of dispersion, it can be noticed that Liao *et al.* (2015) model presented the most concentrated distribution, with the majority of results in a range of approximately 50% of relative error. He and Liu (2010), Conforti *et al.* (2016b) and Boye *et al.* (2019) models presented similar ranges with magnitudes higher than 200%. The Guyon (1953) model showed segregation in results under -50% and results with more than-25% of relative errors. This segregation can indicate some influence of geometrical parameters (such as width ratio or specimen's aspect ratio) in the overall response.

In order to analyze the shape of the response's distributions, Figure 25 shows a smoothed density estimates (by means of Kernel density estimate) and normal qqplots for each model. The density estimates shown two peaks for all models with different intensities for the second peaks. The magnitude of these peaks is related to the highest positive relative errors exhibited in each model. It can be noticed that Liao *et al.* (2015) model presented the more abrupt second peak (coherent with the two highest values observed in the boxplot) while Guyon (1953) model showed the more dispersed second peak (related to the results segregation). For the other models the second peak was less evident.

Figure 25 - Probability density estimates and normal qqplots for the relative errors (%) per model

Besides the second peaks, the shapes of the distributions have shown a normal appearance. The normal qqplots presented the adherence of the observed values with the equivalent assumed normal distribution. It can be seen that Guyon (1953) model was the least adherent, due to the mentioned segregation. He and Liu (2010), Conforti *et al.* (2016b) and Boye *et al.* (2019) models showed better adjusts for the central portion of data, with less concordance in the extremities of their distributions. Liao *et al.* (2015) model showed the most adherent distribution, with only two points significantly apart from an assumed normal distribution (represented by the purple straight line), both located in the positive tail. As mentioned in the boxplot analysis, a greater number of usable experimental results with the configurations present in those two higher values (real scale segments with more than one jack thrust), could help to evaluate if this tail behavior is due to different populations (and, thus, need to segregate the data) or consequence of the intrinsic randomness of the sampling process.

As indicated in some model's deductions, besides materials inputs/characteristics (evaluated in parametric analysis), some geometric parameters such as the width ratio (b_1/b) and specimens aspect ratio (h/b) are expected to influence the prediction. Thus, they can also be relevant in models' relative errors. Aiming at evaluating the influence of specimens' width

and aspect ratios, in the relative errors, some scatter plots with linear regression models (with the linear regressions confidence intervals) are exposed in Figure 26 and Figure 27.

Figure 26 - Scatter plots per model – Relative error x b_1/b – F_{cr} Analysis

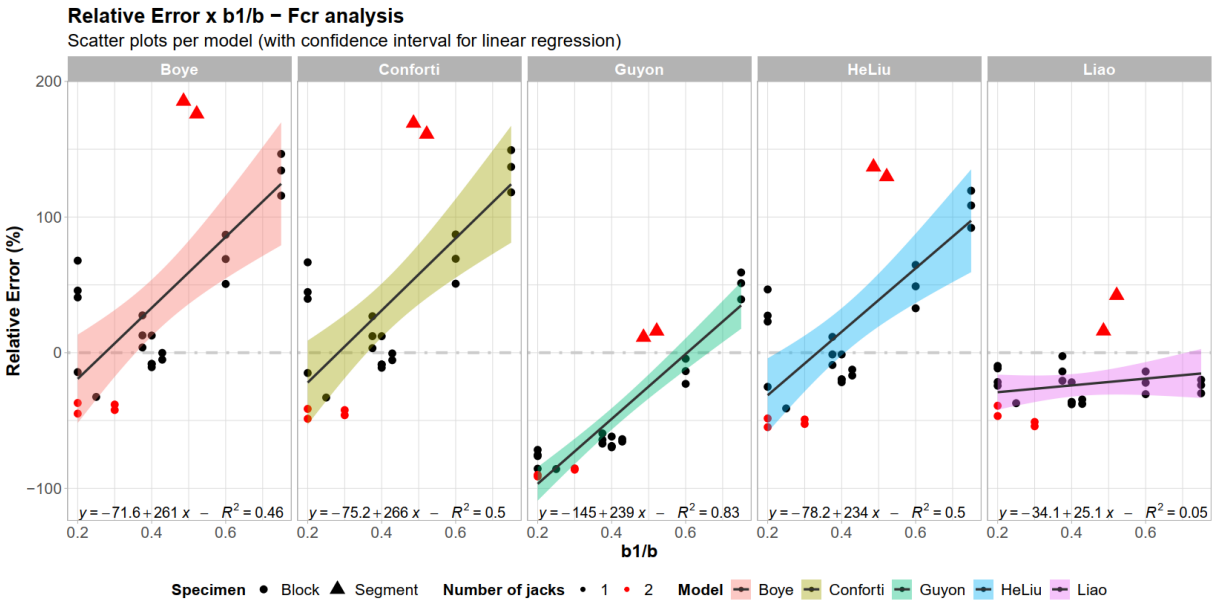

Figure 27 – Scatter plots per model – Relative error x h/b – F_{cr} Analysis

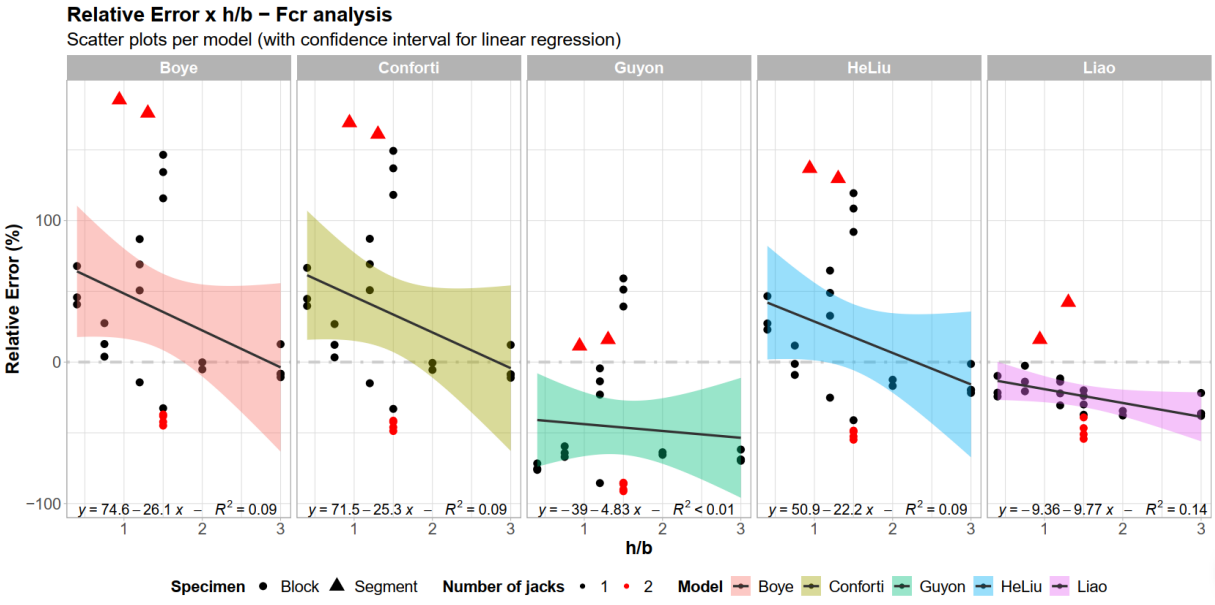

As can be seen in Figure 26, all models but Liao *et al.* (2015) showed relative errors tendencies as function of the width ratio (b_1/b). The variance in relative errors explained by the linear regression (i.e., the coefficient of determination R^2) was about 50% for Boye *et al.* (2019), Conforti *et al.* (2016b) and He and Liu (2010) models. Guyon (1953) model showed the best explanation with and R^2 of 83%. Liao *et al.* (2015) model showed no affected behavior in relative errors as b_1/b changed. The results for blocks with two jacks (red points) seemed closer

to the configurations with a single jack (black points) for all models. As for the segments tested with two jacks (red triangles) Guyon (1953) model presented the closest responses to regression, while the other models exhibited some values apart from the expected ones. The limited number of usable results in this condition makes comparison analysis impossible.

For the aspect ratio analysis presented in Figure 27, it can be noticed that only Liao *et al.* (2015) model exhibited some influence on relative errors as h/b increased, but with a small fraction of variance explanation (R^2=14%). The other models showed an explicit distinct behavior at the h/b=1.5. As the aspect ratios came between 0.5 and 1.5, an increase in relative errors was found. After this aspect ratio, an abrupt change in behavior was observed, with more than 80% difference between neighboring points. No tendency was observed with an increase in h/b after this point. The lack of influence of specimens' aspect ratio for these models can be explained by the assumptions of developed solutions considering semi-infinite strips, i.e., height enough specimens to overcome the disturbance length. For all models it can be concluded that the relative errors showed no influence by the h/b factor with poor adherence with the generated linear regressions.

From the F_{cr} analysis it can be concluded that: More results with blocks and/or segments with two (or more) jacks are necessary in order to verify if the results can be assumed as originated from the same population or if a separation is needed; Liao *et al.* (2015) model presented the least dispersive response, with a great accordance with a normal distribution for its relative errors centered at, approximately, -25% with none or poor influence by specimens' width ratio (b_1/b) and aspect ratio (h/b); Guyon (1953) model showed the best responses for real scale segments with two jacks, first in its values (less than 25% of positive relative error) as for the accordance in the regression model based on the width ratio; A segregation in Guyon (1953) model responses was observed and the behavior of its relative errors was greatly descripted as function of width ratio (b_1/b), with a high coefficient of determination (R^2=83%); He and Liu (2010), Conforti *et al.* (2016b) and Boye *et al.* (2019) models showed similar tendencies and results with significant influence as function of width ratio; neither models presented good adherences in the linear regressions as function of specimens aspect ratios.

In order to predict splitting load for future experimental campaigns, two main options are suggested for enhancing the splitting load prediction from the applicability analysis performed: the use of Liao et al. (2015) model with a correction for bias, assuming a normal distribution of the relative errors (centered at -25%) and the use of Guyon (1953) equation with a parametric

correction obtained from the linear regression between relative error and width ratio (b_1/b). Table 7 presents the improved analytical models suggested from the applicability analysis.

Table 7 - Improved analytical models suggested from the applicability analysis

Model	Assumptions	Improved F_{cr}	Improvement
Guyon (1953)	Semi-infinite strip	$(2{,}45 - 2{,}39\frac{b_1}{b})\frac{b_1.t}{1{,}1\ (0{,}47)\left(1-\left(\frac{b1}{b}\right)\right)}f_t$	Equation with parametric correction obtained in the linear regression between relative error and b_1/b
Liao *et al*. (2015)	Short blocks	$1.25\frac{8t(h-2k_1b_1)(h-k_1b_1)}{3(b-b_1)}f_t$	Correction for bias, assuming a normal distribution of the relative errors centered at -25%
	Long blocks	$1.25\frac{8t(h-2k_1b_1)(h-k_1b_1)}{3(4a_2-b_1)}f_t$	

5.2 NUMERICAL MODELING – SPLITTING

As described previously, the numerical modeling approach present in this work is discussed in terms of simulation of the local behavior of concrete tunnel segments with a focus on splitting crack initiation. Unlike the analytical models discussed in topic 5.1, the numerical simulation can take into account the reinforcement effect on splitting crack development. Thus, the numerical simulation can be used complementarily with the analytical models: while the latter is used to predict the splitting load as function of specimens' dimensions and concrete parameters, the second also considers the reinforcement effect at cracking early stages, contributing to extend the analysis after achieving the splitting crack load.

In order to evaluate the numerical approach suggested in this work, two numerical simulations are conducted considering a plain concrete configuration and a fiber reinforced concrete configuration. The plain concrete simulation is conducted based on the experimental campaign proposed in Tiberti *et al.* (2015), while the fiber reinforced concrete simulation is based on the Schnutgen and Erdem (2001) experimental campaign. The latter was used for other model validations such as in Burgers (2006) and Nogales *et al*. (2020).

The numerical analysis present in this chapter was conducted in four steps: definition of test setup; typical failure pattern for splitting tests and campaign results; a simulation with a plain concrete (PC) configuration for Tiberti *et al.* (2015) campaign; and a steel fiber reinforced concrete simulation with a parametric study (on the inputs for the interface fiber-matrix material model) for Schnutgen and Erdem (2001) results.

5.2.1 TIBERTI *ET AL*. (2015)

5.2.1.1 EXPERIMENTAL RESULTS AND TEST SET-UP

The experimental campaign realized in Tiberti *et al*. (2015) consisted in splitting tests with a line and point load configurations (with one jack pad), in specimens with enough height to overcome the disturbance length (250x250x750 mm), and a width ratio of b_1/b = 0.40. The reinforcement strategy varied from plain concrete (no reinforcement) and polypropylene fiber reinforcement with two different casting directions. In order to measure displacements produced by splitting, LVDT transducers were placed on specimens' frontal face (perpendicular to the load). Figure 28 shows the test setup used for the line load condition.

Figure 28 – Experimental test set-up – adapted from Tiberti *et al*. (2015)

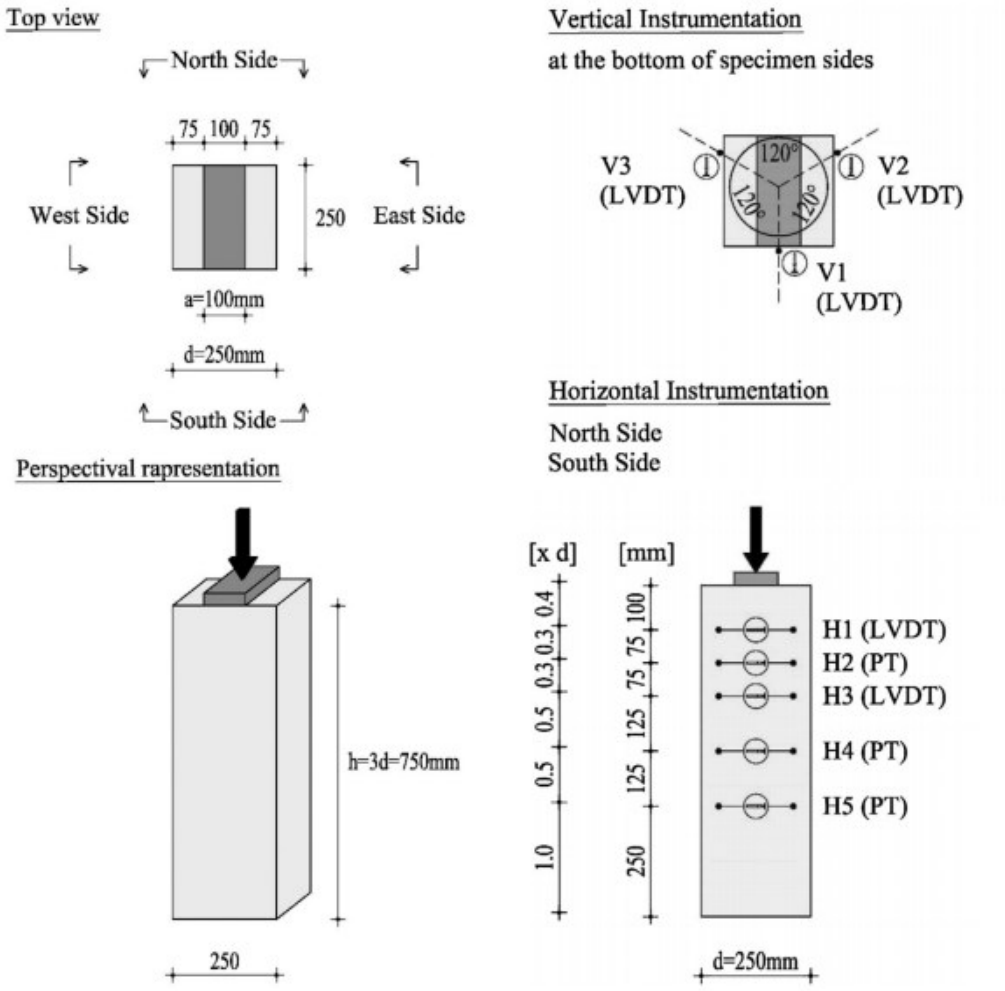

Three blocks were cast in the vertical direction, regarding the line load condition for plain concrete. The average compressive strength was 57.2 MPa.

As for the expected development of stress flow and the typical failure pattern in splitting tests, both can be visualized in Figure 15 and Figure 16. Figure 29 shows the failure pattern in a plain concrete sample. As for the experimental curve results: the results were displayed in

graphs with the LVDT horizontal displacement versus the applied load. Only curves with horizontal displacement for H1 were analyzed, since their location correspond with the expected maximum elastic splitting stress (Figure 15). Figure 30 shows the mean experimental curves for the line load tests. It can be noticed the adherence of fiber reinforced samples to the expected qualitative behavior indicated in Figure 16. The plain concrete samples failed after reaching the splitting load (that, in this case, is also the maximum applied load) with significant smaller horizontal displacements. Table 8 shows the splitting loads and summary statistics such as mean, upper and lower 95-percent confidence limits (denoted as “mean”, “UCL-95” and “LCL-95”, respectively) for the plain concrete samples.

Figure 29 - Experimental cracking pattern in plain concrete sample - Tiberti *et al*. (2015)

Figure 30 - Experimental results for plain and fiber reinforced concrete in Tiberti *et al*. (2015)

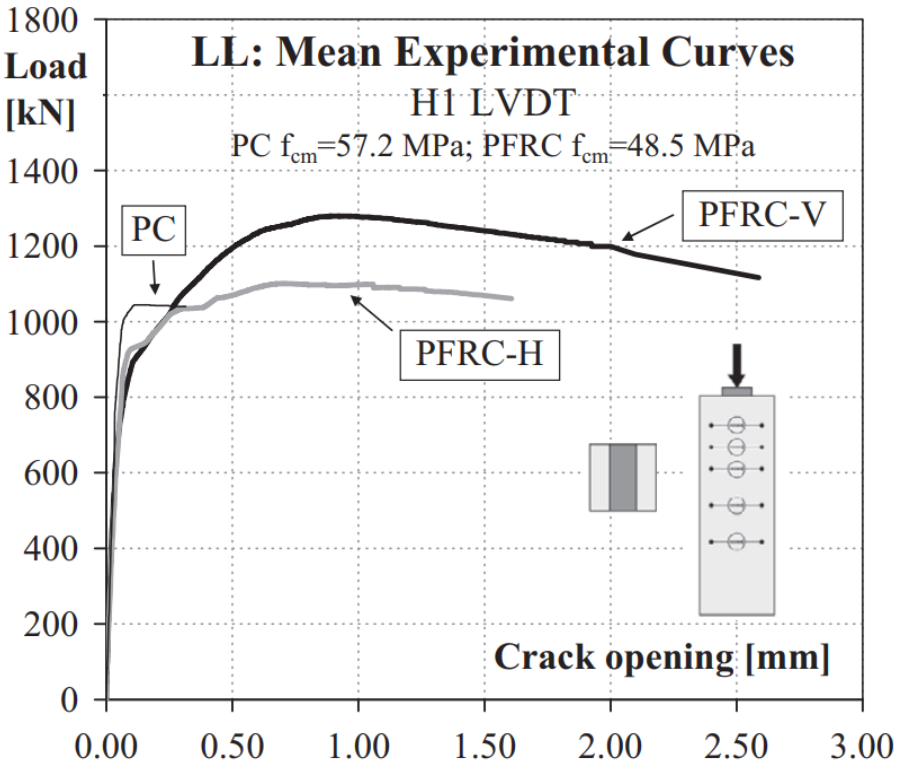

Table 8 – Experimental splitting results for plain concrete samples – Tiberti *et al*. (2015)

Specimen	Splitting load (kN)
LL-PC-1	1152
LL-PC-2	1011
LL-PC-3	970
Mean	1044,3
UCL-95	1151,8
LCL-95	936,8

As presented in the F_{cr} Analysis, the analytical models' prediction for this campaign underestimated the mean splitting load (F_{obs}), although Boye and Conforti's predictions were higher than the lower 95-percent confidence limit. Figure 31 (extracted from Appendix A.4) shows these results, while Figure 32 indicates it in the graphical curves perspective (with a more detailed x-axis in comparison to Figure 30).

Figure 31 - Analytical models prediction for Tiberti *et al*. (2015) plain concrete configuration

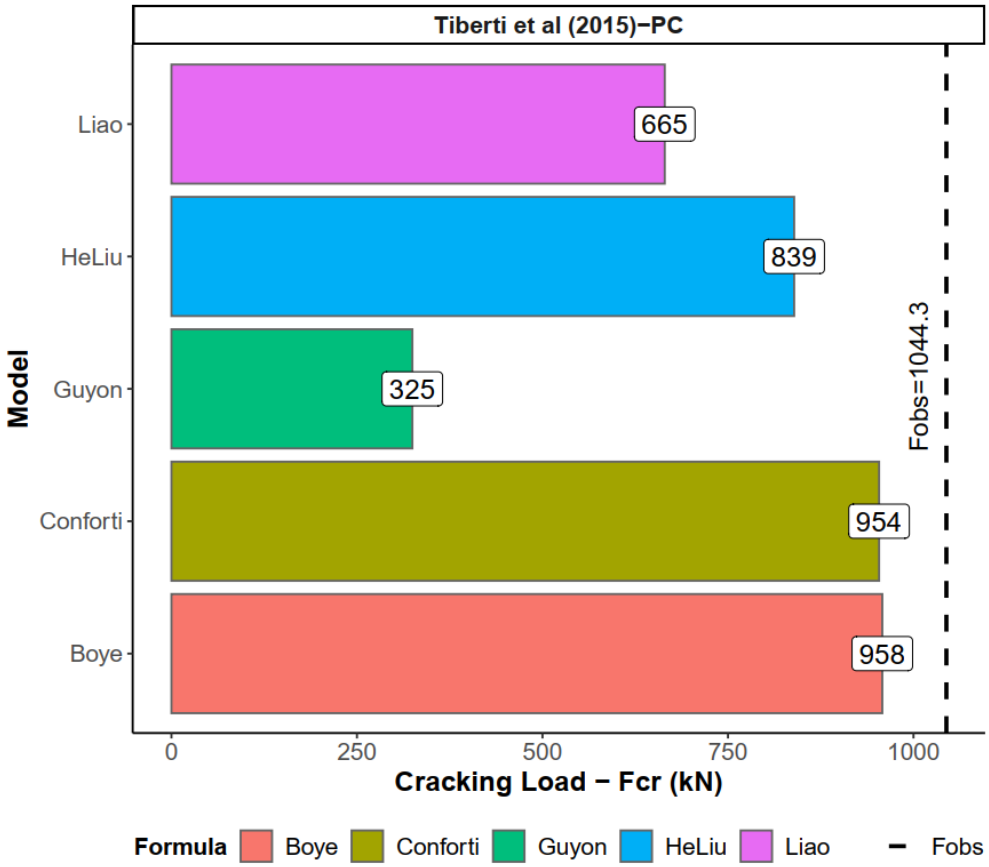

Figure 32 – Experimental results and analytical predictions – Tiberti *et al*. (2015)

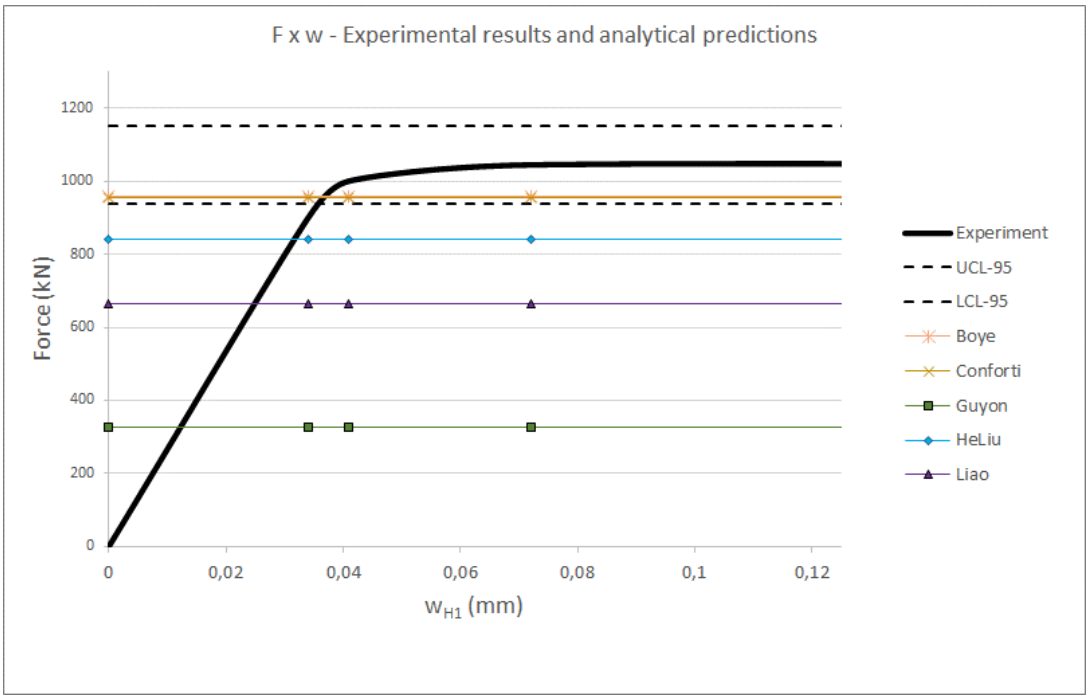

5.2.1.2 PLAIN CONCRETE NUMERICAL SIMULATION

For plain concrete numerical simulation, a mathematical model was developed with a plane stress assumption, and a vertical applied displacement horizontally restricted at the top of the specimen. Also, a vertical restriction at its base, with one point (at the middle axis) with horizontal restriction was imposed. As for the elements' type, the Constant Strain Triangle (CST) was adopted. A mesh containing 17126 elements (8764 nodes) was automatically generated, and the model was simulated with 2500 loading incremental steps. Figure 33 indicates a schematic sketch of the mathematical model and the generated mesh.

Figure 33 - Schematic sketch of mathematical model and mesh generated for FEM simulations – plain concrete

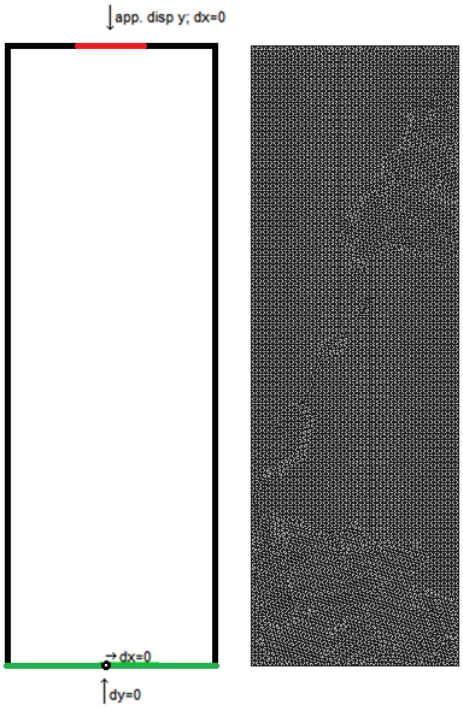

The parameters used in concretes model material are exposed in Table 9. The parameters E and G_F were calculated though formulas (22) and (23), presented in fib Model Code 2010 (2013). The compressive input (f_{c0}) was adopted as sixty percent of mean compressive strength ($0.6f_{cm}$). The tensile input adopted (f_{ct}) was calibrated in order to represent the structural curve as well as the failure pattern.

$$E = E_{c0} \times \alpha_E \times \left(\frac{f_{cm}}{10}\right)^{1/3}, \text{ with } f_{cm} \text{ in MPa and } \alpha_E=1,\ E_{c0}=21.5\text{x}10^3 \text{ MPa} \quad (22)$$

$$G_F = \frac{73}{1000} f_{cm}{}^{0.18}, \text{ with } f_{cm} \text{ in MPa} \quad (23)$$

Table 9 – Parameters used on the numerical model for plain concrete configuration (PC)

Parameter	Value	Unit
f_{ct}	2,33	MPa
E	38450,7	MPa
ν	0,2	-
G_F	0,151	N/mm
f_{c0}	34,32	MPa
A^-	1,0	-
B^-	0,89	-
β	1,16	-

The results are exposed in terms of graphical curves, principal stresses distributions, evolution of the tensile damage variable and type of failure observed.

Figure 34 shows the numerical results obtained. The numerical curve showed positive agreement with the experimental one. The numerical splitting load was approximately 1106 kN and, thus, within the 95-percent confidence interval for the mean experimental splitting load (this is, within the experimental dispersion for the mean splitting load).

For an applied load about 550kN, (still in the specimens' linear elastic behavior), the principal stresses distributions were analyzed (Figure 35). It can be noticed that the numerical model agrees with the expected elastic stress flow.

Figure 34 – Experimental and numerical results – Tiberti *et al*. (2015)

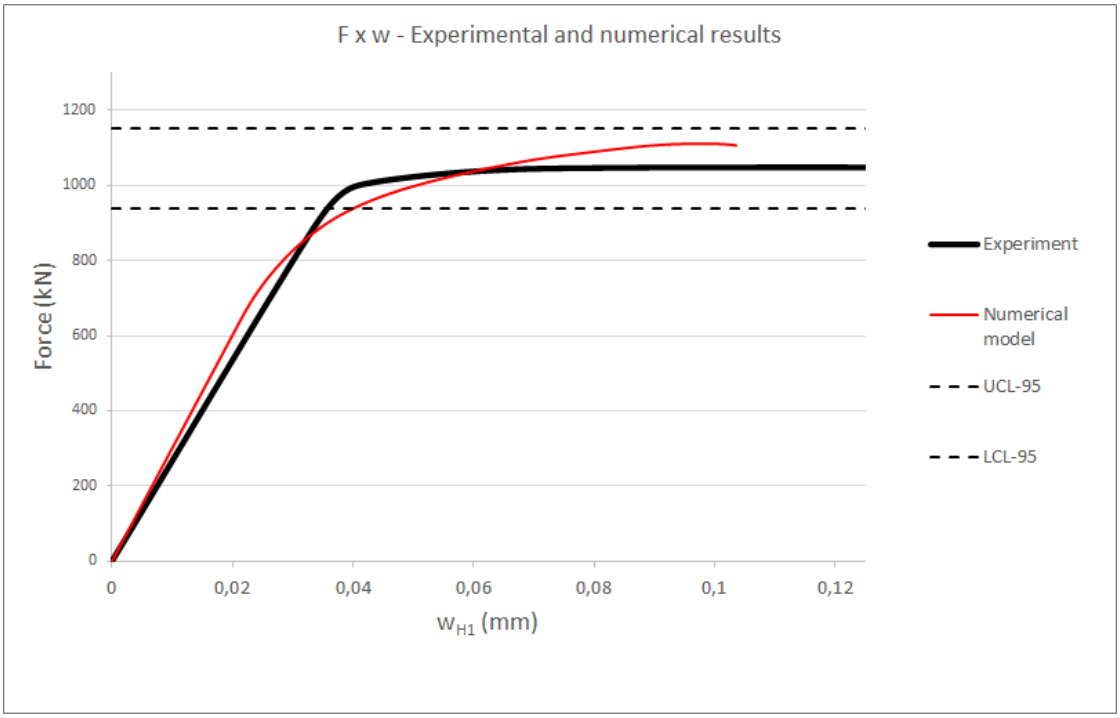

Figure 35 – Expected elastic stress flow – Leonhardt (1973) (left); and minimum and maximum principal stresses obtained in numerical model (center and right)

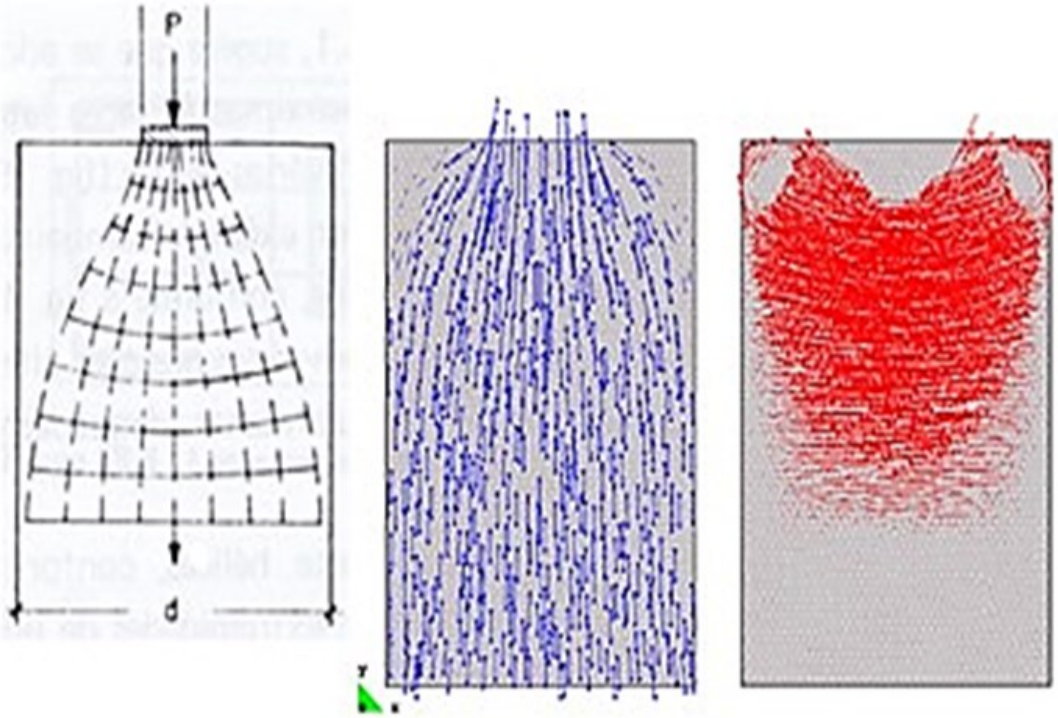

For an applied load about 693 kN, the tensile damage variable at the specimen's center line was initiated (i.e., presented a value higher than zero). As the applied load increased, the evolution of the tensile damage variable presented higher values in a conical arrangement, starting at the tips of the loading region with a path to specimens' center line. Also, it can be observed a vertical damage evolution at the center line. The behavior mentioned is presented in Figure 36, with a visual damage evolution in three loading increments. It can be observed that the numerical type of failure was consistent with the expected experimental one. Figure 37 illustrates this comparison.

Figure 36 – Numerical model results (PC) – F x w_{H1} curve with tensile damage evolution

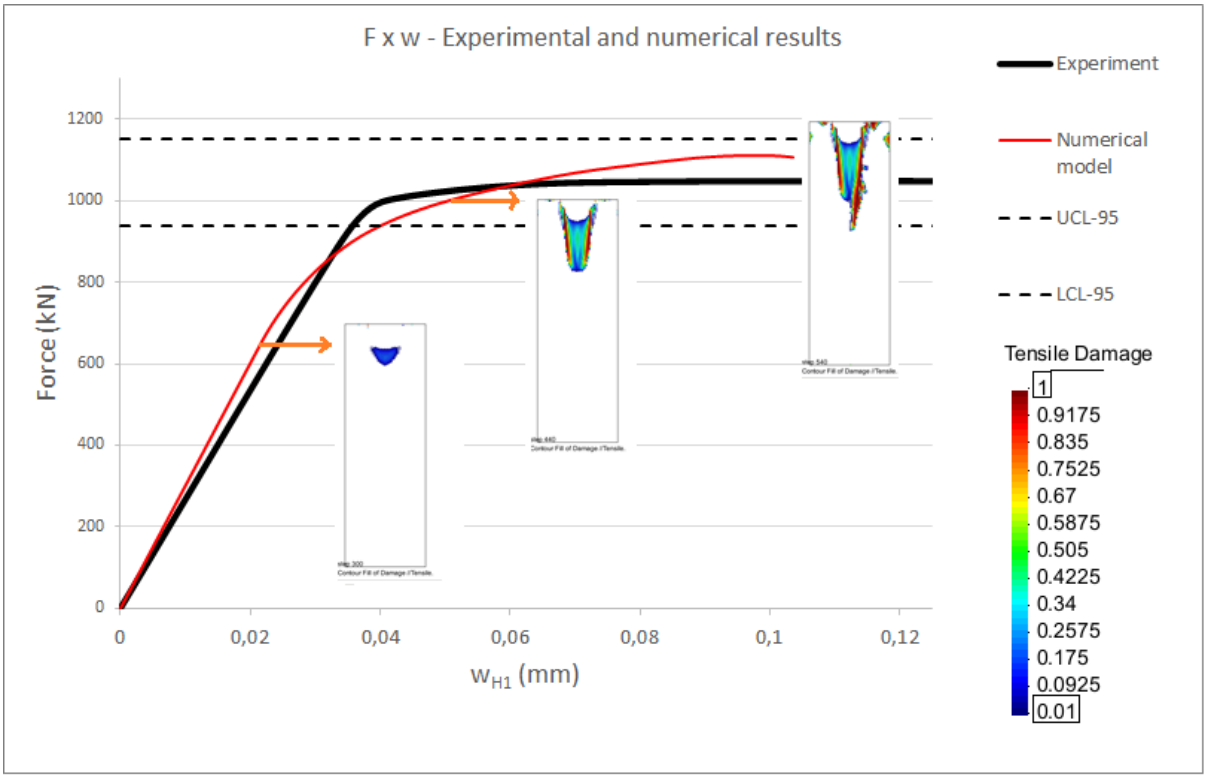

Figure 37 – Experimental and numerical type of failures: PC configuration – Tiberti *et al.* (2015) (left); Numerical model (right)

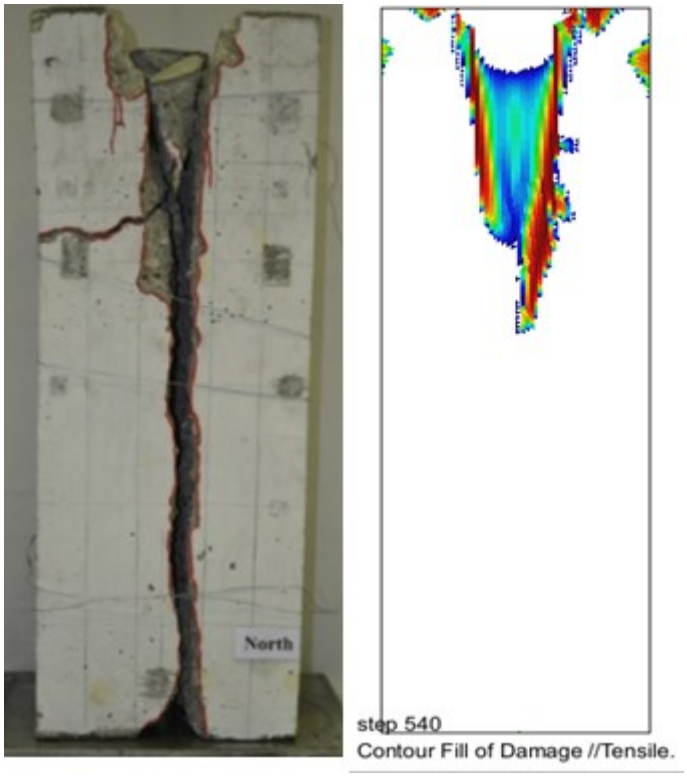

From the plain concrete numerical simulation, it can be concluded that: the FEM model was able to reproduce the essential behavior of concrete subjected to high localized compression

loads, such as the stress flow and the failure mode. Also, the evolution of the tensile damage variable was proven useful to represent cracking propagation and splitting failure.

5.2.2 SCHNUTGEN AND ERDEM (2001)

5.2.2.1 EXPERIMENTAL RESULTS AND TEST SET-UP

The experimental campaign realized in Schnutgen and Erdem (2001) consisted in a splitting test with a line load configuration (one jack pad) in specimens with height enough to overcome the disturbance length (350x350x700 mm) and a width ratio of $b_1/b = 0.429$. In order to measure displacements produced by splitting, LVDT transducers were placed on specimens' frontal face (perpendicular to the load). Figure 38 shows the test setup utilized.

Twelve blocks were cast with three different SFRC mixes. 35 kg/m³ (SFRC-A) and 60 kg/m³ (SFRC-B) of hooked-end steel fibers were used for produce the SFRC mixes. The fibers' length and diameter were, respectively, 60mm and 0.75mm. The average compressive strengths for SFRC-A and SFRC-B were, respectively, 58.2 MPa and 50.2 MPa.

As for the expected development of stress flow and the typical failure pattern in splitting tests, both can be visualized in Figure 15 and Figure 16. Nogales *et al*. (2020) presented an schematic image with the experimental cracking pattern obtained in Schnutgen and Erdem (2001) results (Figure 39).

Figure 38 – Test setup for Schnutgen and Erdem (2001) experimental campaign (adapted from Nogales *et al*. (2020))

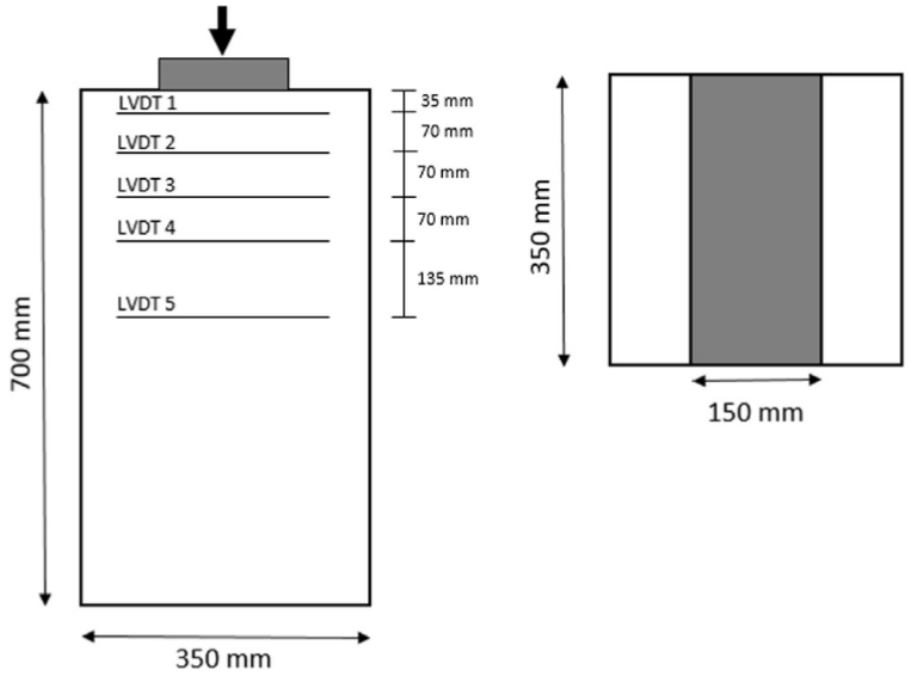

Figure 39 – Schematic image from Nogales (2020) for experimental cracking pattern observed in Schnutgen and Erdem (2001) results

As for the experimental curve results: the results were displayed in graphs with the LVDT horizontal displacement versus the applied load. Only curves with the horizontal displacement for the LVDT 3 were analyzed, since their location corresponds with the expected maximum elastic splitting stress (Figure 15). Figure 40 shows the experimental results for the SFRC-A configuration.

Figure 40 - Experimental curves for SFRC-A configuration - Schnutgen and Erdem (2001)

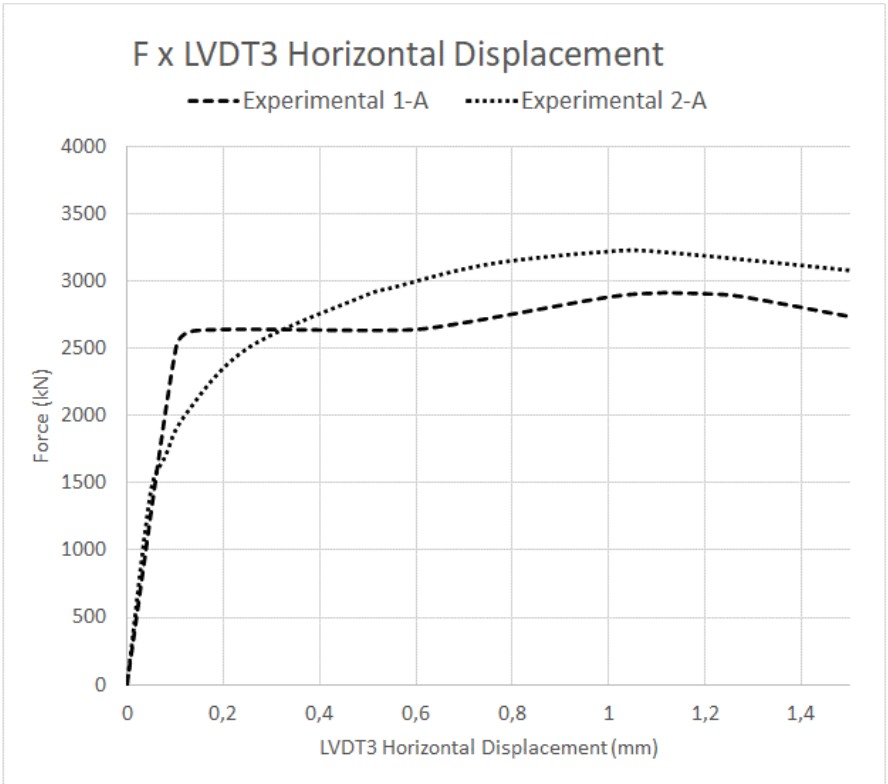

The specimen “Experimental 2” showed a behavior similar to the one expected for this type of tests in fiber reinforced concretes (Figure 16) with a splitting load around 1500 kN and a peak load about 3300 kN. The specimen “Experimental 1” showed a linear branch after its splitting load (about 2500 kN) and only after a horizontal displacement of 0.5mm, an ascending branch was observed, correspondent to the second stage of the expected experimental curve.

The strategy to analyze this experimental campaign with numerical modeling consisted in two steps: first, the SFRC-A campaign was calibrated, modeled and interpreted. Then, two different fiber contents are modeled, the SFRC-B with 60 kg/m³ and SFRC-C with 20 kg/m³.

5.2.2.2 SFRC-A NUMERICAL SIMULATION

For the SFRC-A numerical simulation, a mathematical model was developed with a plane stress assumption, and a vertical applied displacement horizontally restricted at the top of the specimen. Also, a vertical restriction at its base, with one point (at the middle axis) with horizontal restriction was imposed. As for the elements’ type, the Constant Strain Triangle (CST) was adopted. A mesh containing 99343 elements (57007 nodes) was automatically generated considering concrete, fiber and coupling elements. The model was simulated with 4000 loading incremental steps. Figure 41 indicates a schematic sketch of the mathematical model and the mesh generated, showing only the concrete elements. The simulation was conducted starting with a set of input parameters taken as “reference” for concrete-fiber interaction and, then, a parametric study was made to better comprehend the influence of each input parameter in the overall numerical response. The input parameters adopted for the fiber material and concrete-fiber interface are exposed in Table 11.

The parameters utilized in concretes material model are exposed in Table 10. The parameters E and G_F were calculated with the same approach adopted for Tiberti *et al*. (2015) simulation. In order to avoid compressive damage which may influence numerical type of failure, specially at the tips of the applying load region, a value of 2500 MPa was adopted for f_{c0} parameter. As consequence, the numerical model can simulate the structural curve only until the end of second stage (Figure 16). The Cervera’s model inputs A^-, B^- and β adopted were based on the recommendations presented in Cervera *et al*. (1996) for concrete.

Figure 41 – Schematic sketch of mathematical model and mesh generated for FEM simulations

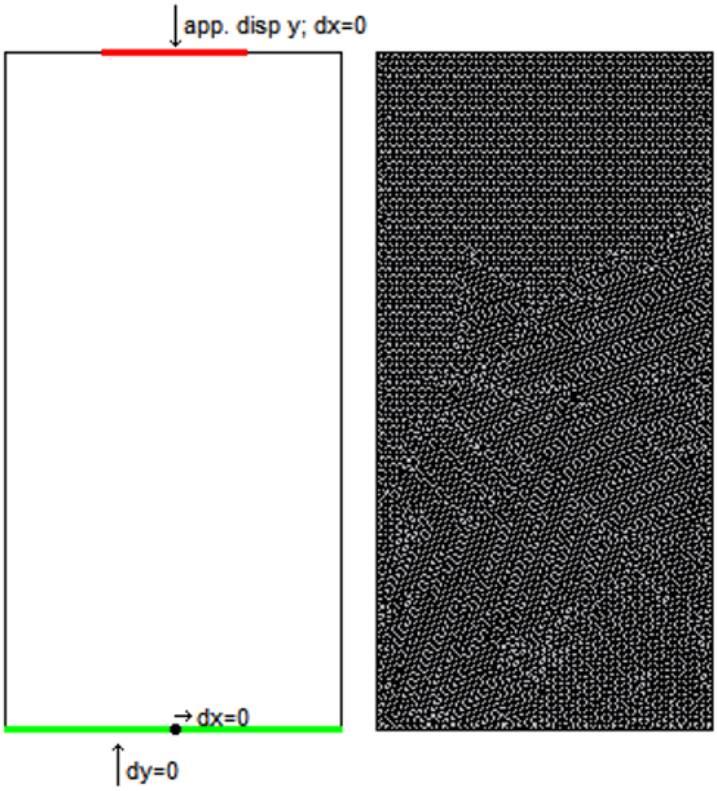

Table 10 – Parameters utilized for concrete material model

Parameter	Value	Unit
f_{ct}	2,0	MPa
E	34000	MPa
ν	0,2	-
G_F	0,152	N/mm
f_{c0}	2500	MPa
A^-	1,0	-
B^-	0,89	-
β	1,16	-

Table 11 – Reference input parameters for fiber and concrete-fiber interface – SFRC simulation

Parameter	Value	Unit
Fiber input parameters		
E	210000	MPa
f_Y	1100	MPa
Concrete-fiber interface parameters		
K_X	10^3	

$K_Y=K_Z$	10^6	
$\tau_{b,Máx}$	4,0	MPa
$\tau_{b,f}$	0,5	MPa
$s_1=s_2$	0,1	mm
s_3	2,0	mm
α	0,4	

Figure 42 indicates the results of loading versus LVDT3 horizontal displacement for the numerical model tested, denominated “Numerical SFRC-A”. It can be noticed that the numerical curve presents good agreement with both experimental results in the linear stage and is more like the “Experimental 2-A” in the second stage. In order to analyze the evolution of damage tensile variable and the axial stress in fiber elements, the loading steps of 1200 kN, 1500 kN, 2200 kN and 2900 kN were selected.

Figure 43 shows the evolution of damage tensile variable and the axial stress in fiber elements (restricted to positive values, indicating only tensile stresses, in MPa) for each loading step. Even though they’re different experimental campaigns, it can be observed that the initial tensile damage for the SFRC-A numerical model is more dispersed when compared to the plain concrete numerical simulation. Figure 44 shows this qualitative difference, indicating that the numerical approach adopted can reproduce SFRC behavior of local redistribution of tensile stresses in the structure. In advanced loading steps, such as up to 2000 kN, the stress redistribution provided by fiber reinforcement can be seen in the ramification of more than one vertical pattern of tensile damage at the mid-axis.

As for the axial stress in fiber elements, it can be noticed that: as the loading increased, more axial stress was observed in fibers, but far away from their yield stress (1100 MPa). The fibers more solicitated were mostly orientated in a horizontal direction. This behavior represents the bridging effect that fiber reinforcement develops when fibers are perpendicular to the cracking plane. The experimental campaign proposed in Trabucchi *et al* (2021) shows this mechanism in a similar splitting test.

It is also relevant to mention that the visualization provided by the adopted numerical approach was proven useful to evaluate and represent the reinforcement response during the loading.

Figure 42 - Numerical model results (SFRC) – F x LVDT 3 curves with tensile damage evolution

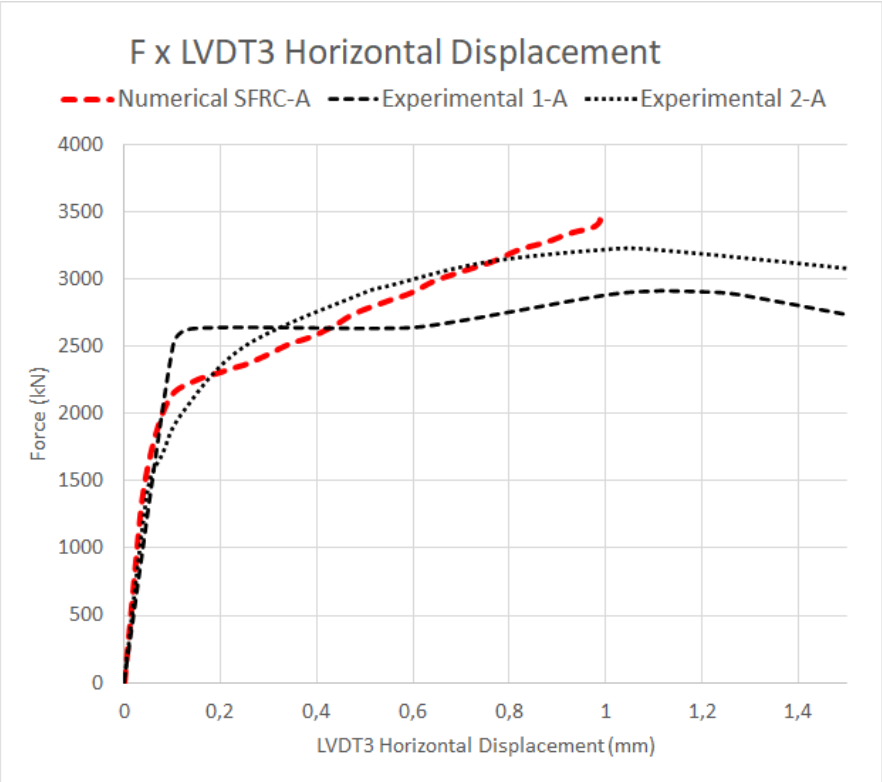

Figure 43 - Evolution of damage tensile variable (up) and Axial stress in fiber elements (down), in MPa, at 1200, 1500, 2200 and 2900– SFRC A numerical simulation

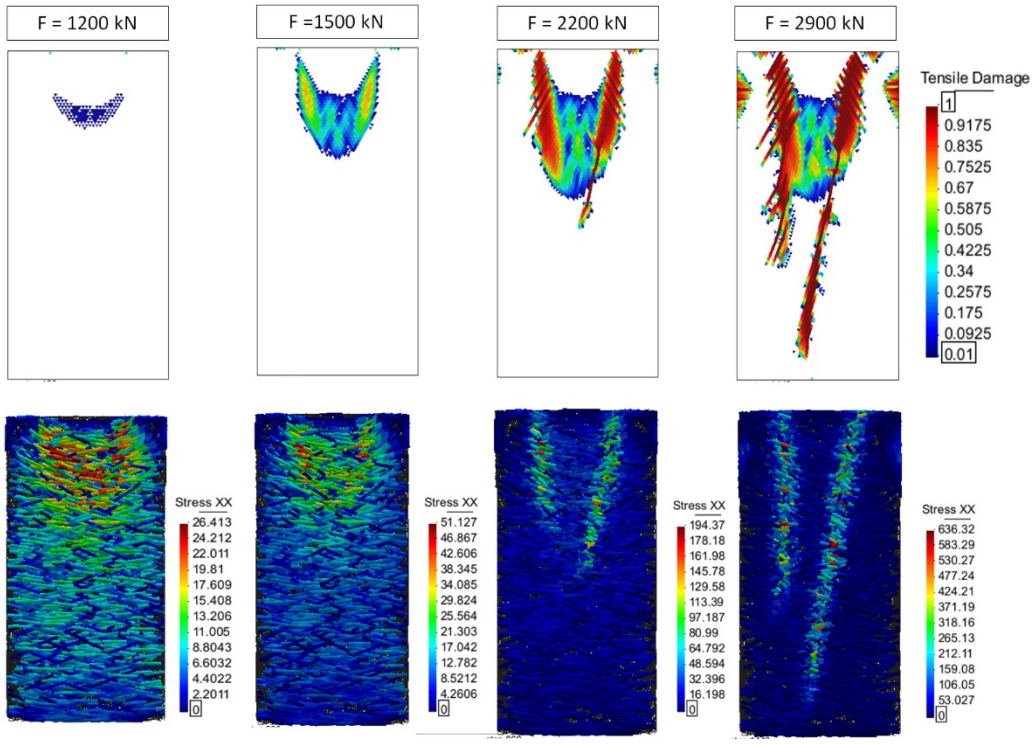

Figure 44 - Initial damage tensile variable qualitative comparison - plain and SFRC numerical simulations

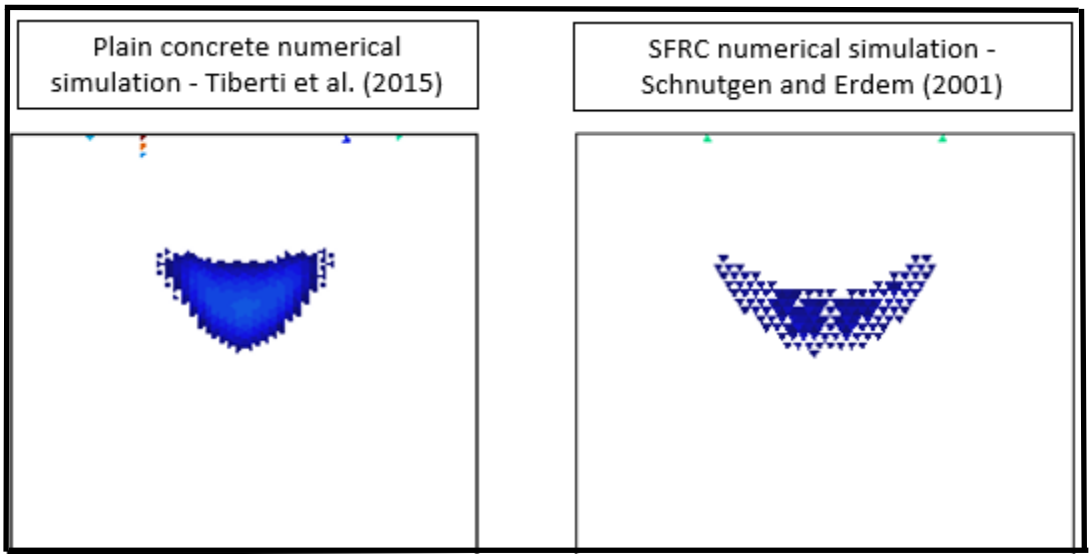

5.2.2.3 SFRC B AND C NUMERICAL SIMULATION

For the SFRC-B and SFRC-C numerical simulations, the mathematical model was the same adopted for SFRC-A. The material parameters were also the same as indicated in Table 10 and Table 11.

For SFRC-B, the increase in fiber content was numerically made by increasing fiber elements properties such as transversal area and perimeter. As consequence, the resultant mesh presented the same number of elements that SFRC-A numerical model (99343 elements with 57007 nodes). For SFRC-C a new cloud of fibers was generated in order to achieve the desired content (20 kg/m³). The resultant mesh with the same density presented 61015 elements (34761 nodes) considering concrete, fiber and coupling elements. The models were simulated with 4000 loading incremental steps.

Figure 45 indicates the results of loading versus LVDT3 horizontal displacement for the numerical models. The numerical splitting load (i.e., the loading in which the numerical model presents central damage tensile) was very similar for all models, since it's governed by concretes tensile strength. In terms of stiffness at the second stage, the numerical response was proportional to fiber content. This is, as the fiber content increased, the curves slope at the second stage also increased. It can be noticed that with higher slopes, higher maximum loads were obtained. This behavior was also verified in the experimental campaign proposed in Trabucchi *et al* (2021).

Figure 46 and Figure 47 shows the evolution of damage tensile variable and the axial stress in fiber elements (in MPa) for each loading step for SFRC-B and SFRC-C, respectively. It can be observed that the tensile damage pattern is more concentrated as fiber content decreases. Figure 48 shows this qualitative difference for the loading step of 2200 kN, indicating that the redistribution of tensile stresses is more accentuated when higher fiber contents are present in the structure. As for the axial stress in fiber elements, a similar pattern and magnitude of maximum stresses was observed.

Figure 45 - Numerical model results (SFRC-B and SFRC-C) – F x LVDT 3 curves with tensile damage evolution

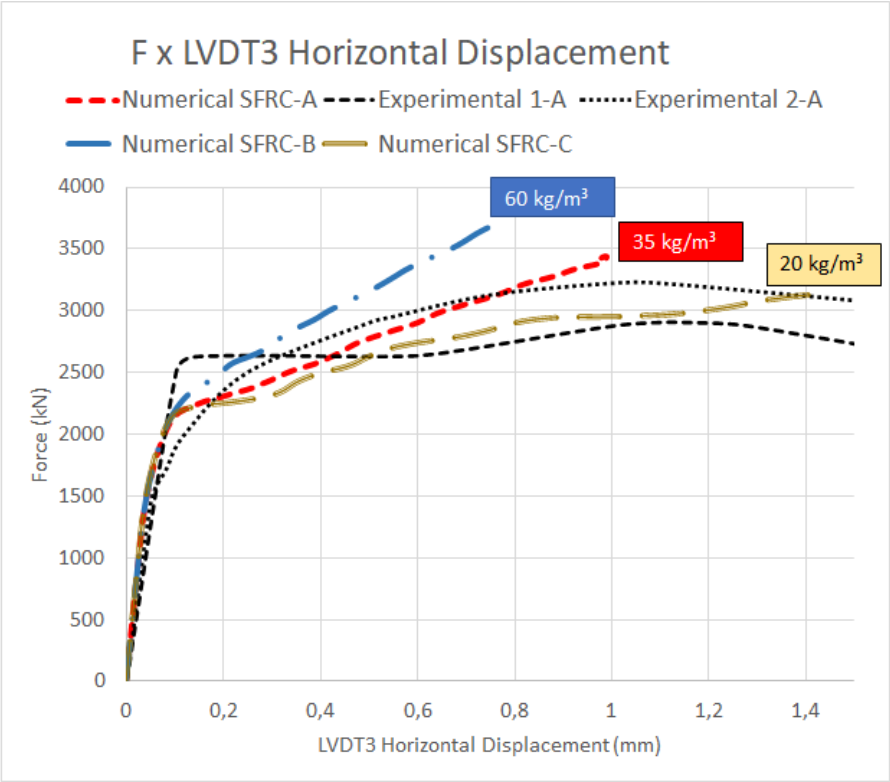

Figure 46 - Evolution of damage tensile variable (up) and Axial stress in fiber elements (down), in MPa, at 1200, 1500, 2200 and 2900– SFRC B numerical simulation

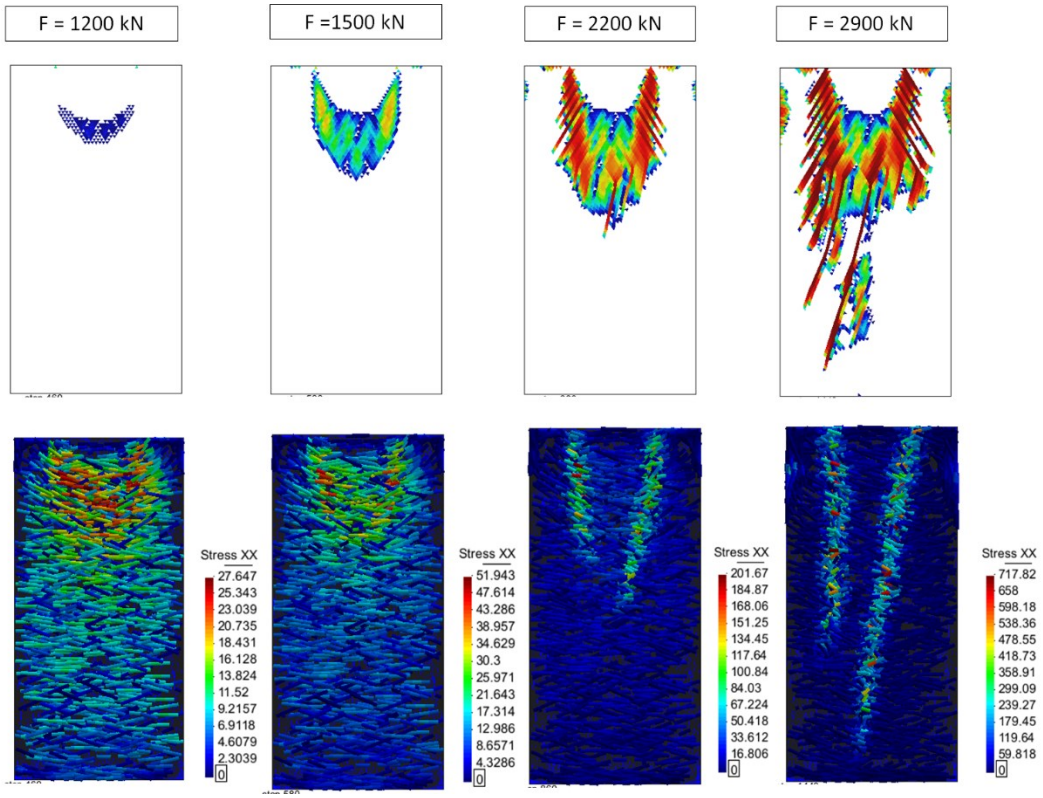

Figure 47 - Evolution of damage tensile variable (up) and Axial stress in fiber elements (down), in MPa, at 1200, 1500, 2200 and 2900– SFRC C numerical simulation

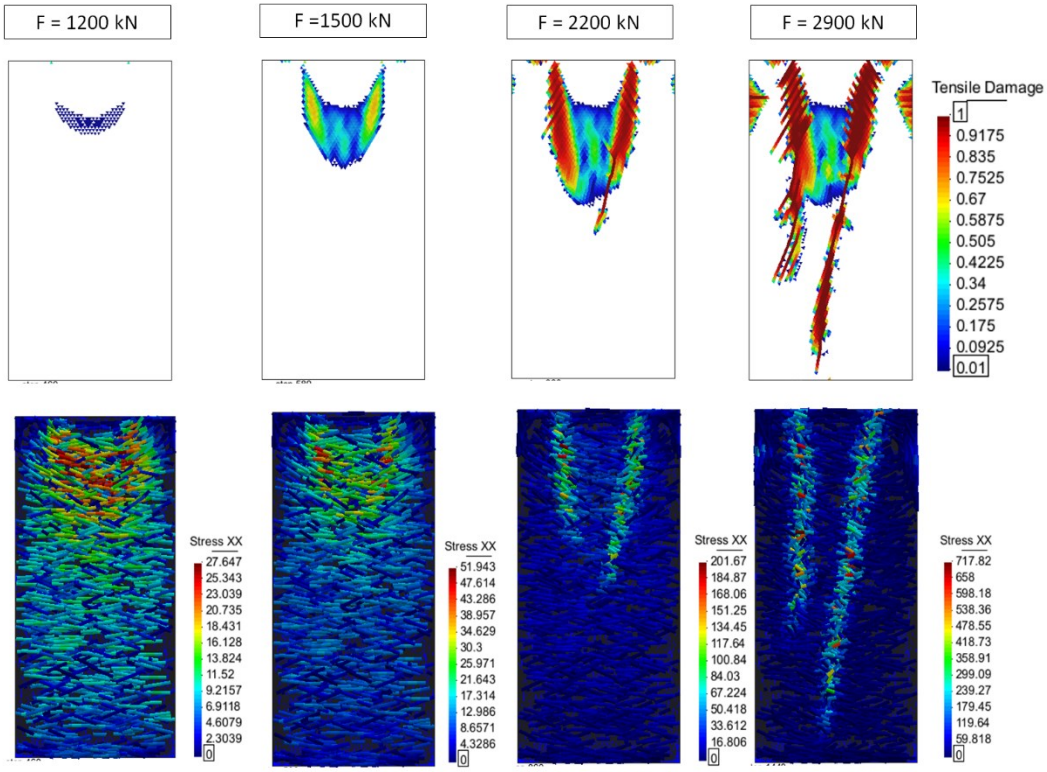

Figure 48 - Damage tensile variable qualitative comparison at loading step of 2200kN – SFRC A, B and C

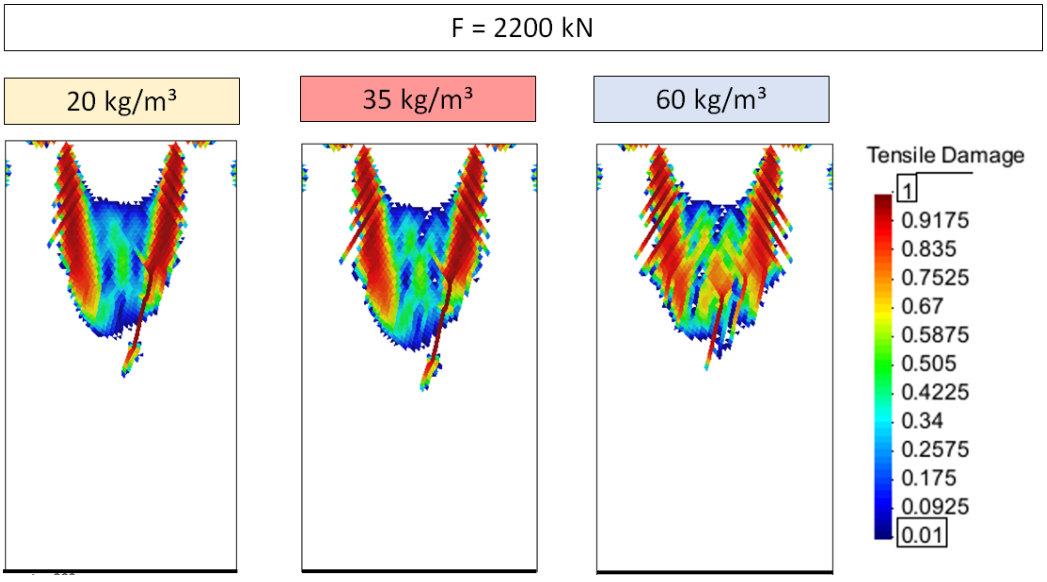

6 CONCLUSIONS

The present work discussed the applicability of analytical models to predict splitting in concrete, and also discussed a numerical modeling approach to investigate the effect of reinforcement by discrete fibers on local behavior with focus on cracking initiation. These results can help to reduce costs related to repair interventions on TBM tunnels construction, once they're related to ensure a better cracking control in the most critical construction phase of these tunnels, the thrust phase. The splitting phenomena was evaluated in terms of concrete tensile strength and fiber reinforcement response in the post-cracking stage. The study suggested two different analytical models with corrections to estimate the load to initiate splitting in concretes. These models with the suggested corrections can be used to design precast segments considering concrete parameters. As for the cracking initiation and development, the study concluded that numerical modeling approach adopted was proven useful to evaluate and represent the concrete and the reinforcement response with sensitivity to variations in fiber content and damage patterns.

At the end of the work, all knowledge and discussions evolved in the latter topic gave an embracing contribution to TBM-constructed tunnels context concerning the splitting failure.

Complementarily, the specific conclusions of the present work can be listed below:

- The parametric analysis showed the sensitivity of each analytical model regarding the tensile input, with less significance and better prediction for Liao *et al.* (2015) model;
- The F_{cr} analyses showed the differences between analytical models regarding different test setups, such as specimens' type and geometry, and loading configurations. Liao *et al.* (2015) model presented the least dispersive response, while Guyon (1953) model showed the best responses for real scale segments with two jacks;
- In order to predict splitting load for future experimental campaigns, two main options were suggested from the F_{cr} analysis: the use of Liao *et al.* (2015) model with a correction for bias, or the use of Guyon (1953) equation with a parametric correction;
- The numerical analysis on plain concrete was able to reproduce the essential behavior of concrete subjected to high localized compression loads, such as the stress flow, the test curve and the failure mode.
- The numerical analysis was able to reproduce SFRC behavior of local redistribution of tensile stresses in the structure and post-cracking response

- The numerical analysis was sensitive about the variation in fiber reinforcement contents with changes in the structural curve and tensile damage pattern
- The damage tensile variable and the axial stress on each fiber element was proven useful tools to evaluate and represent the initiation and development of splitting cracking in concretes subjected to concentrated loads

7 SUGGESTIONS FOR FUTURE RESEARCH

The suggestions for future research are listed below:

- To conduct a reliability analysis for the splitting failure in concrete segments considering the analytical models with corrections and numerical modeling
- To conduct numerical simulations regarding local segment behavior varying reinforcement strategies such as: conventional reinforcement, different types of fiber reinforcement and contents and hybrid reinforcement
- To conduct numerical simulations regarding local segment behavior varying loading ratios and elements aspect ratios
- To conduct numerical simulations regarding global segment behavior, with varying boundary conditions and loading conditions (such as eccentricity effects)

8 REFERENCES

ABBAS, S.; SOLIMAN, A.; NEHDI, M. Structural behaviour of ultra-high performance fibre reinforced concrete tunnel lining segments. **FRC 2014 Joint ACI-fib International Workshop. Fibre Reinforced Concrete Applications.**, n. June 2017, p. 532–543, 2014.

ALTENBACH, H. Sumio Murakami, Continuum Damage Mechanics – A Continuum Mechanics Approach to the Analysis of Damage and Fracture, Springer: Dordrecht, Heidelberg, London, New York, 2012. **ZAMM Journal of applied mathematics and mechanics: Zeitschrift für angewandte Mathematik und Mechanik**, v. 92, 2012.

BÄPPLER, K. New developments in TBM tunnelling for changing grounds. **Tunnelling and Underground Space Technology**, v. 57, p. 18–26, 2016.

BEŇO, J.; HILAR, M. Steel fibre reinforced concrete for tunnel lining - Verification by extensive laboratory testing and numerical Modelling. **Acta Polytechnica**, v. 53, n. 4, p. 329–337, 2013.

BENTUR, A.; MINDESS, S. **Fibre Reinforced Cementitious Composites**. 2nd. ed. [s.l.] Modern Concrete Technology Series, 2007.

BITENCOURT JÚNIOR, L. A. G. **Modelagem do processo de falha em materiais cimentícios reforçados com fibras de aço.** São Paulo: Universidade de São Paulo, 2015.

BOYE, B. A.; ABBEY, S. J.; NGAMBI, S.; FONTE, J. Development of improved models for estimation of bursting stresses in elements under high-concentrated load. **Latin American Journal of Solids and Structures**, v. 16, n. 1, p. 1–15, 2019.

BREITENBÜCHER, R.; MESCHKE, G.; SONG, F.; HOFMAN, M.; ZHAN, Y. Experimental and numerical study on the load-bearing behaviour of steel fibre reinforced concrete for precast tunnel lining segments under concentrated loads. **FRC 2014 Joint ACI-fib International Workshop. Fibre Reinforced Concrete Applications.**, n. December, p. 417–429, 2014.

BURGERS, R. Non-linear FEM modelling of steel fibre reinforced concrete. **Delft University**, n. September, p. 133, 2006.

CARATELLI, A.; MEDA, A.; RINALDI, Z. Design according to MC2010 of a fibre-

reinforced concrete tunnel in Monte Lirio, Panama. **Structural Concrete**, v. 13, n. 3, p. 166–173, 2012.

CARATELLI, A.; MEDA, A.; RINALDI, Z.; ROMUALDI, P. Structural behaviour of precast tunnel segments in fiber reinforced concrete. **Tunnelling and Underground Space Technology**, v. 26, n. 2, p. 284–291, 2011.

CAVALARO, S. H. P.; BLOM, C. B. M.; WALRAVEN, J. C.; AGUADO, A. Structural analysis of contact deficiencies in segmented lining. **Tunnelling and Underground Space Technology**, v. 26, n. 6, p. 734–749, 2011.

CAVALARO, S. H. P.; BLOM, C. B. M.; WALRAVEN, J. C.; AGUADO, A. Formation and accumulation of contact deficiencies in a tunnel segmented lining. **Applied Mathematical Modelling**, v. 36, n. 9, p. 4422–4438, 2012.

CEB-FIP, F. **Bulletin 83 - Precast tunnel segments in fibre-reinforced concrete: State-of-the-art report**. [s.l: s.n.].

CERVERA, M.; OLIVER, J.; MANZOLI, O. A rate-dependent isotropic damage model for the seismic analysis of concrete dams. **Earthquake Engineering and Structural Dynamics**, v. 25, n. 9, p. 987–1010, 1996.

CONFORTI, A.; TIBERTI, G.; PLIZZARI, G. A. Combined effect of high concentrated loads exerted by TBM hydraulic jacks. **Magazine of Concrete Research**, v. 68, n. 21, p. 1122–1132, 2016a.

CONFORTI, A.; TIBERTI, G.; PLIZZARI, G. A.. Splitting and crushing failure in FRC elements subjected to a high concentrated load. **Composites Part B: Engineering**, v. 105, p. 82–92, 2016b.

CONFORTI, A.; TIBERTI, G.; PLIZZARI, G. A.; CARATELLI, A.; MEDA, A. Precast tunnel segments reinforced by macro-synthetic fibers. **Tunnelling and Underground Space Technology**, v. 63, p. 1–11, 2017.

FIB. **fib Model Code for Concrete Structures 2010**. Weinheim, Germany: Wiley-VCH Verlag GmbH & Co. KGaA, 2013.

GARCÍA, M. **Estudio experimental de bloques de hormigón para el análisis de macizos**

de hormigón. Barcelona: Universitat Politècnica de Catalunya, 2012.

GETTU, R.; BARRAGÁN, B.; GARCÍA, T.; FERNÁNDEZ, C.; OLIVER, R. Steel fiber reinforced concrete for the Barcelona metro line 9 tunnel lining. **6th International RILEM Symposium on Fibre Reinforced Concretes**, n. September, p. 141–156, 2004.

GROENEWEG, T. W. Shield driven tunnels in ultra high strength concrete. 2007.

GUYON, Y. **Prestressed Concrete**. London: [s.n.].

HE, Z.-Q.; LIU, Z. Investigation of Bursting Forces in Anchorage Zones: Compression-Dispersion Models and Unified Design Equation. **Journal of Bridge Engineering**, v. 16, n. 6, p. 820–827, 2010.

HILAR, M.; VÍTEK, J.; VÍTEK, P.; PUKL, R. Load testing and numerical modelling of SFRC segments. p. 1–10, 2012.

IYENGAR, K. S. R. Two-dimensional theories of anchorage zone stresses in post-tensioned prestressed beams. **Journal Proceedings**, v. 59, n. 10, p. 1443–1446, 1962.

LANCE, G. A. The risk to third parties from bored tunnelling in soft ground. **Health and Safety Executive 2006**, 2006.

LEONHARDT, F.; MONNIG, E. Lectures about reinforced concrete. **Springer**, 1973.

LIAO, L.; LA FUENTE, A. DE; CAVALARO, S.; AGUADO, A.; CARBONARI, G. Experimental and analytical study of concrete blocks subjected to concentrated loads with an application to TBM-constructed tunnels. **Tunnelling and Underground Space Technology**, v. 49, p. 295–306, 2015.

MEDA, A.; RINALDI, Z.; CARATELLI, A.; CIGNITTI, F. Experimental investigation on precast tunnel segments under TBM thrust action. **Engineering Structures**, v. 119, p. 174–185, 2016.

MORSCH, E. Uber die Berchnung der Gelenkquader. **Beton u**, 1924.

MUDADU, A.; TIBERTI, G.; CONFORTI, A.; TRABUCCHI, I.; PLIZZARI, G. A. An experimental study on the post-cracking behavior of Polypropylene Fiber Reinforced Concrete core samples drilled from precast tunnel segments. **Tunnels and Underground**

Cities: Engineering and Innovation meet Archaeology, Architecture and Art, v. 2010, n. 2013, p. 2734–2743, 2019.

NEHDI, M. L.; ABBAS, S.; SOLIMAN, A. M. Exploratory study of ultra-high performance fiber reinforced concrete tunnel lining segments with varying steel fiber lengths and dosages. **Engineering Structures**, v. 101, p. 733–742, 2015.

NEU, G. E.; EDLER, P.; FREITAG, S.; GUDŽULIĆ, V.; MESCHKE, G. Reliability based optimization of steel-fibre segmental tunnel linings subjected to thrust jack loadings. **Engineering Structures**, v. 254, n. January, p. 113752, 2022.

NOGALES, A.; LA FUENTE, A. DE. **Crack width design approach for fibre reinforced concrete tunnel segments for TBM thrust loadsTunnelling and Underground Space Technology**, 2020.

OLIVER, J.; HUESPE, A. E.; CANTE, J. C. An implicit/explicit integration scheme to increase computability of non-linear material and contact/friction problems. **Computer Methods in Applied Mechanics and Engineering**, v. 197, n. 21–24, p. 1865–1889, 2008.

POH, J.; TAN, K. H.; PETERSON, G. L.; WEN, D. Structural testing of steel fibre reinforced concrete (SFRC) tunnel lining segments in Singapore. **Proceedings of the World Tunnel Congress 2009**, p. 1–17, 2009.

RODRIGUES, E. A. Um modelo multiescala concorrente para representar o processo de fissuração do concreto. p. 192, 2015.

SORELLI, L. G.; TOUTLEMONDE, F. On the Design of Steel Fibre Reinforced Concrete Tunnel Lining Segments. **11th International Conference on Fracture**, n. January 2014, 2005.

SCHNUTGEN, B.; ERDEM, E. Sub-task 4.4 – Splitting of SFRC induced by local forces. Annex A, 2001.

SPAGNUOLO, S. Influence of non-uniform support on FRC and hybrid precast tunnel segments with glass fiber reinforced polymer bars under TBM thrust Influence of non-uniform support on FRC and hybrid precast tunnel segments with glass fiber reinforced polymer bars under . n. October 2019, 2020.

SUGIMOTO, M. Causes of Shield Segment Damages During Construction. **International Symposium on Underground Excavation and Tunnelling**, n. February, p. 67–74, 2006.

TEJCHMAN, J.; BOBIŃSKI, J. **Continuous and Discontinuous Modelling of Fracture in Concrete Using FEM**. Berlin, Heidelberg: Springer Berlin Heidelberg, 2013.

TIBERTI, G.; CONFORTI, A.; PLIZZARI, G. A. Precast segments under TBM hydraulic jacks: Experimental investigation on the local splitting behavior. **Tunnelling and Underground Space Technology**, v. 50, p. 438–450, 2015.

TRABUCCHI, I.; TIBERTI, G.; CONFORTI, A.; MEDEGHINI, F.; PLIZZARI, G. A. Experimental study on Steel Fiber Reinforced Concrete and Reinforced Concrete elements under concentrated loads. **Construction and Building Materials**, v. 307, n. August, p. 124834, 2021.

TRINDADE, Y. T. **Numerical modeling of the post-cracking behavior of SFRC and its application on design of beams according to fib Model Code 2010**. [s.l: s.n.].

UNE-EN 12390-6. Testing hardened concrete - Part 6: Tensile splitting strength of test specimens. Brazilian Test. **Spanish Association for Standardization and Certification, AENOR**, 2010.

WAAL, R. G. A. DE. **Steel fibre reinforced tunnel segments - for the application in shield driven tunnel linings**. [s.l.] Delft, 2000.

APPENDIX A.1

Table 12 – Parametric analysis on f_{ct} results for the analytical models evaluated

Configuration	Model	Model and f_{ct} input	F_{cr} (kN)	F_{obs} (kN)	Relative Error (%)
Liao *et al*. (2015)-b200-PC40	Liao	Liao	284,8	406,5	-29,9%
Liao *et al*. (2015)-b200-PC40	Liao	Liao_ft1	379,1	406,5	-6,7%
Liao *et al*. (2015)-b200-PC40	Liao	Liao_ft2	379,1	406,5	-6,7%
Liao *et al*. (2015)-b200-PC40	Boye	Boye	877,1	406,5	115,8%
Liao *et al*. (2015)-b200-PC40	Boye	Boye_ft1	1167,6	406,5	187,2%
Liao *et al*. (2015)-b200-PC40	Boye	Boye_ft2	1167,6	406,5	187,2%
Liao *et al*. (2015)-b200-PC40	Conforti	Conforti	887,1	406,5	118,2%
Liao *et al*. (2015)-b200-PC40	Conforti	Conforti_ft1	1180,9	406,5	190,5%
Liao *et al*. (2015)-b200-PC40	Conforti	Conforti_ft2	1180,9	406,5	190,5%
Liao *et al*. (2015)-b200-PC40	Guyon	Guyon	566,2	406,5	39,3%
Liao *et al*. (2015)-b200-PC40	Guyon	Guyon_ft1	753,8	406,5	85,4%
Liao *et al*. (2015)-b200-PC40	Guyon	Guyon_ft2	753,8	406,5	85,4%
Liao *et al*. (2015)-b200-PC40	HeLiu	HeLiu	780,6	406,5	92,0%
Liao *et al*. (2015)-b200-PC40	HeLiu	HeLiu_ft1	1039,2	406,5	155,6%
Liao *et al*. (2015)-b200-PC40	HeLiu	HeLiu_ft2	1039,2	406,5	155,6%
Liao *et al*. (2015)-b200-PC50	Liao	Liao	333,8	417,0	-20,0%
Liao *et al*. (2015)-b200-PC50	Liao	Liao_ft1	385,2	417,0	-7,6%
Liao *et al*. (2015)-b200-PC50	Liao	Liao_ft2	358,1	417,0	-14,1%
Liao *et al*. (2015)-b200-PC50	Boye	Boye	1028,0	417,0	146,5%
Liao *et al*. (2015)-b200-PC50	Boye	Boye_ft1	1186,5	417,0	184,5%
Liao *et al*. (2015)-b200-PC50	Boye	Boye_ft2	1102,9	417,0	164,5%
Liao *et al*. (2015)-b200-PC50	Conforti	Conforti	1039,7	417,0	149,3%
Liao *et al*. (2015)-b200-PC50	Conforti	Conforti_ft1	1200,0	417,0	187,8%
Liao *et al*. (2015)-b200-PC50	Conforti	Conforti_ft2	1115,5	417,0	167,5%
Liao *et al*. (2015)-b200-PC50	Guyon	Guyon	663,6	417,0	59,1%
Liao *et al*. (2015)-b200-PC50	Guyon	Guyon_ft1	766,0	417,0	83,7%
Liao *et al*. (2015)-b200-PC50	Guyon	Guyon_ft2	712,0	417,0	70,7%
Liao *et al*. (2015)-b200-PC50	HeLiu	HeLiu	915,0	417,0	119,4%
Liao *et al*. (2015)-b200-PC50	HeLiu	HeLiu_ft1	1056,0	417,0	153,2%
Liao *et al*. (2015)-b200-PC50	HeLiu	HeLiu_ft2	981,6	417,0	135,4%
Liao *et al*. (2015)-b200-SFRC40	Liao	Liao	254,5	405,5	-37,2%
Liao *et al*. (2015)-b200-SFRC40	Liao	Liao_ft1	404,0	405,5	-0,4%
Liao *et al*. (2015)-b200-SFRC40	Liao	Liao_ft2	340,1	405,5	-16,1%
Liao *et al*. (2015)-b200-SFRC40	Boye	Boye	273,3	405,5	-32,6%
Liao *et al*. (2015)-b200-SFRC40	Boye	Boye_ft1	433,9	405,5	7,0%
Liao *et al*. (2015)-b200-SFRC40	Boye	Boye_ft2	365,2	405,5	-9,9%
Liao *et al*. (2015)-b200-SFRC40	Conforti	Conforti	271,4	405,5	-33,1%

Liao *et al*. (2015)-b200-SFRC40	Conforti	Conforti_ft1	430,9	405,5	6,3%
Liao *et al*. (2015)-b200-SFRC40	Conforti	Conforti_ft2	362,7	405,5	-10,5%
Liao *et al*. (2015)-b200-SFRC40	Guyon	Guyon	57,8	405,5	-85,8%
Liao *et al*. (2015)-b200-SFRC40	Guyon	Guyon_ft1	91,7	405,5	-77,4%
Liao *et al*. (2015)-b200-SFRC40	Guyon	Guyon_ft2	77,2	405,5	-81,0%
Liao *et al*. (2015)-b200-SFRC40	HeLiu	HeLiu	238,9	405,5	-41,1%
Liao *et al*. (2015)-b200-SFRC40	HeLiu	HeLiu_ft1	379,2	405,5	-6,5%
Liao *et al*. (2015)-b200-SFRC40	HeLiu	HeLiu_ft2	319,2	405,5	-21,3%
Liao *et al*. (2015)-b200-SFRC50	Liao	Liao	326,4	429,0	-23,9%
Liao *et al*. (2015)-b200-SFRC50	Liao	Liao_ft1	393,1	429,0	-8,4%
Liao *et al*. (2015)-b200-SFRC50	Liao	Liao_ft2	378,2	429,0	-11,8%
Liao *et al*. (2015)-b200-SFRC50	Boye	Boye	1005,2	429,0	134,3%
Liao *et al*. (2015)-b200-SFRC50	Boye	Boye_ft1	1210,8	429,0	182,2%
Liao *et al*. (2015)-b200-SFRC50	Boye	Boye_ft2	1164,9	429,0	171,5%
Liao *et al*. (2015)-b200-SFRC50	Conforti	Conforti	1016,6	429,0	137,0%
Liao *et al*. (2015)-b200-SFRC50	Conforti	Conforti_ft1	1224,5	429,0	185,4%
Liao *et al*. (2015)-b200-SFRC50	Conforti	Conforti_ft2	1178,2	429,0	174,6%
Liao *et al*. (2015)-b200-SFRC50	Guyon	Guyon	648,9	429,0	51,3%
Liao *et al*. (2015)-b200-SFRC50	Guyon	Guyon_ft1	781,6	429,0	82,2%
Liao *et al*. (2015)-b200-SFRC50	Guyon	Guyon_ft2	752,0	429,0	75,3%
Liao *et al*. (2015)-b200-SFRC50	HeLiu	HeLiu	894,6	429,0	108,5%
Liao *et al*. (2015)-b200-SFRC50	HeLiu	HeLiu_ft1	1077,6	429,0	151,2%
Liao *et al*. (2015)-b200-SFRC50	HeLiu	HeLiu_ft2	1036,8	429,0	141,7%
Liao *et al*. (2015)-b250-PC40	Liao	Liao	319,0	409,5	-22,1%
Liao *et al*. (2015)-b250-PC40	Liao	Liao_ft1	424,6	409,5	3,7%
Liao *et al*. (2015)-b250-PC40	Liao	Liao_ft2	424,6	409,5	3,7%
Liao *et al*. (2015)-b250-PC40	Boye	Boye	692,2	409,5	69,0%
Liao *et al*. (2015)-b250-PC40	Boye	Boye_ft1	921,5	409,5	125,0%
Liao *et al*. (2015)-b250-PC40	Boye	Boye_ft2	921,5	409,5	125,0%
Liao *et al*. (2015)-b250-PC40	Conforti	Conforti	693,0	409,5	69,2%

Liao *et al*. (2015)-b250-PC40	Conforti	Conforti_ft1	922,6	409,5	125,3%
Liao *et al*. (2015)-b250-PC40	Conforti	Conforti_ft2	922,6	409,5	125,3%
Liao *et al*. (2015)-b250-PC40	Guyon	Guyon	353,9	409,5	-13,6%
Liao *et al*. (2015)-b250-PC40	Guyon	Guyon_ft1	471,1	409,5	15,0%
Liao *et al*. (2015)-b250-PC40	Guyon	Guyon_ft2	471,1	409,5	15,0%
Liao *et al*. (2015)-b250-PC40	HeLiu	HeLiu	609,9	409,5	48,9%
Liao *et al*. (2015)-b250-PC40	HeLiu	HeLiu_ft1	811,9	409,5	98,3%
Liao *et al*. (2015)-b250-PC40	HeLiu	HeLiu_ft2	811,9	409,5	98,3%
Liao *et al*. (2015)-b250-PC50	Liao	Liao	373,9	434,0	-13,9%
Liao *et al*. (2015)-b250-PC50	Liao	Liao_ft1	431,5	434,0	-0,6%
Liao *et al*. (2015)-b250-PC50	Liao	Liao_ft2	401,1	434,0	-7,6%
Liao *et al*. (2015)-b250-PC50	Boye	Boye	811,4	434,0	86,9%
Liao *et al*. (2015)-b250-PC50	Boye	Boye_ft1	936,4	434,0	115,8%
Liao *et al*. (2015)-b250-PC50	Boye	Boye_ft2	870,5	434,0	100,6%
Liao *et al*. (2015)-b250-PC50	Conforti	Conforti	812,3	434,0	87,2%
Liao *et al*. (2015)-b250-PC50	Conforti	Conforti_ft1	937,5	434,0	116,0%
Liao *et al*. (2015)-b250-PC50	Conforti	Conforti_ft2	871,4	434,0	100,8%
Liao *et al*. (2015)-b250-PC50	Guyon	Guyon	414,8	434,0	-4,4%
Liao *et al*. (2015)-b250-PC50	Guyon	Guyon_ft1	478,7	434,0	10,3%
Liao *et al*. (2015)-b250-PC50	Guyon	Guyon_ft2	445,0	434,0	2,5%
Liao *et al*. (2015)-b250-PC50	HeLiu	HeLiu	714,8	434,0	64,7%
Liao *et al*. (2015)-b250-PC50	HeLiu	HeLiu_ft1	825,0	434,0	90,1%
Liao *et al*. (2015)-b250-PC50	HeLiu	HeLiu_ft2	766,9	434,0	76,7%
Liao *et al*. (2015)-b250-SFRC40	Liao	Liao	330,8	374,0	-11,6%
Liao *et al*. (2015)-b250-SFRC40	Liao	Liao_ft1	525,1	374,0	40,4%
Liao *et al*. (2015)-b250-SFRC40	Liao	Liao_ft2	442,0	374,0	18,2%
Liao *et al*. (2015)-b250-SFRC40	Boye	Boye	320,5	374,0	-14,3%
Liao *et al*. (2015)-b250-SFRC40	Boye	Boye_ft1	508,7	374,0	36,0%
Liao *et al*. (2015)-b250-SFRC40	Boye	Boye_ft2	428,2	374,0	14,5%
Liao *et al*. (2015)-b250-SFRC40	Conforti	Conforti	318,1	374,0	-14,9%
Liao *et al*. (2015)-b250-SFRC40	Conforti	Conforti_ft1	505,0	374,0	35,0%
Liao *et al*. (2015)-b250-SFRC40	Conforti	Conforti_ft2	425,1	374,0	13,7%
Liao *et al*. (2015)-b250-SFRC40	Guyon	Guyon	54,1	374,0	-85,5%
Liao *et al*. (2015)-b250-SFRC40	Guyon	Guyon_ft1	86,0	374,0	-77,0%
Liao *et al*. (2015)-b250-SFRC40	Guyon	Guyon_ft2	72,4	374,0	-80,7%
Liao *et al*. (2015)-b250-SFRC40	HeLiu	HeLiu	279,9	374,0	-25,2%
Liao *et al*. (2015)-b250-SFRC40	HeLiu	HeLiu_ft1	444,4	374,0	18,8%

Liao *et al*. (2015)-b250-SFRC40	HeLiu	HeLiu_ft2	374,1	374,0	0,0%
Liao *et al*. (2015)-b250-SFRC50	Liao	Liao	365,6	526,5	-30,6%
Liao *et al*. (2015)-b250-SFRC50	Liao	Liao_ft1	440,3	526,5	-16,4%
Liao *et al*. (2015)-b250-SFRC50	Liao	Liao_ft2	423,6	526,5	-19,5%
Liao *et al*. (2015)-b250-SFRC50	Boye	Boye	793,3	526,5	50,7%
Liao *et al*. (2015)-b250-SFRC50	Boye	Boye_ft1	955,6	526,5	81,5%
Liao *et al*. (2015)-b250-SFRC50	Boye	Boye_ft2	919,4	526,5	74,6%
Liao *et al*. (2015)-b250-SFRC50	Conforti	Conforti	794,2	526,5	50,9%
Liao *et al*. (2015)-b250-SFRC50	Conforti	Conforti_ft1	956,7	526,5	81,7%
Liao *et al*. (2015)-b250-SFRC50	Conforti	Conforti_ft2	920,5	526,5	74,8%
Liao *et al*. (2015)-b250-SFRC50	Guyon	Guyon	405,6	526,5	-23,0%
Liao *et al*. (2015)-b250-SFRC50	Guyon	Guyon_ft1	488,5	526,5	-7,2%
Liao *et al*. (2015)-b250-SFRC50	Guyon	Guyon_ft2	470,0	526,5	-10,7%
Liao *et al*. (2015)-b250-SFRC50	HeLiu	HeLiu	698,9	526,5	32,8%
Liao *et al*. (2015)-b250-SFRC50	HeLiu	HeLiu_ft1	841,9	526,5	59,9%
Liao *et al*. (2015)-b250-SFRC50	HeLiu	HeLiu_ft2	810,0	526,5	53,8%
Liao *et al*. (2015)-b400-PC40	Liao	Liao	545,0	632,5	-13,8%
Liao *et al*. (2015)-b400-PC40	Liao	Liao_ft1	725,5	632,5	14,7%
Liao *et al*. (2015)-b400-PC40	Liao	Liao_ft2	725,5	632,5	14,7%
Liao *et al*. (2015)-b400-PC40	Boye	Boye	713,2	632,5	12,8%
Liao *et al*. (2015)-b400-PC40	Boye	Boye_ft1	949,5	632,5	50,1%
Liao *et al*. (2015)-b400-PC40	Boye	Boye_ft2	949,5	632,5	50,1%
Liao *et al*. (2015)-b400-PC40	Conforti	Conforti	709,7	632,5	12,2%
Liao *et al*. (2015)-b400-PC40	Conforti	Conforti_ft1	944,7	632,5	49,4%
Liao *et al*. (2015)-b400-PC40	Conforti	Conforti_ft2	944,7	632,5	49,4%
Liao *et al*. (2015)-b400-PC40	Guyon	Guyon	226,5	632,5	-64,2%
Liao *et al*. (2015)-b400-PC40	Guyon	Guyon_ft1	301,5	632,5	-52,3%
Liao *et al*. (2015)-b400-PC40	Guyon	Guyon_ft2	301,5	632,5	-52,3%
Liao *et al*. (2015)-b400-PC40	HeLiu	HeLiu	624,5	632,5	-1,3%
Liao *et al*. (2015)-b400-PC40	HeLiu	HeLiu_ft1	831,4	632,5	31,4%
Liao *et al*. (2015)-b400-PC40	HeLiu	HeLiu_ft2	831,4	632,5	31,4%
Liao *et al*. (2015)-b400-SFRC40	Liao	Liao	500,3	630,5	-20,7%
Liao *et al*. (2015)-b400-SFRC40	Liao	Liao_ft1	794,2	630,5	26,0%

Liao *et al*. (2015)-b400-SFRC40	Liao	Liao_ft2	668,5	630,5	6,0%
Liao *et al*. (2015)-b400-SFRC40	Boye	Boye	654,7	630,5	3,8%
Liao *et al*. (2015)-b400-SFRC40	Boye	Boye_ft1	1039,4	630,5	64,8%
Liao *et al*. (2015)-b400-SFRC40	Boye	Boye_ft2	874,9	630,5	38,8%
Liao *et al*. (2015)-b400-SFRC40	Conforti	Conforti	651,5	630,5	3,3%
Liao *et al*. (2015)-b400-SFRC40	Conforti	Conforti_ft1	1034,2	630,5	64,0%
Liao *et al*. (2015)-b400-SFRC40	Conforti	Conforti_ft2	870,5	630,5	38,1%
Liao *et al*. (2015)-b400-SFRC40	Guyon	Guyon	207,9	630,5	-67,0%
Liao *et al*. (2015)-b400-SFRC40	Guyon	Guyon_ft1	330,1	630,5	-47,7%
Liao *et al*. (2015)-b400-SFRC40	Guyon	Guyon_ft2	277,8	630,5	-55,9%
Liao *et al*. (2015)-b400-SFRC40	HeLiu	HeLiu	573,3	630,5	-9,1%
Liao *et al*. (2015)-b400-SFRC40	HeLiu	HeLiu_ft1	910,1	630,5	44,3%
Liao *et al*. (2015)-b400-SFRC40	HeLiu	HeLiu_ft2	766,1	630,5	21,5%
Liao *et al*. (2015)-b400-SFRC50	Liao	Liao	624,5	641,0	-2,6%
Liao *et al*. (2015)-b400-SFRC50	Liao	Liao_ft1	752,3	641,0	17,4%
Liao *et al*. (2015)-b400-SFRC50	Liao	Liao_ft2	723,8	641,0	12,9%
Liao *et al*. (2015)-b400-SFRC50	Boye	Boye	817,4	641,0	27,5%
Liao *et al*. (2015)-b400-SFRC50	Boye	Boye_ft1	984,6	641,0	53,6%
Liao *et al*. (2015)-b400-SFRC50	Boye	Boye_ft2	947,3	641,0	47,8%
Liao *et al*. (2015)-b400-SFRC50	Conforti	Conforti	813,3	641,0	26,9%
Liao *et al*. (2015)-b400-SFRC50	Conforti	Conforti_ft1	979,6	641,0	52,8%
Liao *et al*. (2015)-b400-SFRC50	Conforti	Conforti_ft2	942,5	641,0	47,0%
Liao *et al*. (2015)-b400-SFRC50	Guyon	Guyon	259,6	641,0	-59,5%
Liao *et al*. (2015)-b400-SFRC50	Guyon	Guyon_ft1	312,6	641,0	-51,2%
Liao *et al*. (2015)-b400-SFRC50	Guyon	Guyon_ft2	300,8	641,0	-53,1%
Liao *et al*. (2015)-b400-SFRC50	HeLiu	HeLiu	715,7	641,0	11,7%
Liao *et al*. (2015)-b400-SFRC50	HeLiu	HeLiu_ft1	862,1	641,0	34,5%

Liao *et al*. (2015)-b400-SFRC50	HeLiu	HeLiu_ft2	829,4	641,0	29,4%
Liao *et al*. (2015)-b750-PC40	Liao	Liao	563,1	744,0	-24,3%
Liao *et al*. (2015)-b750-PC40	Liao	Liao_ft1	749,6	744,0	0,7%
Liao *et al*. (2015)-b750-PC40	Liao	Liao_ft2	749,6	744,0	0,7%
Liao *et al*. (2015)-b750-PC40	Boye	Boye	1047,3	744,0	40,8%
Liao *et al*. (2015)-b750-PC40	Boye	Boye_ft1	1394,2	744,0	87,4%
Liao *et al*. (2015)-b750-PC40	Boye	Boye_ft2	1394,2	744,0	87,4%
Liao *et al*. (2015)-b750-PC40	Conforti	Conforti	1039,5	744,0	39,7%
Liao *et al*. (2015)-b750-PC40	Conforti	Conforti_ft1	1383,9	744,0	86,0%
Liao *et al*. (2015)-b750-PC40	Conforti	Conforti_ft2	1383,9	744,0	86,0%
Liao *et al*. (2015)-b750-PC40	Guyon	Guyon	176,9	744,0	-76,2%
Liao *et al*. (2015)-b750-PC40	Guyon	Guyon_ft1	235,6	744,0	-68,3%
Liao *et al*. (2015)-b750-PC40	Guyon	Guyon_ft2	235,6	744,0	-68,3%
Liao *et al*. (2015)-b750-PC40	HeLiu	HeLiu	914,8	744,0	23,0%
Liao *et al*. (2015)-b750-PC40	HeLiu	HeLiu_ft1	1217,8	744,0	63,7%
Liao *et al*. (2015)-b750-PC40	HeLiu	HeLiu_ft2	1217,8	744,0	63,7%
Liao *et al*. (2015)-b750-SFRC40	Liao	Liao	516,9	659,5	-21,6%
Liao *et al*. (2015)-b750-SFRC40	Liao	Liao_ft1	820,5	659,5	24,4%
Liao *et al*. (2015)-b750-SFRC40	Liao	Liao_ft2	690,7	659,5	4,7%
Liao *et al*. (2015)-b750-SFRC40	Boye	Boye	961,4	659,5	45,8%
Liao *et al*. (2015)-b750-SFRC40	Boye	Boye_ft1	1526,2	659,5	131,4%
Liao *et al*. (2015)-b750-SFRC40	Boye	Boye_ft2	1284,7	659,5	94,8%
Liao *et al*. (2015)-b750-SFRC40	Conforti	Conforti	954,3	659,5	44,7%
Liao *et al*. (2015)-b750-SFRC40	Conforti	Conforti_ft1	1514,9	659,5	129,7%
Liao *et al*. (2015)-b750-SFRC40	Conforti	Conforti_ft2	1275,2	659,5	93,4%
Liao *et al*. (2015)-b750-SFRC40	Guyon	Guyon	162,4	659,5	-75,4%
Liao *et al*. (2015)-b750-SFRC40	Guyon	Guyon_ft1	257,9	659,5	-60,9%
Liao *et al*. (2015)-b750-SFRC40	Guyon	Guyon_ft2	217,1	659,5	-67,1%
Liao *et al*. (2015)-b750-SFRC40	HeLiu	HeLiu	839,8	659,5	27,3%
Liao *et al*. (2015)-b750-SFRC40	HeLiu	HeLiu_ft1	1333,1	659,5	102,1%
Liao *et al*. (2015)-b750-SFRC40	HeLiu	HeLiu_ft2	1122,2	659,5	70,2%
Liao *et al*. (2015)-b750-SFRC50	Liao	Liao	645,3	715,0	-9,7%
Liao *et al*. (2015)-b750-SFRC50	Liao	Liao_ft1	777,3	715,0	8,7%

Liao *et al*. (2015)-b750-SFRC50	Liao	Liao_ft2	747,8	715,0	4,6%
Liao *et al*. (2015)-b750-SFRC50	Boye	Boye	1200,2	715,0	67,9%
Liao *et al*. (2015)-b750-SFRC50	Boye	Boye_ft1	1445,7	715,0	102,2%
Liao *et al*. (2015)-b750-SFRC50	Boye	Boye_ft2	1391,0	715,0	94,5%
Liao *et al*. (2015)-b750-SFRC50	Conforti	Conforti	1191,4	715,0	66,6%
Liao *et al*. (2015)-b750-SFRC50	Conforti	Conforti_ft1	1435,0	715,0	100,7%
Liao *et al*. (2015)-b750-SFRC50	Conforti	Conforti_ft2	1380,7	715,0	93,1%
Liao *et al*. (2015)-b750-SFRC50	Guyon	Guyon	202,8	715,0	-71,6%
Liao *et al*. (2015)-b750-SFRC50	Guyon	Guyon_ft1	244,3	715,0	-65,8%
Liao *et al*. (2015)-b750-SFRC50	Guyon	Guyon_ft2	235,0	715,0	-67,1%
Liao *et al*. (2015)-b750-SFRC50	HeLiu	HeLiu	1048,4	715,0	46,6%
Liao *et al*. (2015)-b750-SFRC50	HeLiu	HeLiu_ft1	1262,8	715,0	76,6%
Liao *et al*. (2015)-b750-SFRC50	HeLiu	HeLiu_ft2	1215,0	715,0	69,9%

Table 13 - F_{cr} analysis for the analytical models evaluated

Configuration	Specimen	n_{jacks}	f_{ct} (MPa)	Model	F_{cr} (kN)	F_{obs} (kN)	Relative Error (%)
Caratelli *et al*. (2012)	Segment	2	3,2	Liao	3822,45	2687,5	42,2%
Caratelli *et al*. (2012)	Segment	2	3,2	Boye	7417,58	2687,5	176,0%
Caratelli *et al*. (2012)	Segment	2	3,2	Conforti	7016,82	2687,5	161,1%
Caratelli *et al*. (2012)	Segment	2	3,2	Guyon	3115,70	2687,5	15,9%
Caratelli *et al*. (2012)	Segment	2	3,2	HeLiu	6174,80	2687,5	129,8%
Conforti *et al*. (2019)	Segment	2	3,2	Liao	2771,18	2388,75	16,0%
Conforti *et al*. (2019)	Segment	2	3,2	Boye	6817,03	2388,75	185,4%
Conforti *et al*. (2019)	Segment	2	3,2	Conforti	6430,74	2388,75	169,2%
Conforti *et al*. (2019)	Segment	2	3,2	Guyon	2660,37	2388,75	11,4%
Conforti *et al*. (2019)	Segment	2	3,2	HeLiu	5659,05	2388,75	136,9%
Conforti *et al*. (a) (2016)	Block	1	3,0	Liao	489,65	790	-38,0%
Conforti *et al*. (a) (2016)	Block	1	3,0	Boye	705,59	790	-10,7%
Conforti *et al*. (a) (2016)	Block	1	3,0	Conforti	702,38	790	-11,1%
Conforti *et al*. (a) (2016)	Block	1	3,0	Guyon	239,11	790	-69,7%
Conforti *et al*. (a) (2016)	Block	1	3,0	HeLiu	618,09	790	-21,8%
Conforti *et al*. (b) (2016)-PC-b1_100	Block	2	4,0	Liao	892,39	1465	-39,1%
Conforti *et al*. (b) (2016)-PC-b1_100	Block	2	4,0	Boye	922,18	1465	-37,1%

Conforti *et al*. (b) (2016)-PC-b1_100	Block	2	4,0	Conforti	858,26	1465	-41,4%
Conforti *et al*. (b) (2016)-PC-b1_100	Block	2	4,0	Guyon	146,09	1465	-90,0%
Conforti *et al*. (b) (2016)-PC-b1_100	Block	2	4,0	HeLiu	755,26	1465	-48,4%
Conforti *et al*. (b) (2016)-PC-b1_150	Block	2	4,0	Liao	832,41	1700	-51,0%
Conforti *et al*. (b) (2016)-PC-b1_150	Block	2	4,0	Boye	1050,26	1700	-38,2%
Conforti *et al*. (b) (2016)-PC-b1_150	Block	2	4,0	Conforti	980,86	1700	-42,3%
Conforti *et al*. (b) (2016)-PC-b1_150	Block	2	4,0	Guyon	250,43	1700	-85,3%
Conforti *et al*. (b) (2016)-PC-b1_150	Block	2	4,0	HeLiu	863,16	1700	-49,2%
Conforti *et al*. (b) (2016)-PFRC_b1_100	Block	2	3,5	Liao	783,82	1470	-46,7%
Conforti *et al*. (b) (2016)-PFRC_b1_100	Block	2	3,5	Boye	809,98	1470	-44,9%
Conforti *et al*. (b) (2016)-PFRC_b1_100	Block	2	3,5	Conforti	753,84	1470	-48,7%
Conforti *et al*. (b) (2016)-PFRC_b1_100	Block	2	3,5	Guyon	128,31	1470	-91,3%
Conforti *et al*. (b) (2016)-PFRC_b1_100	Block	2	3,5	HeLiu	663,38	1470	-54,9%
Conforti *et al*. (b) (2016)-PFRC-b1_150	Block	2	3,5	Liao	731,13	1597,7	-54,2%
Conforti *et al*. (b) (2016)-PFRC-b1_150	Block	2	3,5	Boye	922,48	1597,7	-42,3%
Conforti *et al*. (b) (2016)-PFRC-b1_150	Block	2	3,5	Conforti	861,53	1597,7	-46,1%
Conforti *et al*. (b) (2016)-PFRC-b1_150	Block	2	3,5	Guyon	219,96	1597,7	-86,2%
Conforti *et al*. (b) (2016)-PFRC-b1_150	Block	2	3,5	HeLiu	758,14	1597,7	-52,5%
Liao *et al*. (2015)-b200-PC40	Block	1	3,3	Liao	284,79	406,5	-29,9%
Liao *et al*. (2015)-b200-PC40	Block	1	3,3	Boye	877,11	406,5	115,8%
Liao *et al*. (2015)-b200-PC40	Block	1	3,3	Conforti	887,08	406,5	118,2%
Liao *et al*. (2015)-b200-PC40	Block	1	3,3	Guyon	566,22	406,5	39,3%
Liao *et al*. (2015)-b200-PC40	Block	1	3,3	HeLiu	780,63	406,5	92,0%

Liao *et al*. (2015)-b200-PC50	Block	1	3,8	Liao	333,79	417	-20,0%
Liao *et al*. (2015)-b200-PC50	Block	1	3,8	Boye	1028,04	417	146,5%
Liao *et al*. (2015)-b200-PC50	Block	1	3,8	Conforti	1039,72	417	149,3%
Liao *et al*. (2015)-b200-PC50	Block	1	3,8	Guyon	663,65	417	59,1%
Liao *et al*. (2015)-b200-PC50	Block	1	3,8	HeLiu	914,95	417	119,4%
Liao *et al*. (2015)-b200-SFRC40	Block	1	3,0	Liao	254,51	405,5	-37,2%
Liao *et al*. (2015)-b200-SFRC40	Block	1	3,0	Boye	273,31	405,5	-32,6%
Liao *et al*. (2015)-b200-SFRC40	Block	1	3,0	Conforti	271,44	405,5	-33,1%
Liao *et al*. (2015)-b200-SFRC40	Block	1	3,0	Guyon	57,75	405,5	-85,8%
Liao *et al*. (2015)-b200-SFRC40	Block	1	3,0	HeLiu	238,87	405,5	-41,1%
Liao *et al*. (2015)-b200-SFRC50	Block	1	3,7	Liao	326,38	429	-23,9%
Liao *et al*. (2015)-b200-SFRC50	Block	1	3,7	Boye	1005,21	429	134,3%
Liao *et al*. (2015)-b200-SFRC50	Block	1	3,7	Conforti	1016,64	429	137,0%
Liao *et al*. (2015)-b200-SFRC50	Block	1	3,7	Guyon	648,92	429	51,3%
Liao *et al*. (2015)-b200-SFRC50	Block	1	3,7	HeLiu	894,64	429	108,5%
Liao *et al*. (2015)-b250-PC40	Block	1	3,3	Liao	318,97	409,5	-22,1%
Liao *et al*. (2015)-b250-PC40	Block	1	3,3	Boye	692,24	409,5	69,0%
Liao *et al*. (2015)-b250-PC40	Block	1	3,3	Conforti	693,03	409,5	69,2%
Liao *et al*. (2015)-b250-PC40	Block	1	3,3	Guyon	353,89	409,5	-13,6%
Liao *et al*. (2015)-b250-PC40	Block	1	3,3	HeLiu	609,87	409,5	48,9%
Liao *et al*. (2015)-b250-PC50	Block	1	3,8	Liao	373,85	434	-13,9%
Liao *et al*. (2015)-b250-PC50	Block	1	3,8	Boye	811,36	434	86,9%
Liao *et al*. (2015)-b250-PC50	Block	1	3,8	Conforti	812,28	434	87,2%

Liao *et al*. (2015)-b250-PC50	Block	1	3,8	Guyon	414,78	434	-4,4%
Liao *et al*. (2015)-b250-PC50	Block	1	3,8	HeLiu	714,81	434	64,7%
Liao *et al*. (2015)-b250-SFRC40	Block	1	3,0	Liao	330,75	374	-11,6%
Liao *et al*. (2015)-b250-SFRC40	Block	1	3,0	Boye	320,47	374	-14,3%
Liao *et al*. (2015)-b250-SFRC40	Block	1	3,0	Conforti	318,10	374	-14,9%
Liao *et al*. (2015)-b250-SFRC40	Block	1	3,0	Guyon	54,14	374	-85,5%
Liao *et al*. (2015)-b250-SFRC40	Block	1	3,0	HeLiu	279,93	374	-25,2%
Liao *et al*. (2015)-b250-SFRC50	Block	1	3,7	Liao	365,55	526,5	-30,6%
Liao *et al*. (2015)-b250-SFRC50	Block	1	3,7	Boye	793,35	526,5	50,7%
Liao *et al*. (2015)-b250-SFRC50	Block	1	3,7	Conforti	794,25	526,5	50,9%
Liao *et al*. (2015)-b250-SFRC50	Block	1	3,7	Guyon	405,57	526,5	-23,0%
Liao *et al*. (2015)-b250-SFRC50	Block	1	3,7	HeLiu	698,94	526,5	32,8%
Liao *et al*. (2015)-b400-PC40	Block	1	3,3	Liao	544,95	632,5	-13,8%
Liao *et al*. (2015)-b400-PC40	Block	1	3,3	Boye	713,23	632,5	12,8%
Liao *et al*. (2015)-b400-PC40	Block	1	3,3	Conforti	709,66	632,5	12,2%
Liao *et al*. (2015)-b400-PC40	Block	1	3,3	Guyon	226,49	632,5	-64,2%
Liao *et al*. (2015)-b400-PC40	Block	1	3,3	HeLiu	624,50	632,5	-1,3%
Liao *et al*. (2015)-b400-SFRC40	Block	1	3,0	Liao	500,26	630,5	-20,7%
Liao *et al*. (2015)-b400-SFRC40	Block	1	3,0	Boye	654,74	630,5	3,8%
Liao *et al*. (2015)-b400-SFRC40	Block	1	3,0	Conforti	651,47	630,5	3,3%
Liao *et al*. (2015)-b400-SFRC40	Block	1	3,0	Guyon	207,92	630,5	-67,0%
Liao *et al*. (2015)-b400-SFRC40	Block	1	3,0	HeLiu	573,29	630,5	-9,1%
Liao *et al*. (2015)-b400-SFRC50	Block	1	3,7	Liao	624,54	641	-2,6%

Liao *et al*. (2015)-b400-SFRC50	Block	1	3,7	Boye	817,40	641	27,5%
Liao *et al*. (2015)-b400-SFRC50	Block	1	3,7	Conforti	813,31	641	26,9%
Liao *et al*. (2015)-b400-SFRC50	Block	1	3,7	Guyon	259,57	641	-59,5%
Liao *et al*. (2015)-b400-SFRC50	Block	1	3,7	HeLiu	715,71	641	11,7%
Liao *et al*. (2015)-b750-PC40	Block	1	3,3	Liao	563,06	744	-24,3%
Liao *et al*. (2015)-b750-PC40	Block	1	3,3	Boye	1047,28	744	40,8%
Liao *et al*. (2015)-b750-PC40	Block	1	3,3	Conforti	1039,54	744	39,7%
Liao *et al*. (2015)-b750-PC40	Block	1	3,3	Guyon	176,94	744	-76,2%
Liao *et al*. (2015)-b750-PC40	Block	1	3,3	HeLiu	914,80	744	23,0%
Liao *et al*. (2015)-b750-SFRC40	Block	1	3,0	Liao	516,89	659,5	-21,6%
Liao *et al*. (2015)-b750-SFRC40	Block	1	3,0	Boye	961,40	659,5	45,8%
Liao *et al*. (2015)-b750-SFRC40	Block	1	3,0	Conforti	954,30	659,5	44,7%
Liao *et al*. (2015)-b750-SFRC40	Block	1	3,0	Guyon	162,43	659,5	-75,4%
Liao *et al*. (2015)-b750-SFRC40	Block	1	3,0	HeLiu	839,78	659,5	27,3%
Liao *et al*. (2015)-b750-SFRC50	Block	1	3,7	Liao	645,29	715	-9,7%
Liao *et al*. (2015)-b750-SFRC50	Block	1	3,7	Boye	1200,24	715	67,9%
Liao *et al*. (2015)-b750-SFRC50	Block	1	3,7	Conforti	1191,37	715	66,6%
Liao *et al*. (2015)-b750-SFRC50	Block	1	3,7	Guyon	202,79	715	-71,6%
Liao *et al*. (2015)-b750-SFRC50	Block	1	3,7	HeLiu	1048,41	715	46,6%
Schnutgen and Erdem (2001) - SFRC-B	Block	1	3,6	Liao	1166,99	1875	-37,8%
Schnutgen and Erdem (2001) - SFRC-B	Block	1	3,6	Boye	1778,75	1875	-5,1%
Schnutgen and Erdem (2001) - SFRC-B	Block	1	3,6	Conforti	1771,68	1875	-5,5%
Schnutgen and Erdem (2001) - SFRC-B	Block	1	3,6	Guyon	646,20	1875	-65,5%

Schnutgen and Erdem (2001) - SFRC-B	Block	1	3,6	HeLiu	1559,08	1875	-16,8%
Schnutgen and Erdem (2001)- SFRC-A	Block	1	4,1	Liao	1310,17	2000	-34,5%
Schnutgen and Erdem (2001)- SFRC-A	Block	1	4,1	Boye	1996,99	2000	-0,2%
Schnutgen and Erdem (2001)- SFRC-A	Block	1	4,1	Conforti	1989,05	2000	-0,5%
Schnutgen and Erdem (2001)- SFRC-A	Block	1	4,1	Guyon	725,49	2000	-63,7%
Schnutgen and Erdem (2001)- SFRC-A	Block	1	4,1	HeLiu	1750,36	2000	-12,5%
Tiberti *et al*. (2015) -PC	Block	1	4,0	Liao	664,80	1044,33	-36,3%
Tiberti *et al*. (2015) -PC	Block	1	4,0	Boye	957,97	1044,33	-8,3%
Tiberti *et al*. (2015) -PC	Block	1	4,0	Conforti	953,62	1044,33	-8,7%
Tiberti *et al*. (2015) -PC	Block	1	4,0	Guyon	324,64	1044,33	-68,9%
Tiberti *et al*. (2015) -PC	Block	1	4,0	HeLiu	839,18	1044,33	-19,6%
Tiberti *et al*. (2015) -PFRC	Block	1	3,5	Liao	583,91	917,33	-36,3%
Tiberti *et al*. (2015) -PFRC	Block	1	3,5	Boye	841,42	917,33	-8,3%
Tiberti *et al*. (2015) -PFRC	Block	1	3,5	Conforti	837,59	917,33	-8,7%
Tiberti *et al*. (2015) -PFRC	Block	1	3,5	Guyon	285,14	917,33	-68,9%
Tiberti *et al*. (2015) -PFRC	Block	1	3,5	HeLiu	737,08	917,33	-19,6%
Trabucchi *et al* (2021)	Block	1	3,5	Liao	583,91	746,83	-21,8%
Trabucchi *et al* (2021)	Block	1	3,5	Boye	841,42	746,83	12,7%
Trabucchi *et al* (2021)	Block	1	3,5	Conforti	837,60	746,83	12,2%
Trabucchi *et al* (2021)	Block	1	3,5	Guyon	285,14	746,83	-61,8%
Trabucchi *et al* (2021)	Block	1	3,5	HeLiu	737,08	746,83	-1,3%

APPENDIX A.2

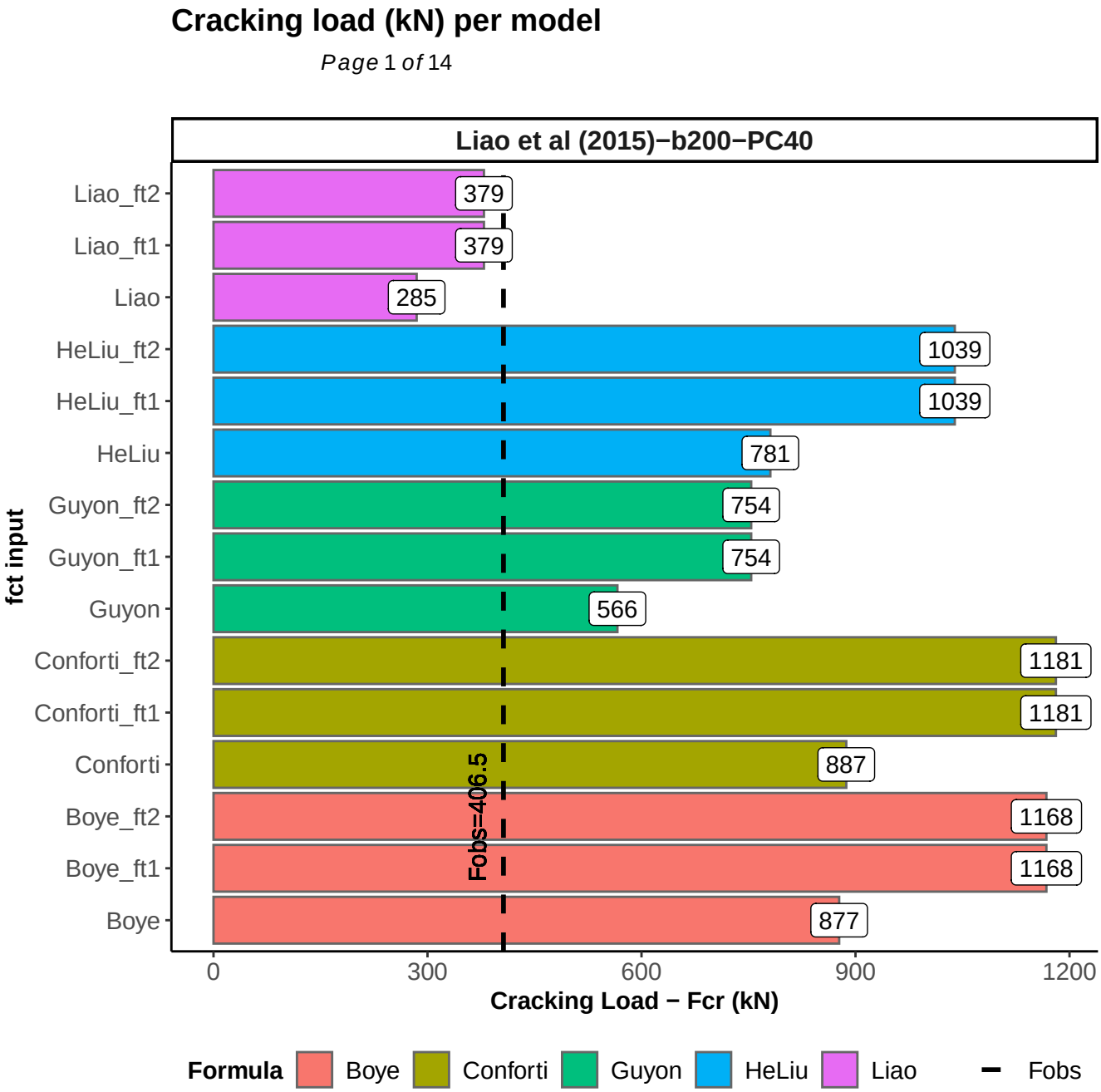
Cracking load (kN) per model
Page 1 of 14
Liao et al (2015)−b200−PC40
fct input
Liao_ft2
Liao_ft1
Liao
HeLiu_ft2
HeLiu_ft1
HeLiu
Guyon_ft2
Guyon_ft1
Guyon
Conforti_ft2
Conforti_ft1
Conforti
Boye_ft2
Boye_ft1
Boye
379
379
285
1039
1039
781
754
754
566
1181
1181
887
1168
1168
877
Fobs=406.5
0
300
600
900
1200
Cracking Load − Fcr (kN)
Formula
Boye
Conforti
Guyon
HeLiu
Liao
Fobs

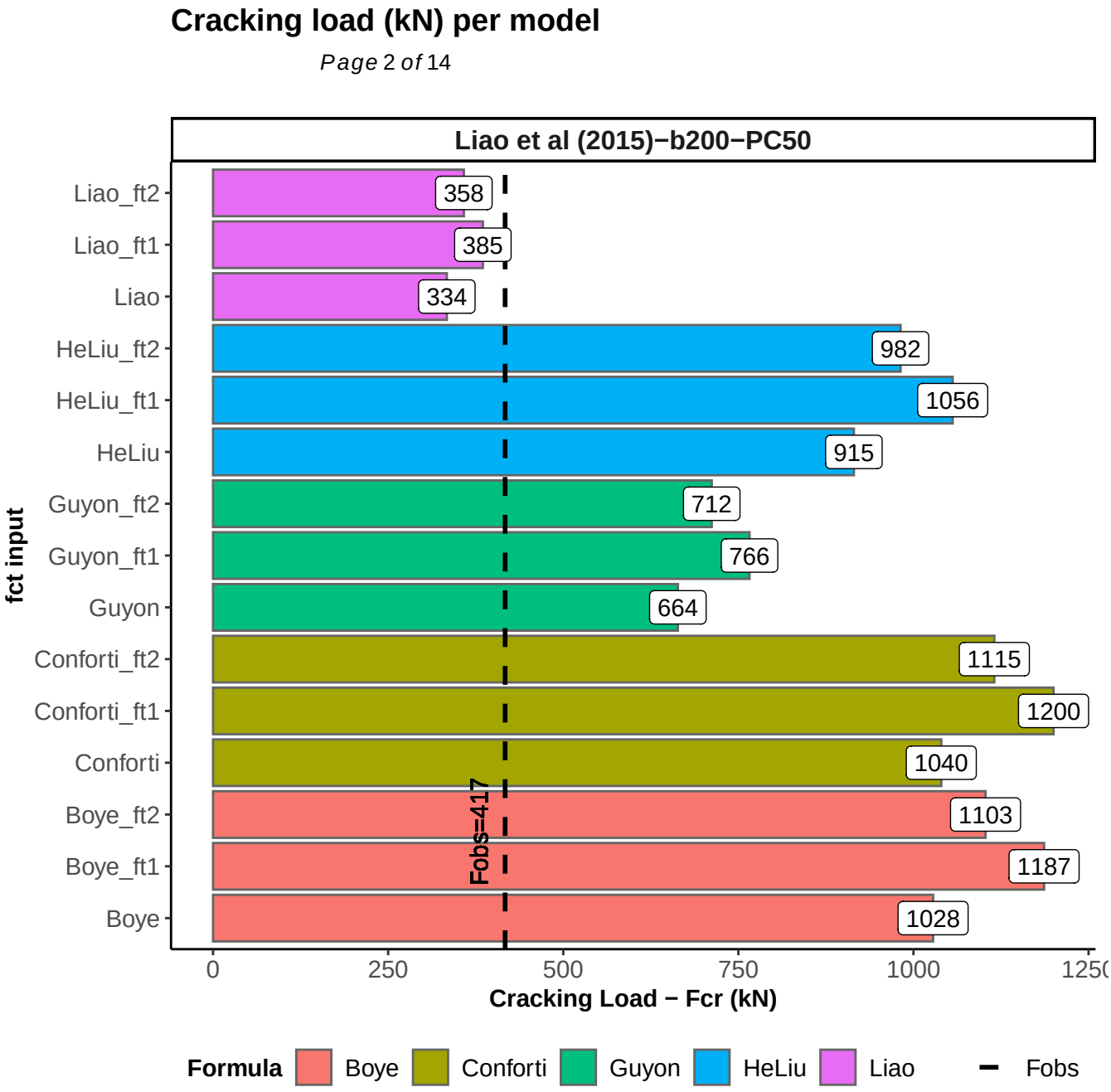
Cracking load (kN) per model
Page 2 of 14
Liao et al (2015)−b200−PC50
fct input
Liao_ft2
Liao_ft1
Liao
HeLiu_ft2
HeLiu_ft1
HeLiu
Guyon_ft2
Guyon_ft1
Guyon
Conforti_ft2
Conforti_ft1
Conforti
Boye_ft2
Boye_ft1
Boye
358
385
334
982
1056
915
712
766
664
1115
1200
1040
1103
1187
1028
Fobs=417
0
250
500
750
1000
1250
Cracking Load − Fcr (kN)
Formula
Boye
Conforti
Guyon
HeLiu
Liao
Fobs

Cracking load (kN) per model

Page 3 *of* 14

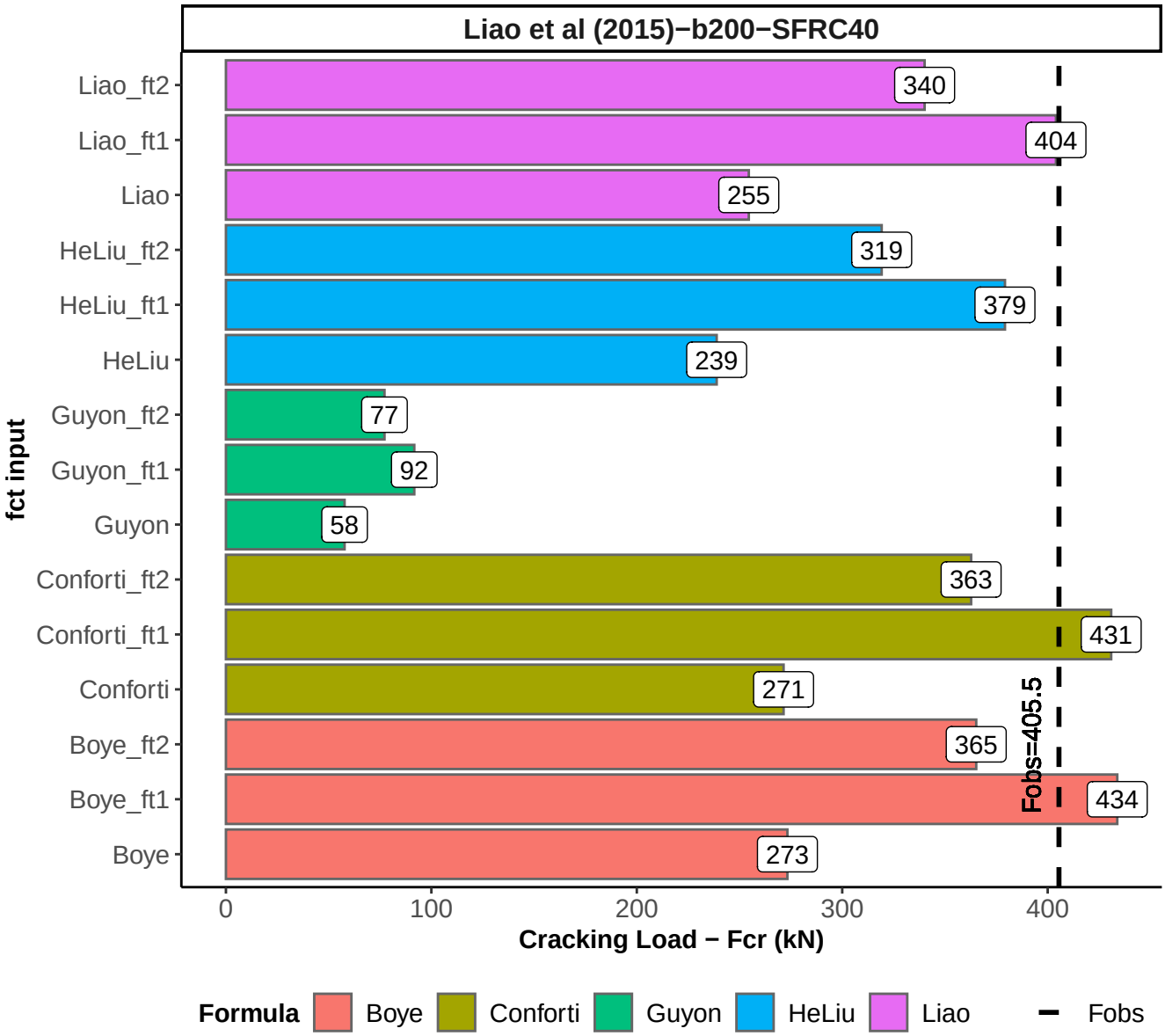

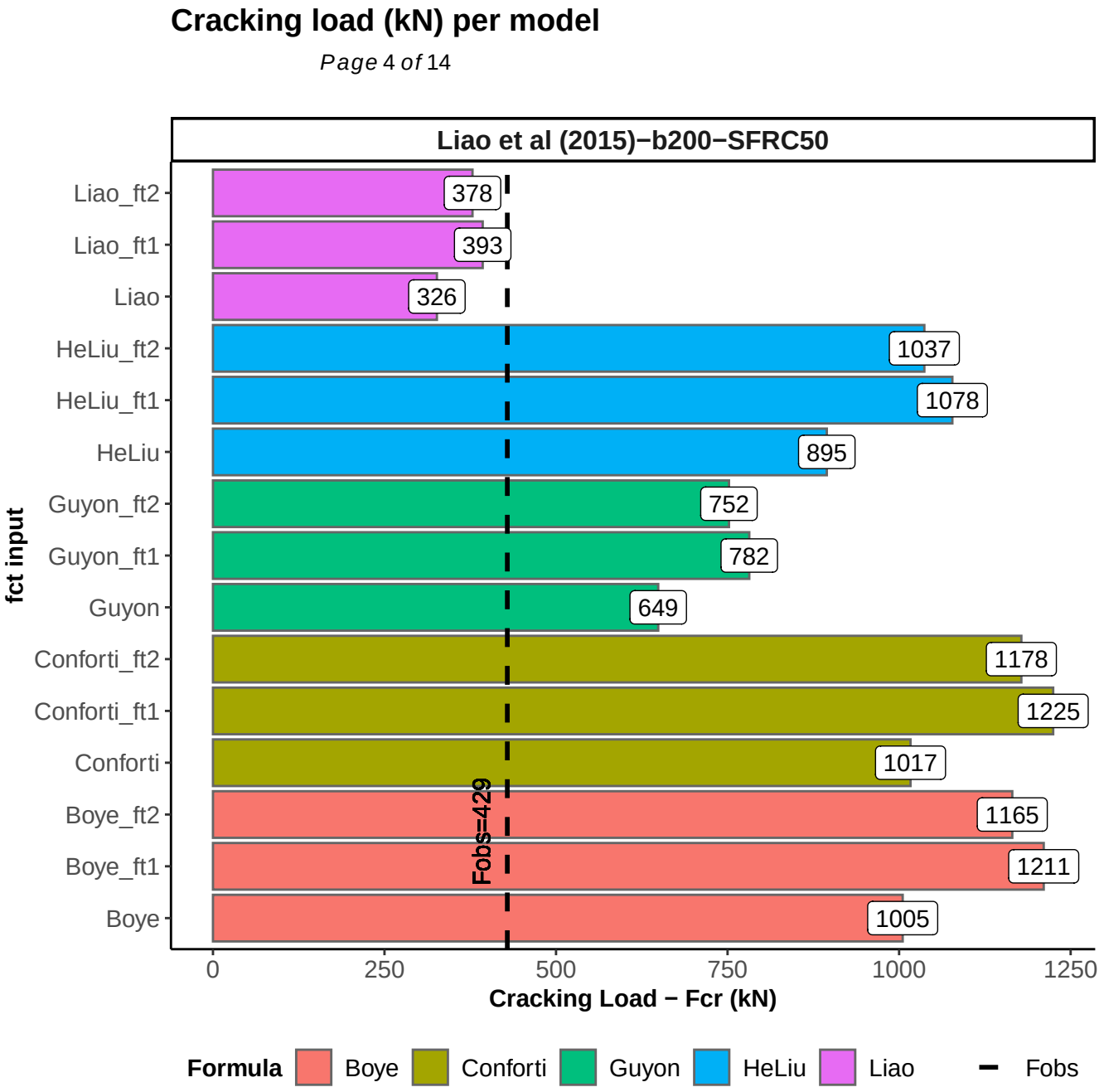
Cracking load (kN) per model
Page 4 of 14
Liao et al (2015)−b200−SFRC50
Liao_ft2
Liao_ft1
Liao
HeLiu_ft2
HeLiu_ft1
HeLiu
Guyon_ft2
Guyon_ft1
Guyon
Conforti_ft2
Conforti_ft1
Conforti
Boye_ft2
Boye_ft1
Boye
378
393
326
1037
1078
895
752
782
649
1178
1225
1017
1165
1211
1005
Fobs=429
fct input
0
250
500
750
1000
1250
Cracking Load − Fcr (kN)
Formula
Boye
Conforti
Guyon
HeLiu
Liao
Fobs

Cracking load (kN) per model

Page 5 *of* 14

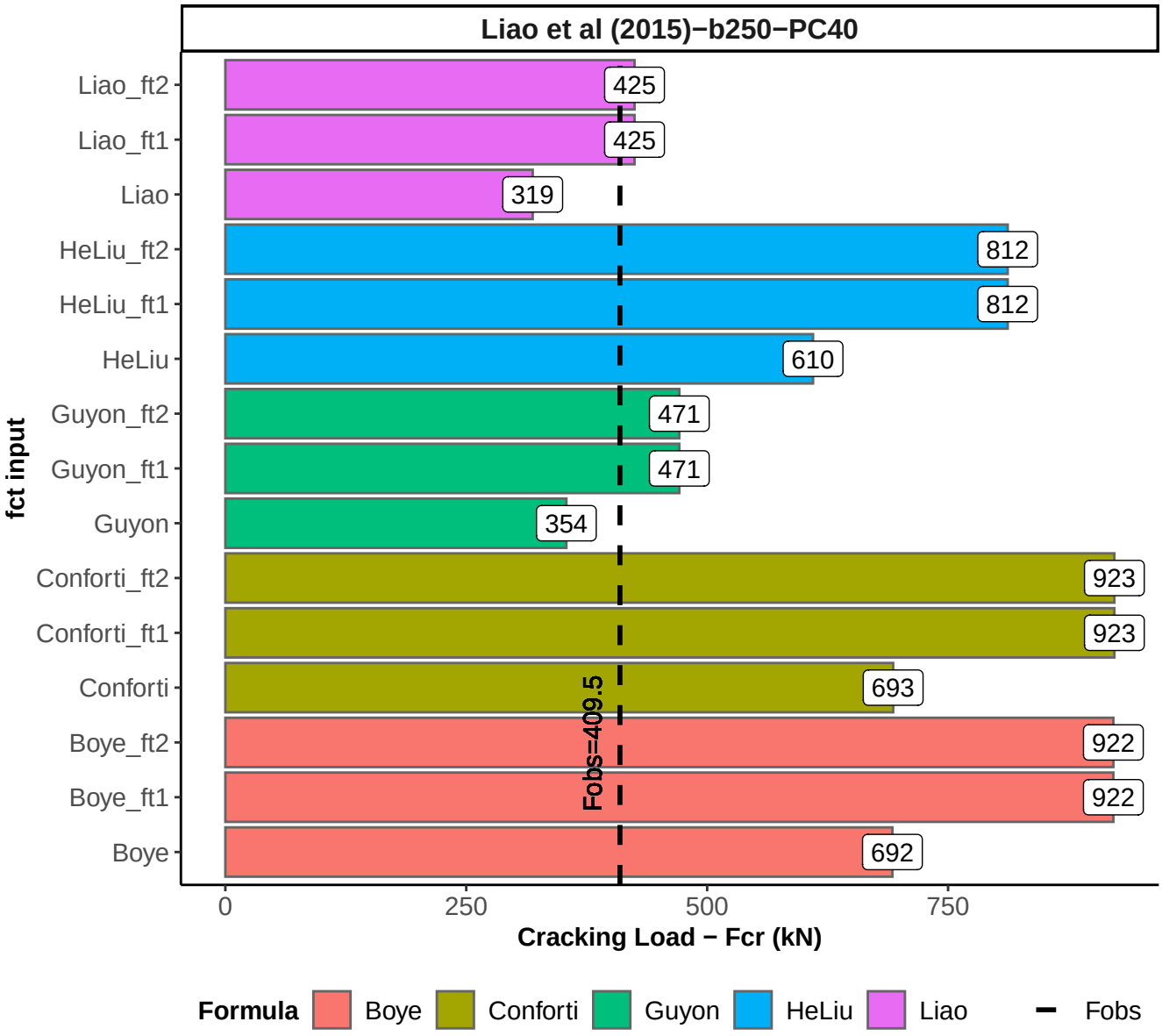

Cracking load (kN) per model

Page 6 *of* 14

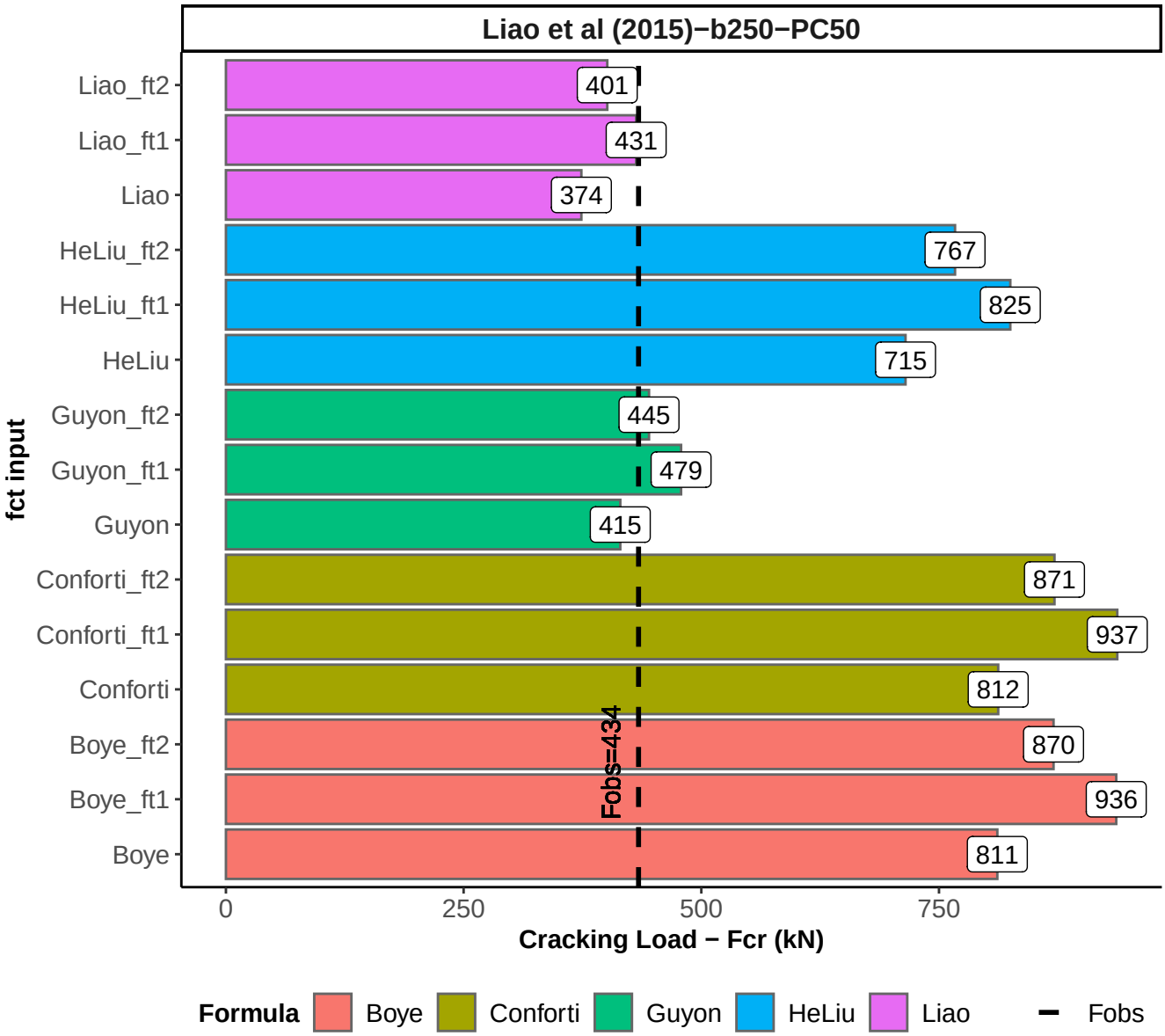

Cracking load (kN) per model

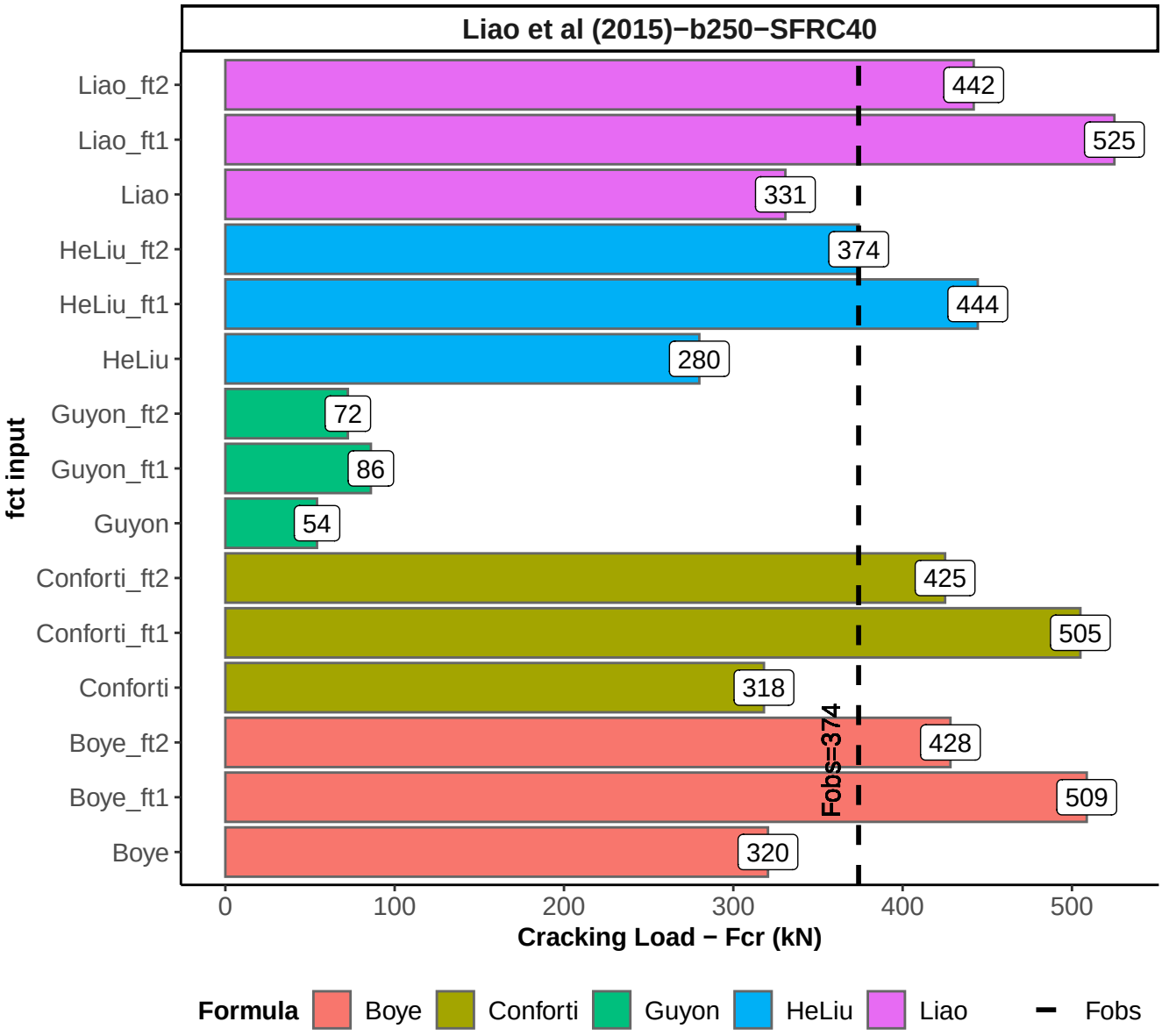

Cracking load (kN) per model

Page 8 *of* 14

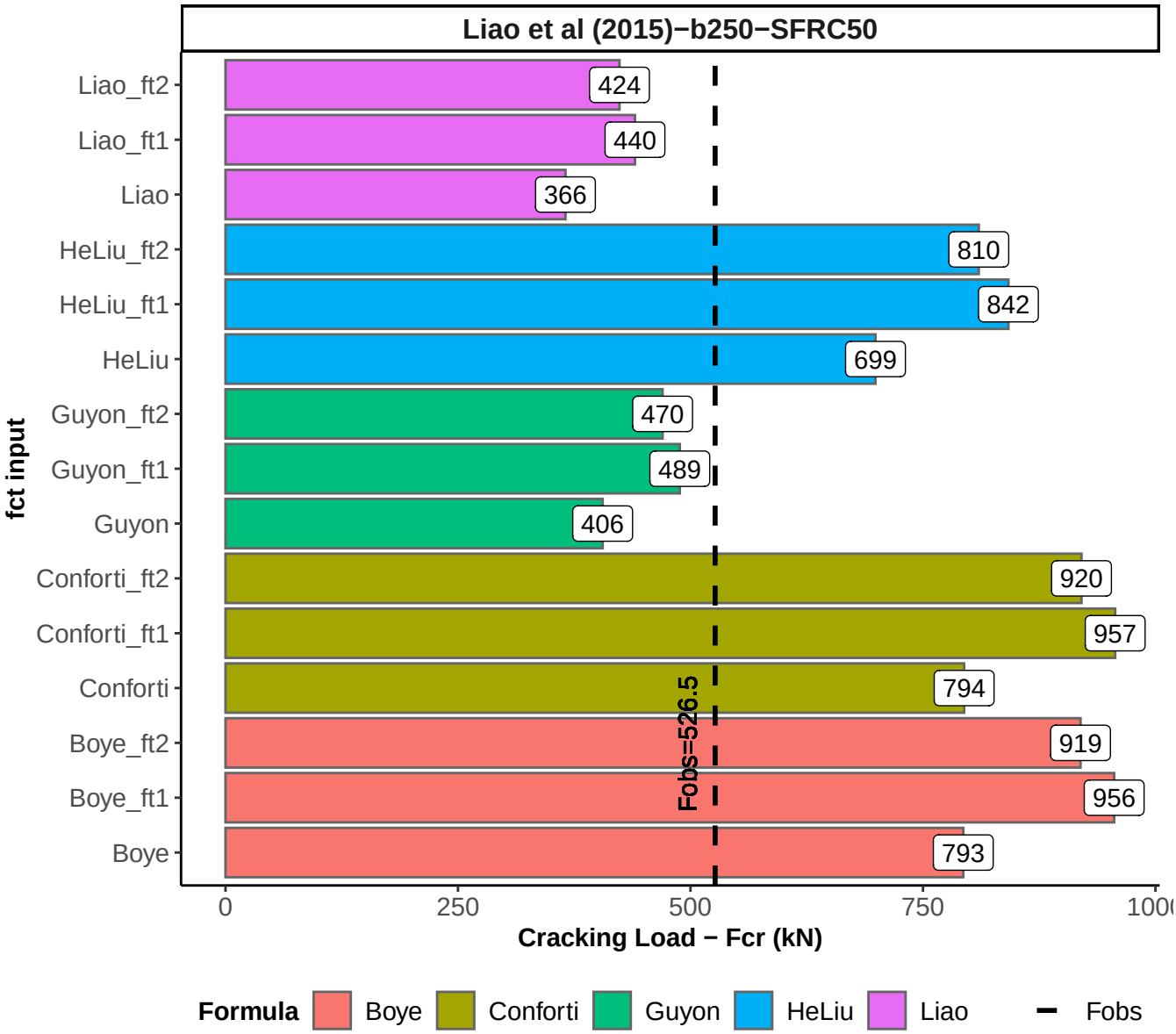

Cracking load (kN) per model

Page 9 *of* 14

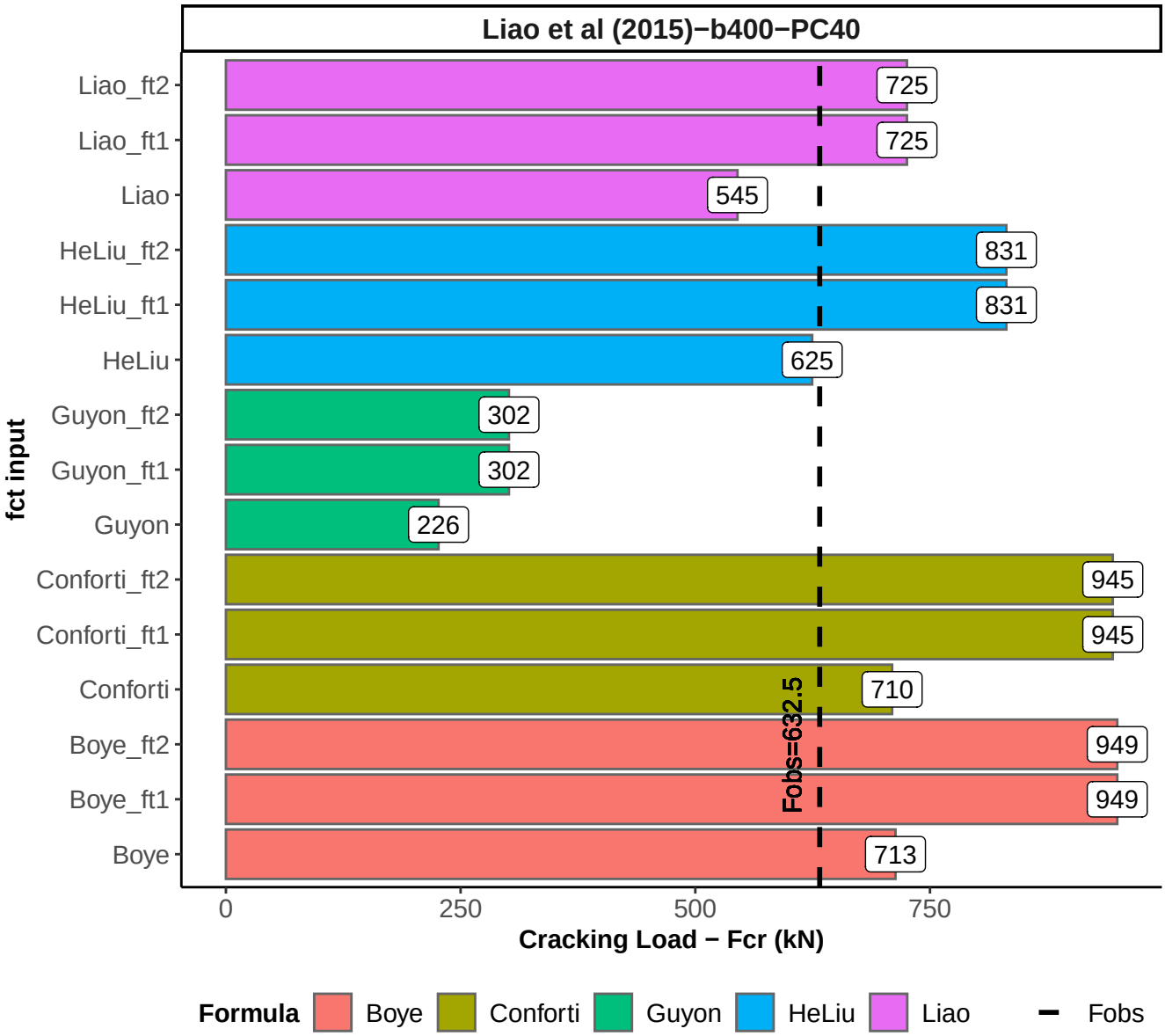

Cracking load (kN) per model

Page 10 *of* 14

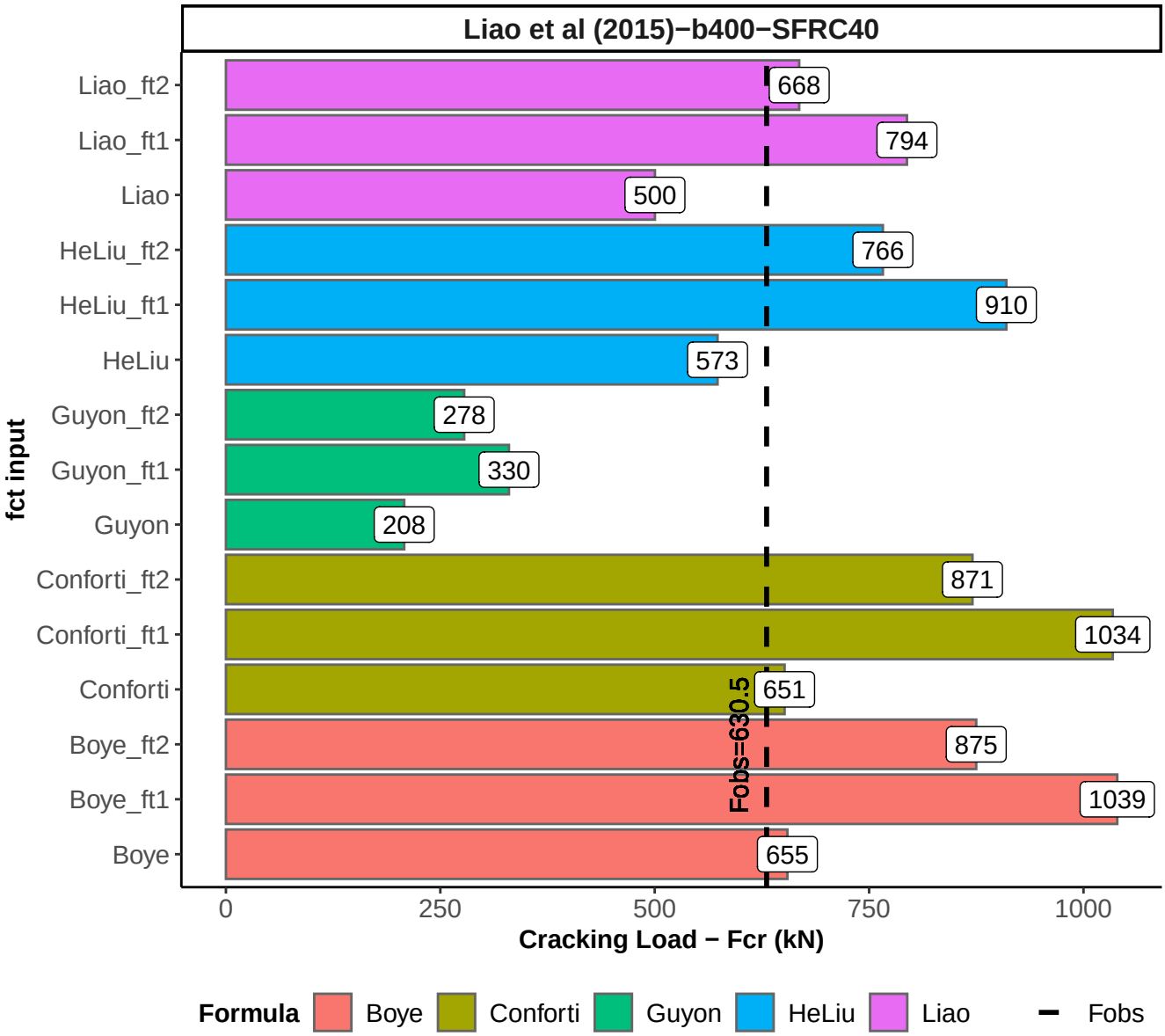

Cracking load (kN) per model

Page 11 *of* 14

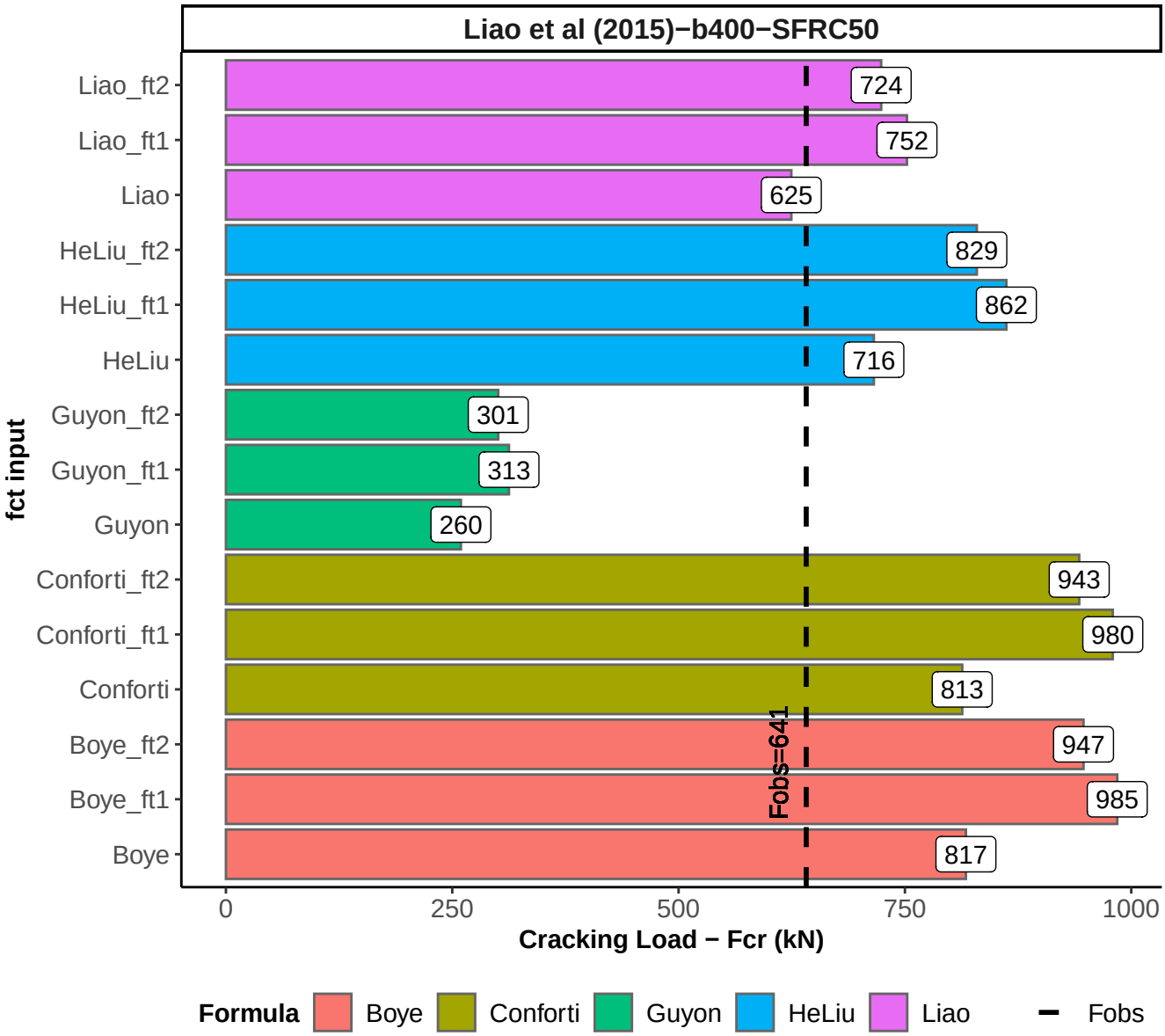

Cracking load (kN) per model

Page 12 *of* 14

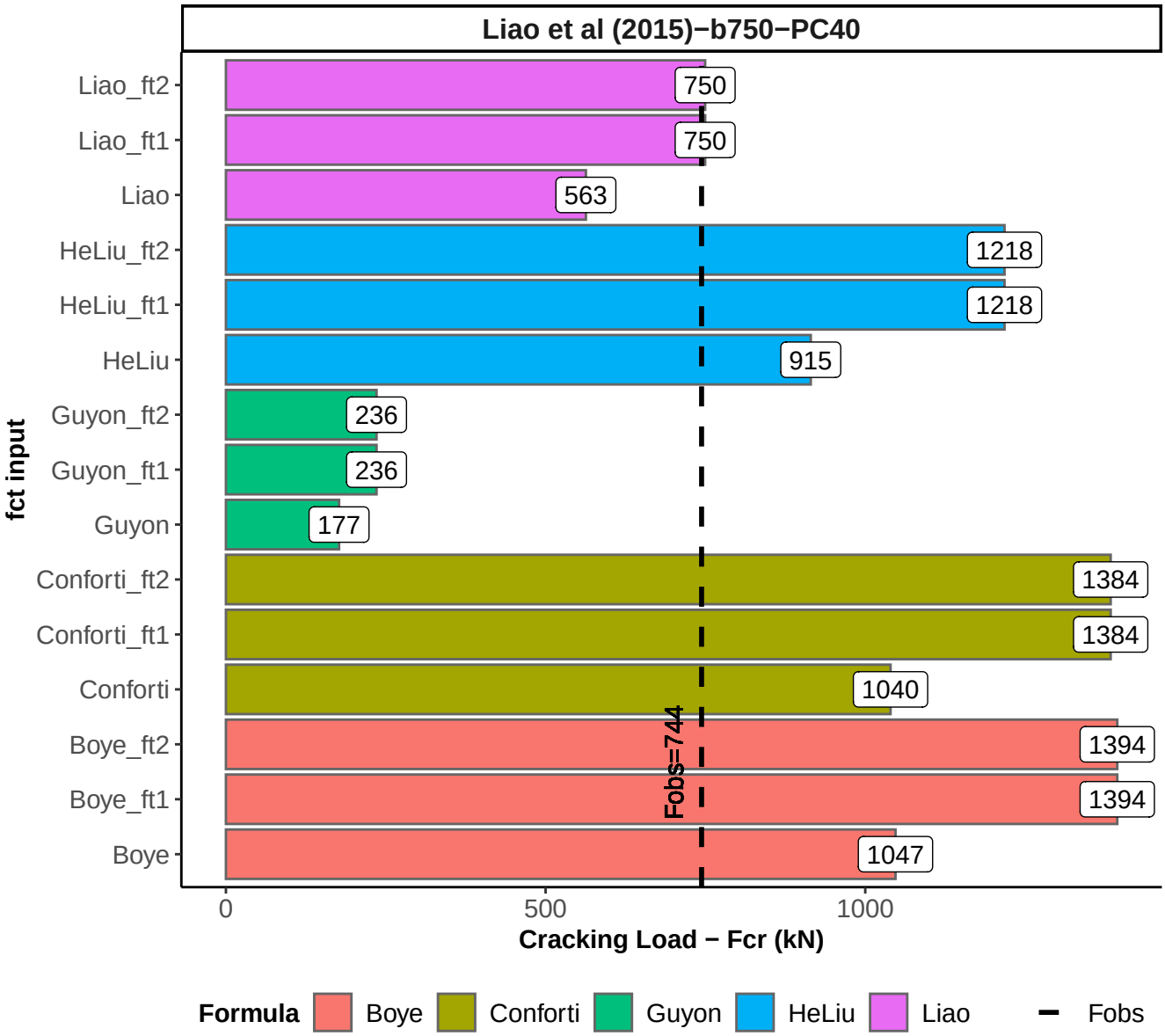

Cracking load (kN) per model

Page 13 *of* 14

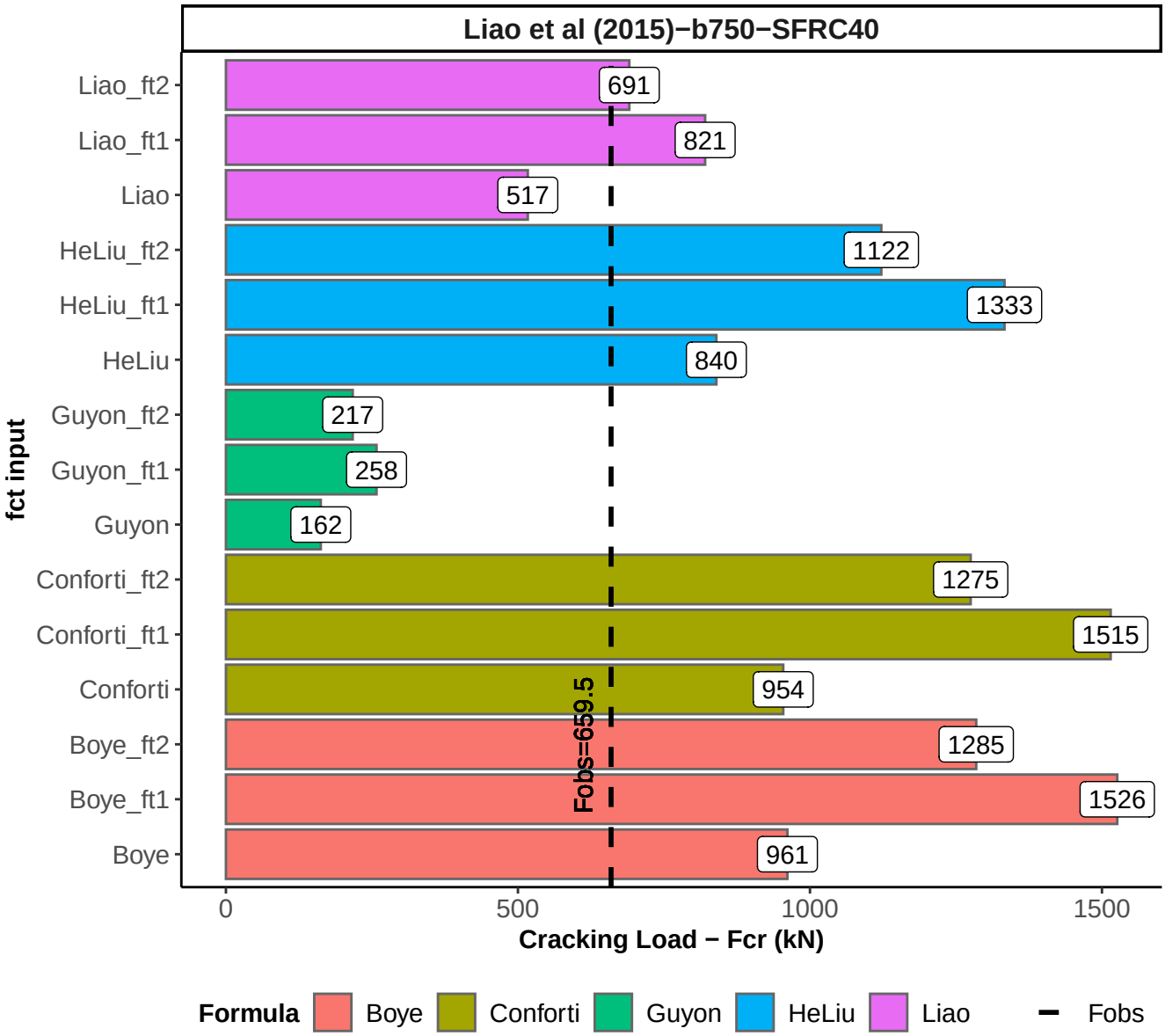

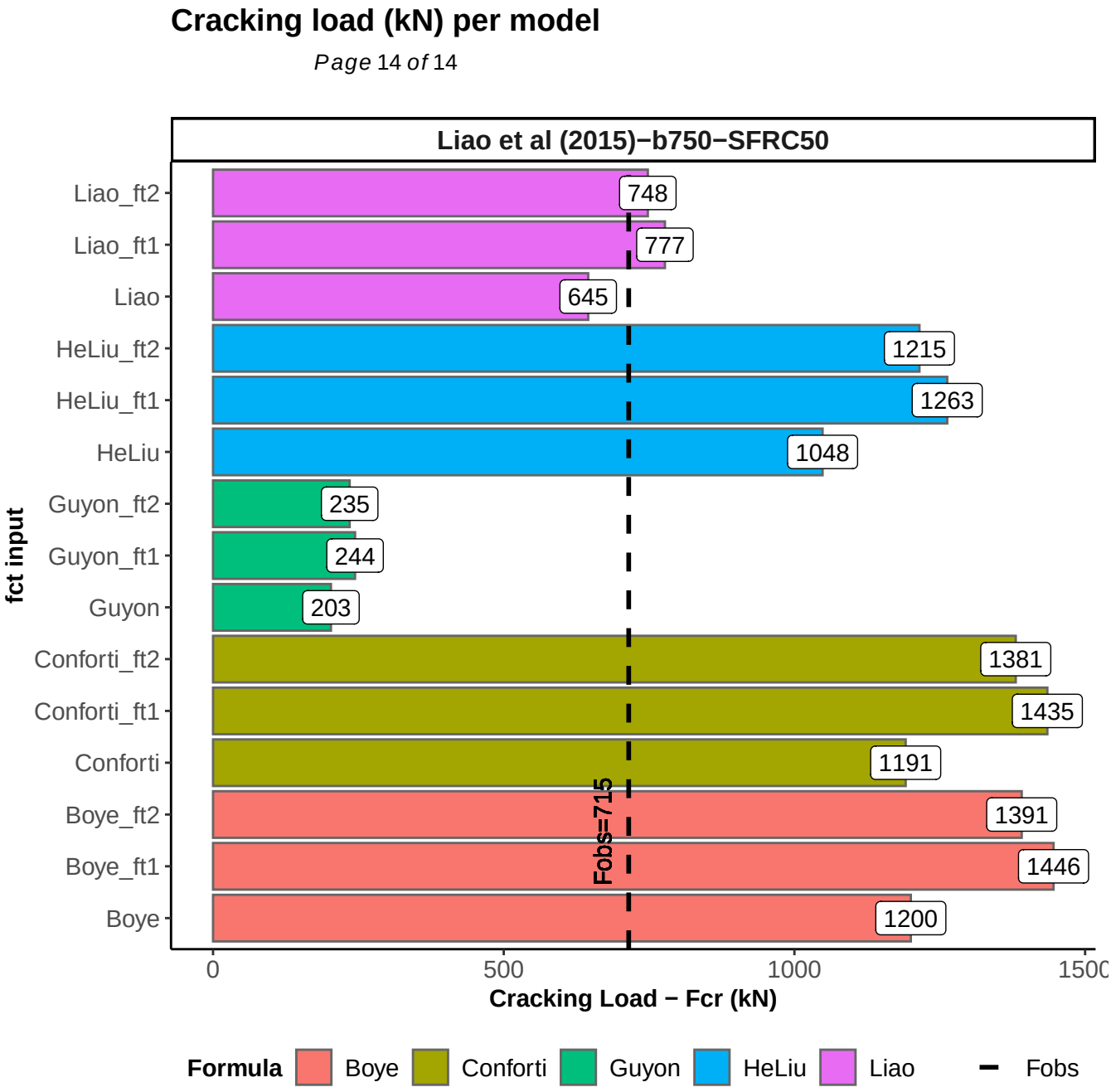
Cracking load (kN) per model
Page 14 of 14
Liao et al (2015)−b750−SFRC50
Liao_ft2
Liao_ft1
Liao
HeLiu_ft2
HeLiu_ft1
HeLiu
Guyon_ft2
Guyon_ft1
Guyon
Conforti_ft2
Conforti_ft1
Conforti
Boye_ft2
Boye_ft1
Boye
748
777
645
1215
1263
1048
235
244
203
1381
1435
1191
1391
1446
1200
Fobs=715
fct input
0
500
1000
1500
Cracking Load − Fcr (kN)
Formula
Boye
Conforti
Guyon
HeLiu
Liao
Fobs

APPENDIX A.3

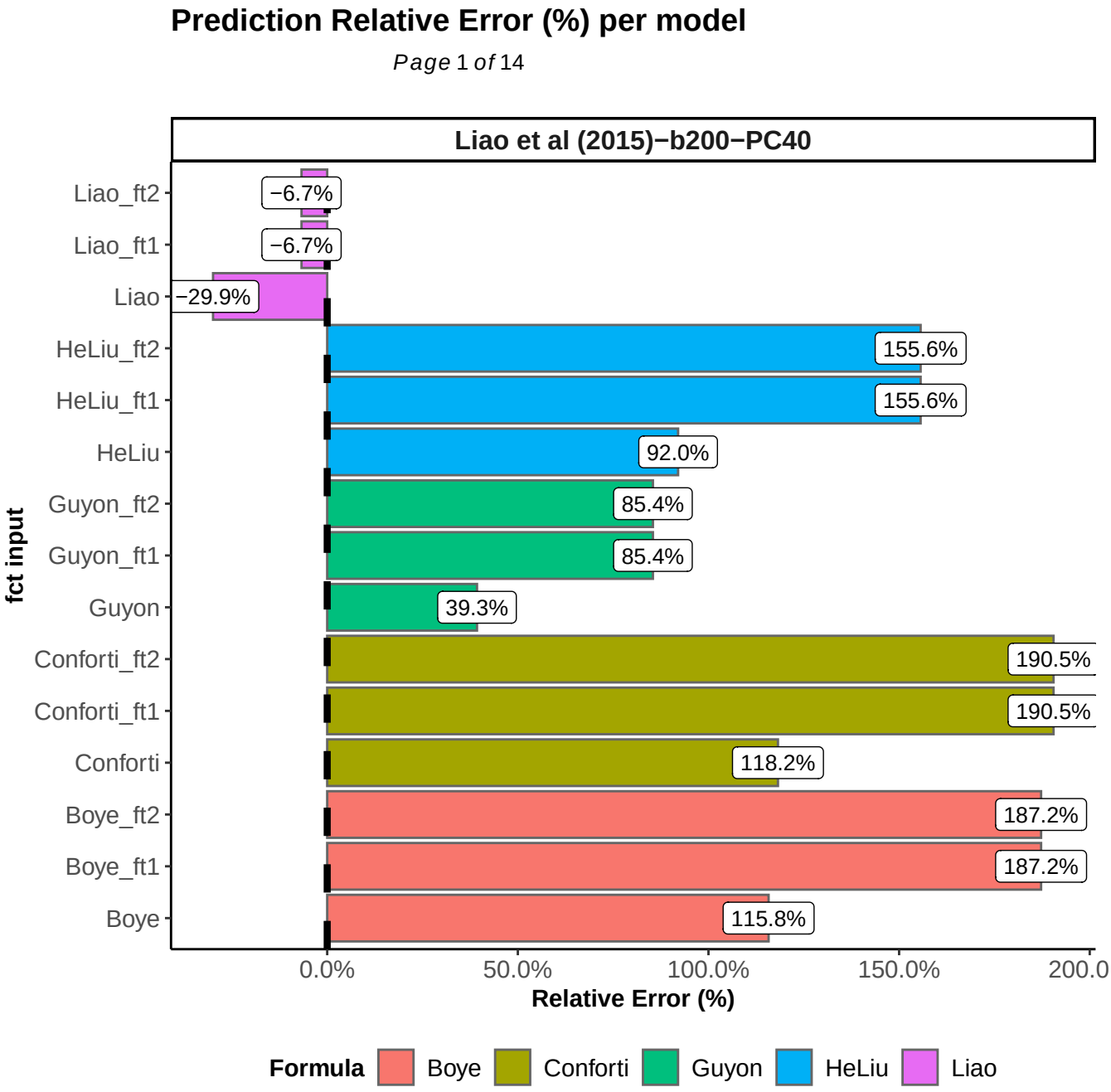
Prediction Relative Error (%) per model
Page 1 of 14
Liao et al (2015)−b200−PC40
Liao_ft2
Liao_ft1
Liao
HeLiu_ft2
HeLiu_ft1
HeLiu
Guyon_ft2
Guyon_ft1
Guyon
Conforti_ft2
Conforti_ft1
Conforti
Boye_ft2
Boye_ft1
Boye
−6.7%
−6.7%
−29.9%
155.6%
155.6%
92.0%
85.4%
85.4%
39.3%
190.5%
190.5%
118.2%
187.2%
187.2%
115.8%
fct input
0.0%
50.0%
100.0%
150.0%
200.0
Relative Error (%)
Formula
Boye
Conforti
Guyon
HeLiu
Liao

Prediction Relative Error (%) per model

Page 2 of 14

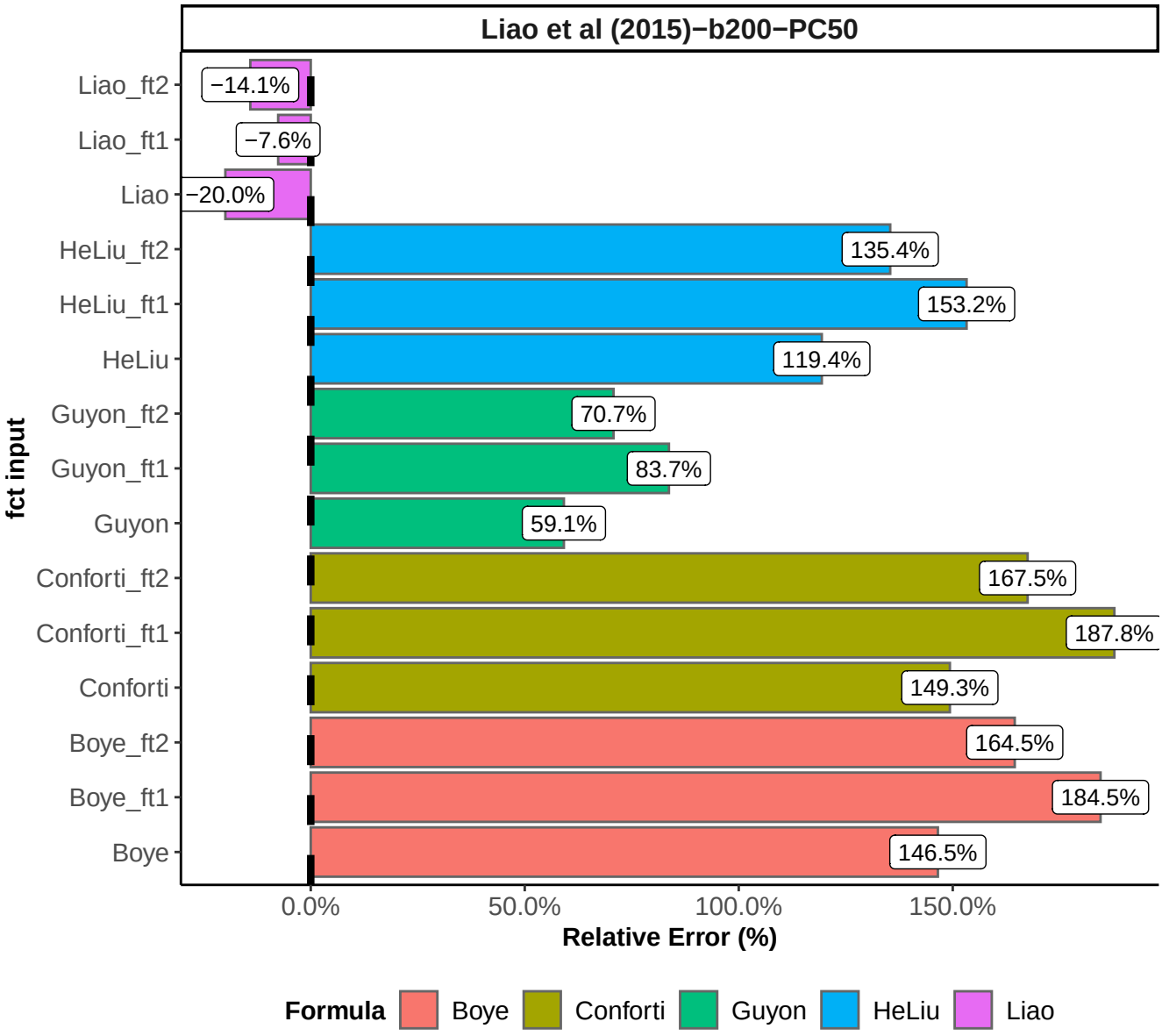

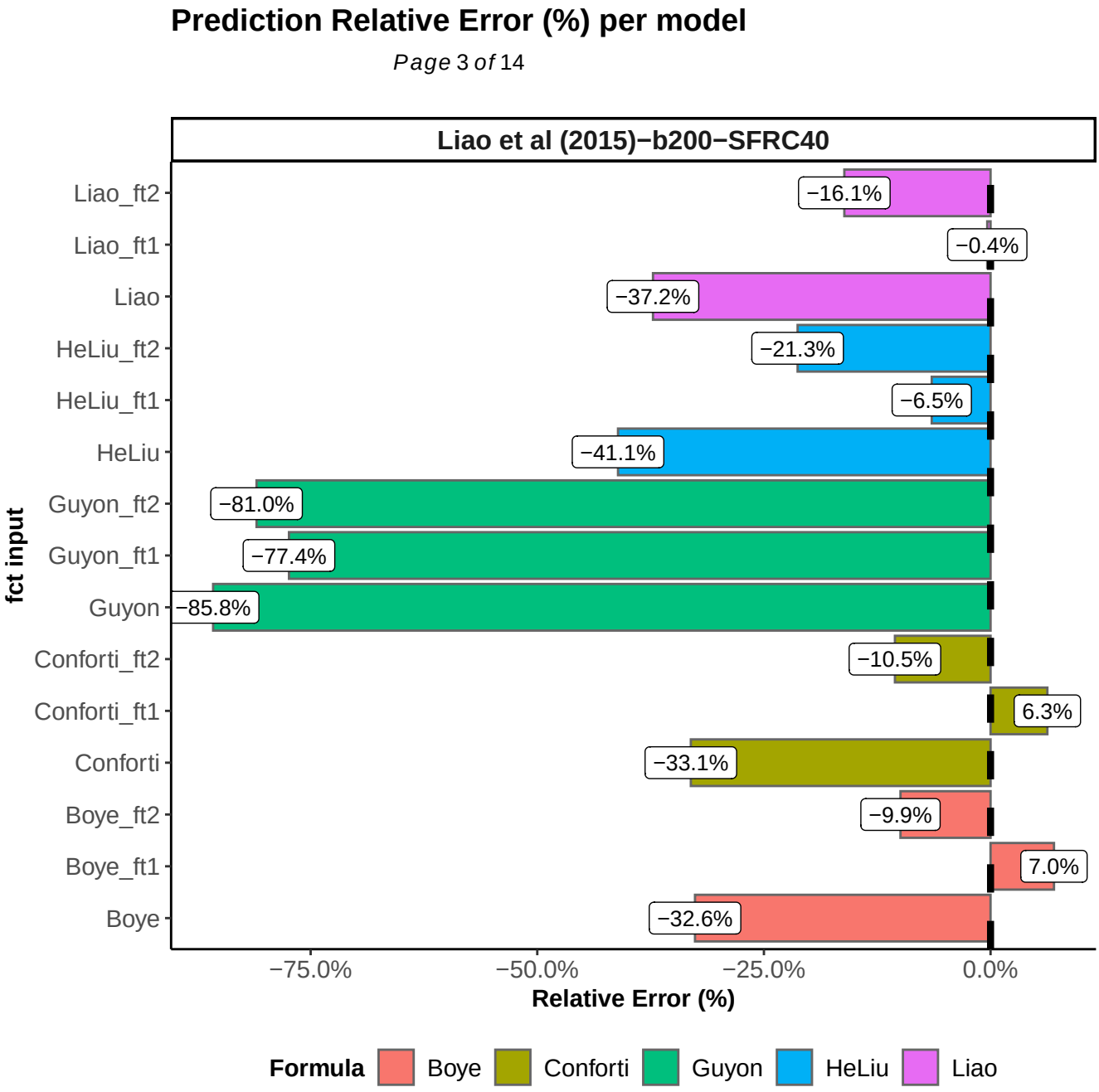
Prediction Relative Error (%) per model
Page 3 of 14
Liao et al (2015)−b200−SFRC40
Liao_ft2
Liao_ft1
Liao
HeLiu_ft2
HeLiu_ft1
HeLiu
Guyon_ft2
Guyon_ft1
Guyon
Conforti_ft2
Conforti_ft1
Conforti
Boye_ft2
Boye_ft1
Boye
−16.1%
−0.4%
−37.2%
−21.3%
−6.5%
−41.1%
−81.0%
−77.4%
−85.8%
−10.5%
6.3%
−33.1%
−9.9%
7.0%
−32.6%
fct input
−75.0%
−50.0%
−25.0%
0.0%
Relative Error (%)
Formula
Boye
Conforti
Guyon
HeLiu
Liao

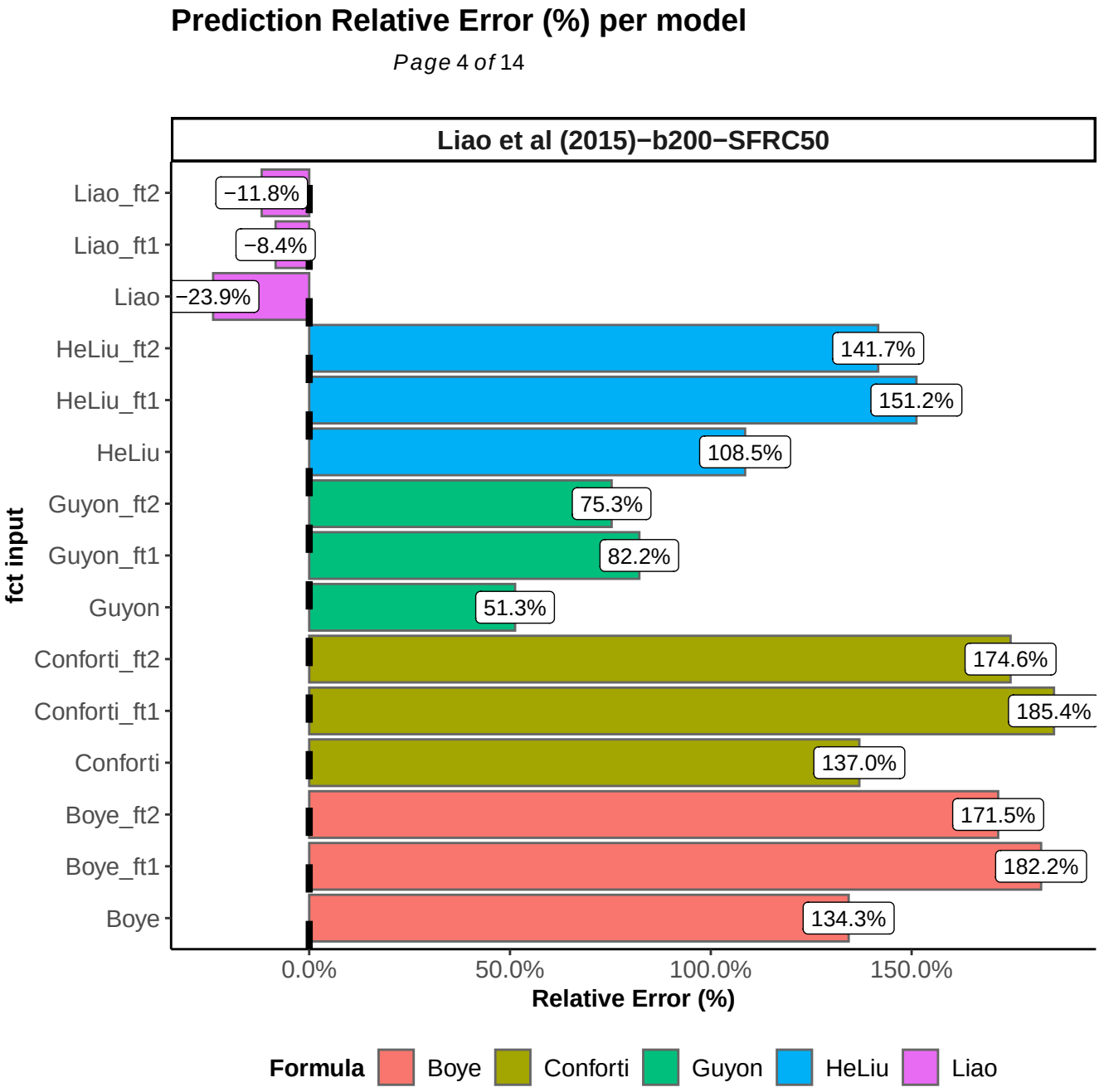
Prediction Relative Error (%) per model
Page 4 of 14
Liao et al (2015)−b200−SFRC50
fct input
Liao_ft2
Liao_ft1
Liao
HeLiu_ft2
HeLiu_ft1
HeLiu
Guyon_ft2
Guyon_ft1
Guyon
Conforti_ft2
Conforti_ft1
Conforti
Boye_ft2
Boye_ft1
Boye
−11.8%
−8.4%
−23.9%
141.7%
151.2%
108.5%
75.3%
82.2%
51.3%
174.6%
185.4%
137.0%
171.5%
182.2%
134.3%
0.0%
50.0%
100.0%
150.0%
Relative Error (%)
Formula
Boye
Conforti
Guyon
HeLiu
Liao

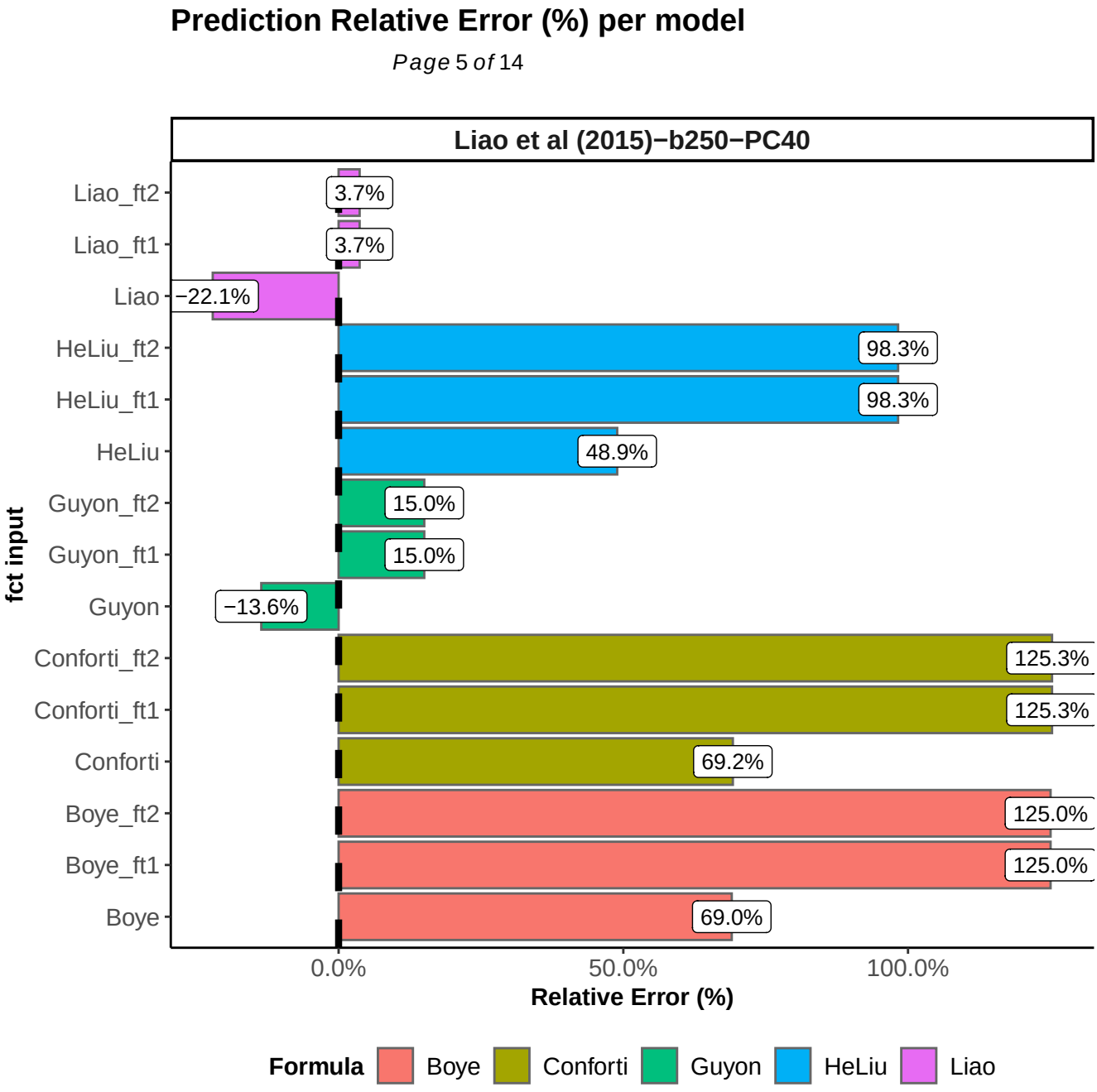
Prediction Relative Error (%) per model
Page 5 of 14
Liao et al (2015)−b250−PC40
fct input
Liao_ft2
Liao_ft1
Liao
HeLiu_ft2
HeLiu_ft1
HeLiu
Guyon_ft2
Guyon_ft1
Guyon
Conforti_ft2
Conforti_ft1
Conforti
Boye_ft2
Boye_ft1
Boye
3.7%
3.7%
−22.1%
98.3%
98.3%
48.9%
15.0%
15.0%
−13.6%
125.3%
125.3%
69.2%
125.0%
125.0%
69.0%
0.0%
50.0%
100.0%
Relative Error (%)
Formula
Boye
Conforti
Guyon
HeLiu
Liao

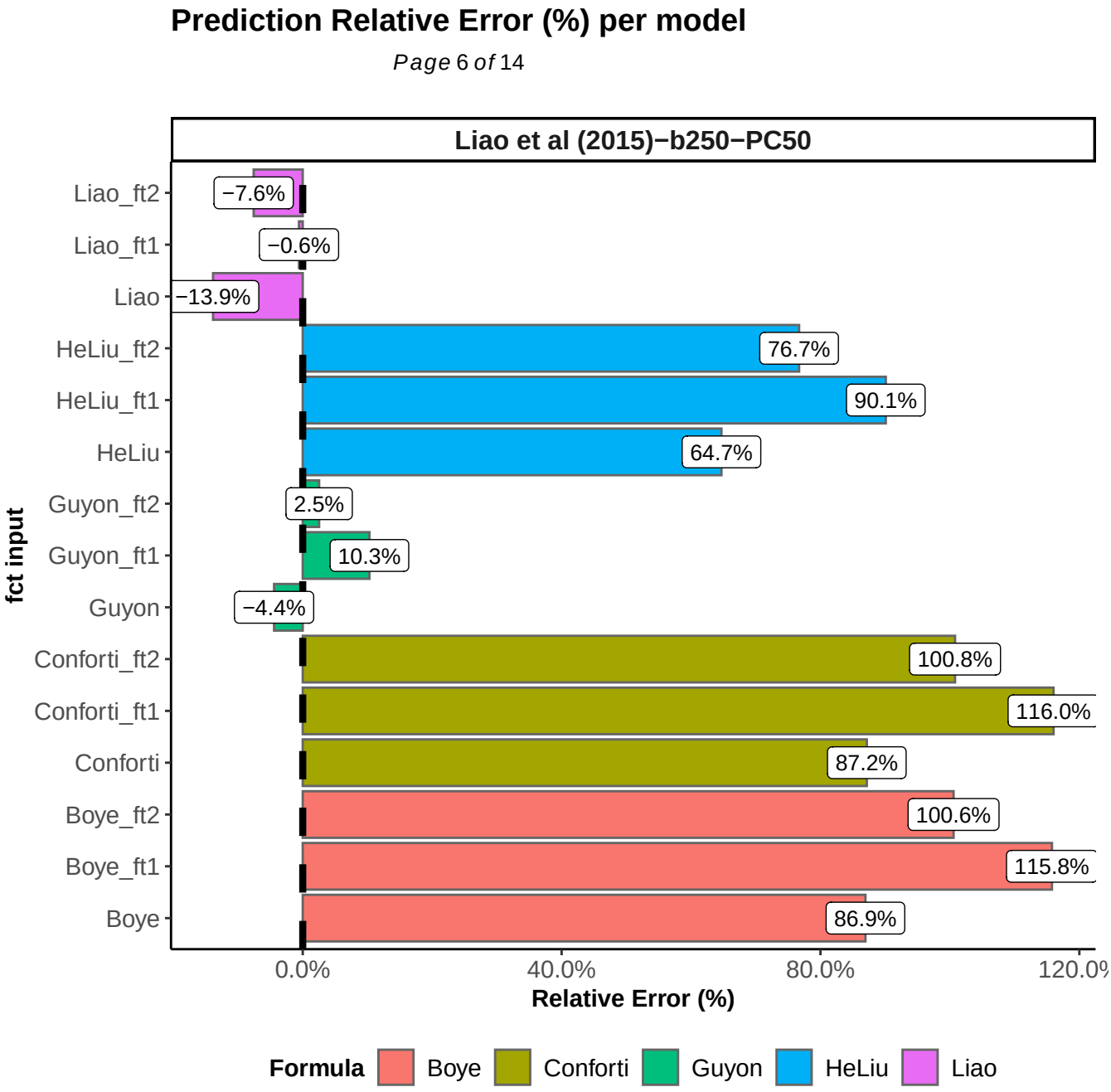
Prediction Relative Error (%) per model
Page 6 of 14
Liao et al (2015)−b250−PC50
fct input
Liao_ft2
Liao_ft1
Liao
HeLiu_ft2
HeLiu_ft1
HeLiu
Guyon_ft2
Guyon_ft1
Guyon
Conforti_ft2
Conforti_ft1
Conforti
Boye_ft2
Boye_ft1
Boye
−7.6%
−0.6%
−13.9%
76.7%
90.1%
64.7%
2.5%
10.3%
−4.4%
100.8%
116.0%
87.2%
100.6%
115.8%
86.9%
0.0%
40.0%
80.0%
120.0%
Relative Error (%)
Formula
Boye
Conforti
Guyon
HeLiu
Liao

Prediction Relative Error (%) per model

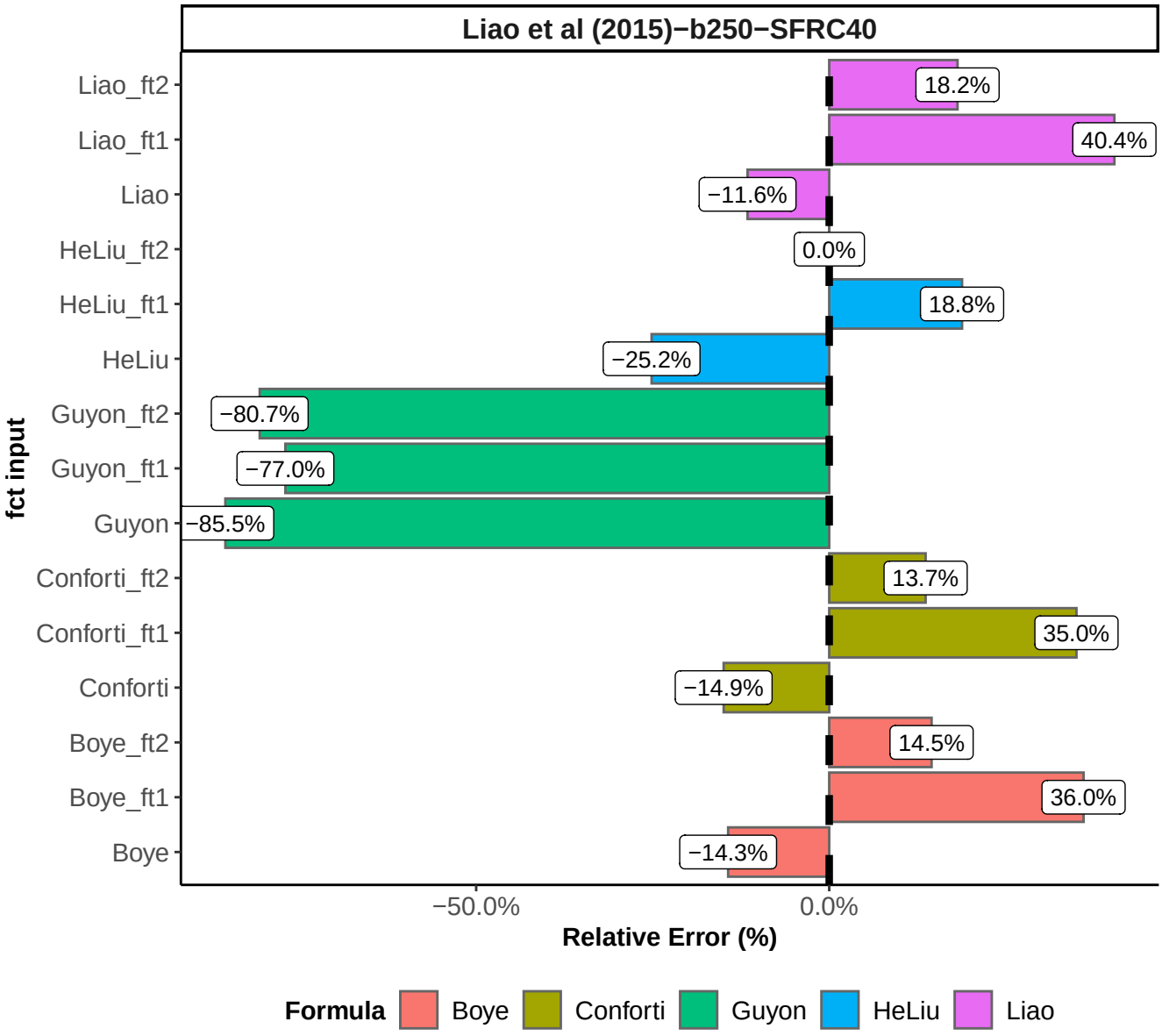

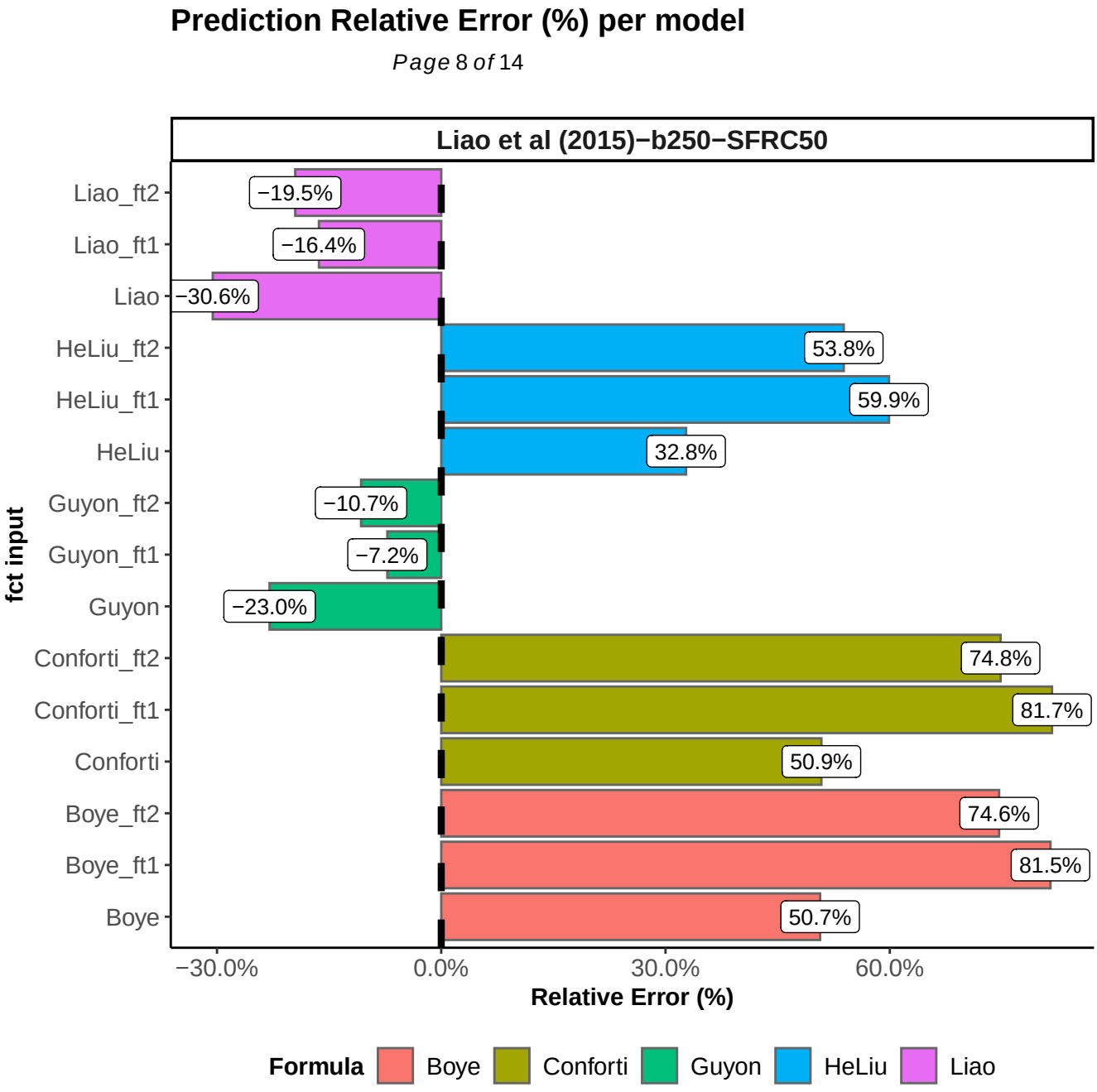
Prediction Relative Error (%) per model
Page 8 of 14
Liao et al (2015)−b250−SFRC50
fct input
Liao_ft2
Liao_ft1
Liao
HeLiu_ft2
HeLiu_ft1
HeLiu
Guyon_ft2
Guyon_ft1
Guyon
Conforti_ft2
Conforti_ft1
Conforti
Boye_ft2
Boye_ft1
Boye
−19.5%
−16.4%
−30.6%
53.8%
59.9%
32.8%
−10.7%
−7.2%
−23.0%
74.8%
81.7%
50.9%
74.6%
81.5%
50.7%
−30.0%
0.0%
30.0%
60.0%
Relative Error (%)
Formula
Boye
Conforti
Guyon
HeLiu
Liao

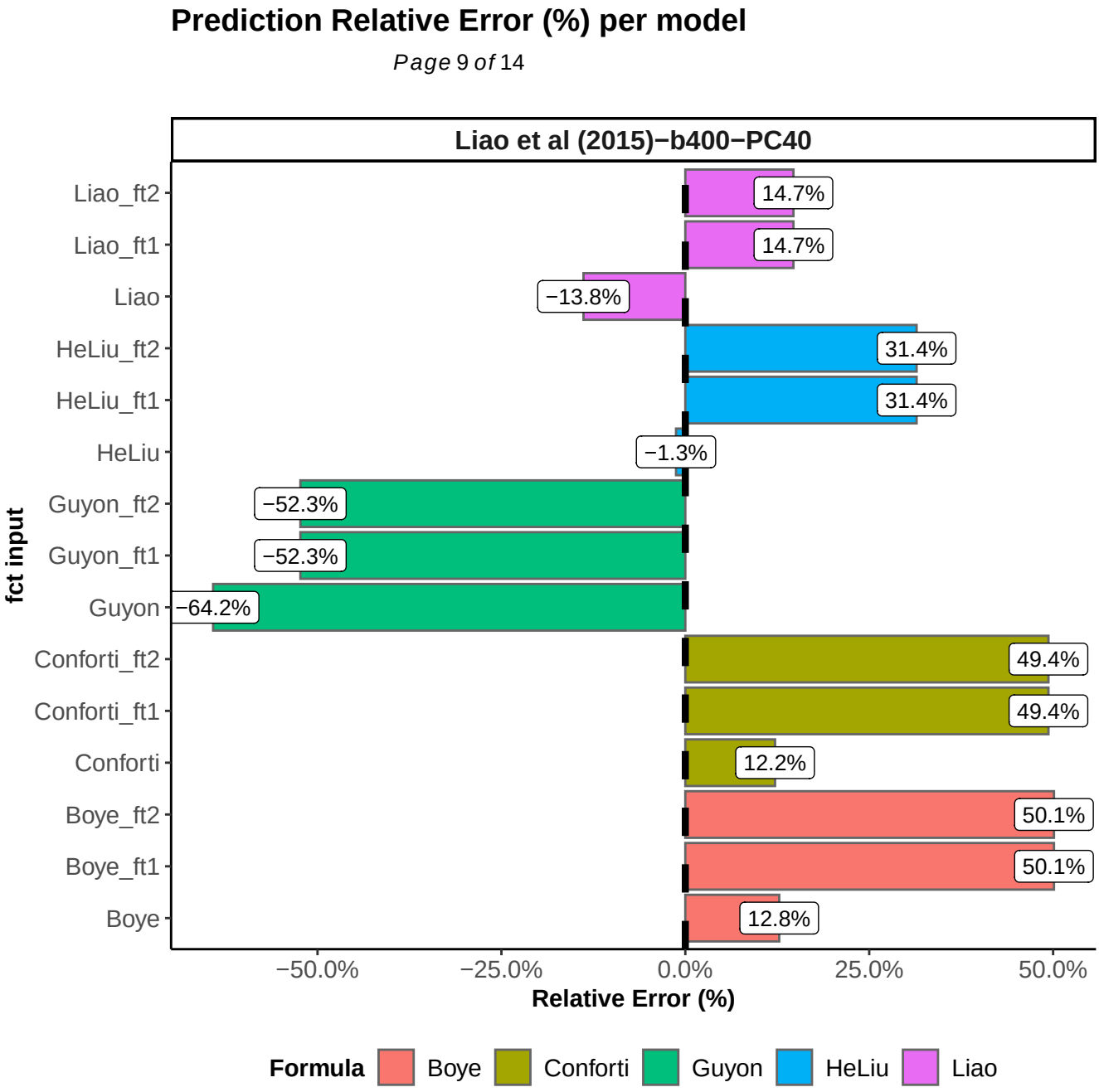
Prediction Relative Error (%) per model
Page 9 of 14
Liao et al (2015)−b400−PC40
fct input
Liao_ft2
Liao_ft1
Liao
HeLiu_ft2
HeLiu_ft1
HeLiu
Guyon_ft2
Guyon_ft1
Guyon
Conforti_ft2
Conforti_ft1
Conforti
Boye_ft2
Boye_ft1
Boye
14.7%
14.7%
−13.8%
31.4%
31.4%
−1.3%
−52.3%
−52.3%
−64.2%
49.4%
49.4%
12.2%
50.1%
50.1%
12.8%
−50.0%
−25.0%
0.0%
25.0%
50.0%
Relative Error (%)
Formula
Boye
Conforti
Guyon
HeLiu
Liao

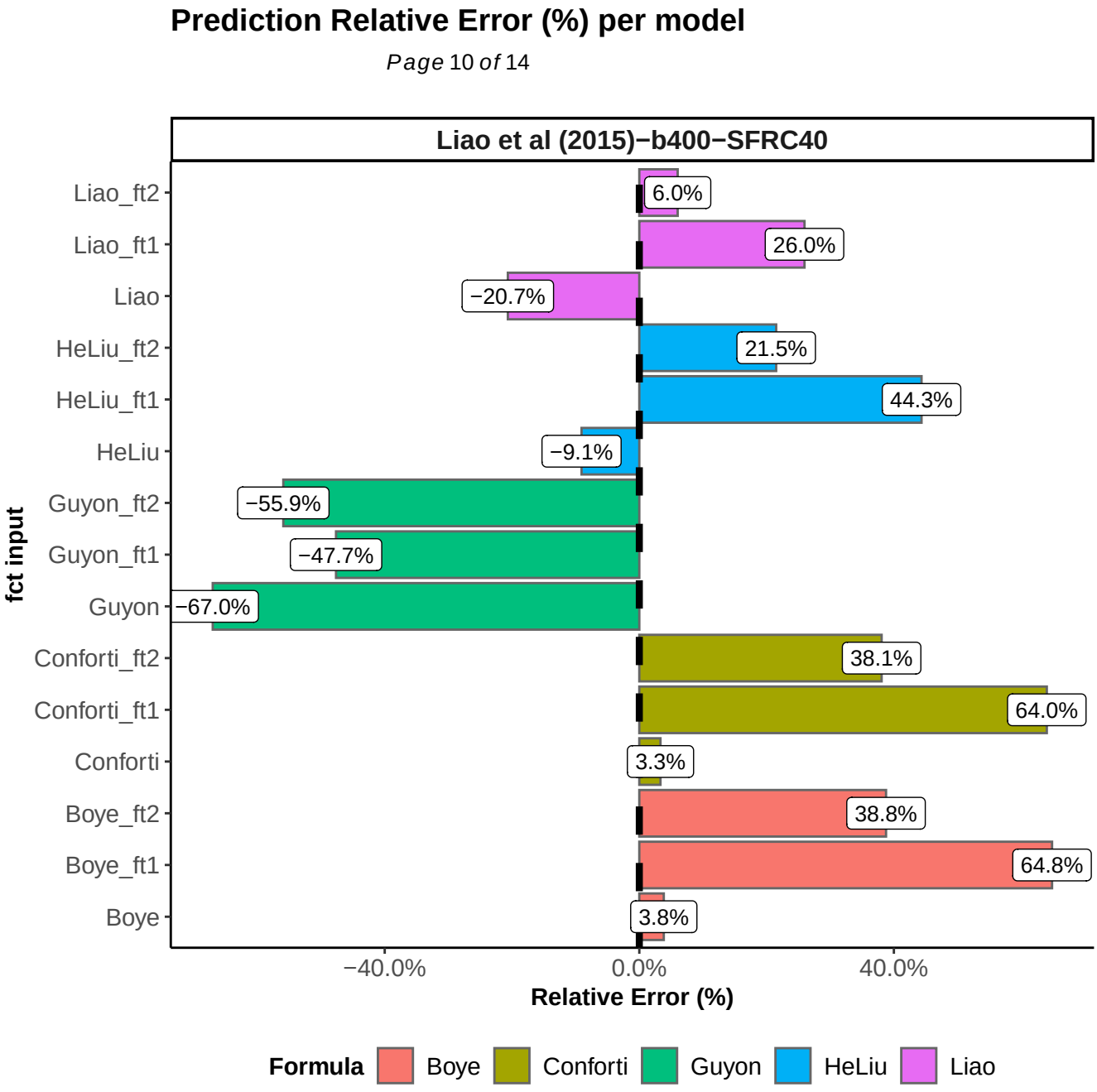
Prediction Relative Error (%) per model
Page 10 of 14
Liao et al (2015)−b400−SFRC40
fct input
Liao_ft2
Liao_ft1
Liao
HeLiu_ft2
HeLiu_ft1
HeLiu
Guyon_ft2
Guyon_ft1
Guyon
Conforti_ft2
Conforti_ft1
Conforti
Boye_ft2
Boye_ft1
Boye
6.0%
26.0%
−20.7%
21.5%
44.3%
−9.1%
−55.9%
−47.7%
−67.0%
38.1%
64.0%
3.3%
38.8%
64.8%
3.8%
−40.0%
0.0%
40.0%
Relative Error (%)
Formula
Boye
Conforti
Guyon
HeLiu
Liao

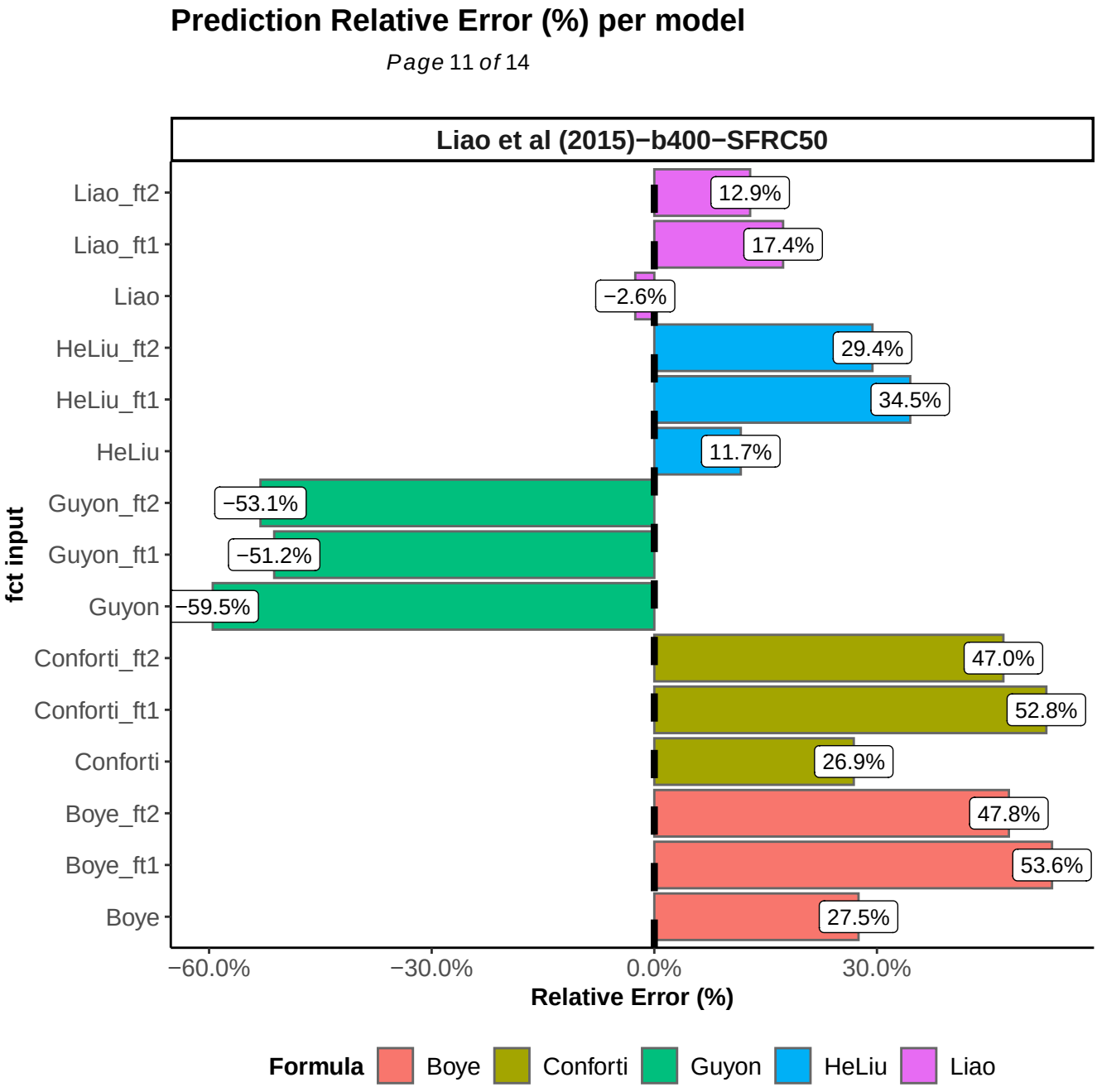
Prediction Relative Error (%) per model
Page 11 of 14
Liao et al (2015)−b400−SFRC50
Liao_ft2
Liao_ft1
Liao
HeLiu_ft2
HeLiu_ft1
HeLiu
Guyon_ft2
Guyon_ft1
Guyon
Conforti_ft2
Conforti_ft1
Conforti
Boye_ft2
Boye_ft1
Boye
12.9%
17.4%
−2.6%
29.4%
34.5%
11.7%
−53.1%
−51.2%
−59.5%
47.0%
52.8%
26.9%
47.8%
53.6%
27.5%
fct input
−60.0%
−30.0%
0.0%
30.0%
Relative Error (%)
Formula
Boye
Conforti
Guyon
HeLiu
Liao

Prediction Relative Error (%) per model

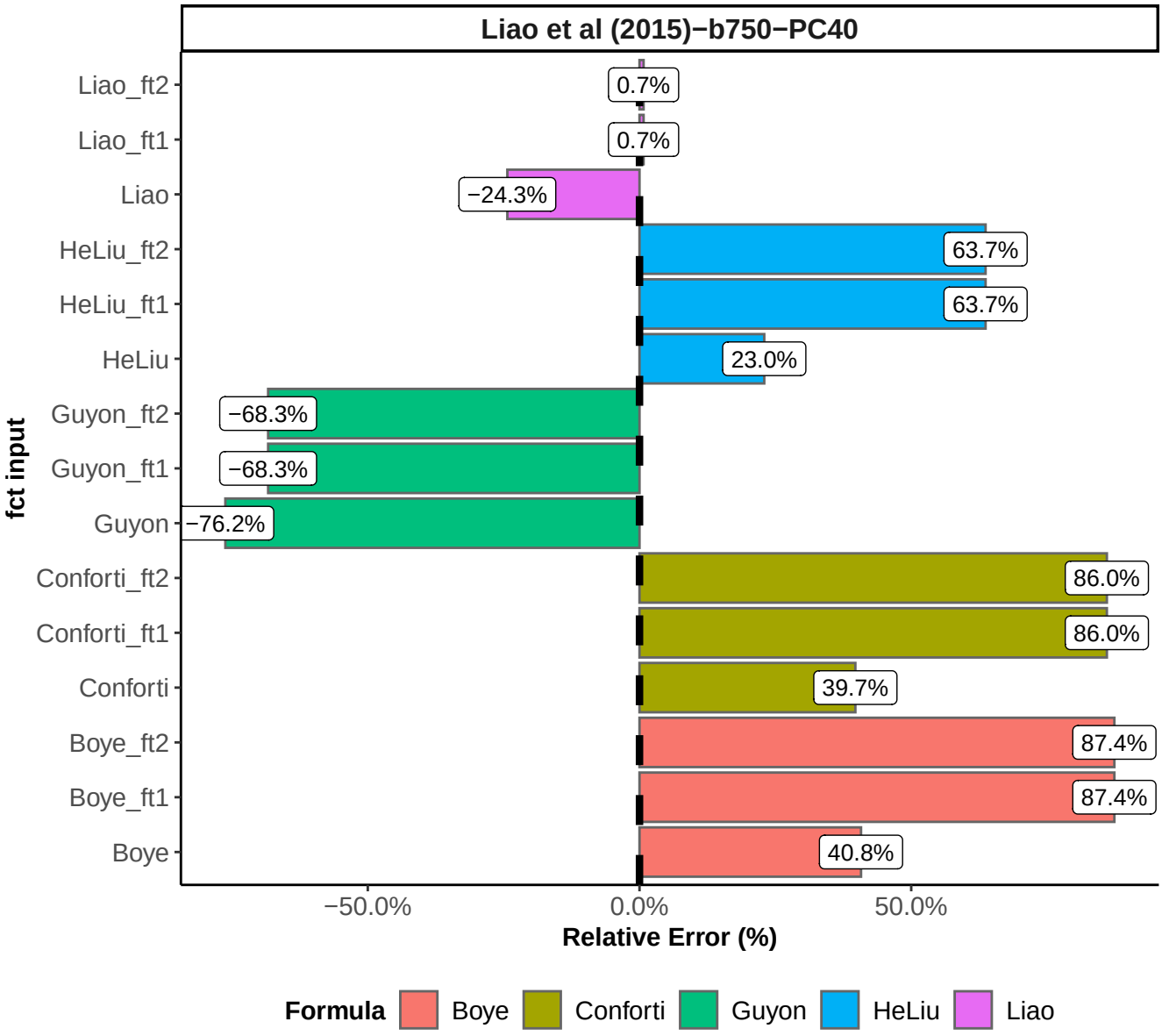

Prediction Relative Error (%) per model

Page 13 *of* 14

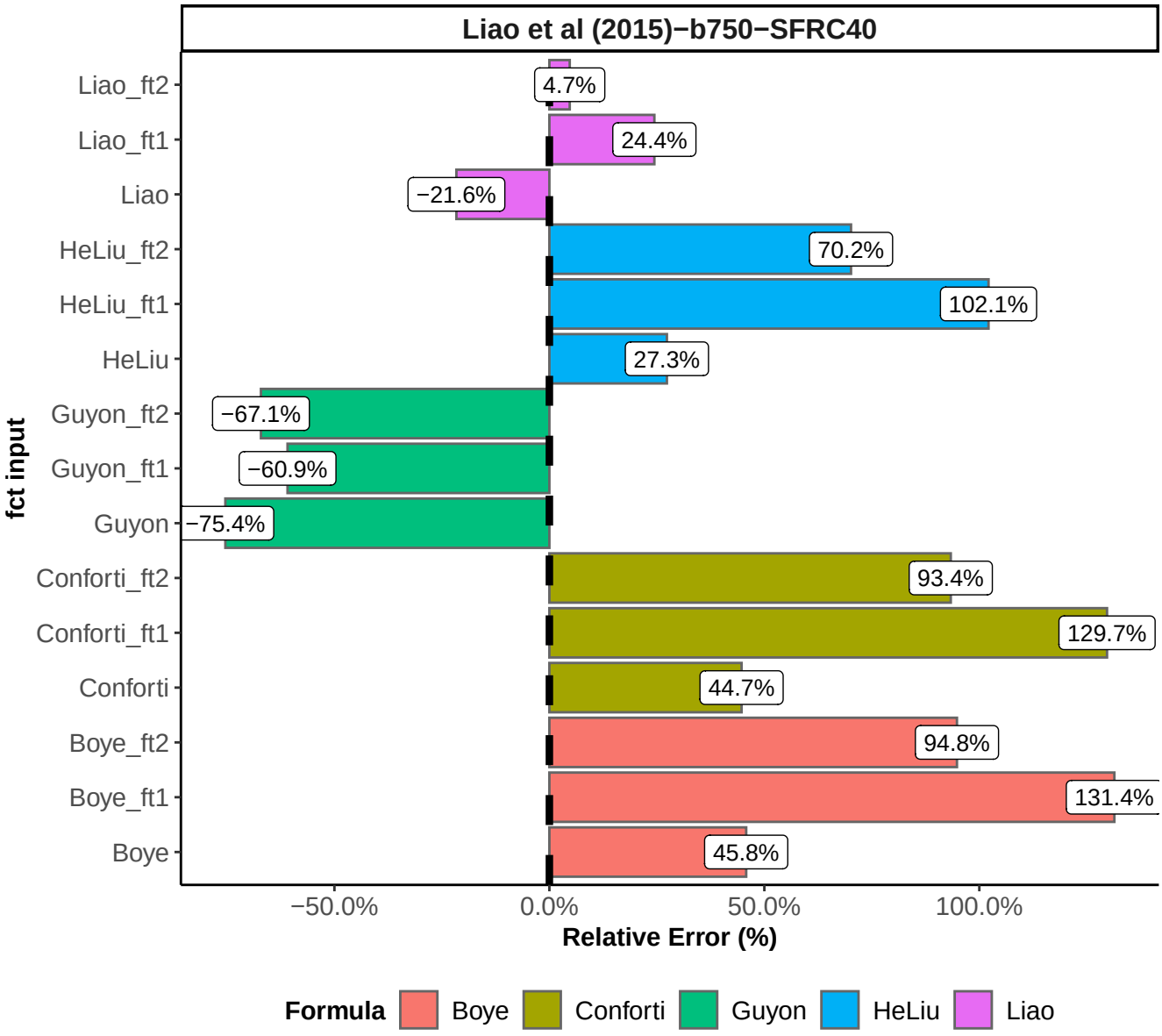

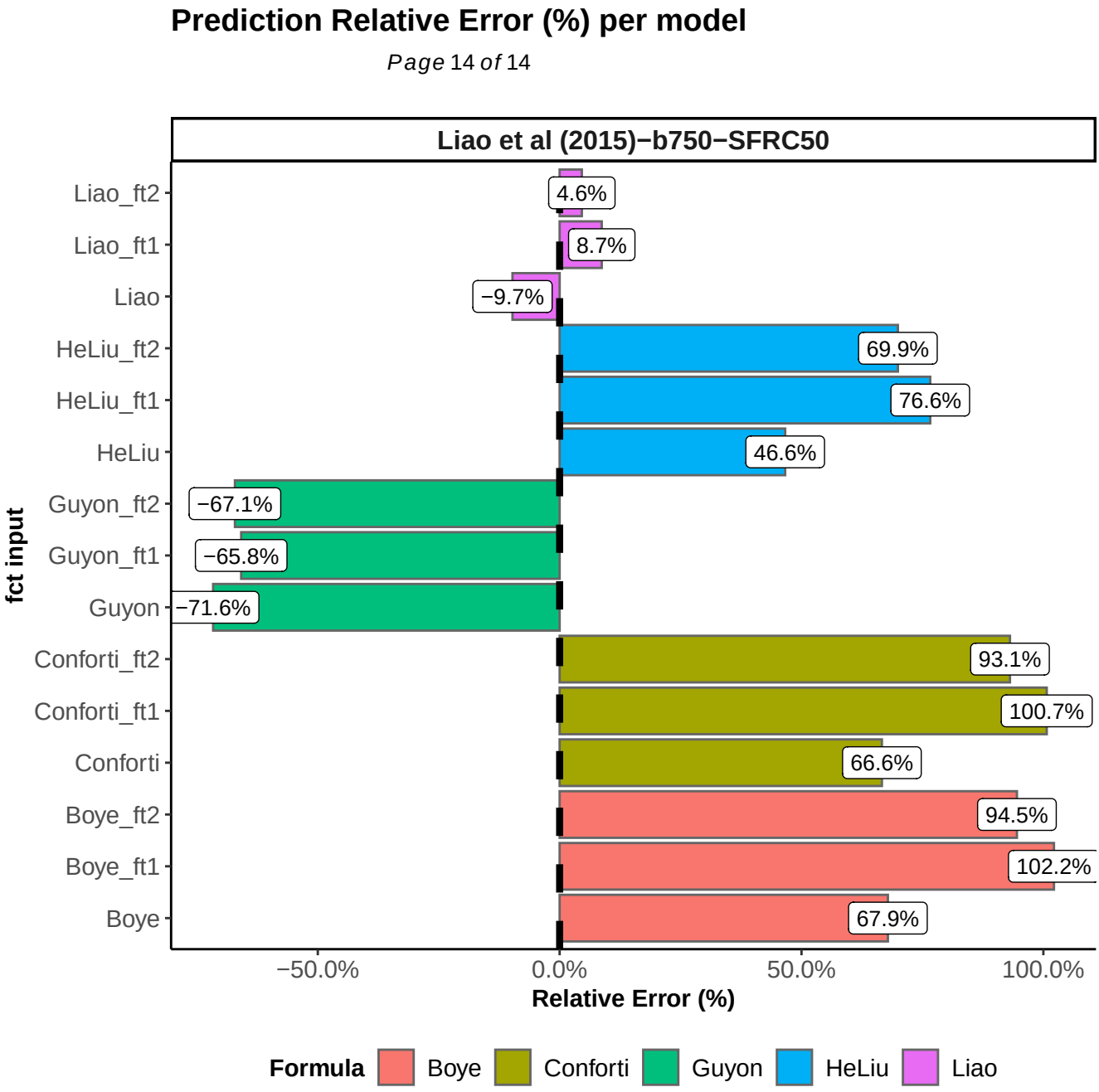
Prediction Relative Error (%) per model
Page 14 of 14
Liao et al (2015)−b750−SFRC50
fct input
Liao_ft2
Liao_ft1
Liao
HeLiu_ft2
HeLiu_ft1
HeLiu
Guyon_ft2
Guyon_ft1
Guyon
Conforti_ft2
Conforti_ft1
Conforti
Boye_ft2
Boye_ft1
Boye
4.6%
8.7%
−9.7%
69.9%
76.6%
46.6%
−67.1%
−65.8%
−71.6%
93.1%
100.7%
66.6%
94.5%
102.2%
67.9%
−50.0%
0.0%
50.0%
100.0%
Relative Error (%)
Formula
Boye
Conforti
Guyon
HeLiu
Liao

APPENDIX A.4

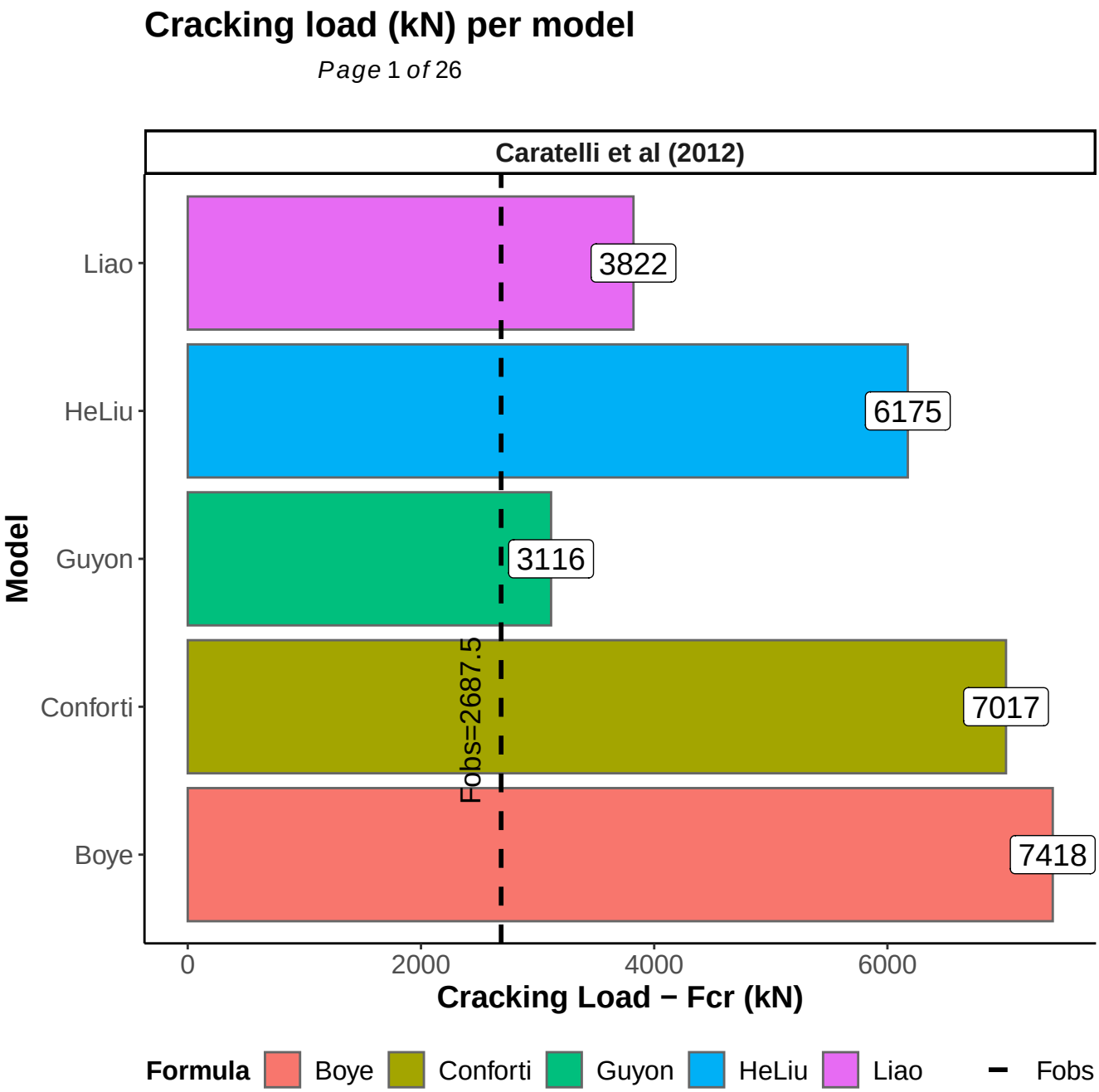
Cracking load (kN) per model
Page 1 of 26
Caratelli et al (2012)
Liao
HeLiu
Guyon
Conforti
Boye
Model
3822
6175
3116
7017
7418
Fobs=2687.5
0
2000
4000
6000
Cracking Load − Fcr (kN)
Formula
Boye
Conforti
Guyon
HeLiu
Liao
Fobs

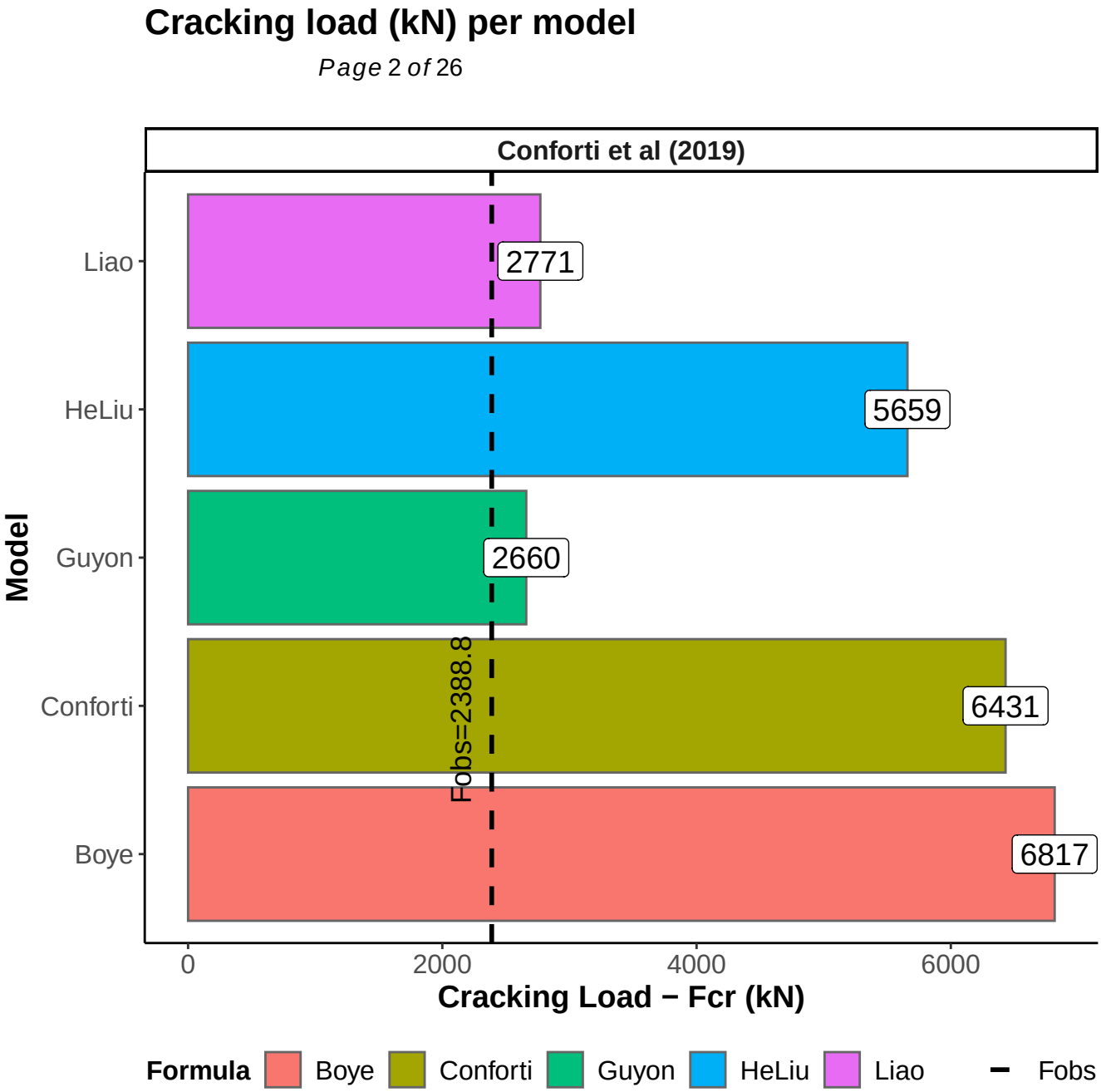
Cracking load (kN) per model
Page 2 of 26
Conforti et al (2019)
Liao
HeLiu
Guyon
Conforti
Boye
Model
2771
5659
2660
6431
6817
Fobs=2388.8
0
2000
4000
6000
Cracking Load − Fcr (kN)
Formula
Boye
Conforti
Guyon
HeLiu
Liao
Fobs

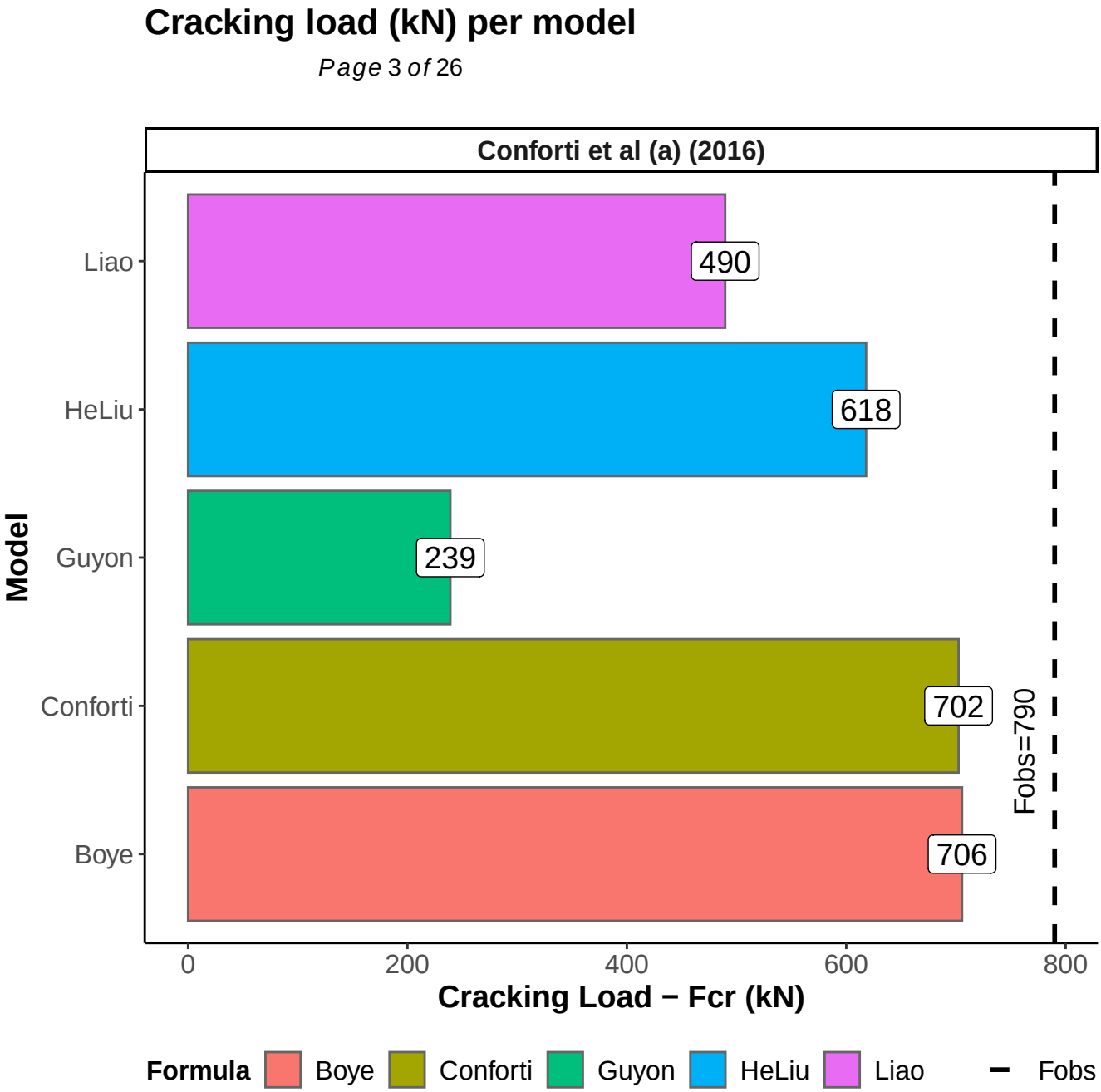
Cracking load (kN) per model
Page 3 of 26
Conforti et al (a) (2016)
Liao
HeLiu
Guyon
Conforti
Boye
490
618
239
702
706
Fobs=790
Model
0
200
400
600
800
Cracking Load − Fcr (kN)
Formula
Boye
Conforti
Guyon
HeLiu
Liao
Fobs

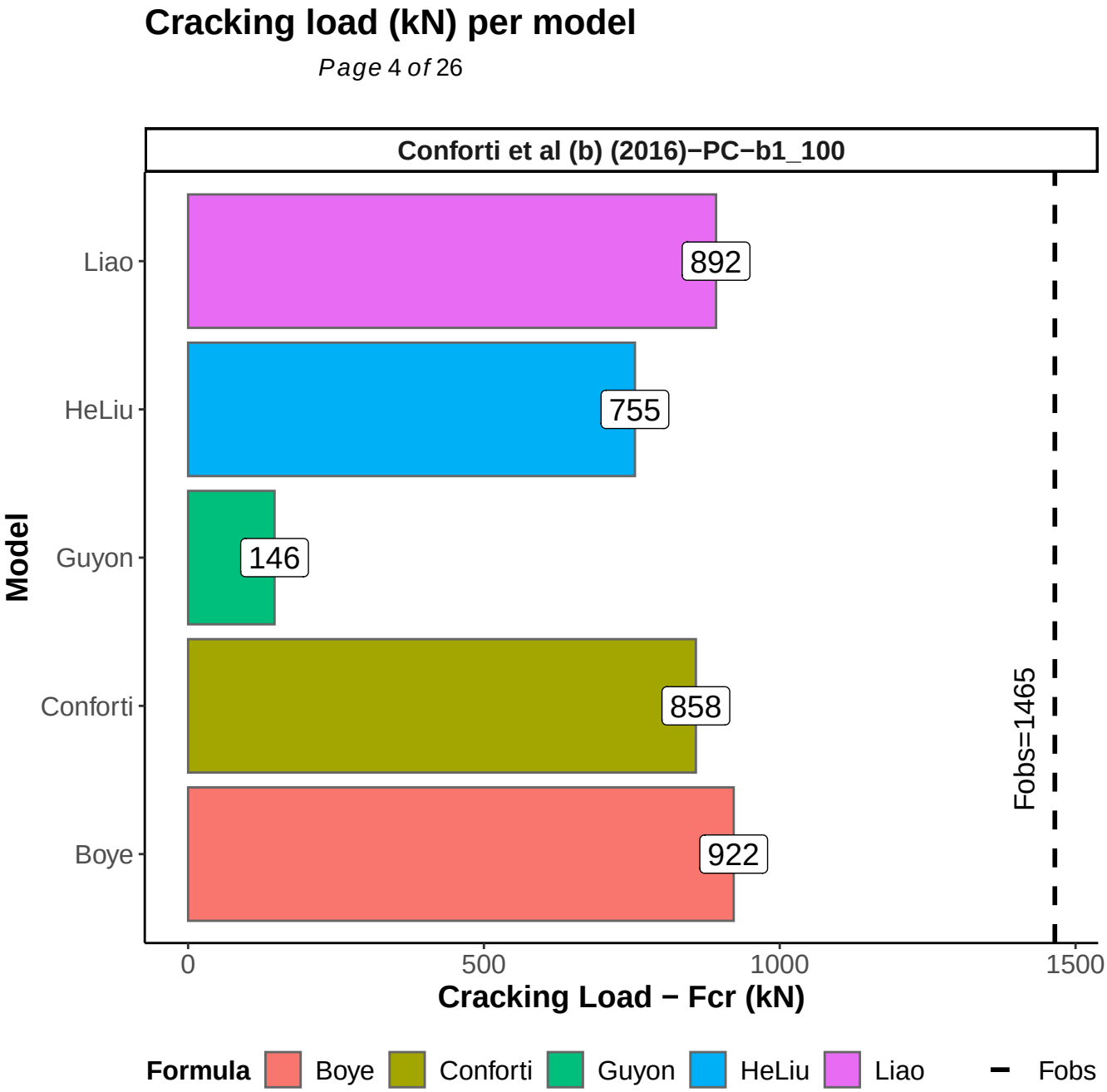
Cracking load (kN) per model
Page 4 of 26
Conforti et al (b) (2016)−PC−b1_100
Liao
HeLiu
Guyon
Conforti
Boye
892
755
146
858
922
Fobs=1465
Model
0
500
1000
1500
Cracking Load − Fcr (kN)
Formula
Boye
Conforti
Guyon
HeLiu
Liao
Fobs

Cracking load (kN) per model

Page 5 *of* 26

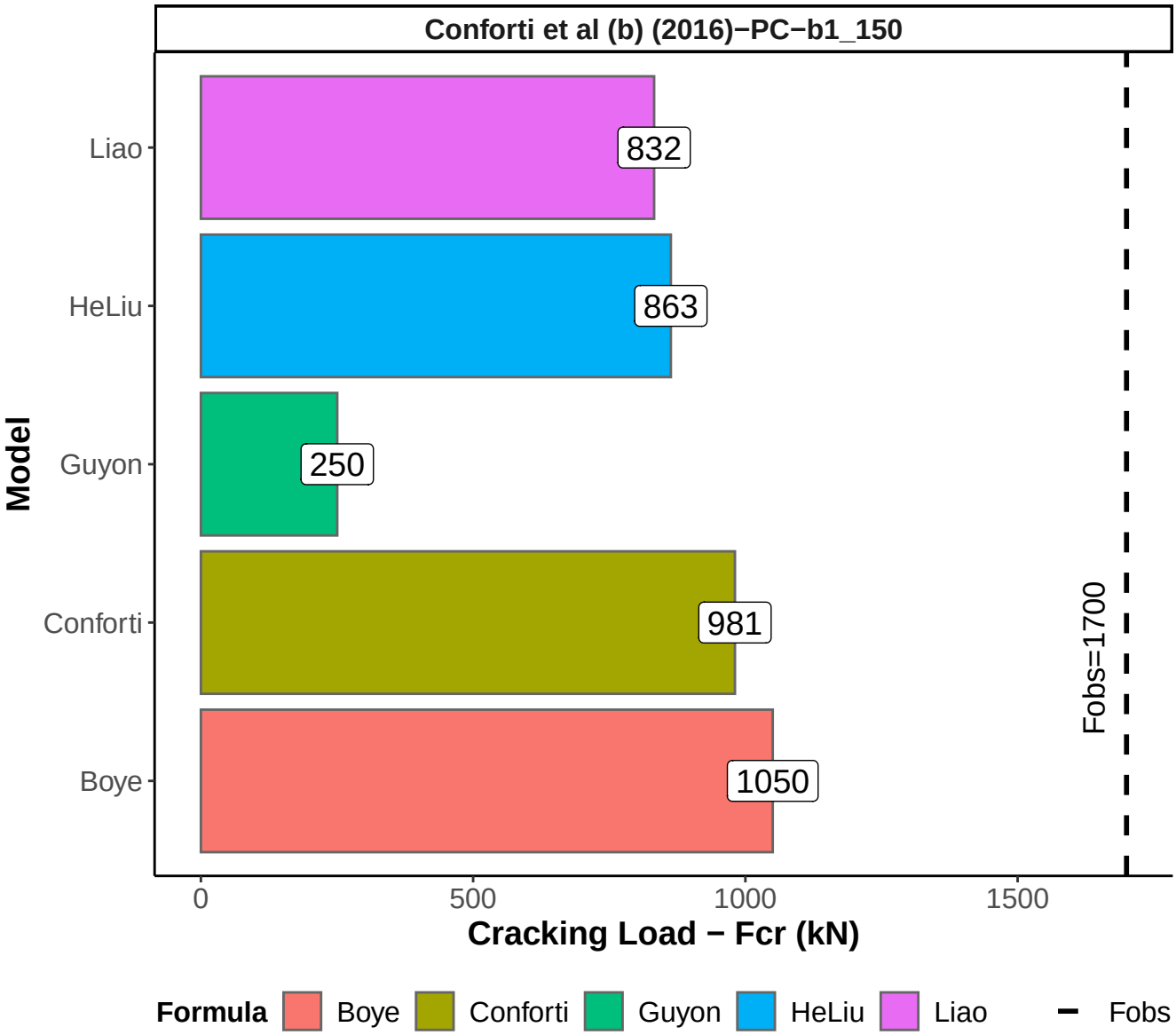

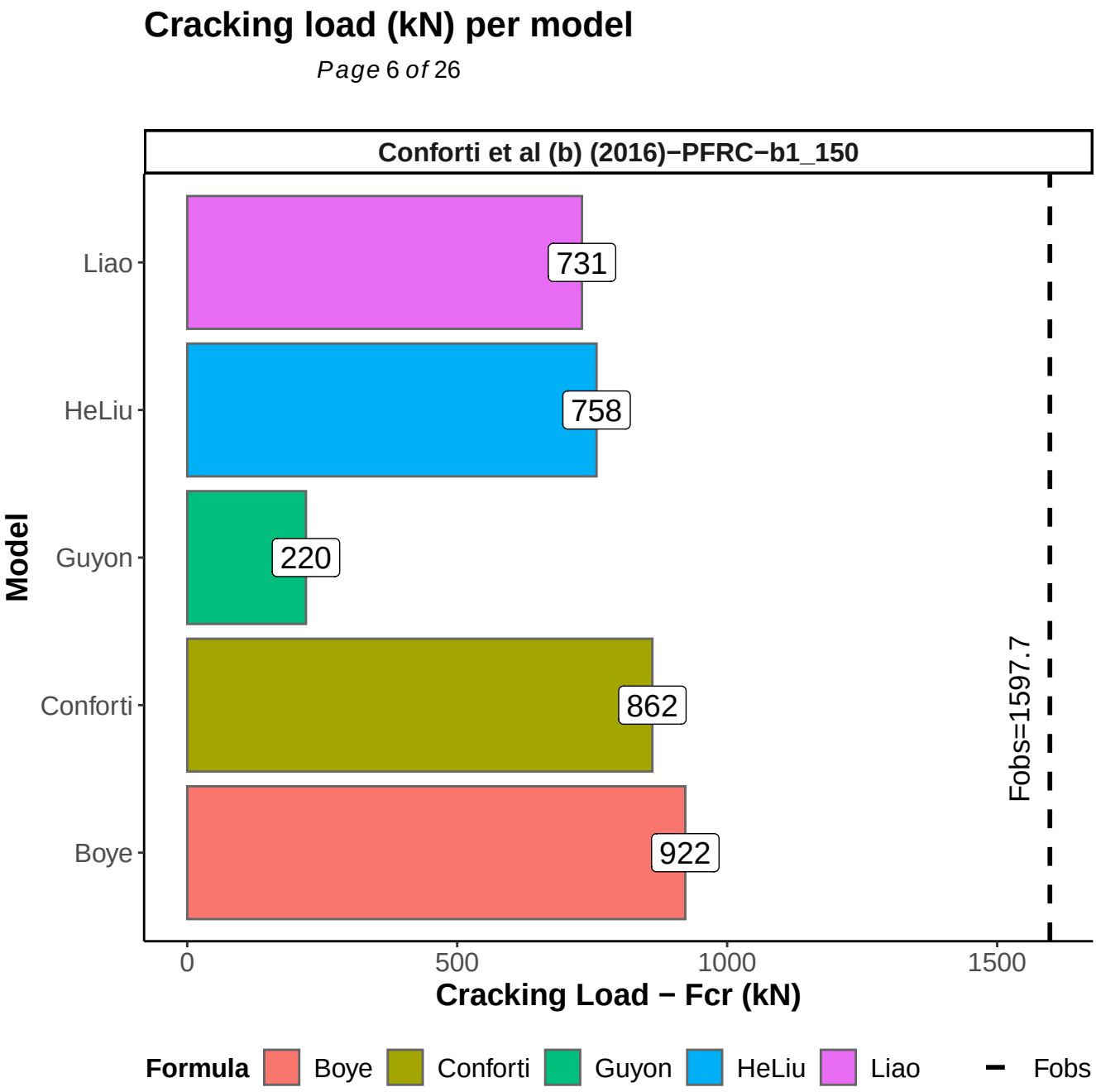
Cracking load (kN) per model
Page 6 of 26
Conforti et al (b) (2016)−PFRC−b1_150
Liao
HeLiu
Guyon
Conforti
Boye
731
758
220
862
922
Fobs=1597.7
Model
0
500
1000
1500
Cracking Load − Fcr (kN)
Formula
Boye
Conforti
Guyon
HeLiu
Liao
Fobs

Cracking load (kN) per model

Page 7 of 26

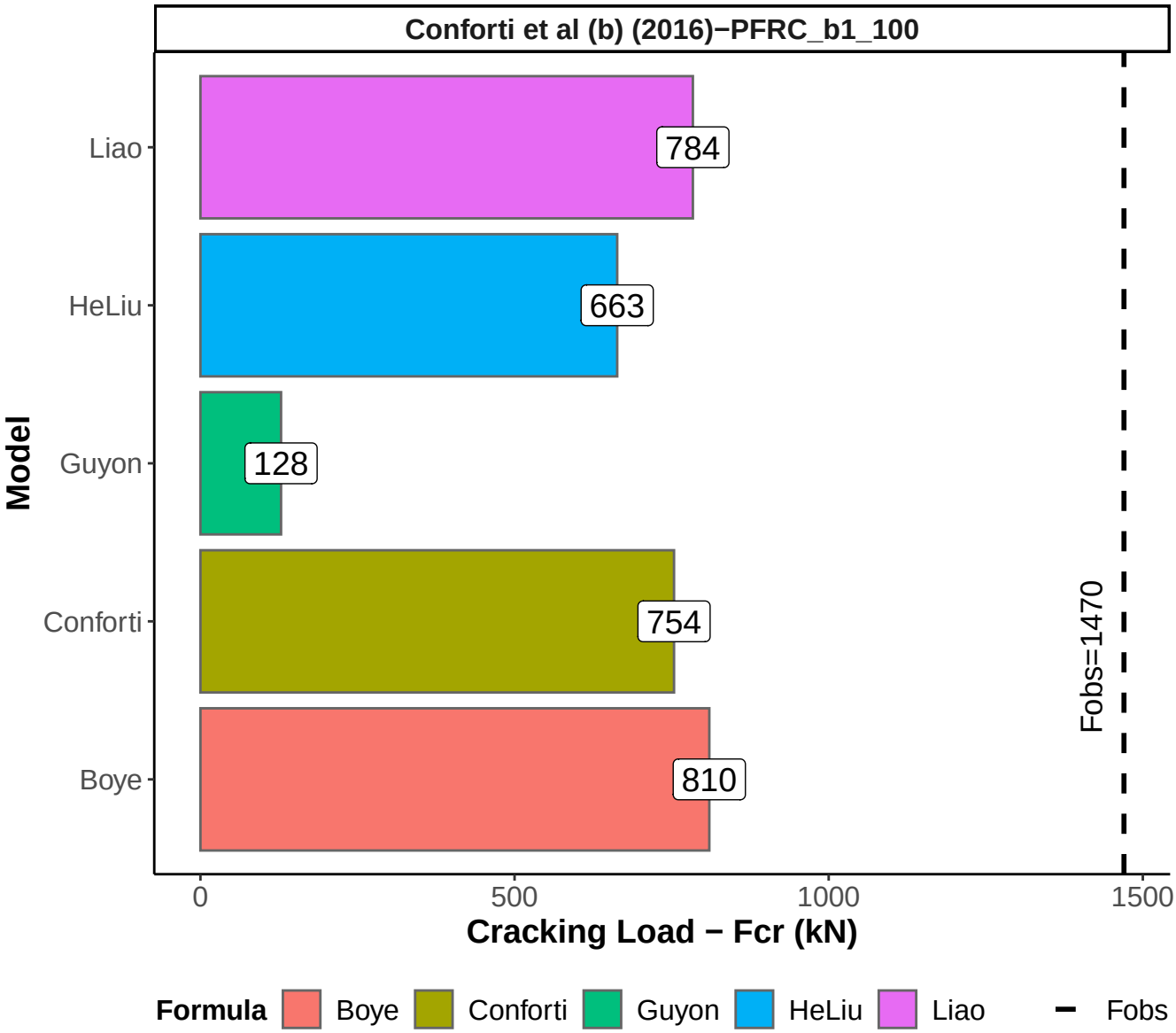

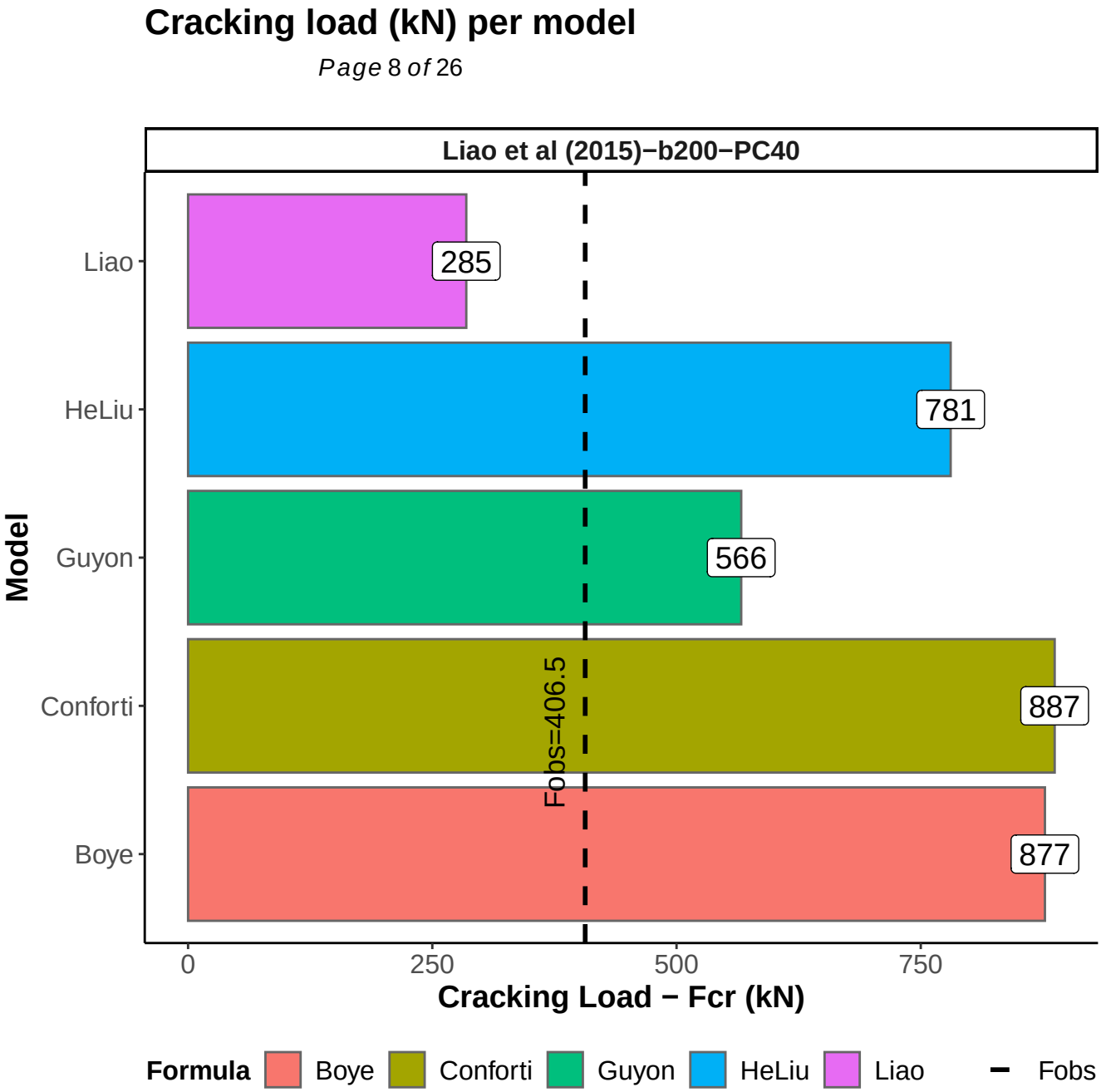
Cracking load (kN) per model
Page 8 of 26
Liao et al (2015)−b200−PC40
Liao
HeLiu
Guyon
Conforti
Boye
285
781
566
887
877
Fobs=406.5
Model
0
250
500
750
Cracking Load − Fcr (kN)
Formula
Boye
Conforti
Guyon
HeLiu
Liao
Fobs

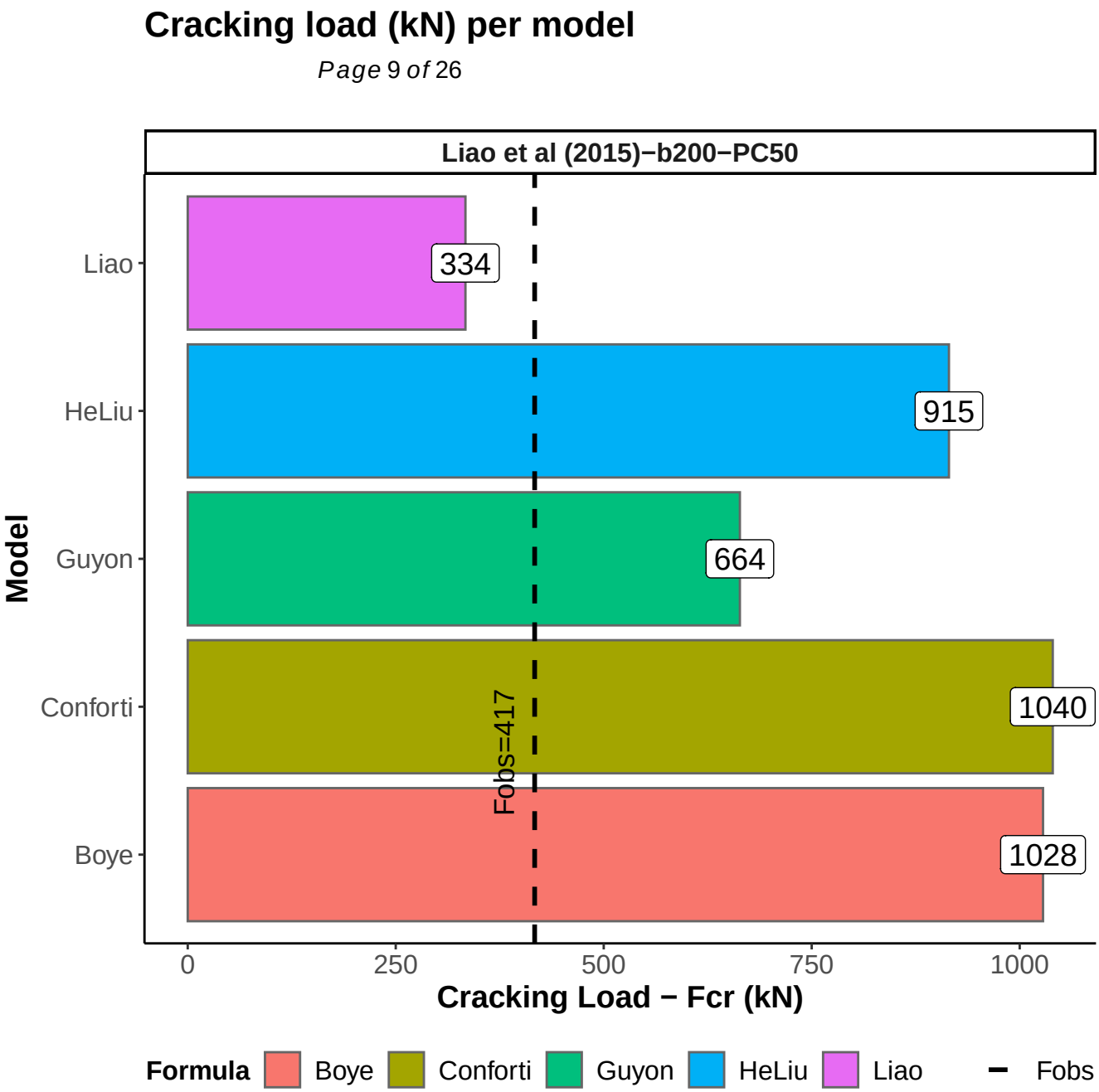
Cracking load (kN) per model
Page 9 of 26
Liao et al (2015)−b200−PC50
Liao
HeLiu
Guyon
Conforti
Boye
Model
334
915
664
1040
1028
Fobs=417
0
250
500
750
1000
Cracking Load − Fcr (kN)
Formula
Boye
Conforti
Guyon
HeLiu
Liao
Fobs

Cracking load (kN) per model

Page 10 *of* 26

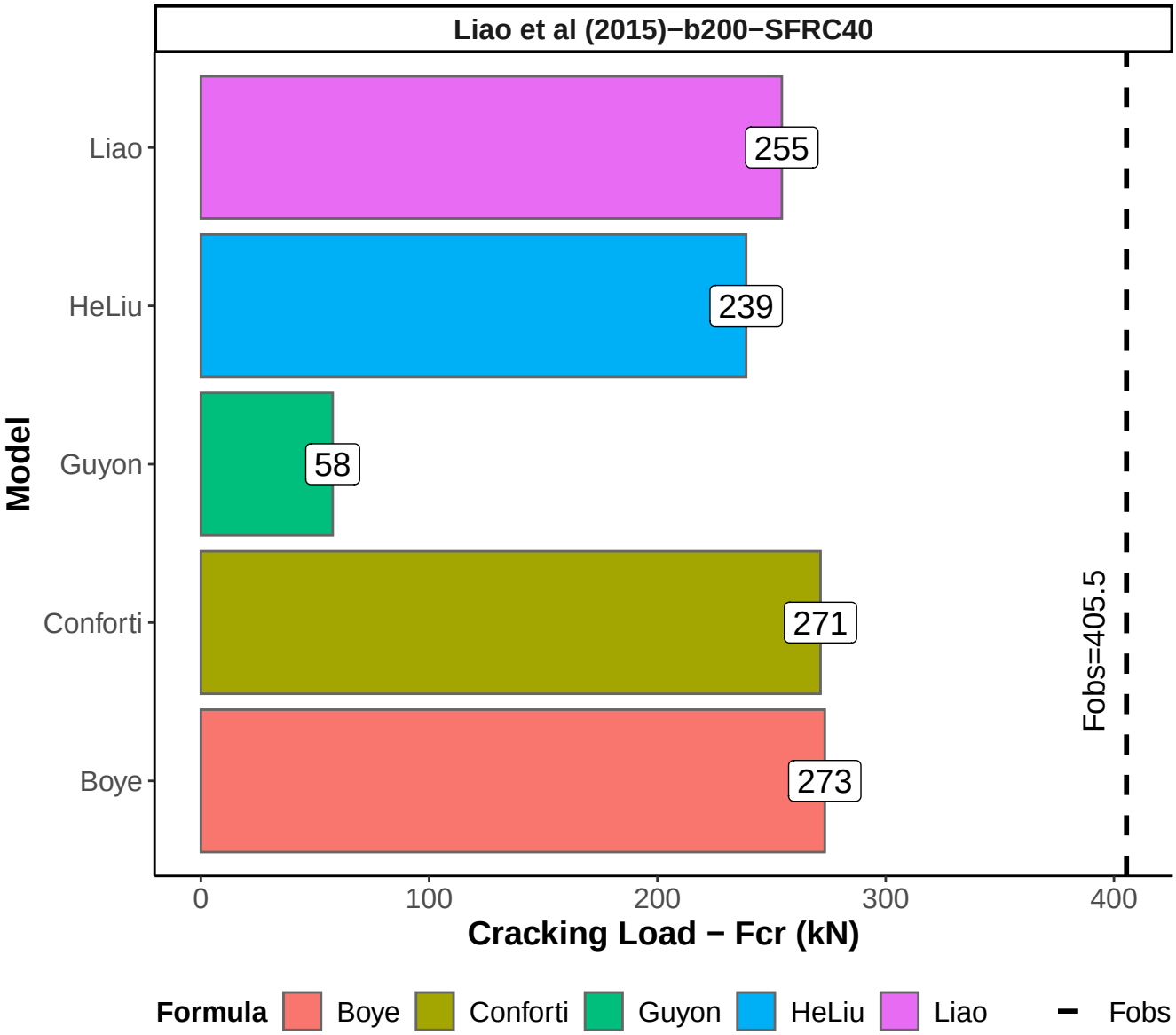

Cracking load (kN) per model

Page 11 *of* 26

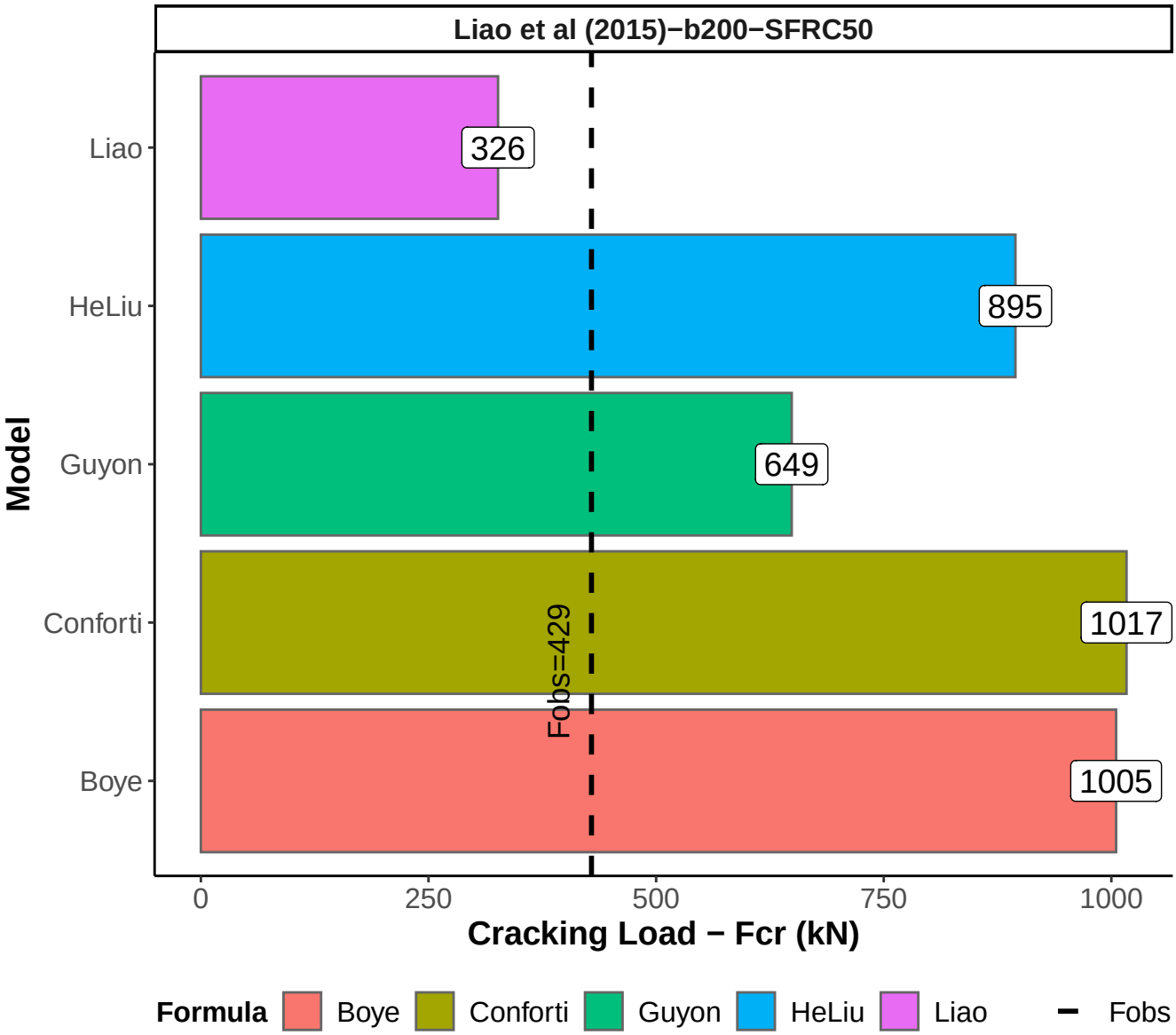

Cracking load (kN) per model

Page 12 *of* 26

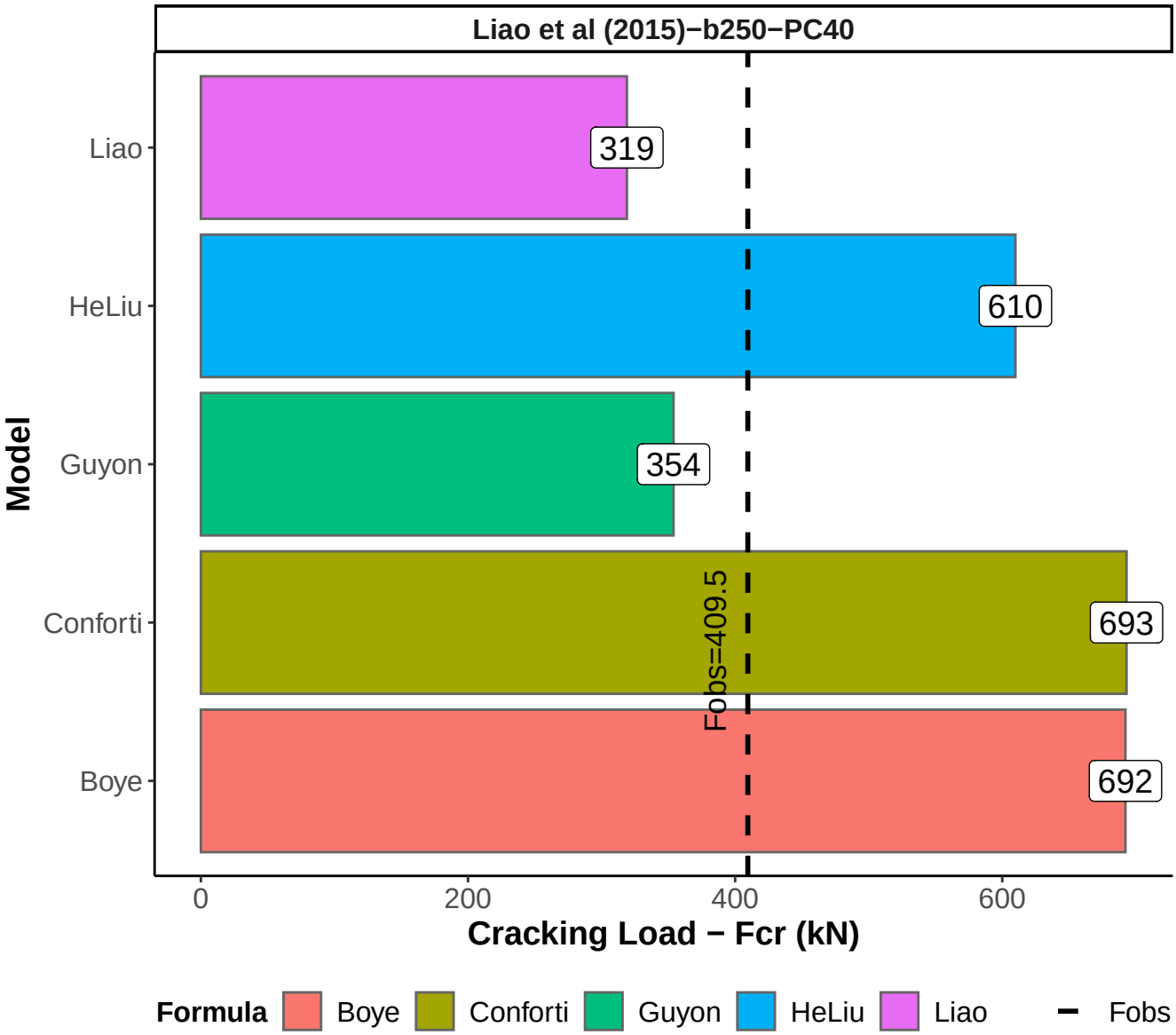

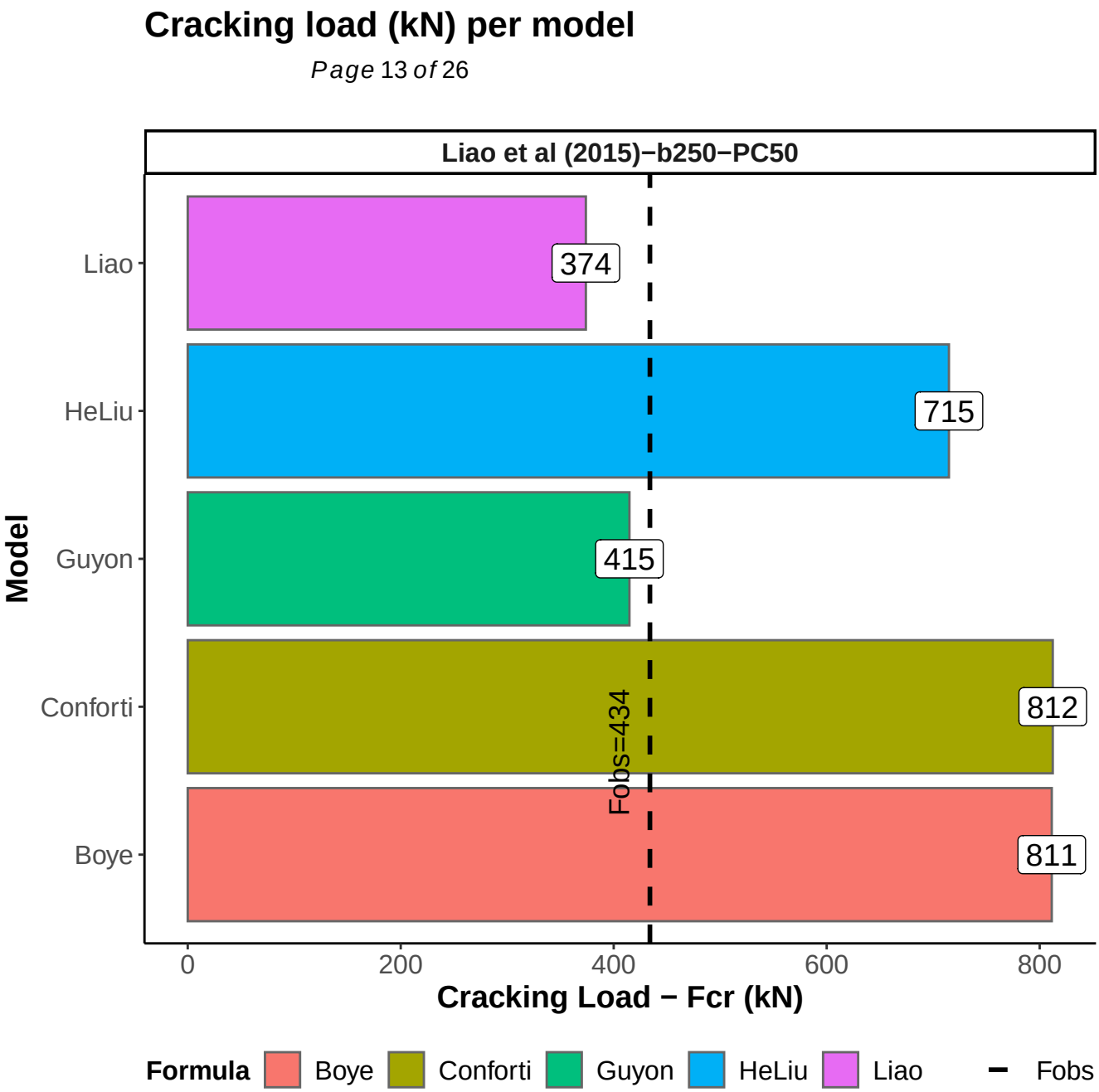
Cracking load (kN) per model
Page 13 of 26
Liao et al (2015)−b250−PC50
Liao
HeLiu
Guyon
Conforti
Boye
Model
374
715
415
812
811
Fobs=434
0
200
400
600
800
Cracking Load − Fcr (kN)
Formula
Boye
Conforti
Guyon
HeLiu
Liao
Fobs

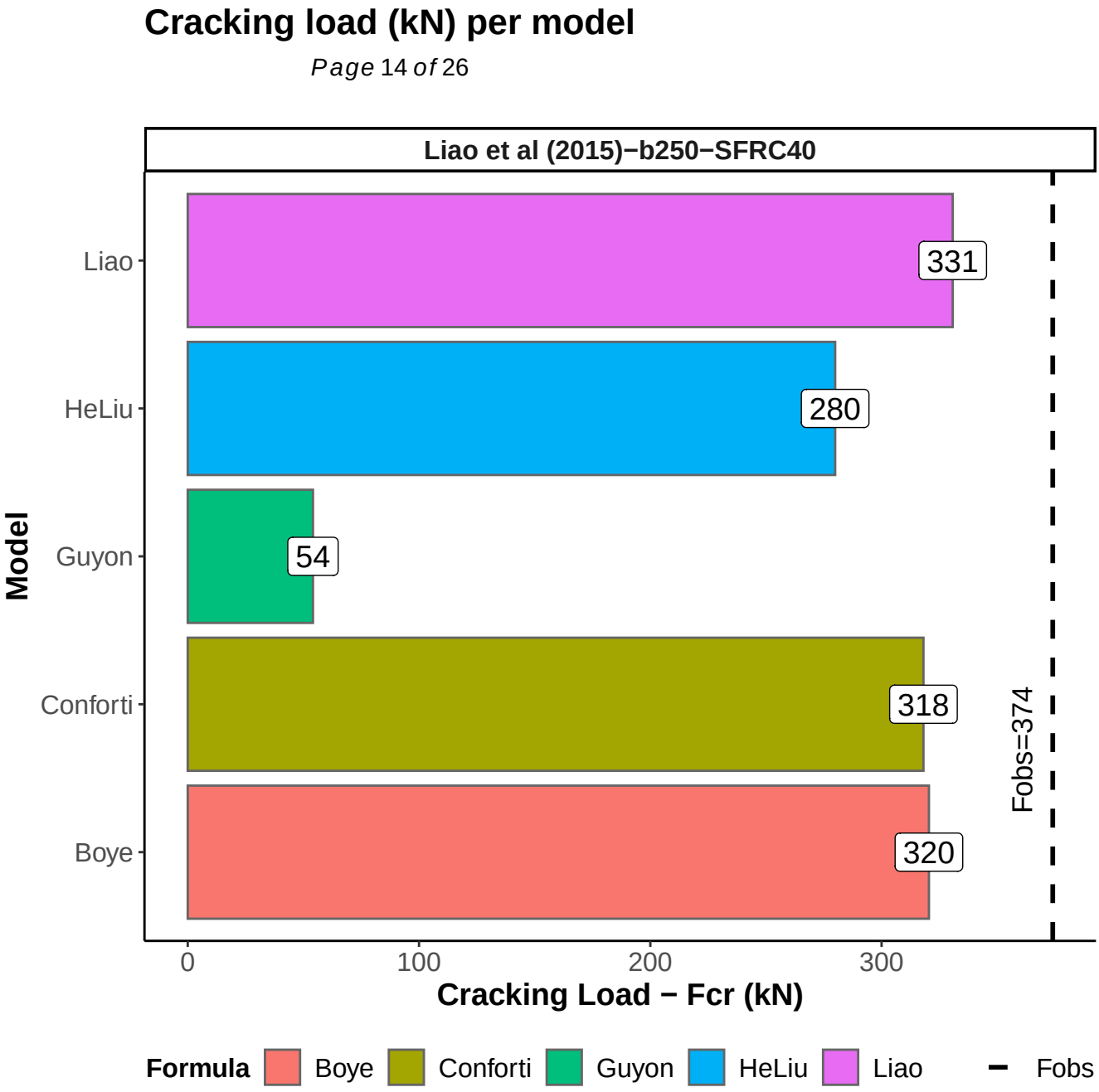
Cracking load (kN) per model
Page 14 of 26
Liao et al (2015)−b250−SFRC40
Liao
HeLiu
Guyon
Conforti
Boye
331
280
54
318
320
Fobs=374
Model
0
100
200
300
Cracking Load − Fcr (kN)
Formula
Boye
Conforti
Guyon
HeLiu
Liao
Fobs

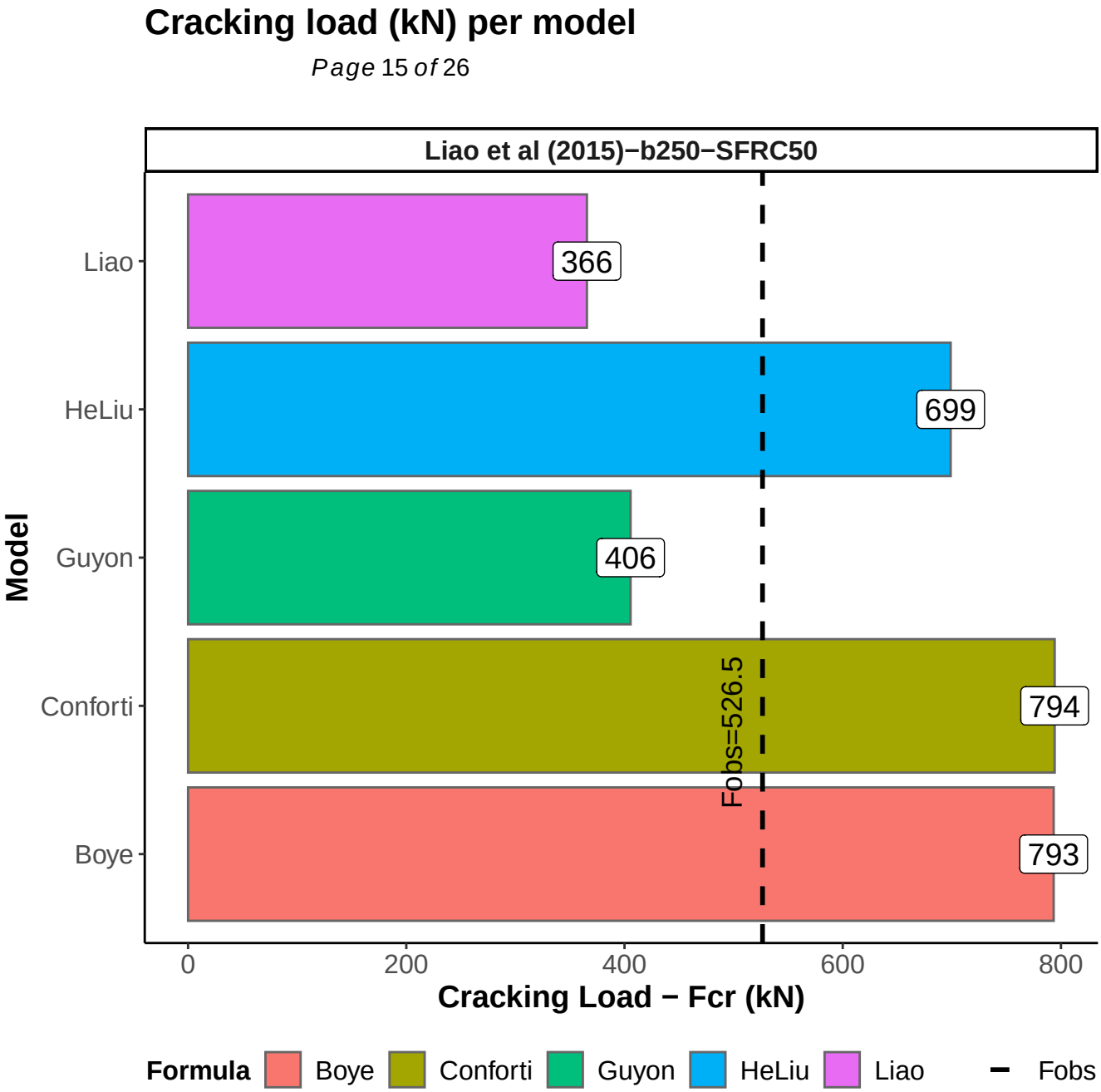
Cracking load (kN) per model
Page 15 of 26
Liao et al (2015)−b250−SFRC50
Liao
HeLiu
Guyon
Conforti
Boye
366
699
406
794
793
Fobs=526.5
Model
0
200
400
600
800
Cracking Load − Fcr (kN)
Formula
Boye
Conforti
Guyon
HeLiu
Liao
Fobs

Cracking load (kN) per model

Page 16 *of* 26

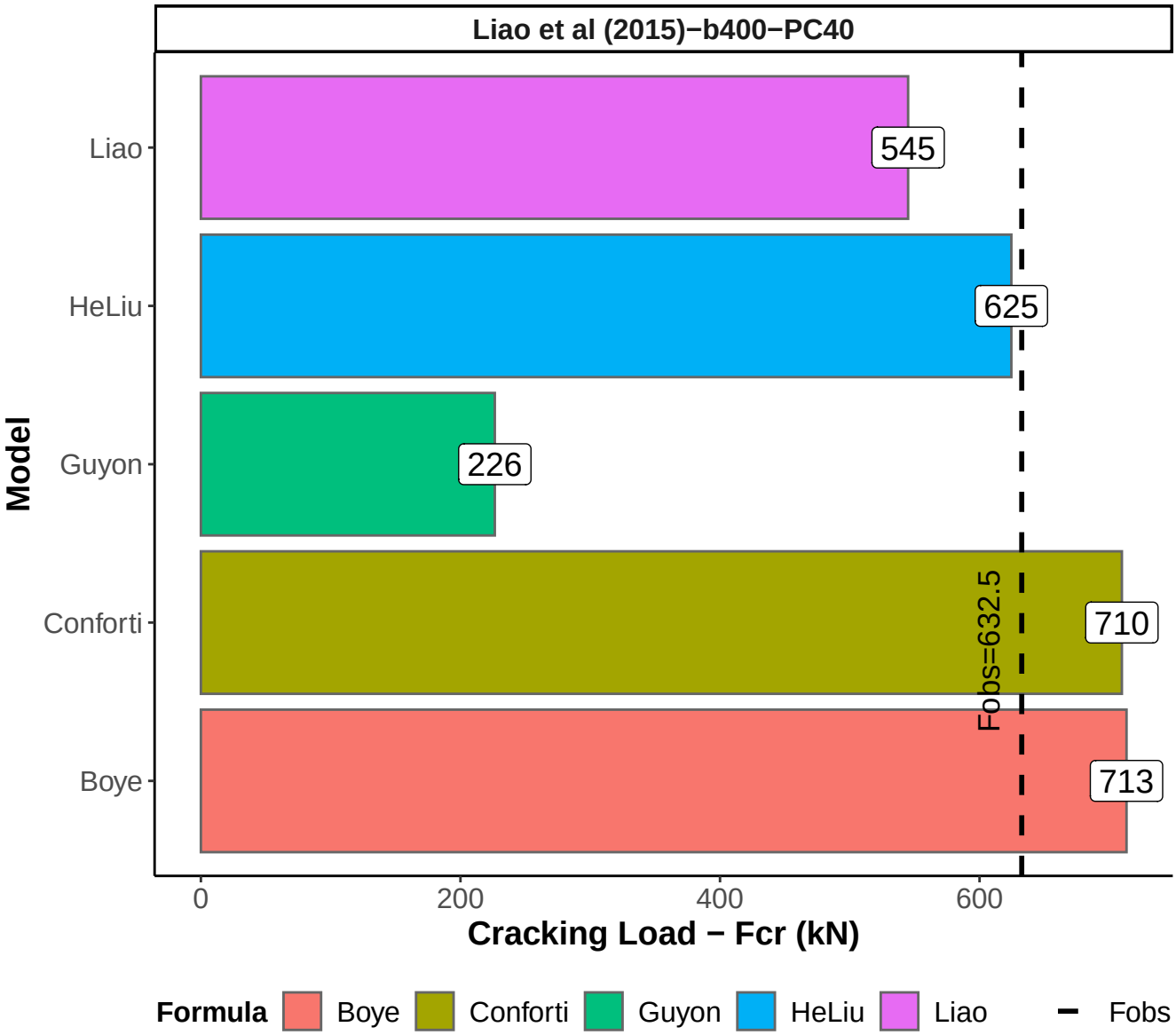

Cracking load (kN) per model

Page 17 *of* 26

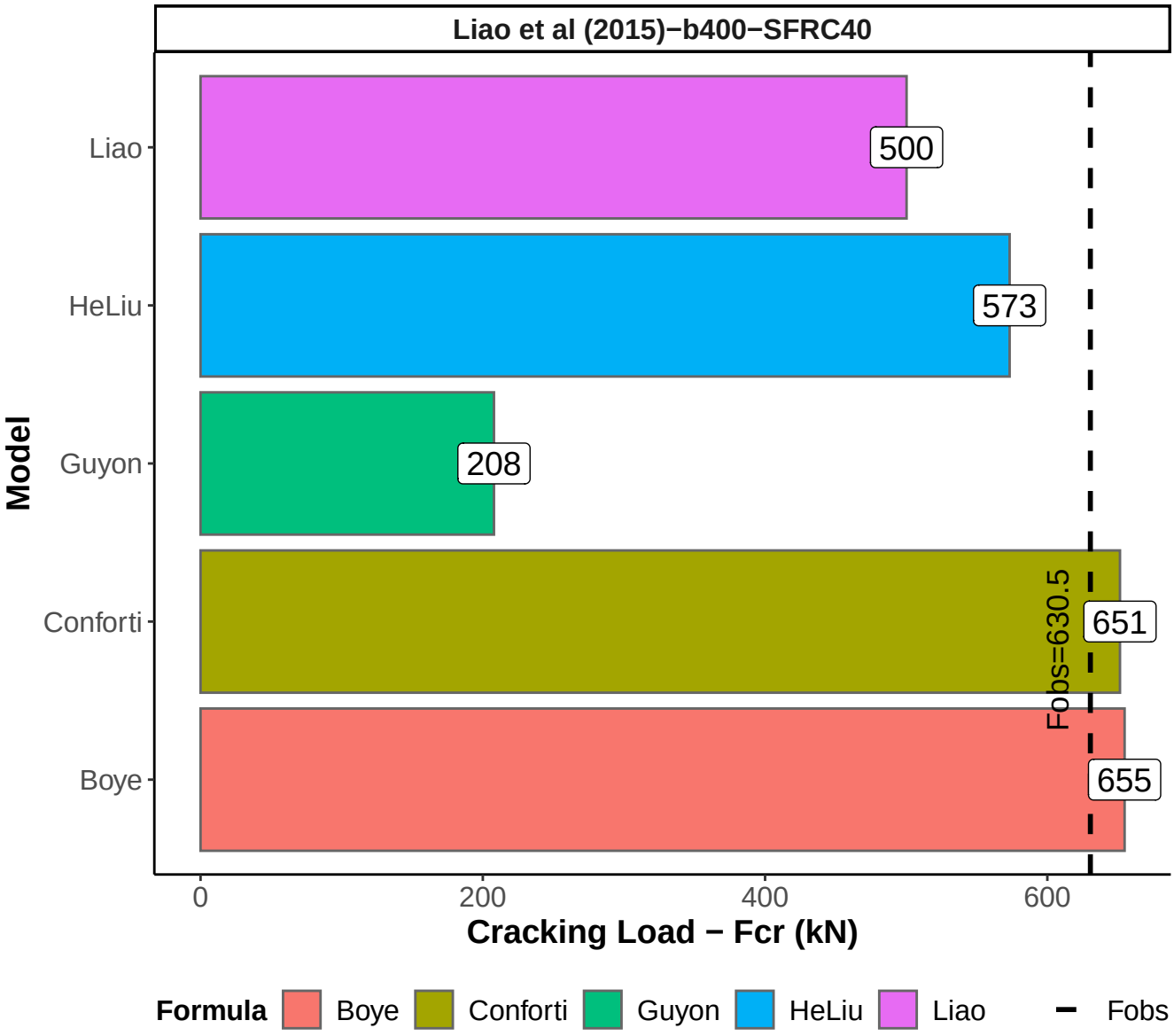

Cracking load (kN) per model

Page 18 *of* 26

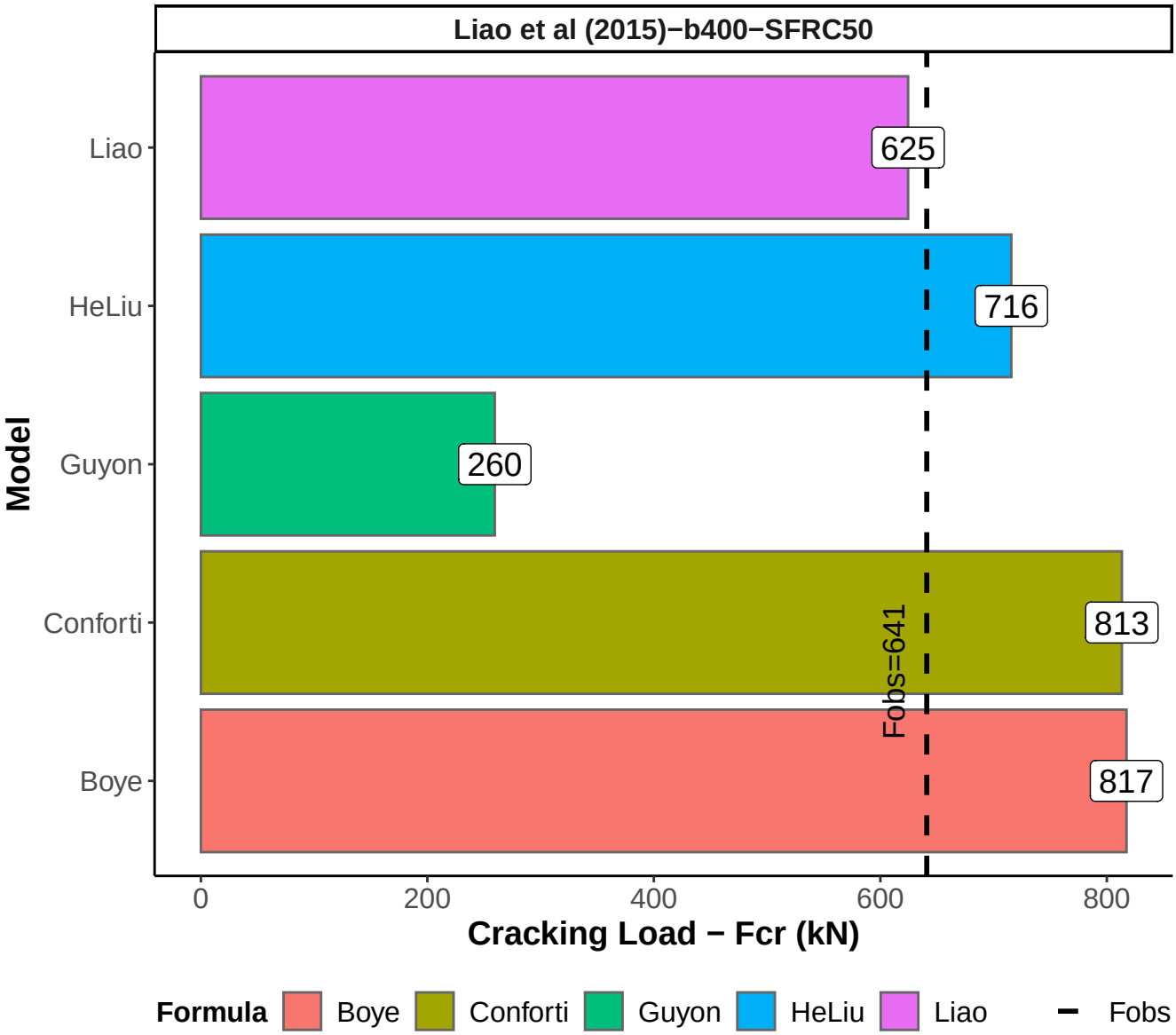

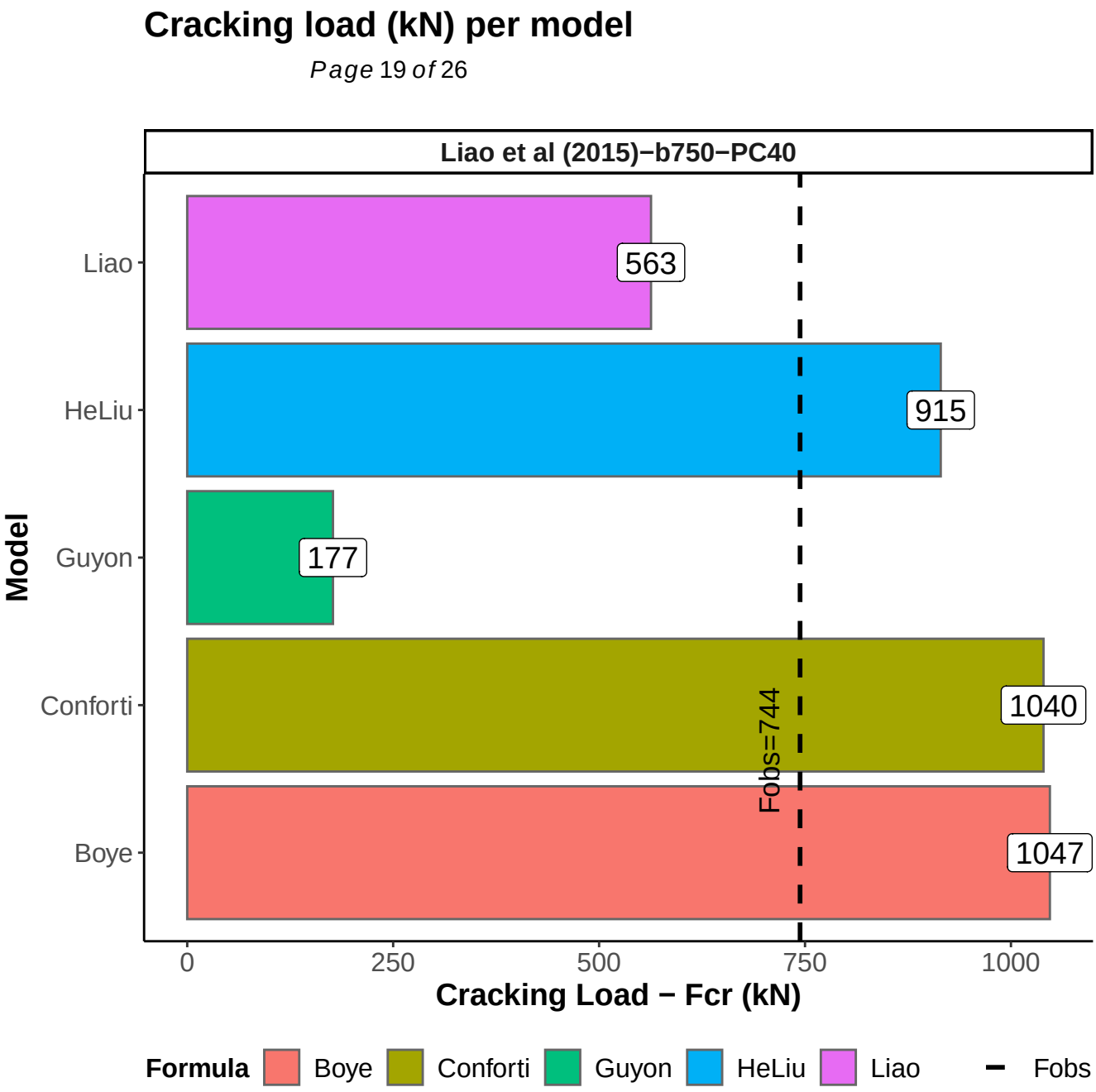
Cracking load (kN) per model
Page 19 of 26
Liao et al (2015)−b750−PC40
Liao
HeLiu
Guyon
Conforti
Boye
Model
563
915
177
1040
1047
Fobs=744
0
250
500
750
1000
Cracking Load − Fcr (kN)
Formula
Boye
Conforti
Guyon
HeLiu
Liao
Fobs

Cracking load (kN) per model

Page 20 *of* 26

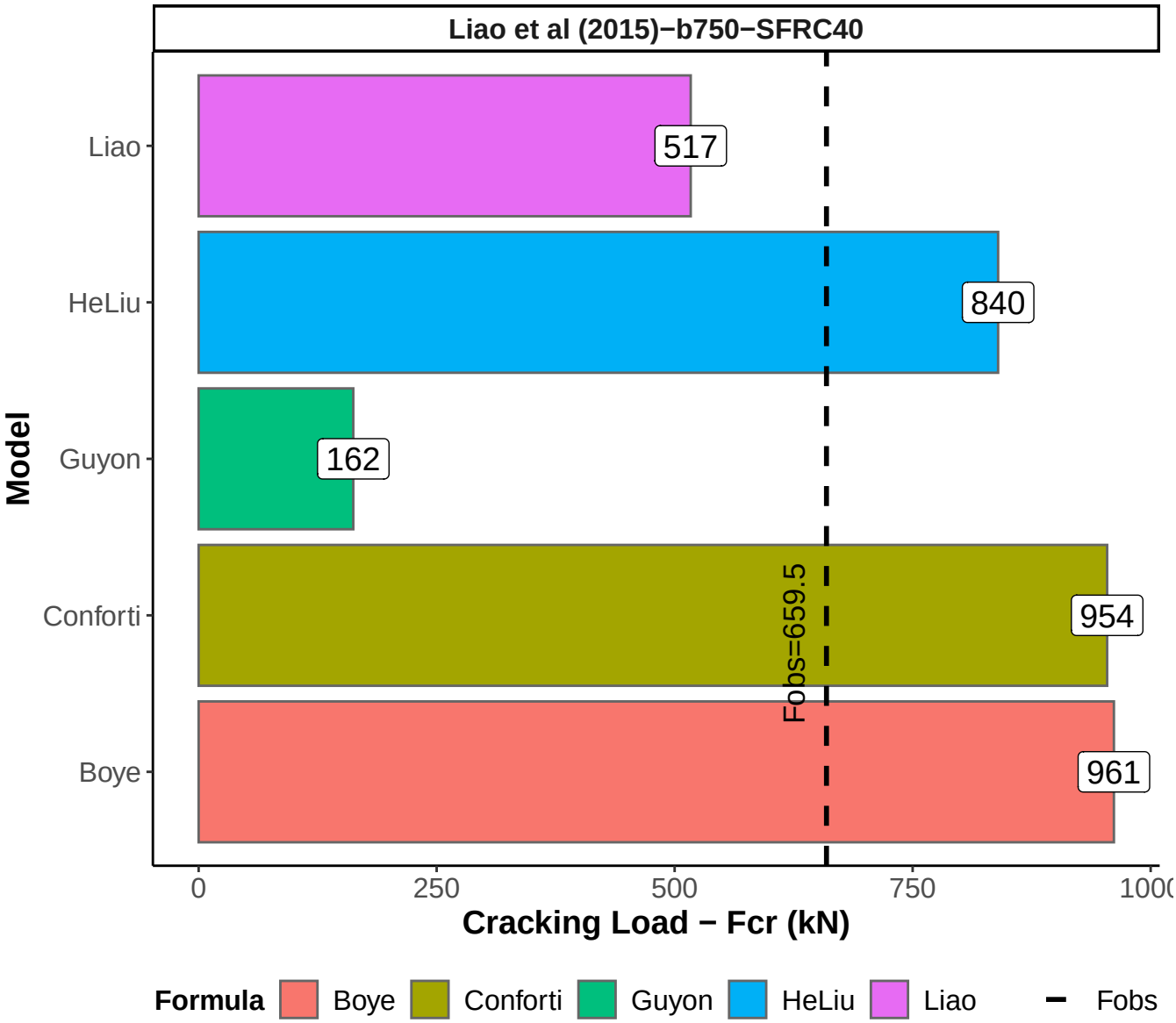

Cracking load (kN) per model

Page 21 *of* 26

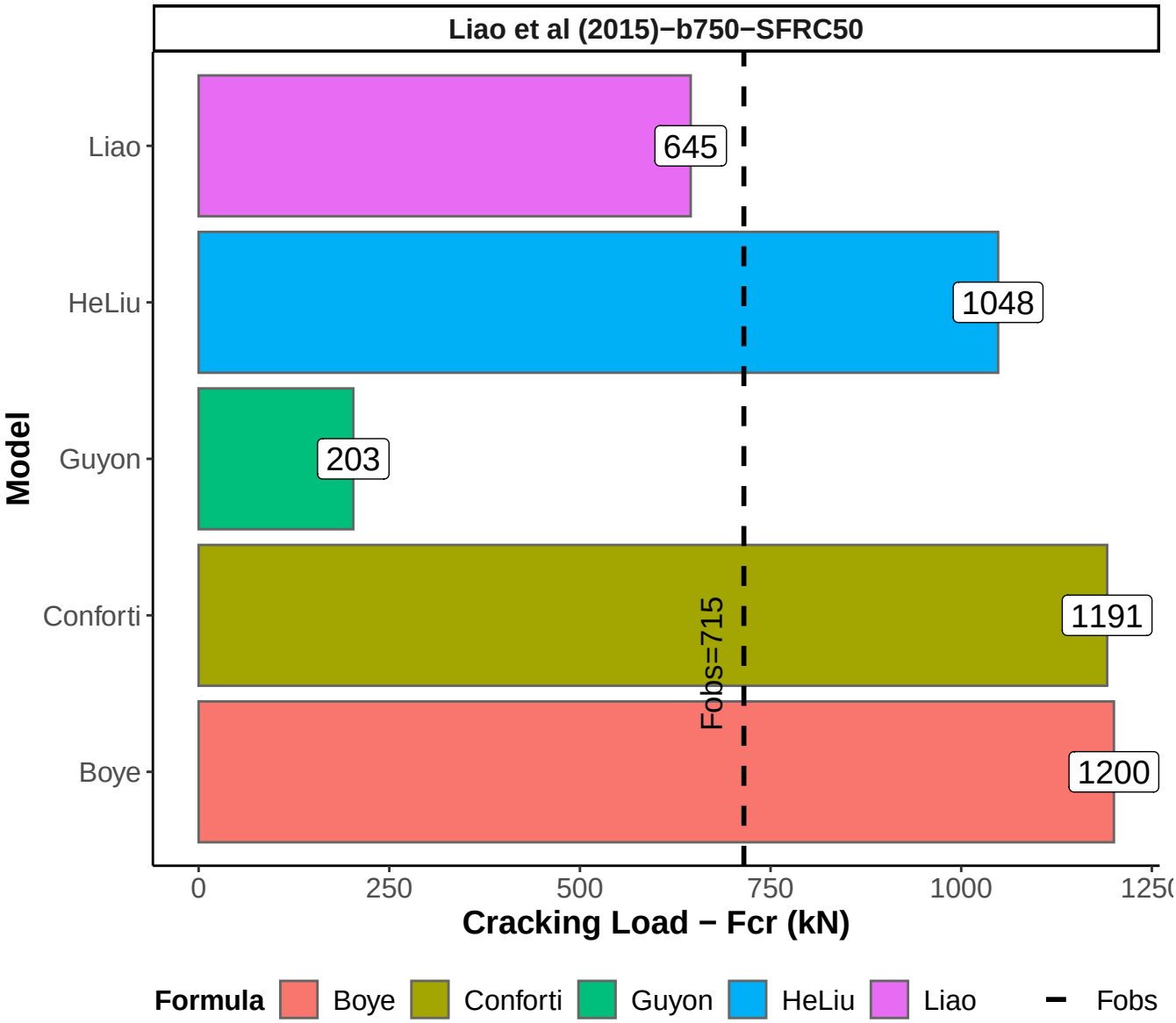

Cracking load (kN) per model

Page 22 of 26

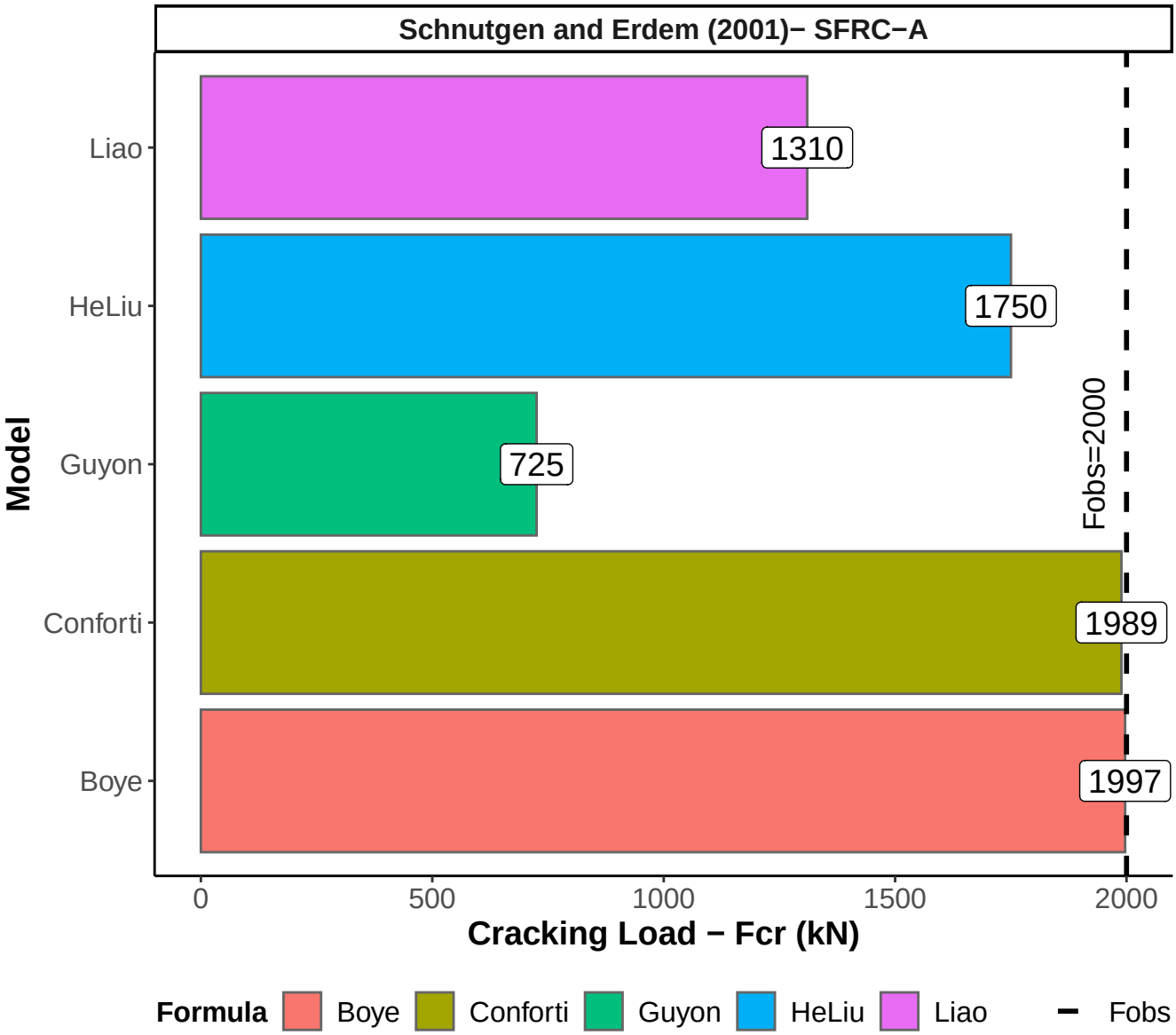

Cracking load (kN) per model

Page 23 of 26

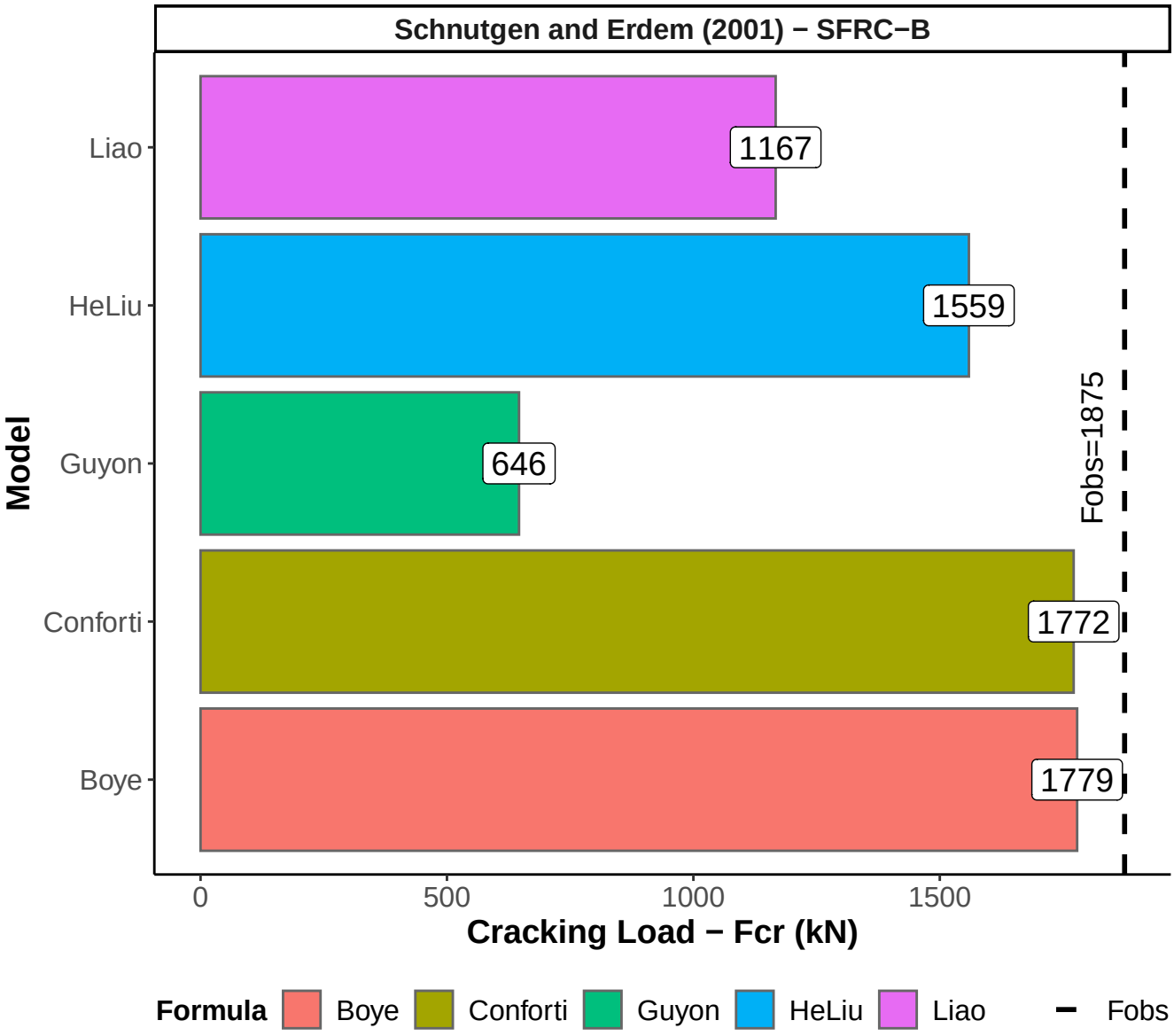

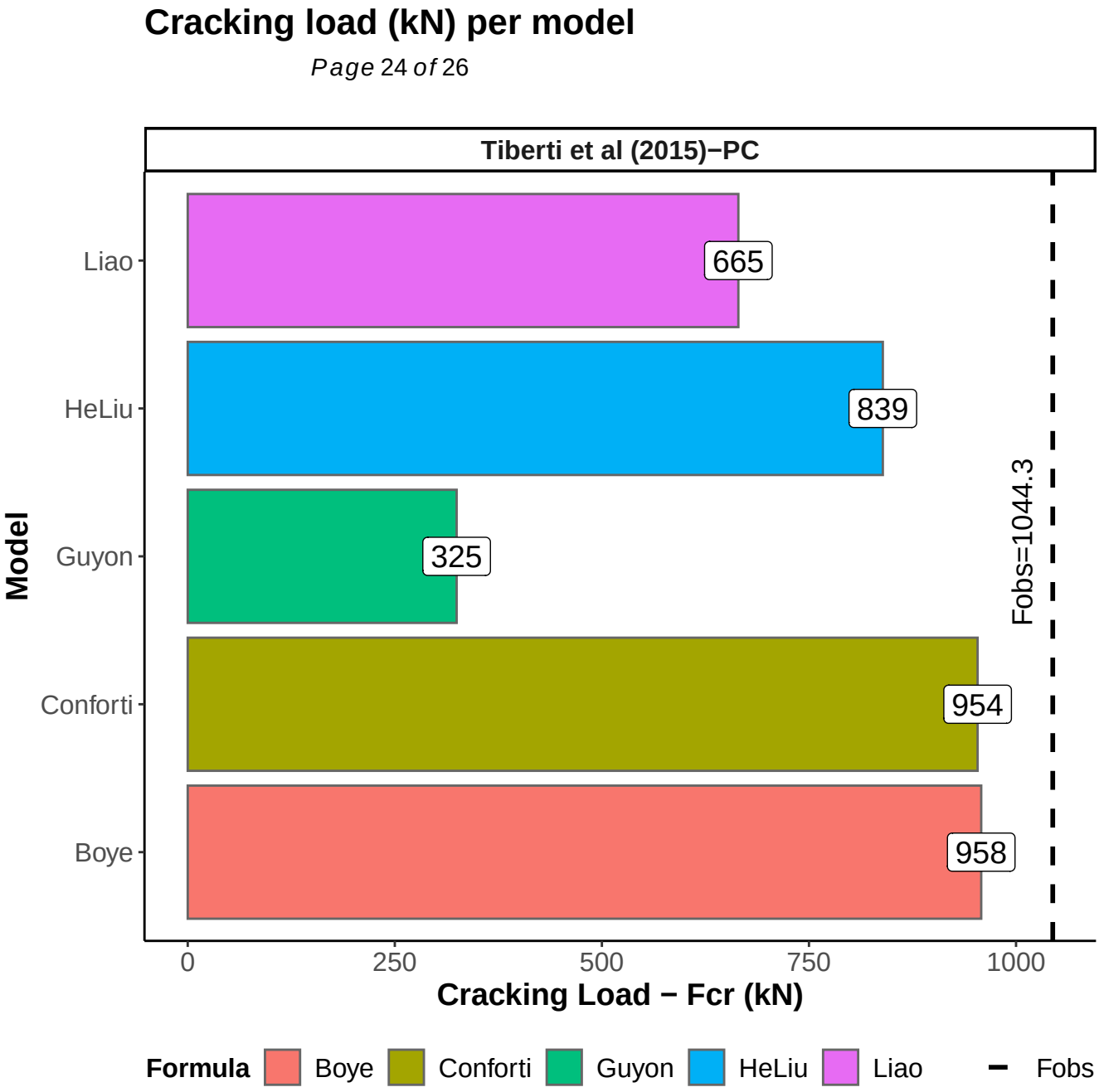
Cracking load (kN) per model
Page 24 of 26
Tiberti et al (2015)−PC
Liao
HeLiu
Guyon
Conforti
Boye
665
839
325
954
958
Fobs=1044.3
Model
0
250
500
750
1000
Cracking Load − Fcr (kN)
Formula
Boye
Conforti
Guyon
HeLiu
Liao
Fobs

Cracking load (kN) per model

Page 25 *of* 26

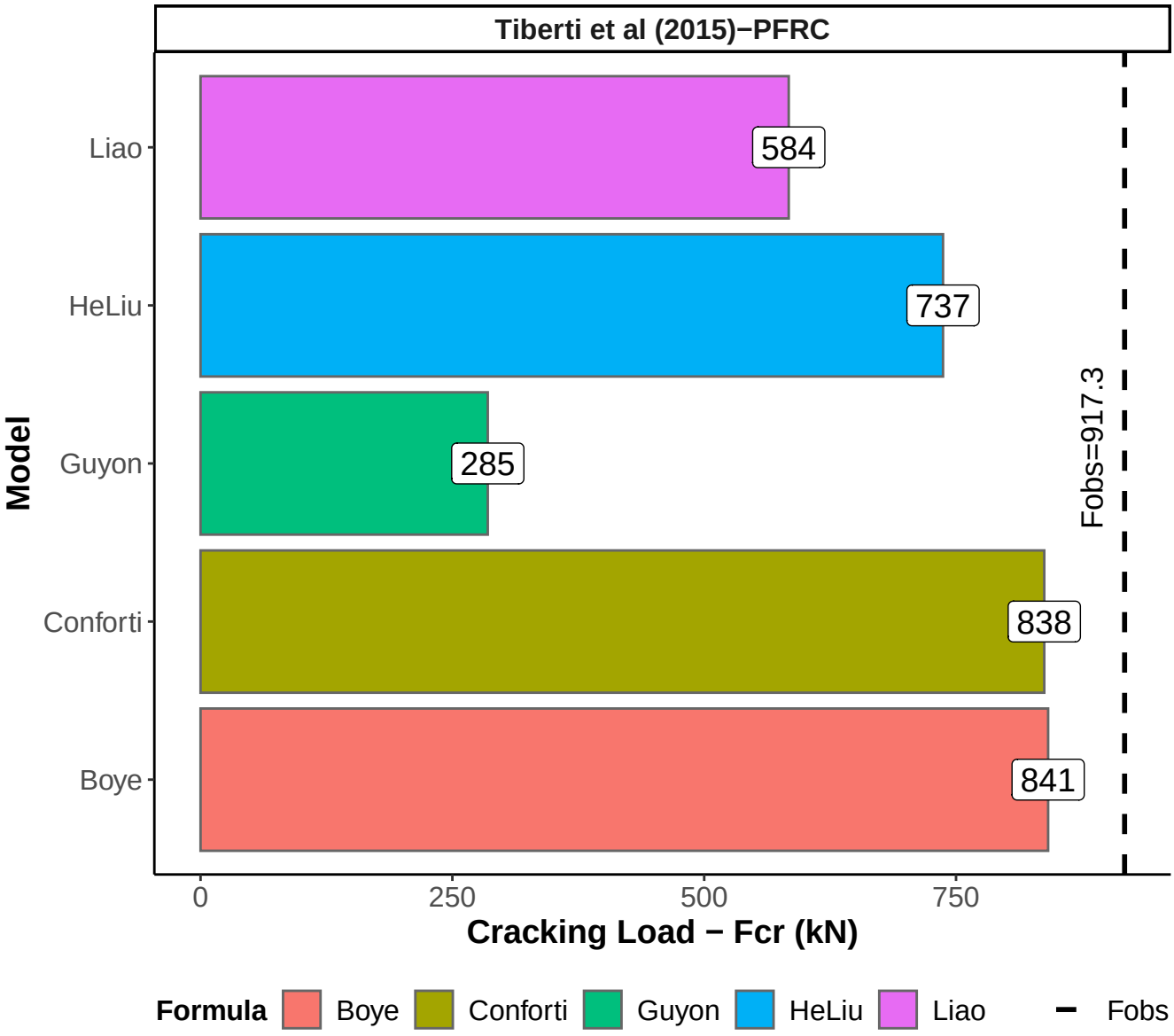

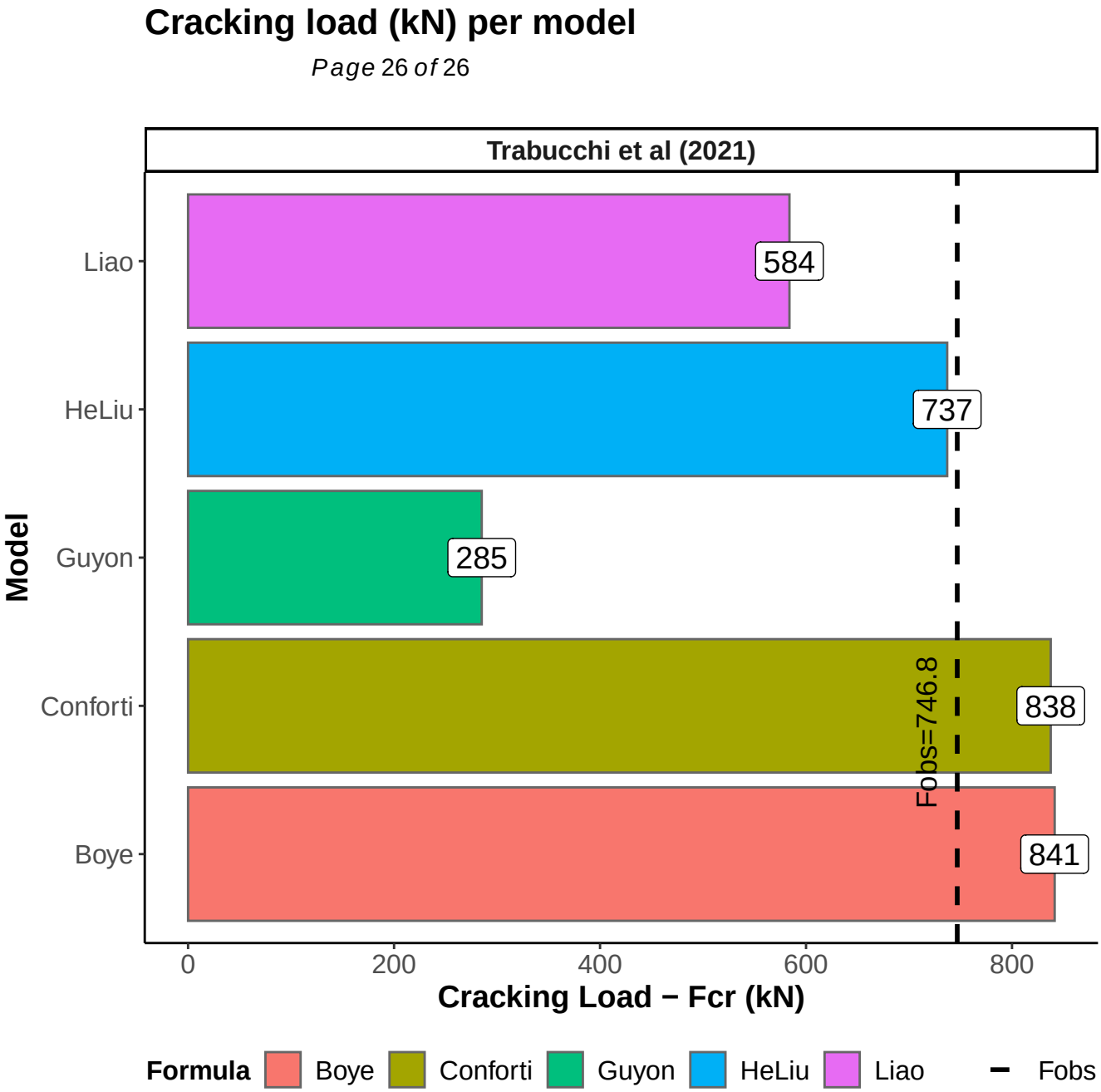
Cracking load (kN) per model
Page 26 of 26
Trabucchi et al (2021)
Liao
HeLiu
Guyon
Conforti
Boye
584
737
285
838
841
Fobs=746.8
Model
0
200
400
600
800
Cracking Load − Fcr (kN)
Formula
Boye
Conforti
Guyon
HeLiu
Liao
Fobs

APPENDIX A.5

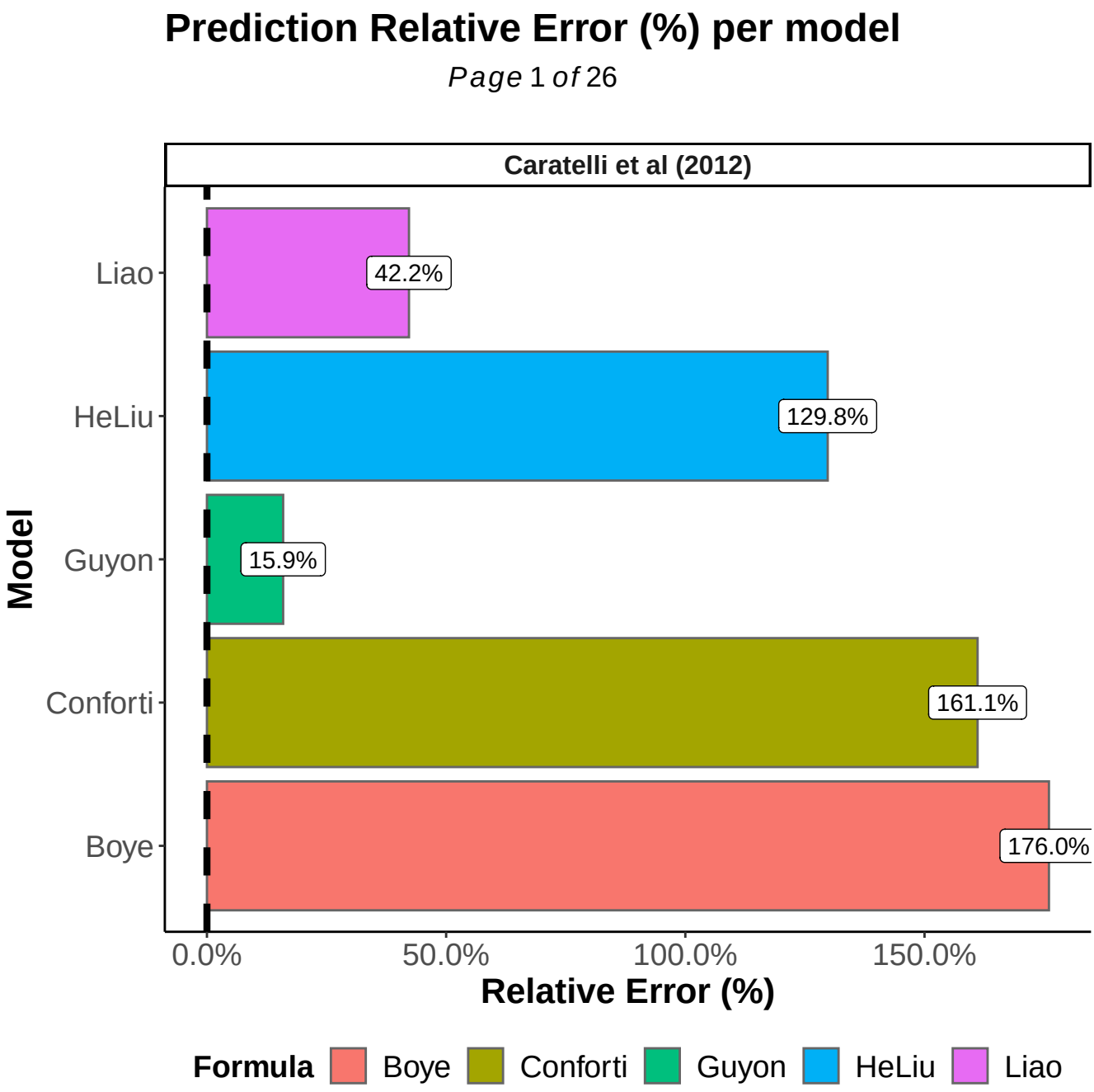
Prediction Relative Error (%) per model
Page 1 of 26
Caratelli et al (2012)
Liao
HeLiu
Guyon
Conforti
Boye
42.2%
129.8%
15.9%
161.1%
176.0%
Model
0.0%
50.0%
100.0%
150.0%
Relative Error (%)
Formula
Boye
Conforti
Guyon
HeLiu
Liao

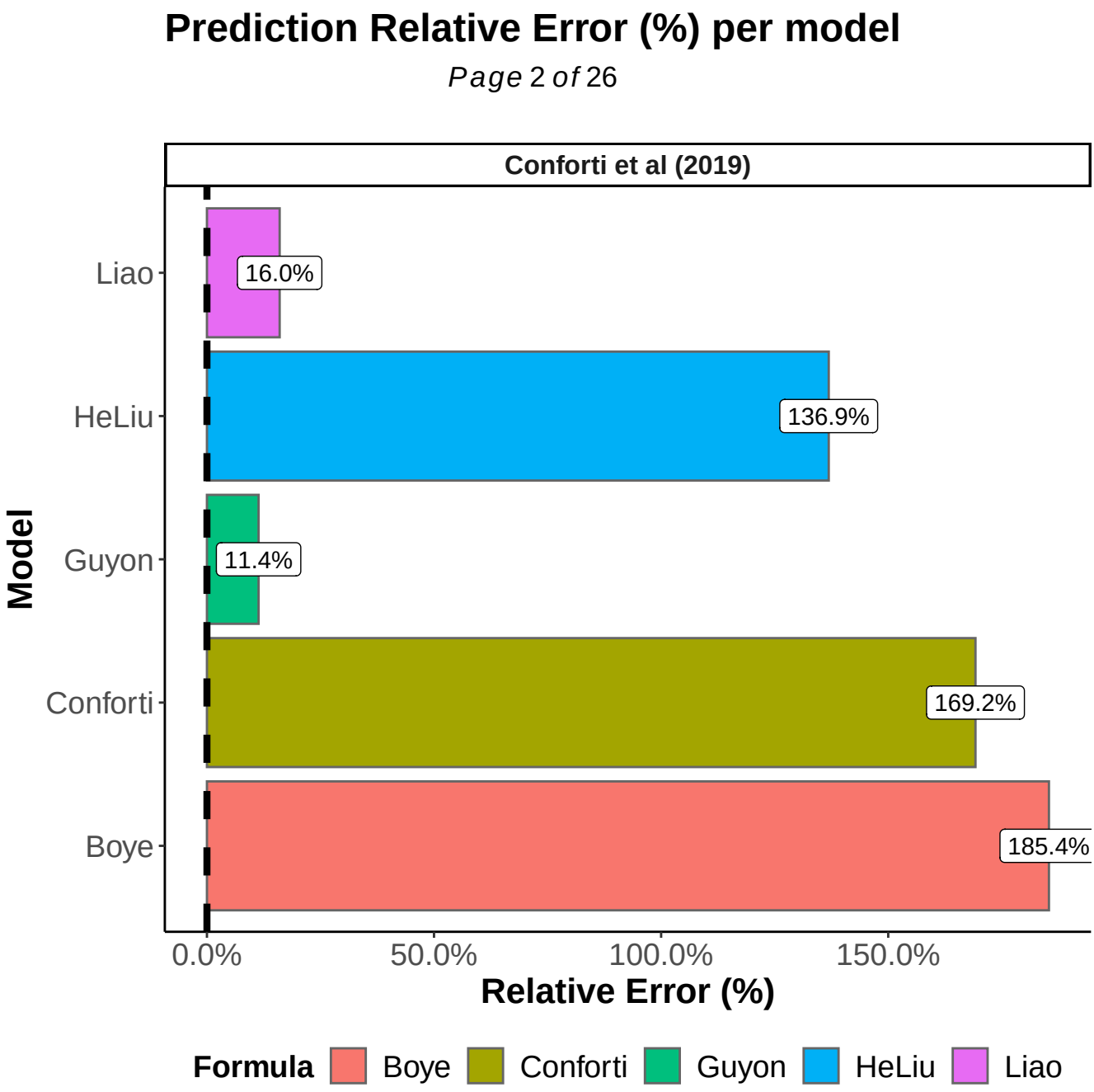
Prediction Relative Error (%) per model
Page 2 of 26
Conforti et al (2019)
Liao
HeLiu
Guyon
Conforti
Boye
16.0%
136.9%
11.4%
169.2%
185.4%
Model
0.0%
50.0%
100.0%
150.0%
Relative Error (%)
Formula
Boye
Conforti
Guyon
HeLiu
Liao

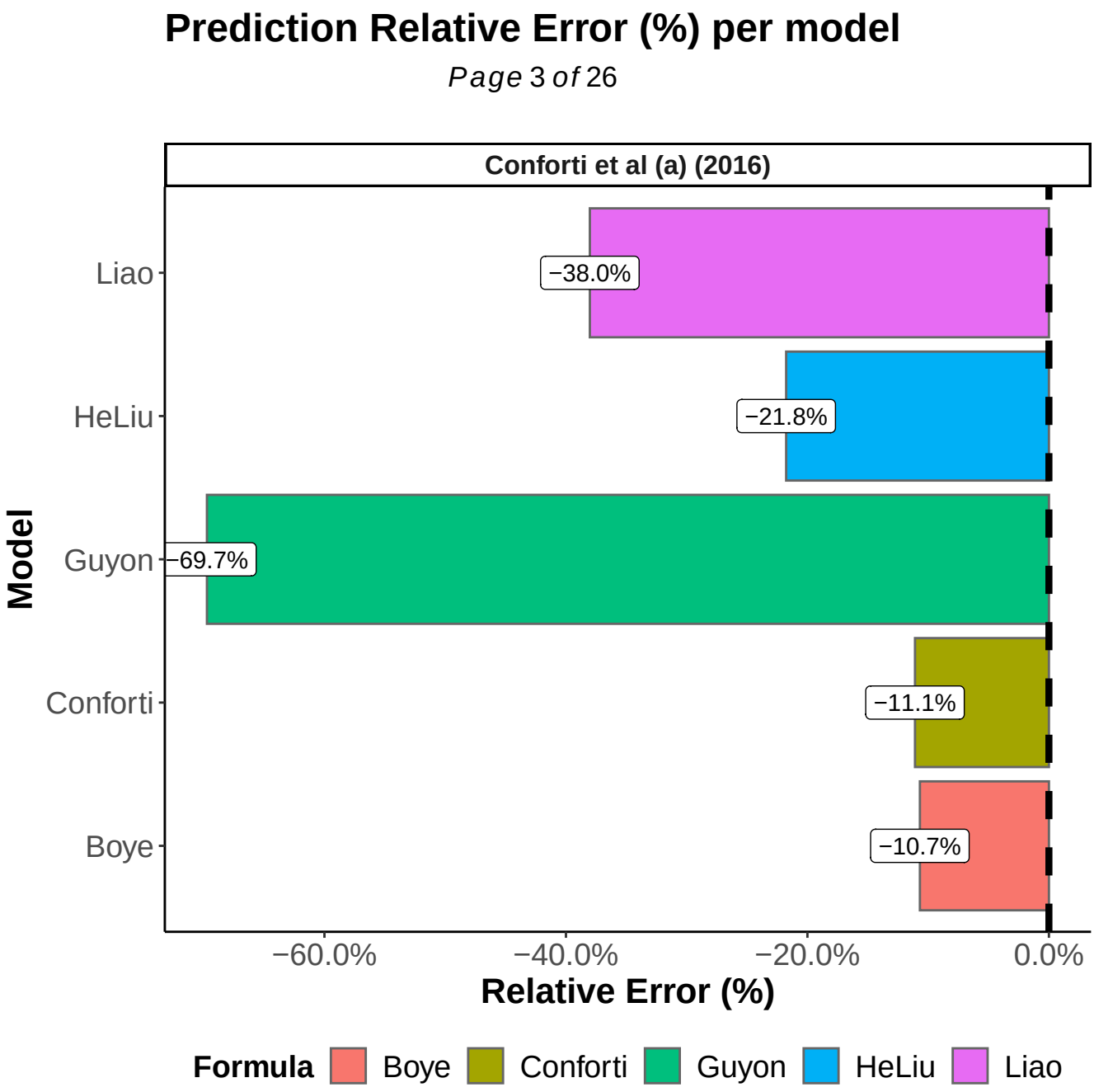
Prediction Relative Error (%) per model
Page 3 of 26
Conforti et al (a) (2016)
Liao
HeLiu
Guyon
Conforti
Boye
−38.0%
−21.8%
−69.7%
−11.1%
−10.7%
Model
−60.0%
−40.0%
−20.0%
0.0%
Relative Error (%)
Formula
Boye
Conforti
Guyon
HeLiu
Liao

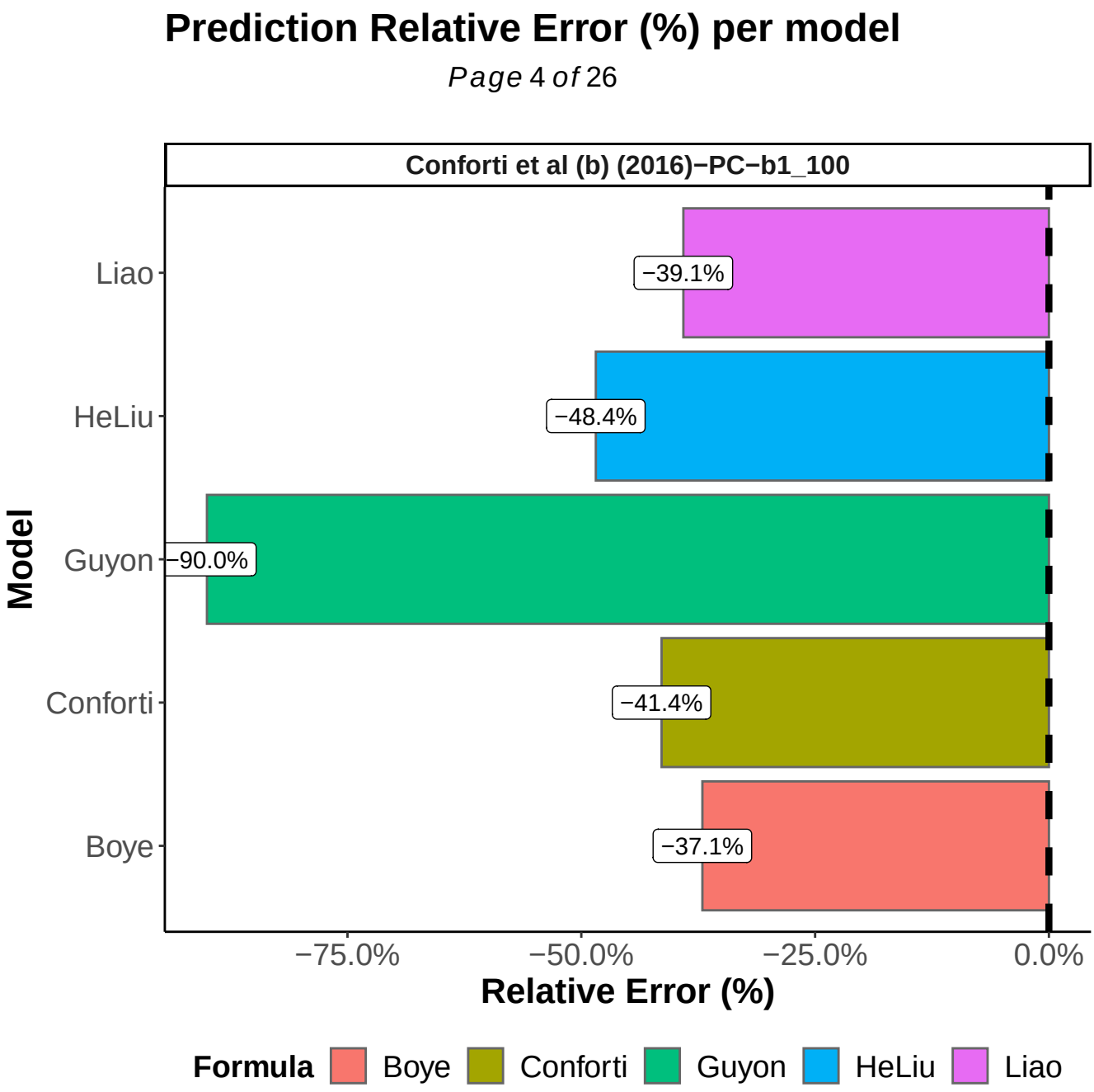
Prediction Relative Error (%) per model
Page 4 of 26
Conforti et al (b) (2016)−PC−b1_100
Liao
HeLiu
Guyon
Conforti
Boye
−39.1%
−48.4%
−90.0%
−41.4%
−37.1%
Model
−75.0%
−50.0%
−25.0%
0.0%
Relative Error (%)
Formula
Boye
Conforti
Guyon
HeLiu
Liao

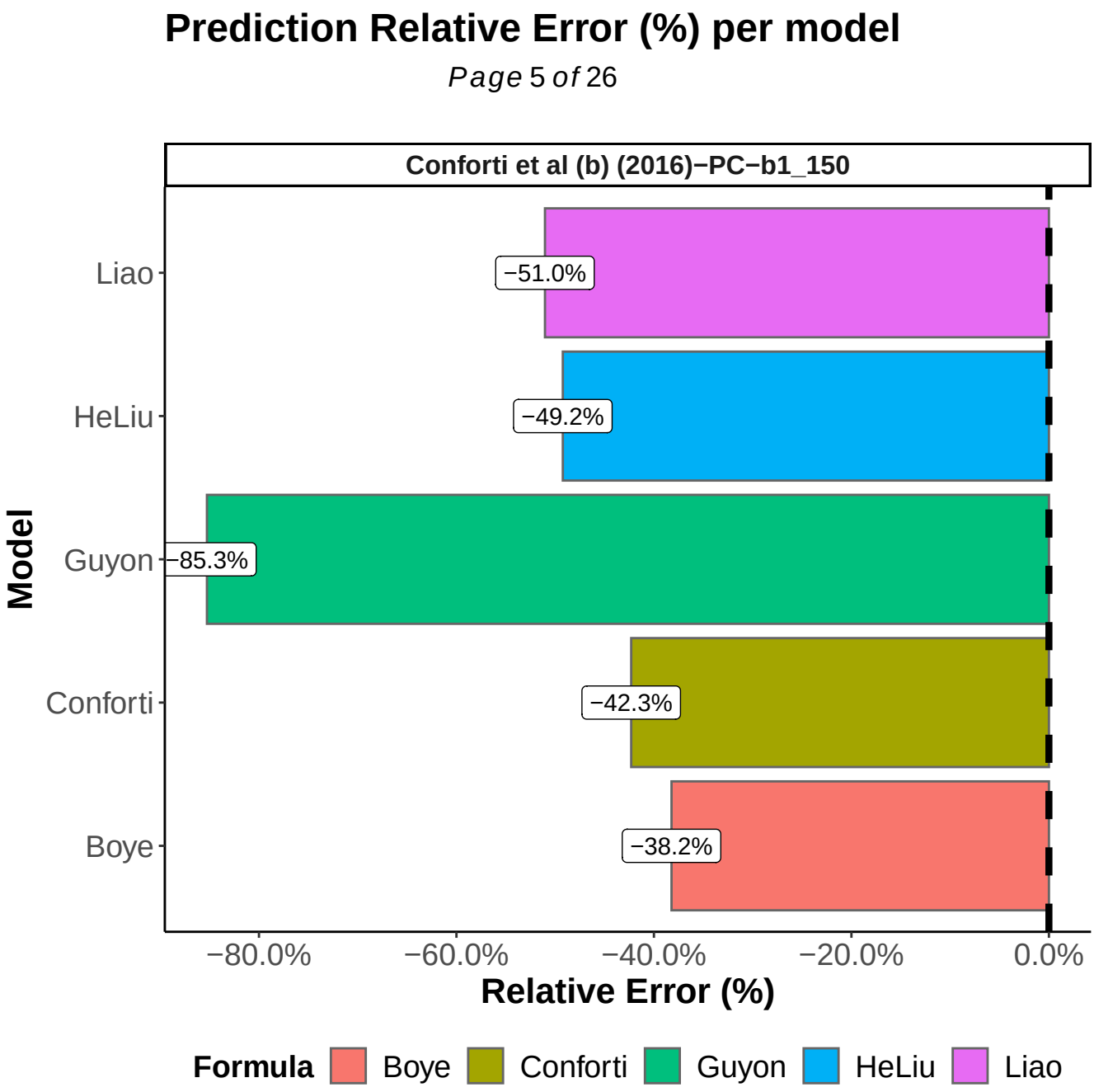
Prediction Relative Error (%) per model
Page 5 of 26
Conforti et al (b) (2016)−PC−b1_150
Liao
HeLiu
Guyon
Conforti
Boye
−51.0%
−49.2%
−85.3%
−42.3%
−38.2%
Model
−80.0%
−60.0%
−40.0%
−20.0%
0.0%
Relative Error (%)
Formula
Boye
Conforti
Guyon
HeLiu
Liao

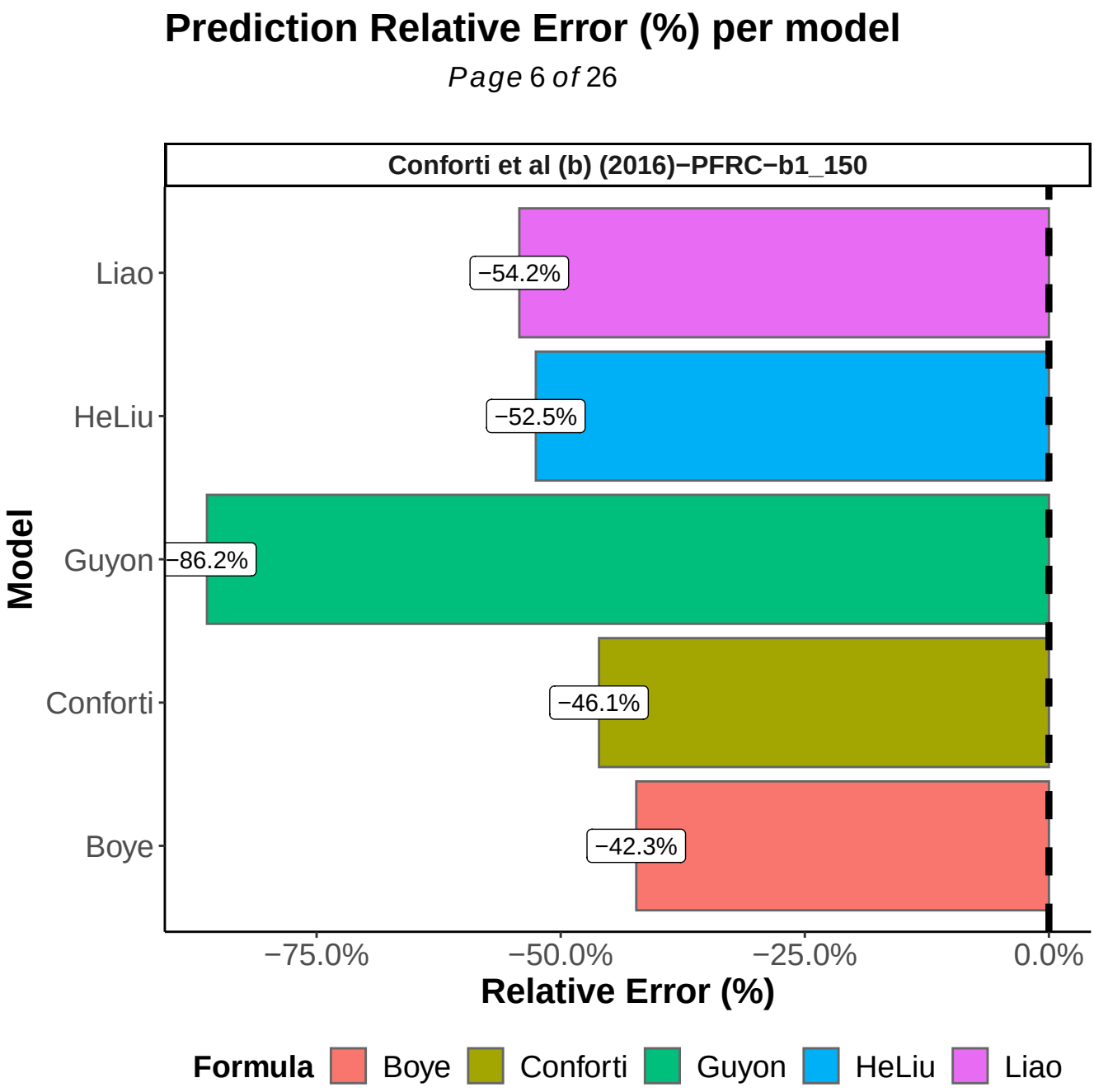
Prediction Relative Error (%) per model
Page 6 of 26
Conforti et al (b) (2016)−PFRC−b1_150
Liao
HeLiu
Guyon
Conforti
Boye
−54.2%
−52.5%
−86.2%
−46.1%
−42.3%
Model
−75.0%
−50.0%
−25.0%
0.0%
Relative Error (%)
Formula
Boye
Conforti
Guyon
HeLiu
Liao

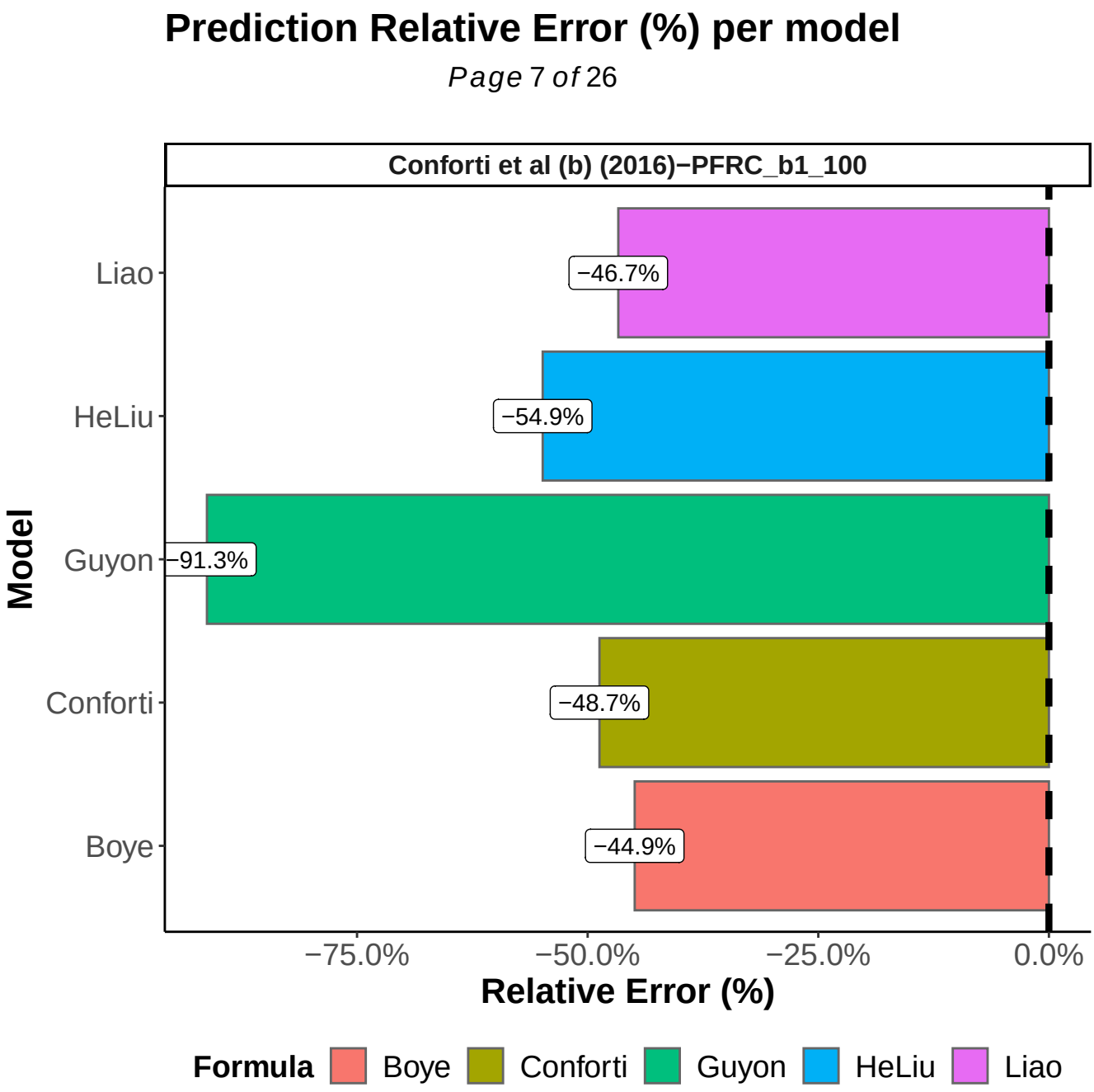
Prediction Relative Error (%) per model
Page 7 of 26
Conforti et al (b) (2016)−PFRC_b1_100
Liao
HeLiu
Guyon
Conforti
Boye
−46.7%
−54.9%
−91.3%
−48.7%
−44.9%
Model
−75.0%
−50.0%
−25.0%
0.0%
Relative Error (%)
Formula
Boye
Conforti
Guyon
HeLiu
Liao

Prediction Relative Error (%) per model

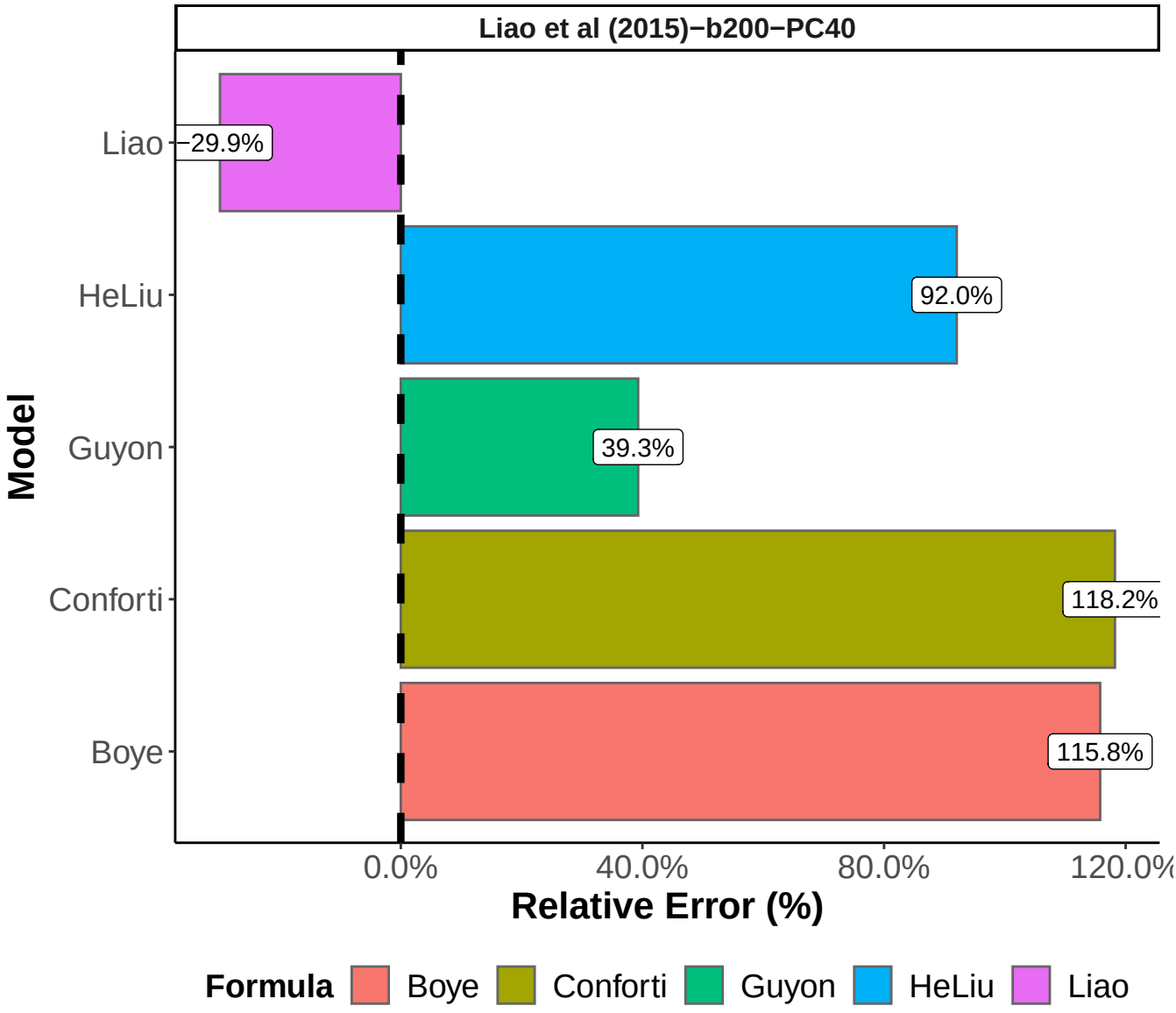

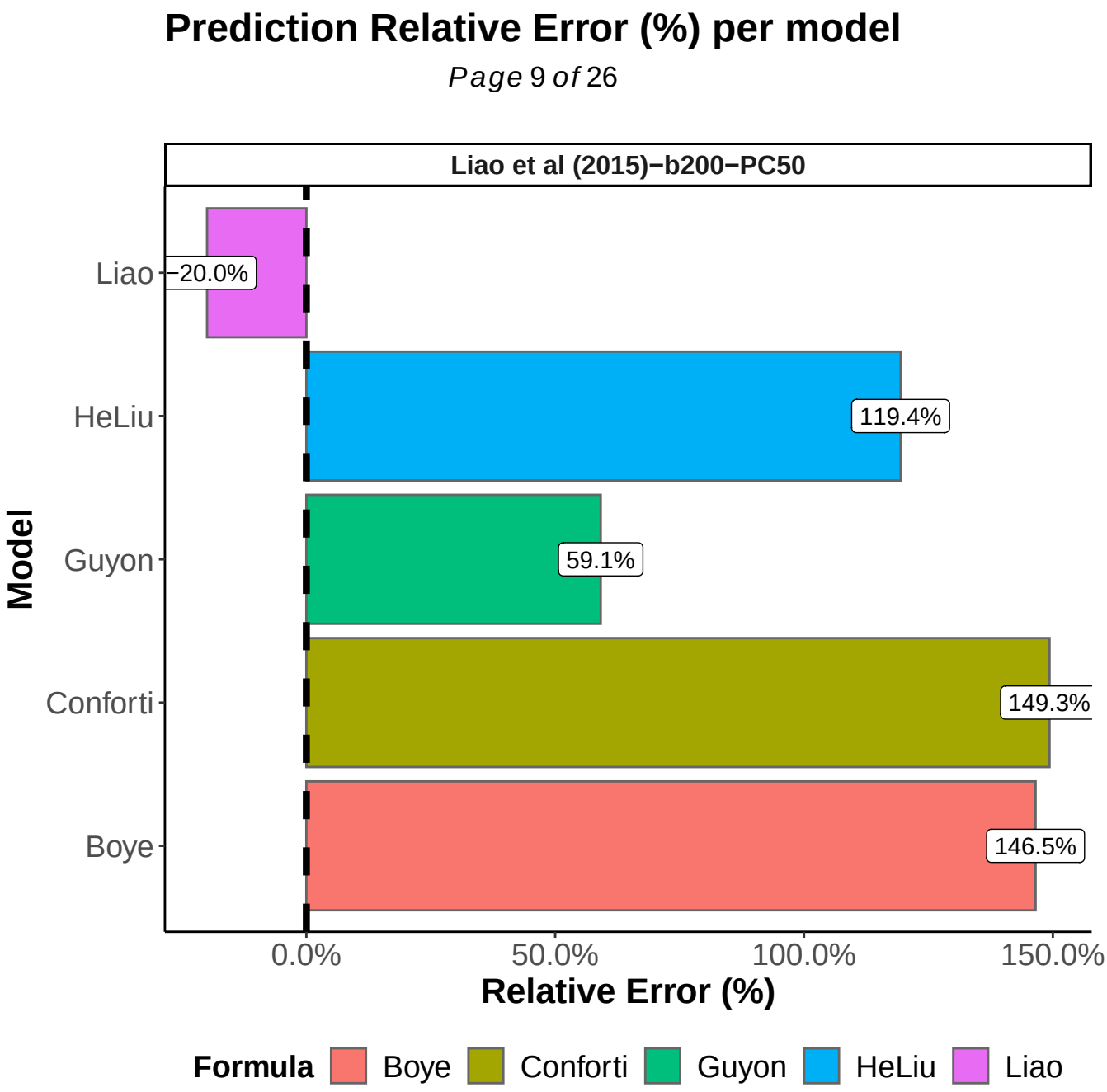
Prediction Relative Error (%) per model
Page 9 of 26
Liao et al (2015)−b200−PC50
Liao
HeLiu
Guyon
Conforti
Boye
Model
−20.0%
119.4%
59.1%
149.3%
146.5%
0.0%
50.0%
100.0%
150.0%
Relative Error (%)
Formula
Boye
Conforti
Guyon
HeLiu
Liao

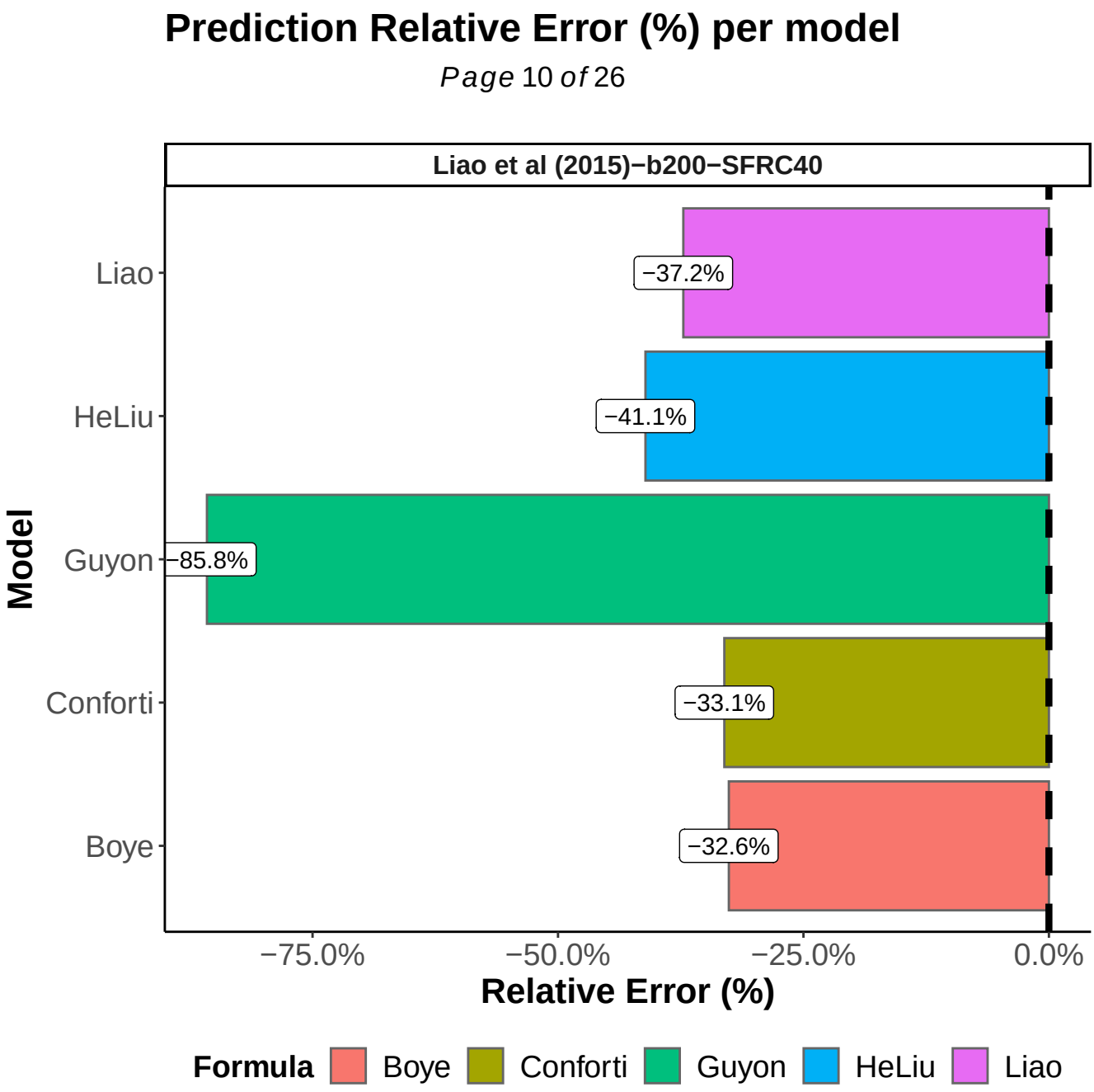
Prediction Relative Error (%) per model
Page 10 of 26
Liao et al (2015)−b200−SFRC40
Liao
HeLiu
Guyon
Conforti
Boye
Model
−37.2%
−41.1%
−85.8%
−33.1%
−32.6%
−75.0%
−50.0%
−25.0%
0.0%
Relative Error (%)
Formula
Boye
Conforti
Guyon
HeLiu
Liao

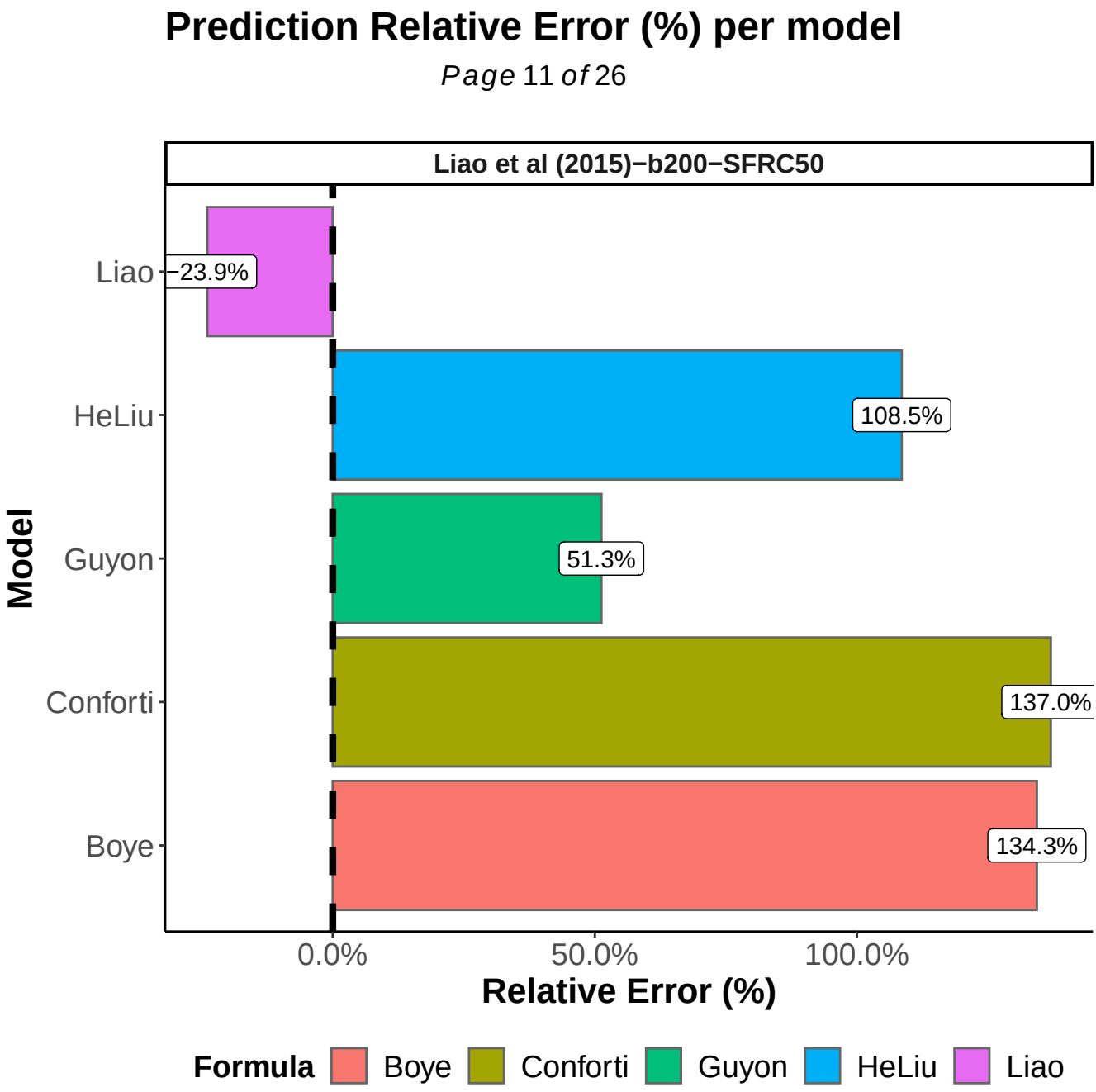
Prediction Relative Error (%) per model
Page 11 of 26
Liao et al (2015)−b200−SFRC50
Liao
HeLiu
Guyon
Conforti
Boye
−23.9%
108.5%
51.3%
137.0%
134.3%
Model
0.0%
50.0%
100.0%
Relative Error (%)
Formula
Boye
Conforti
Guyon
HeLiu
Liao

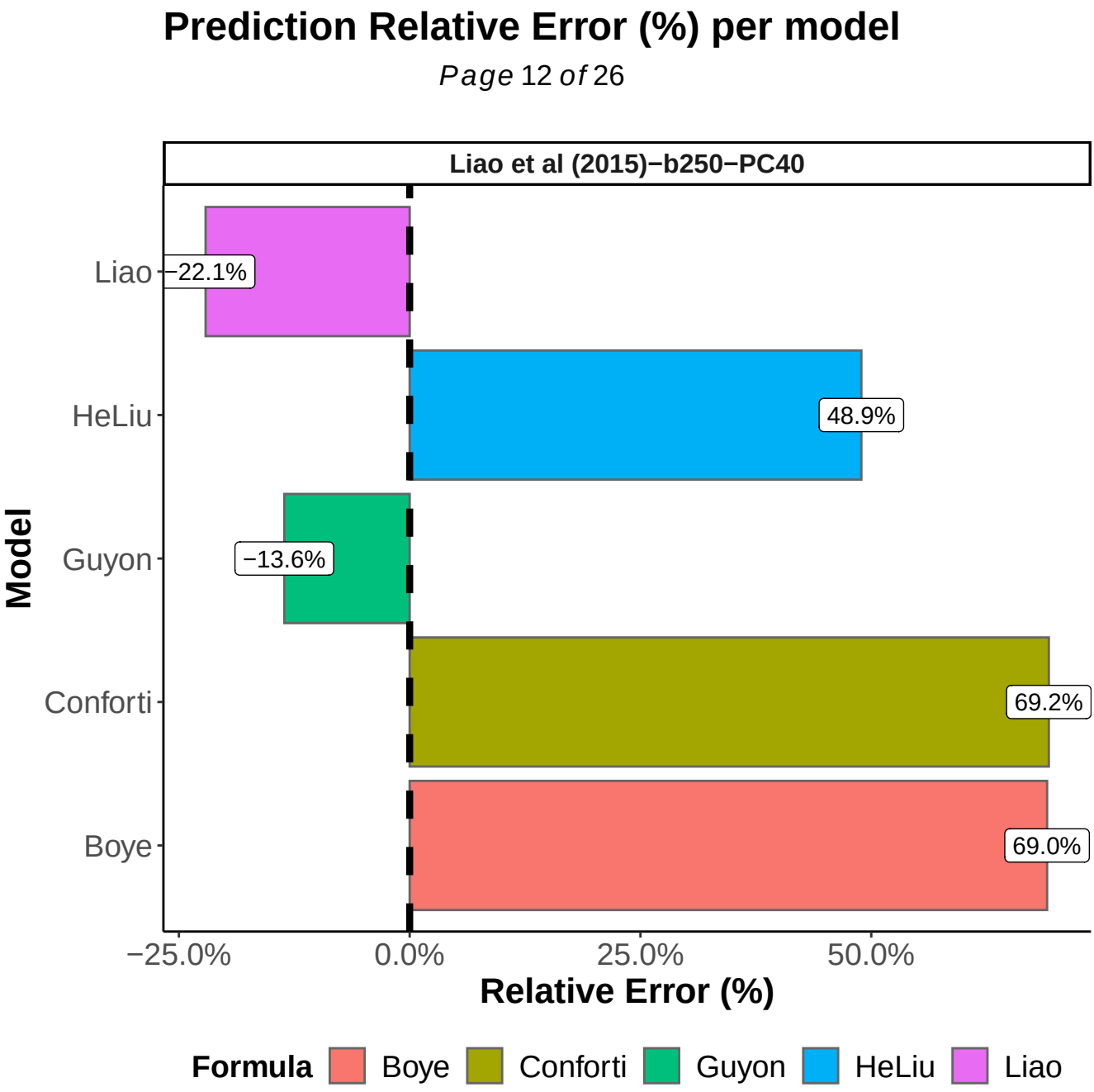
Prediction Relative Error (%) per model
Page 12 of 26
Liao et al (2015)−b250−PC40
Liao
HeLiu
Guyon
Conforti
Boye
Model
−22.1%
48.9%
−13.6%
69.2%
69.0%
−25.0%
0.0%
25.0%
50.0%
Relative Error (%)
Formula
Boye
Conforti
Guyon
HeLiu
Liao

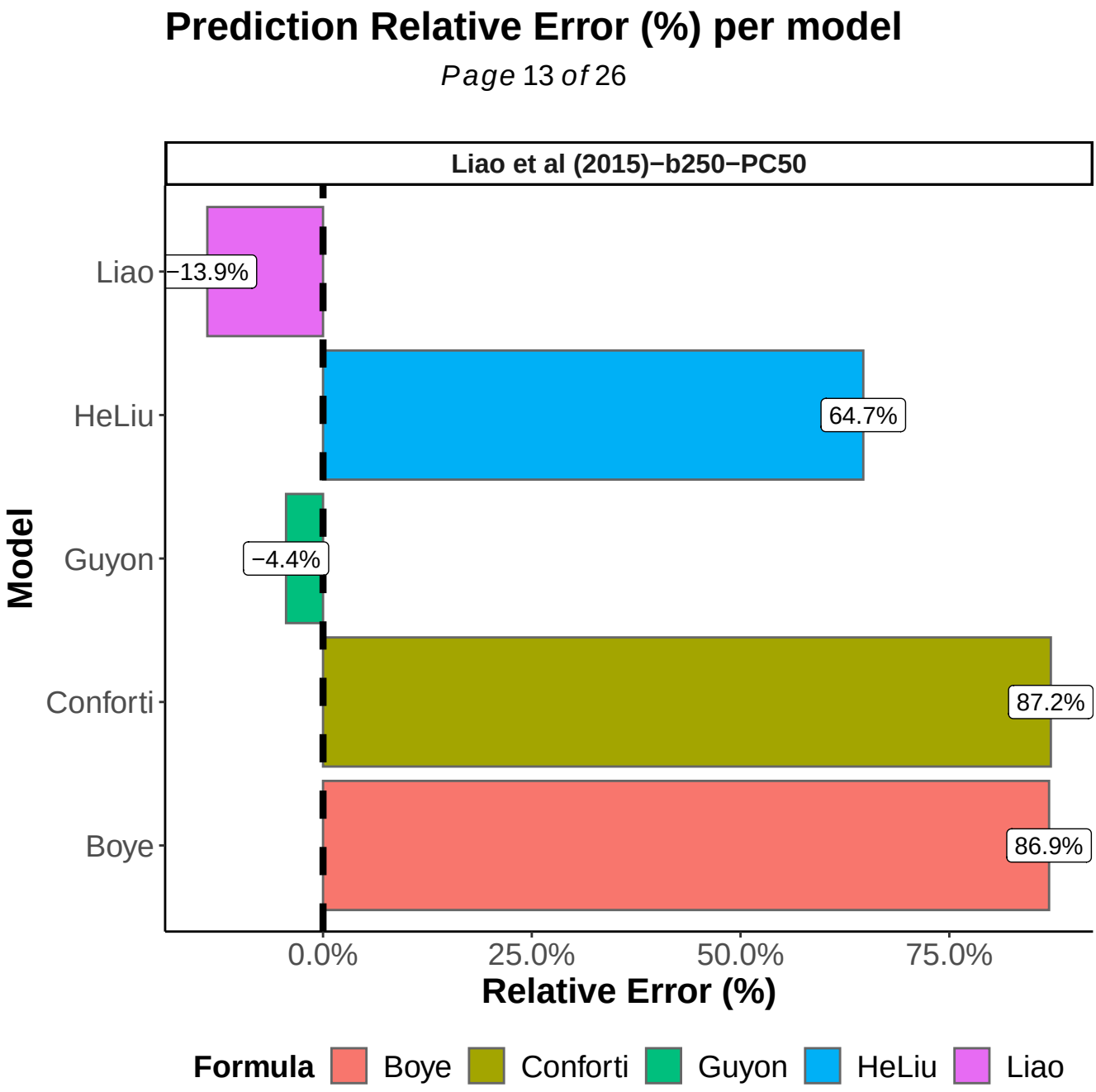
Prediction Relative Error (%) per model
Page 13 of 26
Liao et al (2015)−b250−PC50
Liao
HeLiu
Guyon
Conforti
Boye
−13.9%
64.7%
−4.4%
87.2%
86.9%
Model
0.0%
25.0%
50.0%
75.0%
Relative Error (%)
Formula
Boye
Conforti
Guyon
HeLiu
Liao

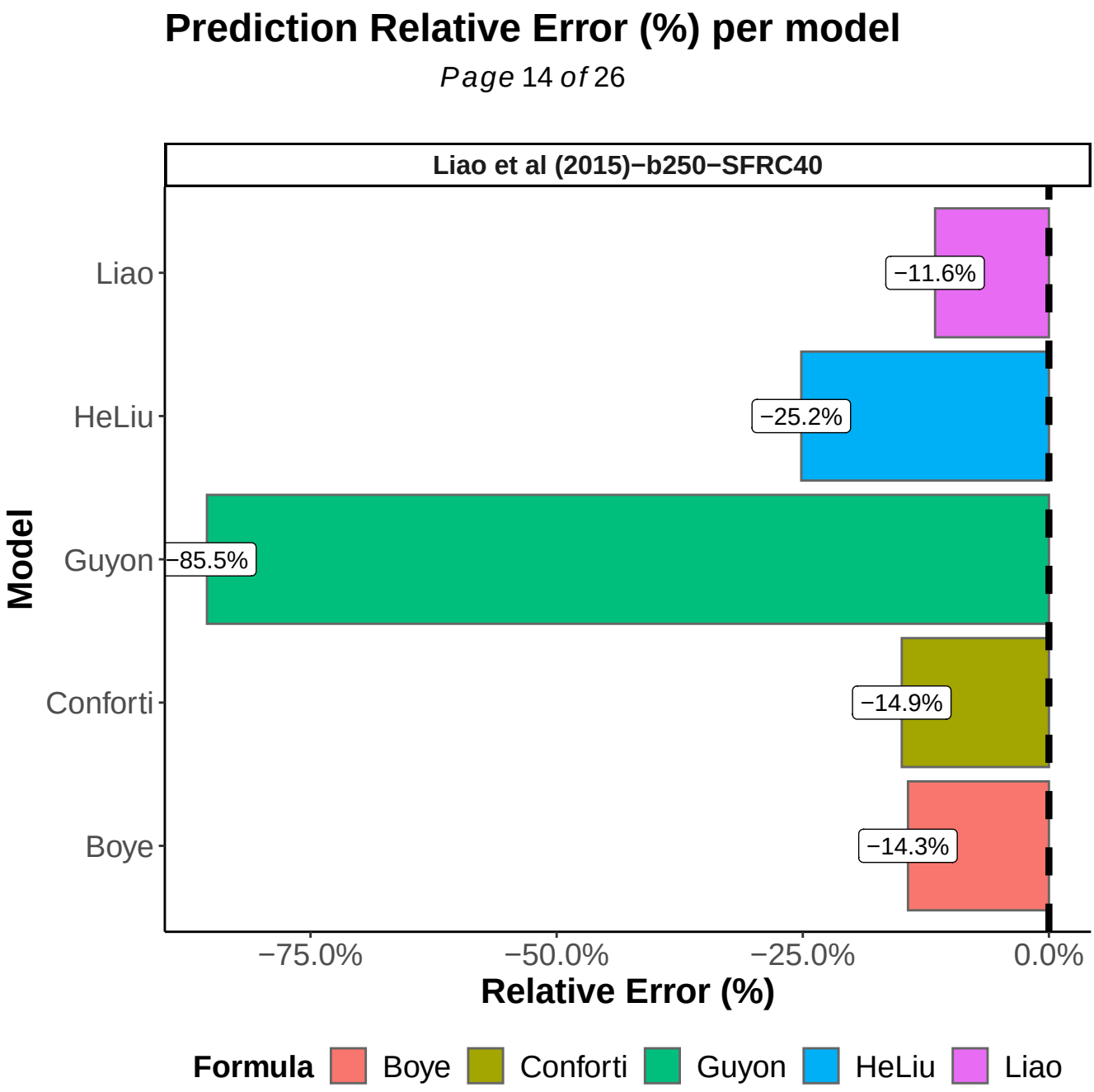
Prediction Relative Error (%) per model
Page 14 of 26
Liao et al (2015)−b250−SFRC40
Liao
HeLiu
Guyon
Conforti
Boye
Model
−11.6%
−25.2%
−85.5%
−14.9%
−14.3%
−75.0%
−50.0%
−25.0%
0.0%
Relative Error (%)
Formula
Boye
Conforti
Guyon
HeLiu
Liao

Prediction Relative Error (%) per model

Page 15 *of* 26

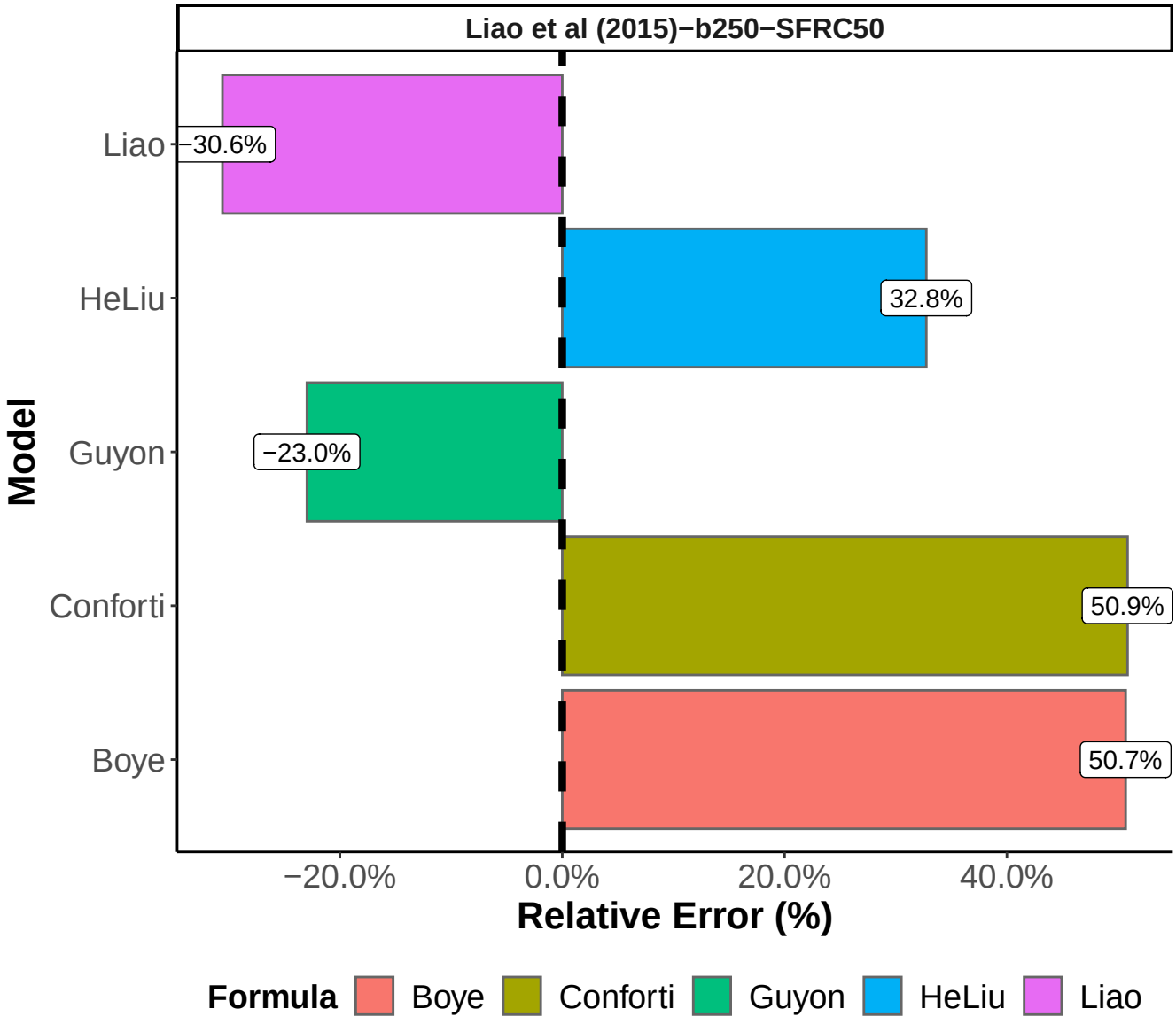

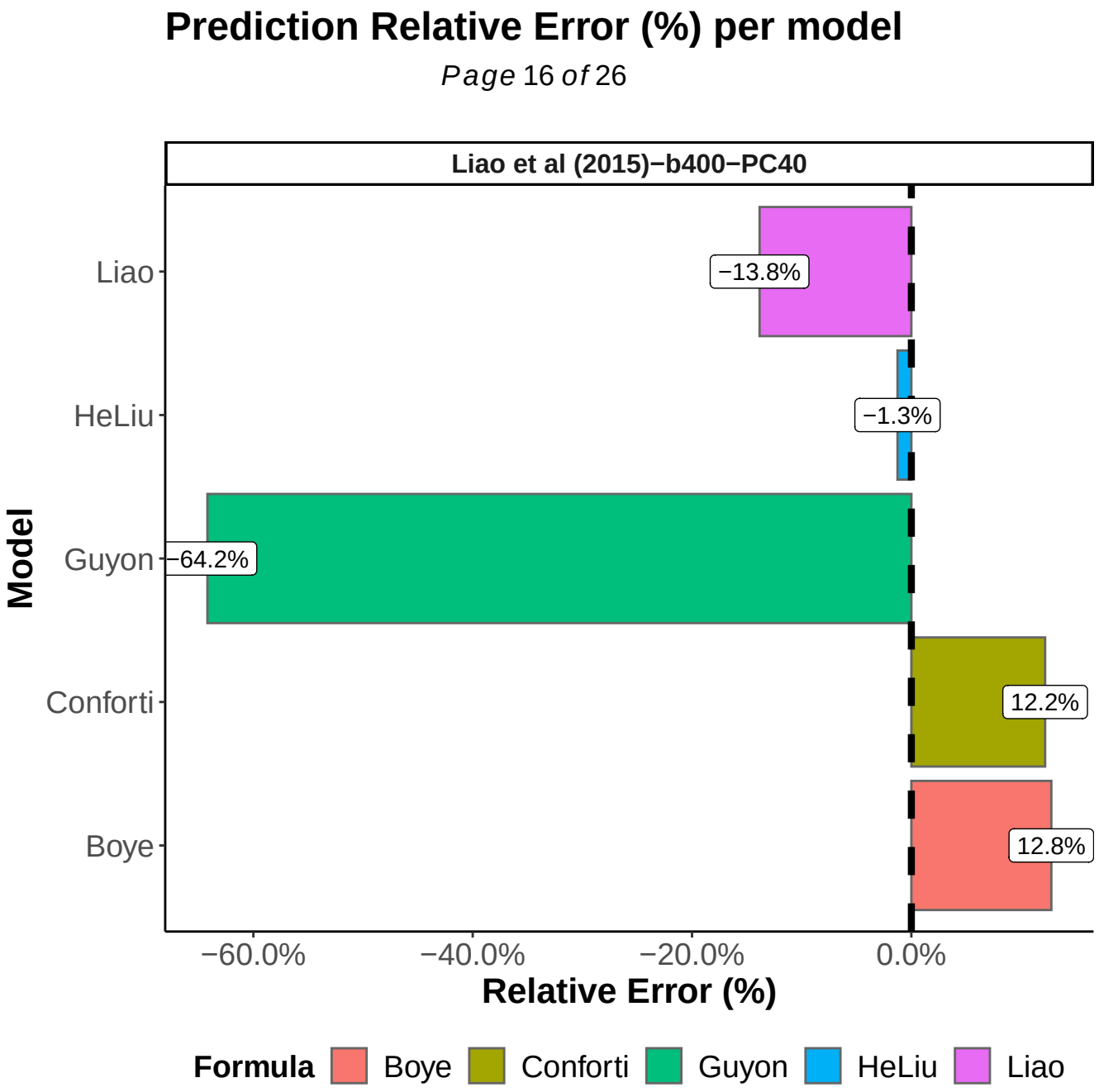
Prediction Relative Error (%) per model
Page 16 of 26
Liao et al (2015)−b400−PC40
Liao
HeLiu
Guyon
Conforti
Boye
Model
−13.8%
−1.3%
−64.2%
12.2%
12.8%
−60.0%
−40.0%
−20.0%
0.0%
Relative Error (%)
Formula
Boye
Conforti
Guyon
HeLiu
Liao

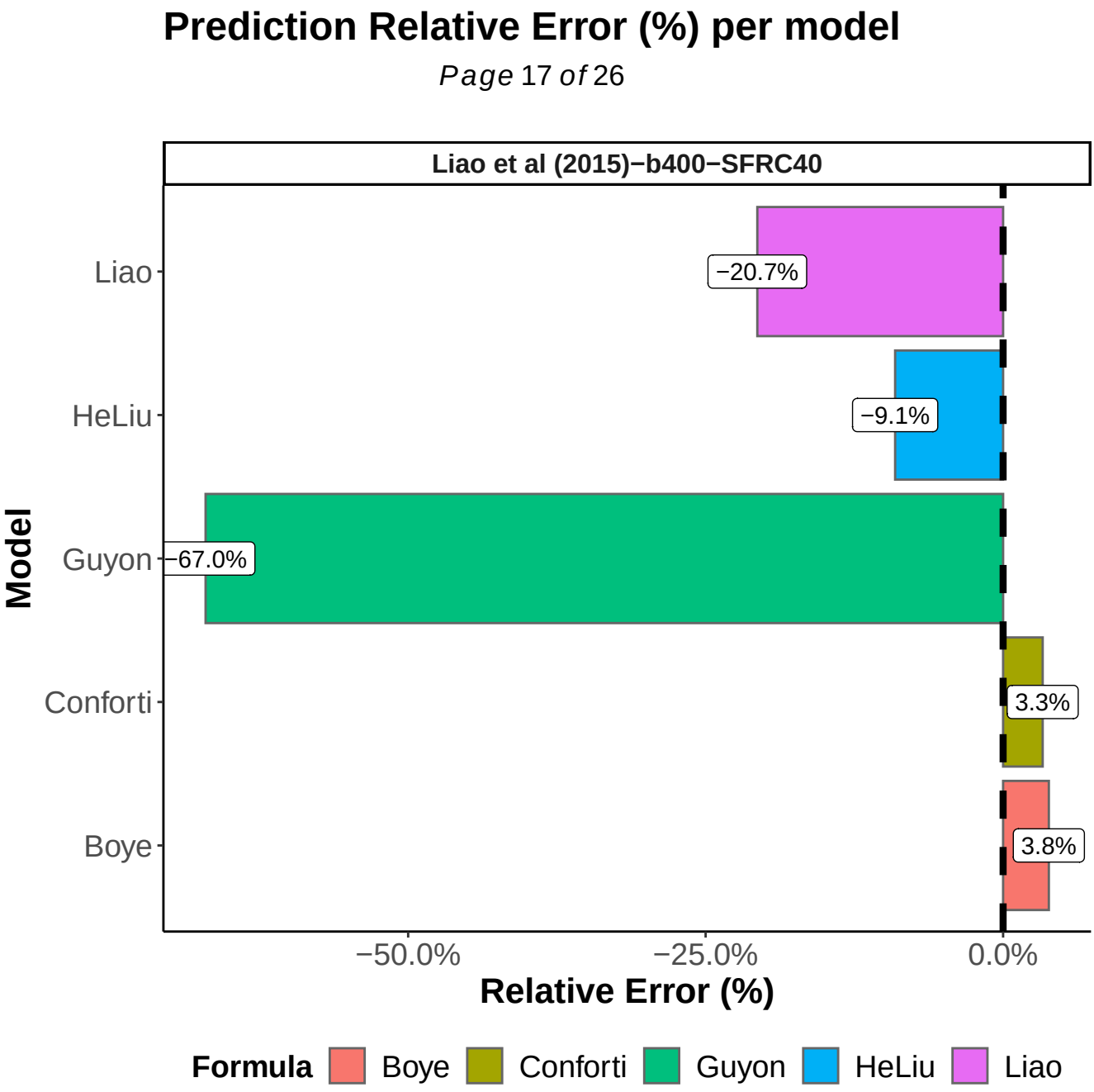
Prediction Relative Error (%) per model
Page 17 of 26
Liao et al (2015)−b400−SFRC40
Liao
HeLiu
Guyon
Conforti
Boye
Model
−20.7%
−9.1%
−67.0%
3.3%
3.8%
−50.0%
−25.0%
0.0%
Relative Error (%)
Formula
Boye
Conforti
Guyon
HeLiu
Liao

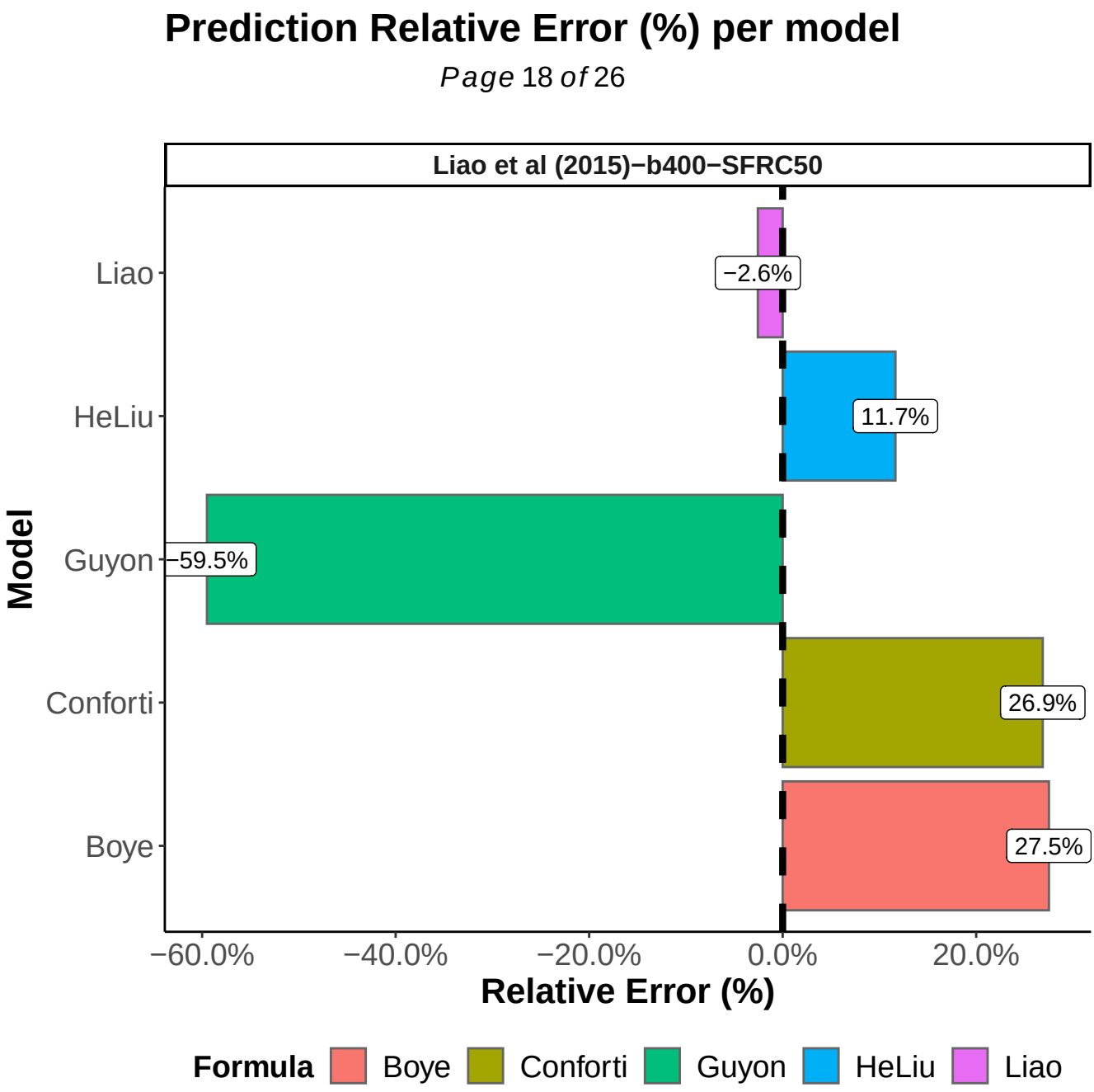
Prediction Relative Error (%) per model
Page 18 of 26
Liao et al (2015)−b400−SFRC50
Liao
HeLiu
Guyon
Conforti
Boye
Model
−2.6%
11.7%
−59.5%
26.9%
27.5%
−60.0%
−40.0%
−20.0%
0.0%
20.0%
Relative Error (%)
Formula
Boye
Conforti
Guyon
HeLiu
Liao

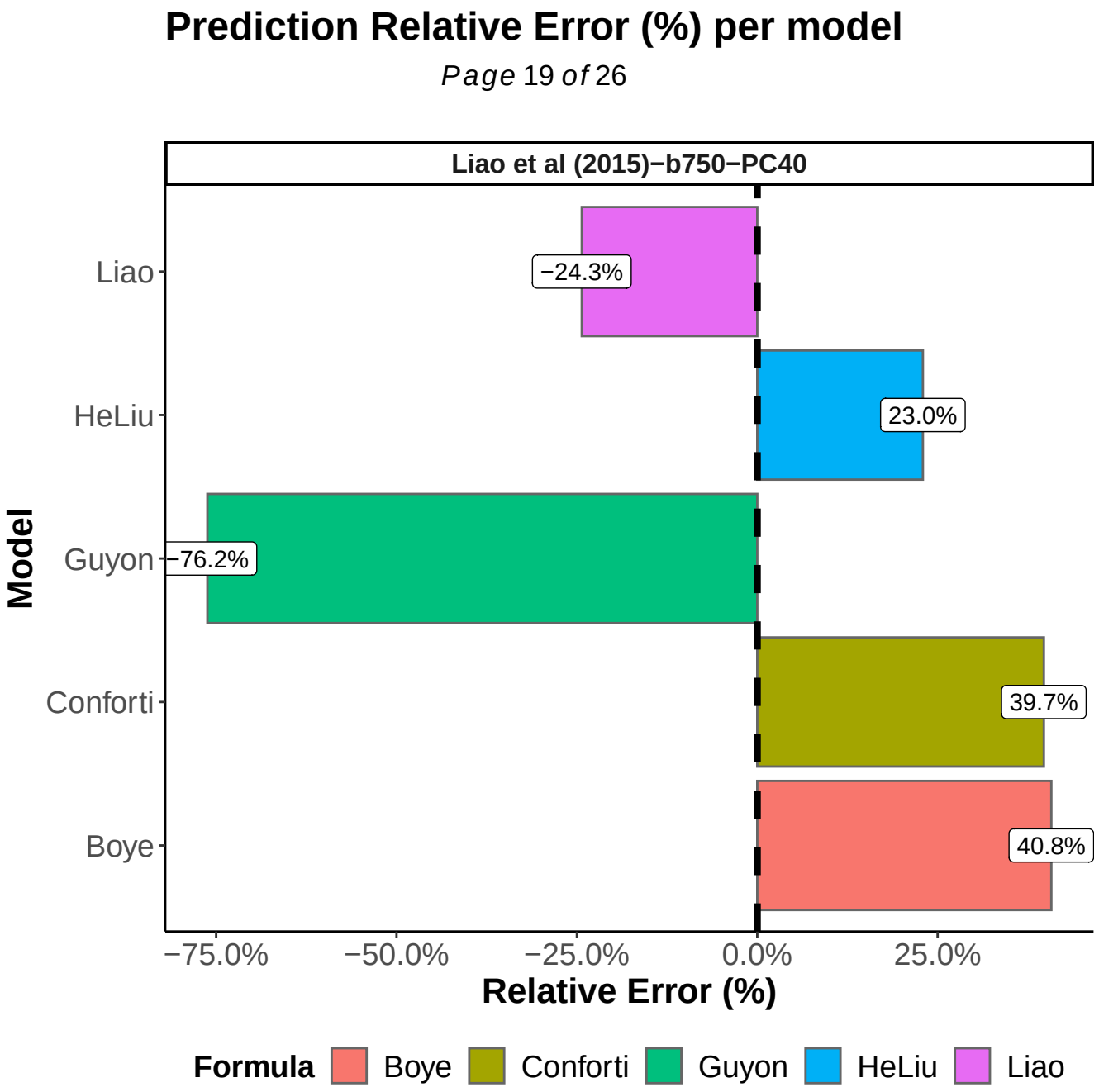
Prediction Relative Error (%) per model
Page 19 of 26
Liao et al (2015)−b750−PC40
Liao
HeLiu
Guyon
Conforti
Boye
Model
−24.3%
23.0%
−76.2%
39.7%
40.8%
−75.0%
−50.0%
−25.0%
0.0%
25.0%
Relative Error (%)
Formula
Boye
Conforti
Guyon
HeLiu
Liao

Prediction Relative Error (%) per model

Page 20 *of* 26

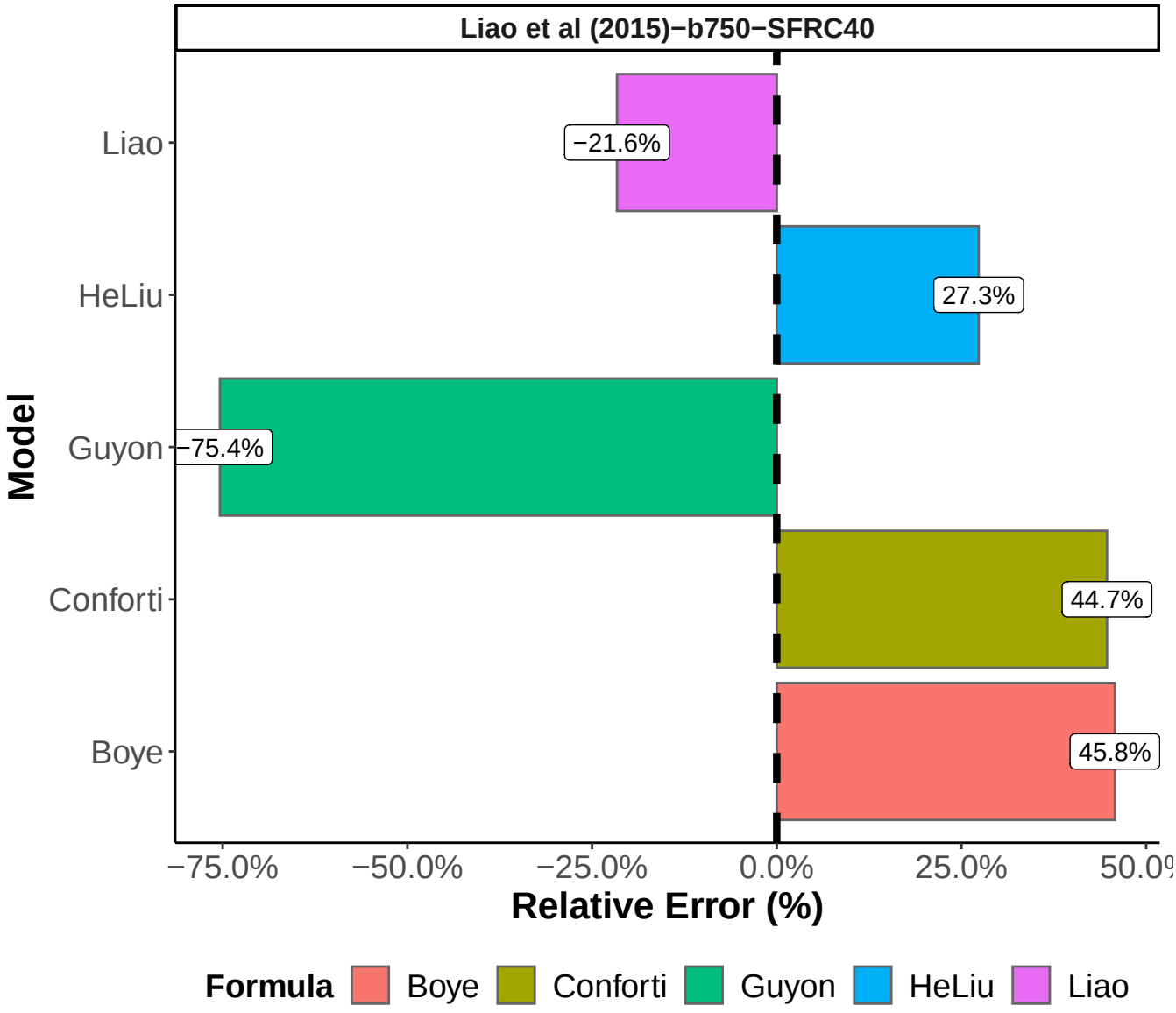

Prediction Relative Error (%) per model

Page 21 *of* 26

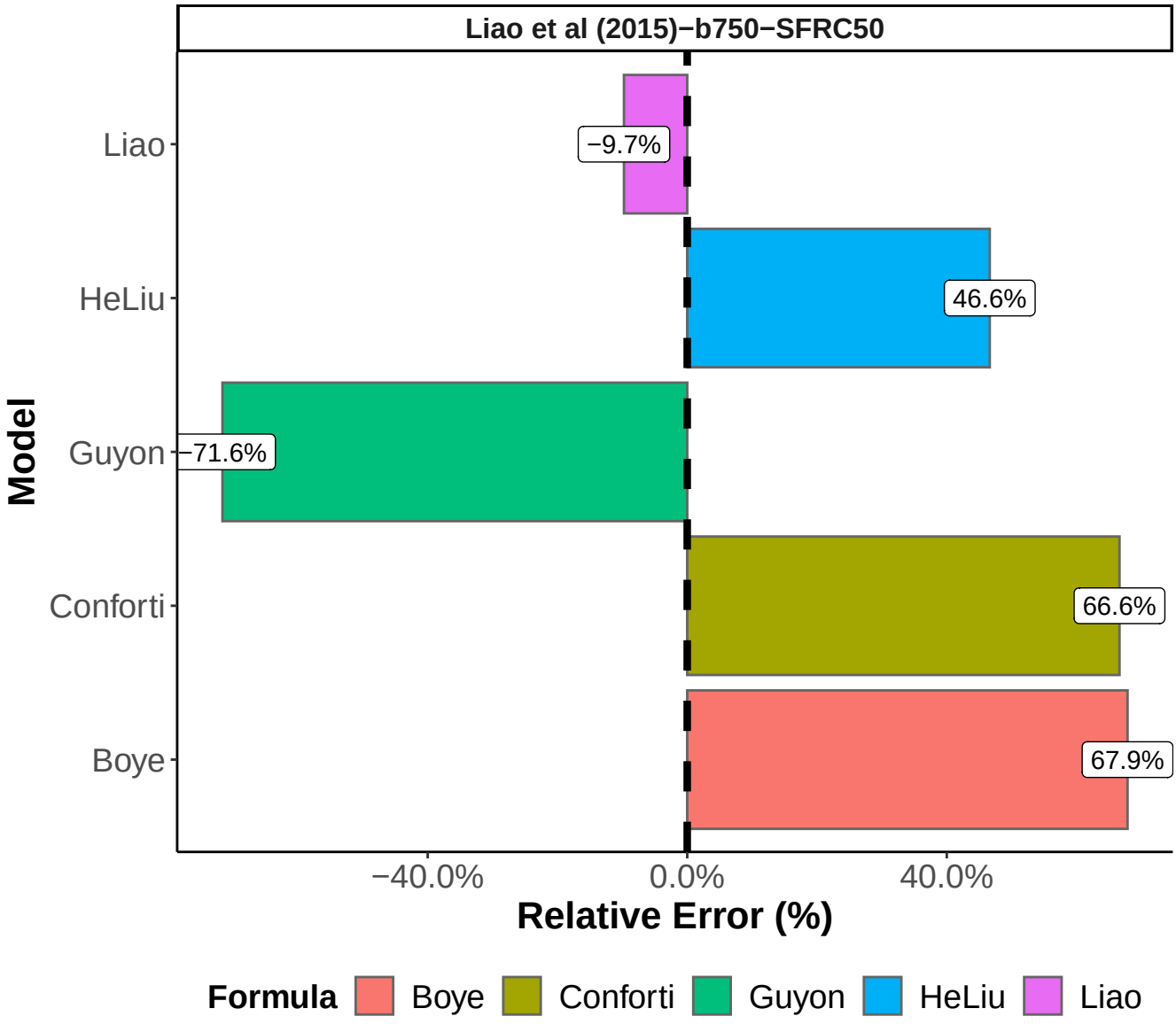

Prediction Relative Error (%) per model

Page 22 of 26

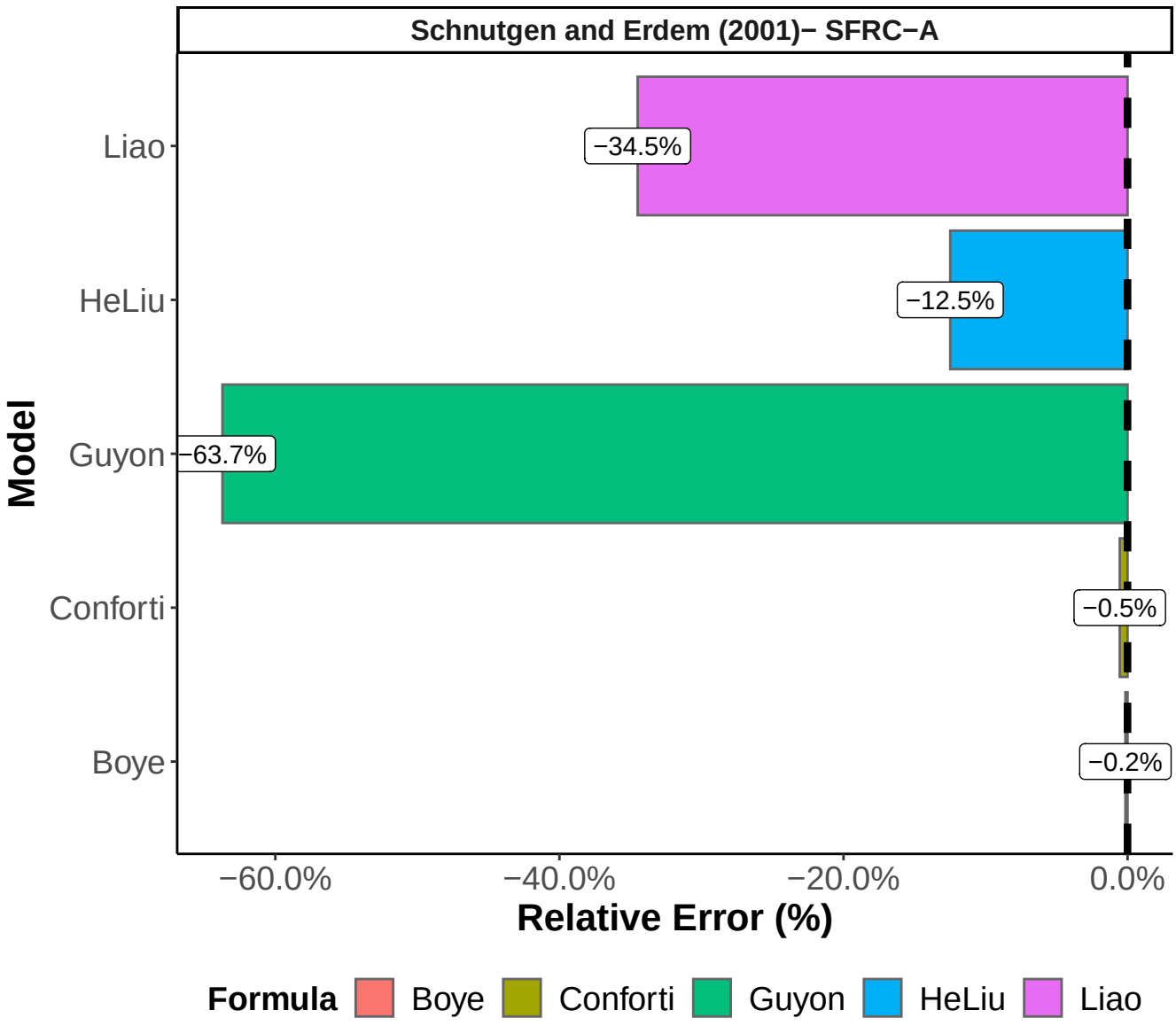

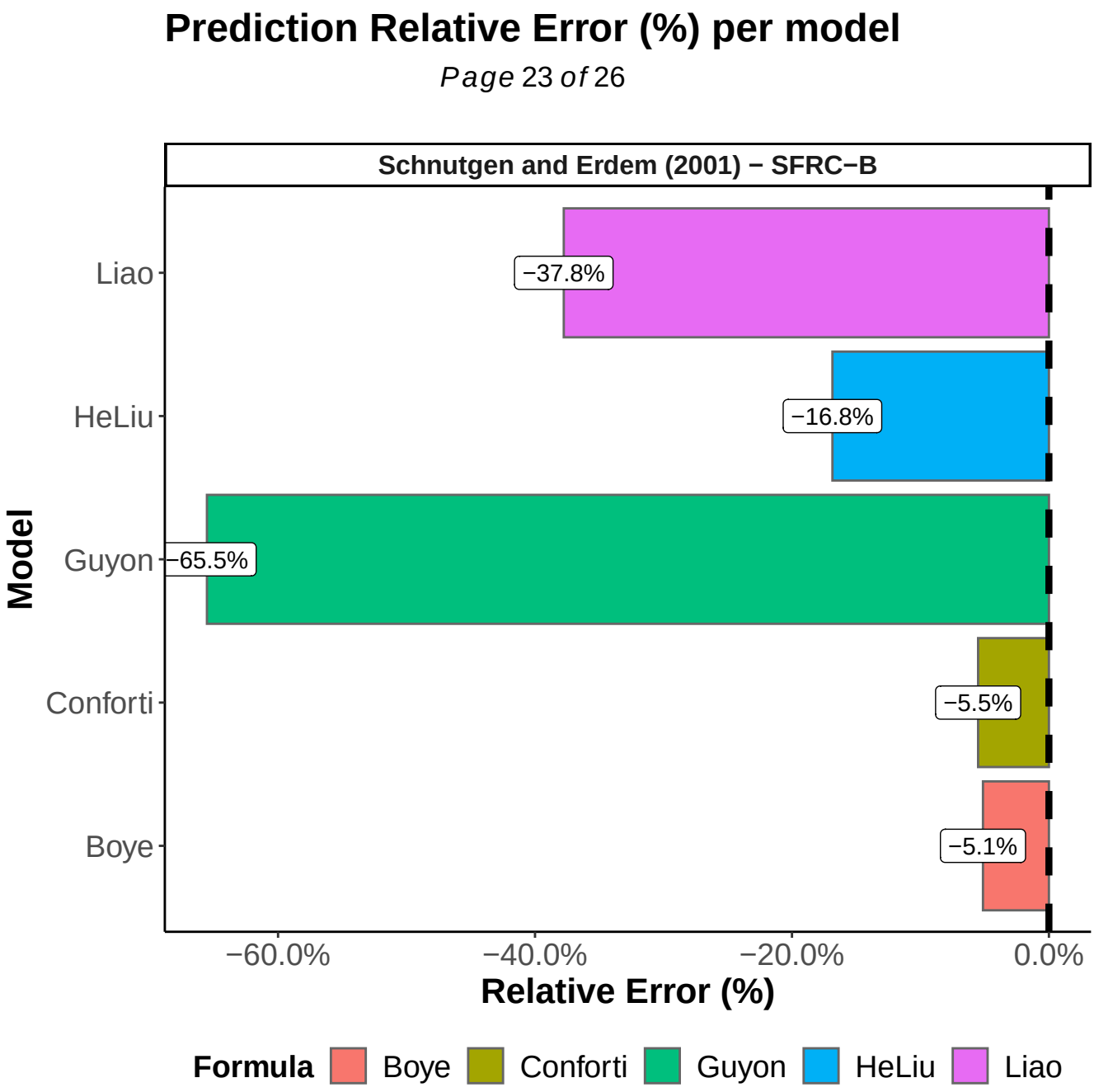
Prediction Relative Error (%) per model
Page 23 of 26
Schnutgen and Erdem (2001) − SFRC−B
Liao
HeLiu
Guyon
Conforti
Boye
−37.8%
−16.8%
−65.5%
−5.5%
−5.1%
Model
−60.0%
−40.0%
−20.0%
0.0%
Relative Error (%)
Formula
Boye
Conforti
Guyon
HeLiu
Liao

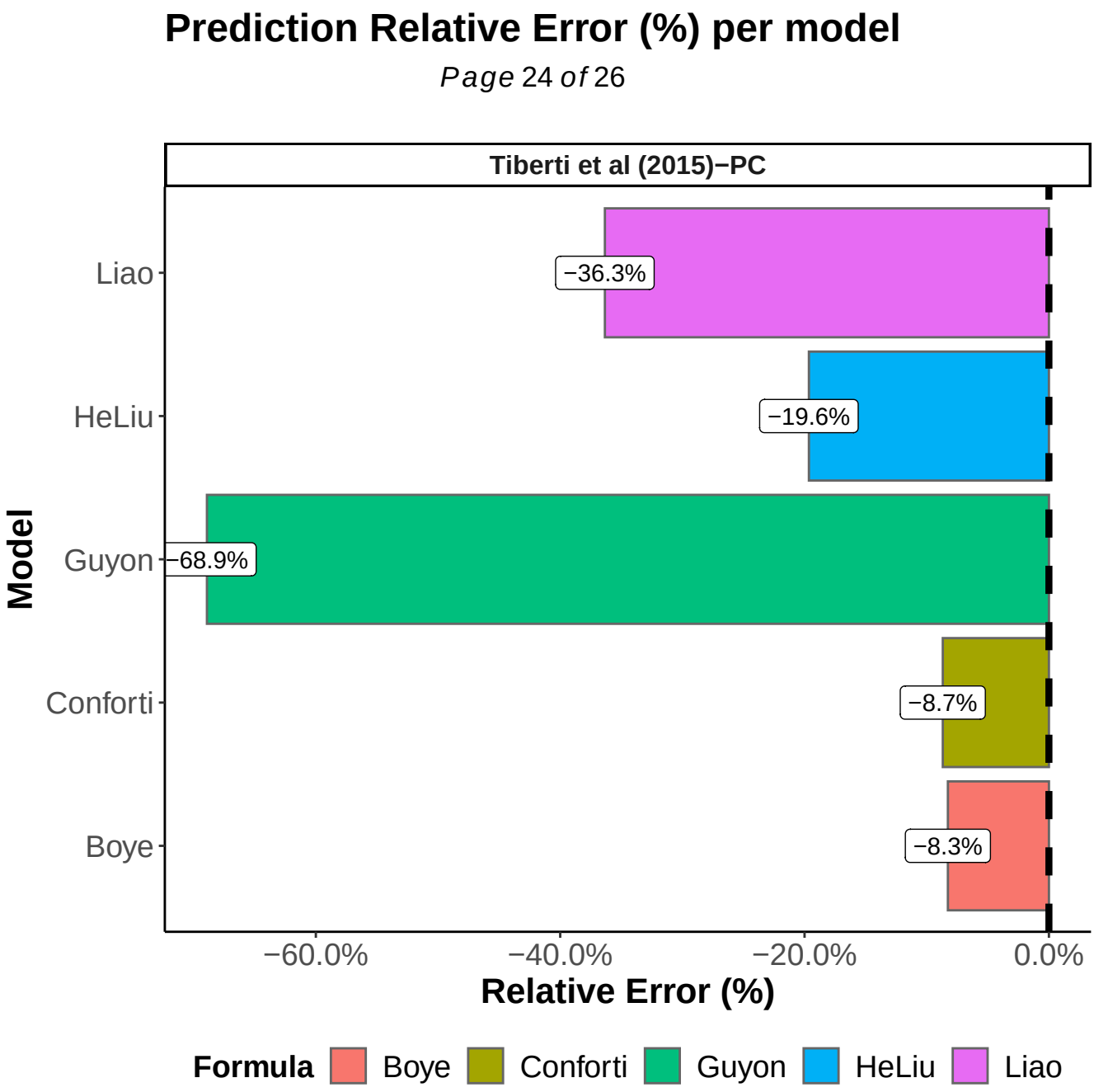
Prediction Relative Error (%) per model
Page 24 of 26
Tiberti et al (2015)−PC
Liao
HeLiu
Guyon
Conforti
Boye
−36.3%
−19.6%
−68.9%
−8.7%
−8.3%
Model
−60.0%
−40.0%
−20.0%
0.0%
Relative Error (%)
Formula
Boye
Conforti
Guyon
HeLiu
Liao

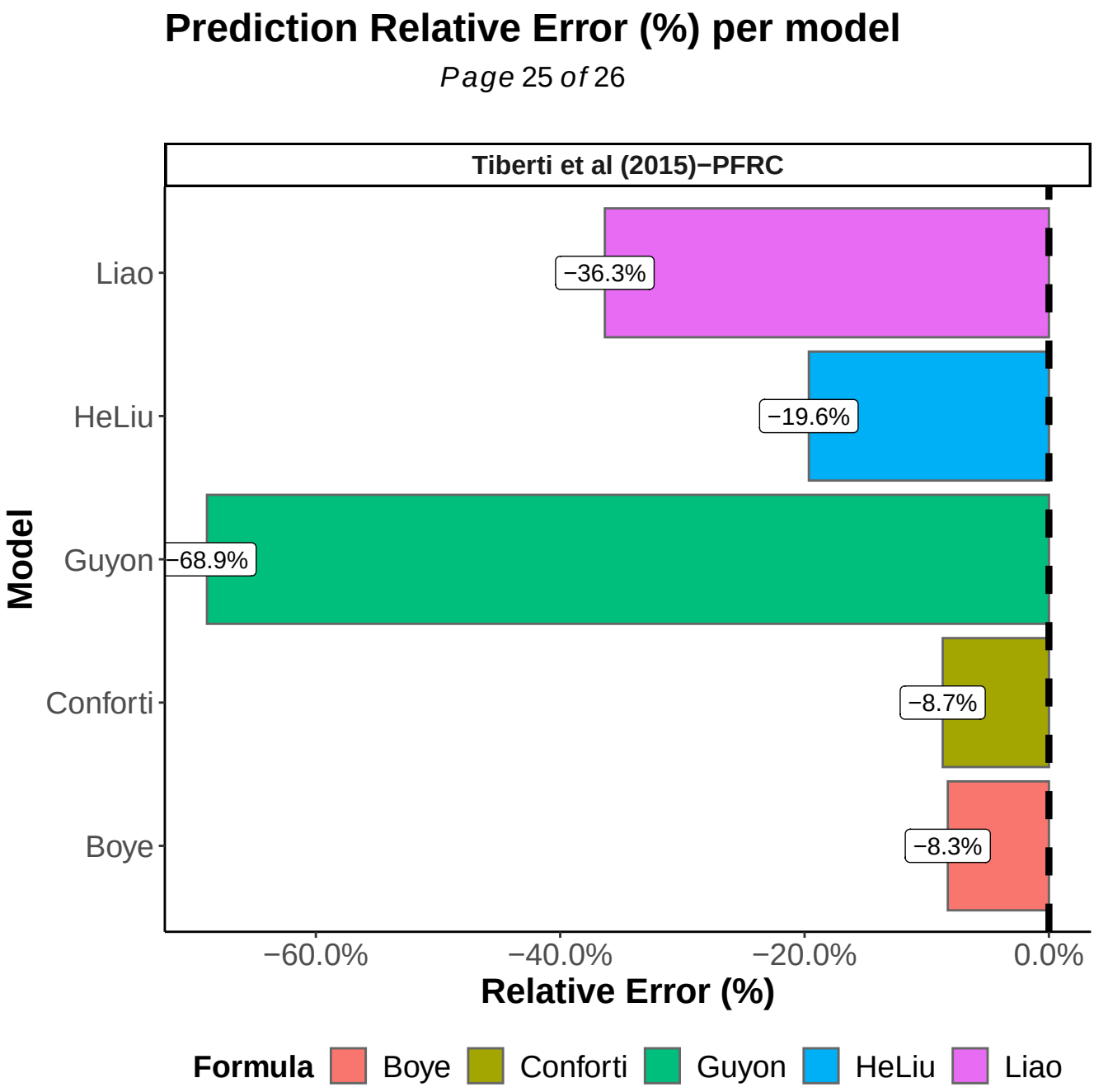
Prediction Relative Error (%) per model
Page 25 of 26
Tiberti et al (2015)−PFRC
Liao
HeLiu
Guyon
Conforti
Boye
−36.3%
−19.6%
−68.9%
−8.7%
−8.3%
Model
−60.0%
−40.0%
−20.0%
0.0%
Relative Error (%)
Formula
Boye
Conforti
Guyon
HeLiu
Liao

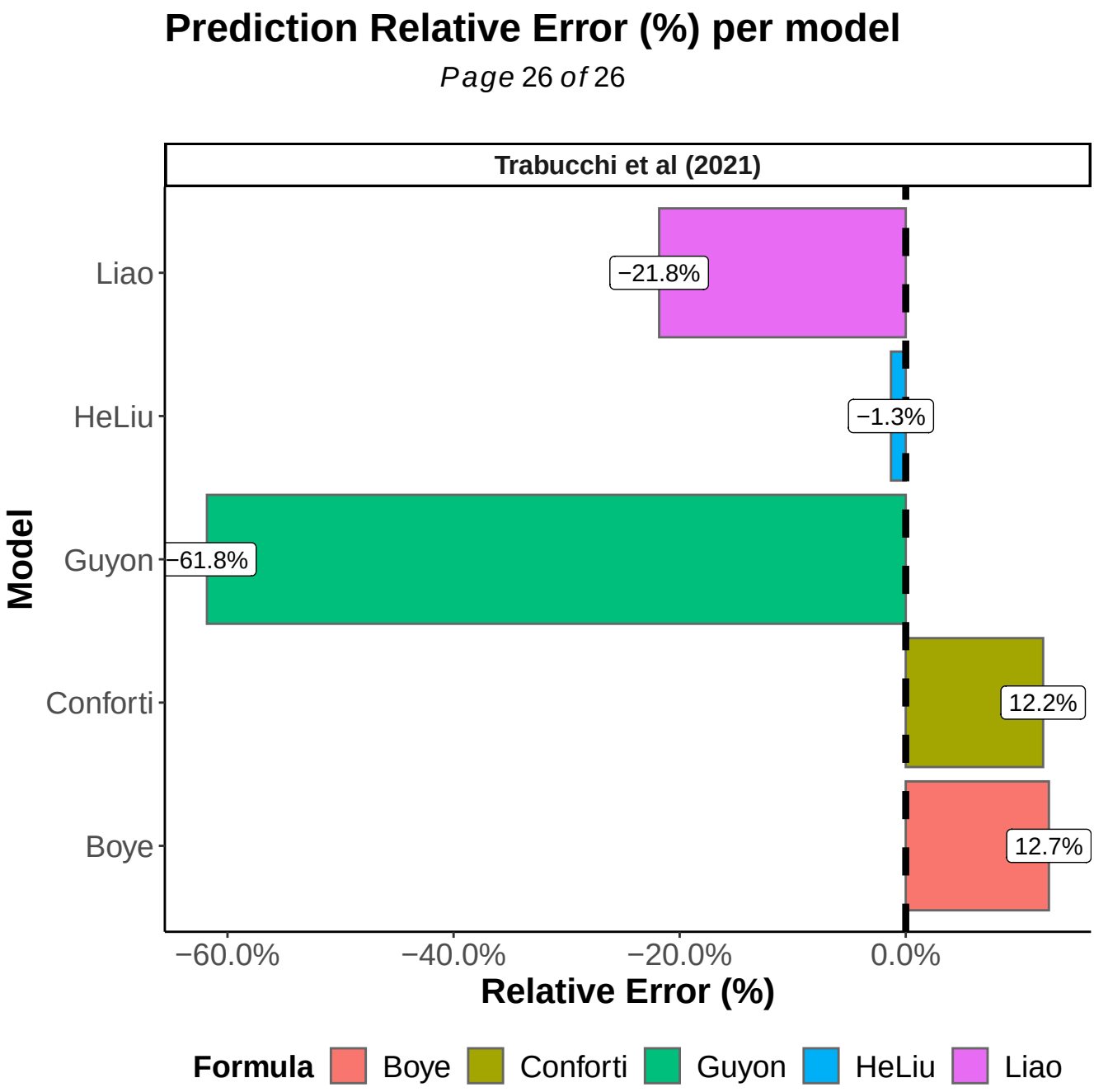
Prediction Relative Error (%) per model
Page 26 of 26
Trabucchi et al (2021)
Liao
HeLiu
Guyon
Conforti
Boye
−21.8%
−1.3%
−61.8%
12.2%
12.7%
Model
−60.0%
−40.0%
−20.0%
0.0%
Relative Error (%)
Formula
Boye
Conforti
Guyon
HeLiu
Liao